Measurement of the charge asymmetry in the top-quark dilepton decay channel in pp collision data at $\sqrt{s} = 7\,\text{TeV}$ using the ATLAS detector

DISSERTATION

zur Erlangung des Grades eines Doktors

der Naturwissenschaften

vorgelegt von

M.Sc. Hendrik Czirr

eingereicht bei der Naturwissenschaftlich-Technischen Fakultät

der Universität Siegen

Siegen 2014

Gutachter der Dissertation:	Prof. Dr. Ivor Fleck Prof. Dr. Markus Risse
Datum der Disputation	24 September 2014

Gedruckt auf alterungsbeständigem holz- und säurefreiem Papier.

Measurement of the charge asymmetry in the top-quark dilepton decay channel in pp collision data at $\sqrt{s} = 7\,\text{TeV}$ using the ATLAS detector

by M.Sc. Hendrik Czirr

Abstract

A measurement of the top-quark pair charge asymmetry in the dileptonic decay channel is presented. The analysis is performed using a dataset corresponding to an integrated luminosity of $4.7\,\text{fb}^{-1}$ of proton-proton collision data at $\sqrt{s} = 7\,\text{Tev}$ recorded by the ATLAS detector. The event selection requires exactly two high energetic charged leptons (electrons or muons), large missing transverse energy and a minimum of two jets. The kinematic system of the initial top-quark pair is reconstructed using the Kinematic Likelihood Fitter. This thesis focuses on the calculation of the central charge asymmetry $A_{C,t\bar{t}}$, as an observable for the top-quark pair charge asymmetry. Iterative Bayesian unfolding is applied to correct for acceptance and detector resolution effects on the observable and to obtain the value of $A_{C,t\bar{t}}$ at parton level. The central asymmetry after application of the unfolding procedure and combination of the three possible dileptonic decay channels is measured to be

$$A_{C,t\bar{t}} = 0.055 \pm 0.041\,(\text{stat.}) \pm 0.029\,(\text{syst.})\,,$$

for an event selection with at least one jet to be tagged by a heavy flavour tagging algorithm. The value is consistent with the Standard model prediction [1, p. 11] (at $\sqrt{s} = 7\,\text{TeV}$) of

$$A_{C,t\bar{t}}^{\text{theory}} = 0.0123 \pm 0.0005\,.$$

Messung der Ladungsasymmetrie im dileptonischen Zerfallskanal eines Top-Quark Paares in pp Kollisionsdaten bei $\sqrt{s} = 7\,\text{TeV}$ aufgezeichnet mit dem ATLAS Detektor

von M.Sc. Hendrik Czirr

Zusammenfassung

In der vorliegenden Arbeit wird eine Messung der Top-Quark-Ladungsasymmetrie im dileptonischen Zerfallskanal vorgestellt. Die Analyse basiert auf einem Datensatz der mit Hilfe des ATLAS-Detektors aufgezeichnet wurde. Der Datensatz entspricht einer integrierten Luminosität von $4.7\,\text{fb}^{-1}$ von Proton-Proton Kollisionen bei einer Schwerpunktsenergie von $\sqrt{s} = 7\,\text{TeV}$. Die Ereignisselektion erfordert genau zwei hochenergetische geladene Leptonen (Elektronen und Myonen), fehlende transversale Energie und mindestens zwei Jets. Das kinematische System des zerfallenden Top-Quark-Paares wird mittels des kinematischen Likelihood-Fitters rekonstruiert. Der Fokus der Arbeit liegt auf der Berechnung der zentralen Ladungsasymmetrie $A_{C,t\bar{t}}$ als Observable der Top-Quark-Ladungsasymmetrie. Eine iterative Bayesianische Entfaltungsmethode wird genutzt um Effekte der Detektorakzeptanz und der Detektorauflösung zu korrigieren und um den Wert von $A_{C,t\bar{t}}$ auf Partonniveau zu bestimmen. Nach Anwendung der Entfaltungsmethode und der Kombination der drei möglichen dileptonischen Zerfallskanäle wurde die zentrale Ladungsasymmetrie bestimmt:

$$A_{C,t\bar{t}} = 0,055 \pm 0,041\,(\text{stat.}) \pm 0,029\,(\text{syst.})\,.$$

Dieser Wert wurde für eine Ereignisselektion bestimmt, die erfordert, dass mindestens ein Jet pro Ereignis von einem heavy flavour tagging-Algorithmus markiert wird. Das Ergebnis ist mit der Vorhersage des Standardmodells [1, p. 11] (für eine Schwerpunktsenergie von $\sqrt{s} = 7\,\text{TeV}$) vereinbar

$$A_{C,t\bar{t}}^{\text{Theorie}} = 0.0123 \pm 0.0005\,.$$

Contents

Chapter 1

Introduction

Over the course of the last fifty years, elementary particle physics has become one of the largest branches of fundamental research in natural sciences. The interplay of theoretical prediction and high precision experimental verification is unprecedented.
A milestone in elementary particle physics was the discovery of the top-quark by the CDF and D0 collaborations at the Tevatron proton-antiproton collider [2], [3]. The discovery of the top-quark completed the structure of six quarks, which is described in the Standard model of particle physics. Ever since the discovery of the top-quark it has been the subject of detailed studies. The reasons are its unique features, which assign the top-quark a special role in the Standard Model of particle physics. The properties of the top-quark provide benchmarks for the validity of the theoretical background of the Standard Model and may also offer information on physics beyond the Standard Model.
The top-quark has a very large mass which is about forty times higher than the mass of the second heaviest quark. The large mass prevents the top-quark from forming bound states before it decays. Therefore, many of the properties of the top-quark can be measured directly from its decay products, which is not possible for other quarks. Although many features of the top-quark are already measured with high precision, e.g. the production cross section or the mass, some properties have so far resisted measurements of sufficient precision.
In 2011, measurements performed by the D0 collaboration at the Tevatron found a discrepancy in the top-quark forward backward (charge) asymmetry of more than three standard deviations above the next-to-leading order Standard Model prediction [4, p. 12]. After the discontinuation of the Tevatron experiments in 2011 the precision of the charge asymmetry measurement was still insufficient to validate the presence of physics beyond the Standard Model. The Large Hadron Collider at CERN features a higher centre of mass energy and instantaneous luminosity than the Tevatron, which makes it a top-quark 'factory', allowing for high precision measurements of top-quark properties. The measurement of the top-quark charge asymmetry is challenging since the production channel in which it occurs is not favoured in the proton-proton collisions at the Large Hadron Collider. Furthermore, the symmetric collision of two protons prevents the measurement of a forward backward asymmetry as it was performed at the Tevatron experiments. Only a smaller central asymmetry can be measured. In 2011, the ATLAS collaboration published a first result of the measurement of the top-quark charge asymmetry compatible with the Standard Model expectation [5, p. 13]. More recent results of the ATLAS and CMS collaborations are also

in agreement with the Standard Model expectation [6, p. 1].
In this thesis the measurement of the central charge asymmetry in the dileptonic decay channel of top-quark pair production is presented. The measurement is based on a dataset corresponding to an integrated luminosity of $4.7\,\mathrm{fb}^{-1}$ of proton-proton collision data at $\sqrt{s} = 7\,\mathrm{TeV}$ recorded by the ATLAS detector.

Chapter 2

Top Quark Charge Asymmetry in the Standard Model of Particle Physics

Since the 1970s the Standard Model of particle physics (SM) has proven to be the most successful theory, which explains a wide variety of experimental results in particle physics. Using the SM it is possible to accurately describe and predict the existence of elementary particles and their interactions with high precision. The most recent discovery consistent with the theories comprised in the SM is the discovery of a new particle in the search for the Higgs-boson which was announced in 2012 by the ATLAS and CMS collaborations [7], [8].

2.1 The Standard Model of Particle Physics

The first and foremost achievement of the SM is the description of three fundamental forces, namely the strong, the weak and the electromagnetic force, in terms of quantum gauge field theories [9, p. 1]. Thus, it provides the means to model the interactions of elementary particles in a unified way. Gravity, as the fourth fundamental force, is too weak to be observed in laboratory experiments involving elementary particles.

The most outstanding difference between the forces described in the SM lies in their ranges and strengths. The typical energy scale at which the strengths are measured is 1 GeV [9, p. 1]. The term strength is ambiguous since it depends on the distance of the interacting particles, therefore the values of the order of magnitude of the different interactions differ in literature. The following descriptions are given relative to the strength of the electromagnetic force. The electromagnetic force dictates most of the macroscopic physics interactions. It mediates between electrically charged particles, has infinite range and its strength is determined by the fine structure constant $\alpha = e^2/4\pi \approx 1/137$ [10, p. 125] (with $c = \hbar = 1$ in the vacuum), where e is the electrical charge of an electron. The strong interaction has a range of 10^{-15} m [9, p. 1] and its strength is approximately 100 times that of the electromagnetic force [11, p. 59]. The strong interaction binds particles carrying a colour charge. The weak force has a range of 10^{-17} m [9, p. 1] and is 10^{11} times weaker than the electromagnetic force [11, p. 59]. The weak charged current interaction is the only

interaction capable of changing the flavour of a quark. In 2012, the ATLAS collaboration found no evidence of a flavour changing neutral current interaction in top-quark pair production, where one top-quark decays via $t \to Zq$ [12, p. 1]. Particles carrying weak isospin are subject to the weak interaction. Gravity has an unlimited range but its strength is 10^{40} times smaller than the strength of the electromagnetic force [11, p. 59]. In the SM the weak and electromagnetic force are different instances of a single electroweak gauge theory.
In the SM the forces are mediated by gauge bosons. A boson is a particle with an integer intrinsic angular momentum (spin). The electromagnetic force is mediated by the massless, electrically neutral photon, the strong force by massless gluons carrying colour and anticolour and the weak force by the massive electrically charged W-bosons and the massive neutral Z-boson. Since the gluon itself carries colour charges, it can couple to other gluons and its coupling strength is increasing with the distance between the quarks. Therefore, quarks and gluons do not appear as free particles, but as bound states with no net colour charge [13] (colour confinement) or, to be more precise, as singlets w.r.t. the SU(3) of colour [14, p. 2]. Bound states can be comprised of a quark-antiquark pair (meson) or three quarks (baryons). Particles comprised of quarks are called hadrons. The electric charge of the W-boson causes possible couplings to photons implying a uniting gauge theory of both mediated forces [9, p. 2]. Furthermore, the W-boson can couple to the Z-boson (WWZ vertex) and has a quartic self coupling ($WWWW$ vertex). The properties of the gauge bosons are listed in Table 2.1.

Gauge boson	Mass	Charge	Mediated force
Photon: γ	$< 1 \times 10^{-18}\,\mathrm{eV}$	$< 1 \times 10^{-35}\,\mathrm{e}$	electromagnetic
Gluon: g	0 (theoretical value)	0 (theoretical value)	strong
$\mathrm{W}^{\pm}$	$(80.385 \pm 0.015)\,\mathrm{GeV}$	$\pm\,\mathrm{e}$	weak
Z	$(91.1876 \pm 0.0021)\,\mathrm{GeV}$	0	weak

Table 2.1.: Overview of the properties of gauge bosons in the SM [13].

Besides the four gauge bosons the SM describes twelve different spin 1/2 particles, and the corresponding antiparticles. They are assumed to bear no further inner structure and are the building blocks of all observable matter. These particles carry half integer spin and are called fermions. The fermions can be divided in six quarks and six leptons, with each group arranged in three generations. The distinction between the individual fermions is made via their mass and their quantum numbers, i.e. the electric charge (Q) and the third component of the weak isospin (I_3). The fermion properties are listed in Table 2.2 for leptons and in Table 2.3 for quarks. Fermions and quarks in each generation form an isospin doublet. The SM combines quantum chromodynamics (QCD), Yang-Mills theory and electroweak physics to a

$$SU(3)_C \times U(2)_L \times U(1)_Y\,, \tag{2.1}$$

gauge symmetry group with the colour charge (C), the weak isospin (L) and the hypercharge (Y) gauge groups [13].

Generation	Lepton		Mass	Q	I_3
1.	Electron neutrino:	ν_e	$< 2\,\mathrm{eV}$	0	1/2
	Electron:	e	$0.510999\,\mathrm{MeV}$	$-\,\mathrm{e}$	$-1/2$
2.	Muon neutrino:	ν_μ	$< 0.19\,\mathrm{MeV}$	0	1/2
	Muon:	μ	$105.66\,\mathrm{MeV}$	$-\,\mathrm{e}$	$-1/2$
3.	Tau neutrino:	ν_τ	$< 18.2\,\mathrm{MeV}$	0	1/2
	Tau:	τ	$(1776.82 \pm 0.16)\,\mathrm{MeV}$	$-\,\mathrm{e}$	$-1/2$

Table 2.2.: Overview of the lepton properties (electric charge Q and third component of the weak isospin I_3) in the SM [13]. If no error is stated the error is significantly smaller than the precision given in this table.

Generation	Quark		Mass	Q	I_3
1.	Up:	u	$(2.3^{+0.7}_{-0.5})\,\mathrm{MeV}$	$2/3\,\mathrm{e}$	1/2
	Down:	d	$(4.8^{+0.5}_{-0.3})\,\mathrm{MeV}$	$-1/3\,\mathrm{e}$	$-1/2$
2.	Charm:	c	$(1.275 \pm 0.025)\,\mathrm{GeV}$	$2/3\,\mathrm{e}$	1/2
	Strange:	s	$(95 \pm 5)\,\mathrm{MeV}$	$-1/3\,\mathrm{e}$	$-1/2$
3.	Top:	t	$(173.07 \pm 0.52 \pm 0.72)\,\mathrm{GeV}$	$2/3\,\mathrm{e}$	1/2
	Bottom:	b	$(4.18 \pm 0.03)\,\mathrm{GeV}$	$-1/3\,\mathrm{e}$	$-1/2$

Table 2.3.: Overview of the quark properties (electric charge Q and third component of the weak isospin I_3) in the SM [13]. If no error is stated the error is significantly smaller than the precision given in this table.

2.1.1 Quantum Electrodynamics and Electroweak Unification

The Noether theorem [15] implies that for each symmetry of a system/theory a conserved quantity can be derived by investigation of the behaviour of the system/theory under symmetry transformations (i.e. gauge transformations in elementary particle physics). The most basic symmetries and conserved quantities are e.g. *translation in time* $\leftrightarrow$ *energy conservation* or *translation in space* $\leftrightarrow$ *momentum conservation*. The concept of global gauge invariance is easily comprehensible since a physics principle is deemed independent of a certain point in space and time. The theory of elementary particle physics demands that a gauge invariance should also hold locally, meaning the theory is invariant under a gauge transformation which depends on a certain point is space and time [11, pp. 358-361]. The global and local phase transformations of a wave function Ψ can be written as

$$\text{global} \leftrightarrow \text{local} : \; e^{-iq\lambda}\Psi \; \leftrightarrow \; e^{-iq\lambda(x)}\Psi \,, \tag{2.2}$$

where q is the charge of the particle involved and $x \equiv x_\mu$ in this case [11, p. 358]. Subsequent phase transformations commute, the underlying symmetry is $U(1)$. The application of a local phase transformation to the Dirac Lagrangian

$$\mathcal{L} = \bar{\Psi}\left(i\gamma^\mu \partial_\mu - m\right)\Psi \tag{2.3}$$

reveals that without modification the Dirac Lagrangian is not locally phase invariant:

$$\mathcal{L} \rightarrow \mathcal{L} + \left(q\bar{\Psi}\gamma^\mu\Psi\right)\partial_\mu\lambda(x) \,, \tag{2.4}$$

where γ^μ are the Dirac matrices. The difference between the global and local phase transformation originates from the calculation of the derivatives of the fields

$$\partial_\mu\left(e^{-iq\lambda(x)}\Psi\right) = -iq\left(\partial_\mu\lambda(x^\mu)\right)e^{-iq\lambda(x)}\Psi + e^{-iq\lambda(x)}\partial_\mu\Psi \,. \tag{2.5}$$

Local gauge invariance is obtained by replacing each derivative ∂_μ by the covariant derivative D_μ:

$$D_\mu = \partial_\mu + iqA_\mu \,, \tag{2.6}$$

where A_μ is a massless vector field which transforms like

$$A_\mu \rightarrow A_\mu + \partial_\mu\lambda(x) \,, \tag{2.7}$$

in coordination with the local phase transformation of Ψ. With this replacement the transformed derivative is given by

$$D_\mu\Psi \rightarrow e^{-iq\lambda(x)}D_\mu\Psi \tag{2.8}$$

and the Lagrangian is invariant under local phase transformations. The application of local phase invariance introduces a coupling of an external field Ψ to a massless vector-field A_μ, i.e. the coupling of an electrically charged particle to a photon. The full expression obtained is the Lagrangian of quantum electrodynamics (QED):

$$\mathcal{L}_{QED} = \sum_n \bar{\Psi}_n\left(i\gamma^\mu D_\mu - m_n\right)\Psi_n - \frac{1}{4}F_{\mu\nu}F^{\mu\nu} \,, \tag{2.9}$$

with $F_{\mu\nu} = \partial_\mu A_\nu - \partial_\nu A_\mu$ and Ψ_n being the bispinor field of the nth electrically charged fermion.

In analogy to the two spin states of an electron in a magnetic field the proton and the neutron can be described as two isospin settings of a nucleus. An isospin transformation is then represented by a 2×2 matrix (U) which has to be unitary in order to conserve the norm. These matrices with determinant one are the generators of the $SU(2)$ group. Considering an infinitesimal transformation [16, pp. 159,160]

$$U = 1 + i\xi \,, \tag{2.10}$$

using unitarity $U^\dagger U = 1$ and $\det(U) = 1$ it can be derived that ξ is Hermitian and fulfils $\mathrm{Tr}(\xi) = 0$. The Pauli matrices τ_j match all these criteria, ξ can therefore be written in terms of τ_j:

$$\xi = \frac{1}{2}\left(\epsilon_1\tau_1 + \epsilon_2\tau_2 + \epsilon_3\tau_3\right). \tag{2.11}$$

A finite rotation around an angle α in the isospin space is then obtained by n infinitesimal transformations with $\epsilon_i = \alpha_i/n$:

$$U = \lim_{n\to\infty}\left(1 + \frac{i}{2n}\vec{\tau}\cdot\vec{\alpha}\right)^n = e^{\frac{i}{2}\vec{\tau}\cdot\vec{\alpha}} \tag{2.12}$$

where $\vec{\tau}$ is a vector containing the three Pauli matrices and $\vec{\alpha}$ a vector containing three rotation angles in isospin space. The differences to the phase transformation described in Equation 2.2 are that $SU(2)$ transformations do not commute, that they form a non Abelian group and that there are three angles α. The derivation of the gauge fields for the weak interaction is achieved in analogy to the QED case.

In the 1960s Glashow, Salam and Weinberg proposed a combination of the $SU(2)_L$ and the $U(1)_Y$ groups to the $SU(2) \times U(1)$ group, thus unifying the theory of the electromagnetic and the weak interaction to the electroweak theory [17], [18], [19]. The generators of the $SU(2)_L$ group are the Pauli matrices (see Equation 2.12) and the generator of the $U(1)$ group is the weak hypercharge $Y = 2\,(Q - I_3)$, where Q is the electric charge and I_3 is the third component of the weak isospin. The $U(1)$ (electromagnetic) gauge field is denoted as $B_{\mu\nu}$:

$$B_{\mu\nu} = \partial_\mu B_\nu - \partial_\nu B_\mu \,. \tag{2.13}$$

The $SU(2)$ gauge field is given by $W^i_{\mu\nu}$ with $i = 1, 2, 3$ and g as the weak coupling constant:

$$W^i_{\mu\nu} = \partial_\mu W^i_\nu - \partial_\nu W^i_\mu - g\epsilon_{ijk}W^j_\mu W^k_\nu \,. \tag{2.14}$$

Using the $SU(2)$ group characteristics fermions can be combined in left-handed doublets (for quarks and leptons) and right handed singlets. The doublets are given by:

$$q^i_L = \begin{pmatrix} q^i_{\text{up-type}} \\ q^i_{\text{down-type}} \end{pmatrix}_L \quad \text{and} \quad l^i_L = \begin{pmatrix} \nu^i_l \\ l^i \end{pmatrix}_L . \tag{2.15}$$

With the isospins listed in Tables 2.2 and 2.3 the corresponding weak hypercharges are $Y_q = 1/3$ for quarks and $Y_l = -1$ for leptons. Right handed singlets (bearing $I_3 = 0$) however do not transform under $SU(2)$. A local $SU(2)_L$ transformation for the left-handed

fermion doublet containing e.g. first generation leptons is then given by [16, p. 163]:

$$\begin{pmatrix}\nu_e\\ e^-\end{pmatrix}_L \rightarrow \exp\left[i\frac{g}{2}\,\vec{\tau}\cdot\vec{\beta}(x)\right]\begin{pmatrix}\nu_e\\ e^-\end{pmatrix}_L , \tag{2.16}$$

with

$$g\,\vec{\beta}(x) = \vec{\alpha}(x)\,, \tag{2.17}$$

where $\vec{\alpha}(x)$ is again a vector containing three rotating angles in isospin space, depending on a certain space-time point x.
The weak hypercharge Y is an additional quantum number which can be described as a phase transformation for the left handed doublet and the right handed singlet [16, p. 163]:

$$\begin{pmatrix}\nu_e\\ e^-\end{pmatrix}_L \rightarrow \exp\left[i\left(\frac{g'}{2}Y_L\right)\chi(x)\right]\begin{pmatrix}\nu_e\\ e^-\end{pmatrix}_L , \tag{2.18}$$

$$e_R \rightarrow \exp\left[i\left(\frac{g'}{2}Y_R\right)\chi(x)\right]e_R\,, \tag{2.19}$$

where g' is the electromagnetic coupling constant, $\chi(x)$ is the local isospinor and $Y_{L,R}$ denote that the weak isospin is different for the doublet and singlet. Since the chirality states transform under $U(1)$ two separate covariant derivatives are defined.

$$D_{\mu,L} = \partial_\mu + i\tau_i\frac{g}{2}W^i_\mu + iY\frac{g'}{2}B_\mu\,, \tag{2.20}$$

$$D_{\mu,R} = \partial_\mu + iY\frac{g'}{2}B_\mu\,. \tag{2.21}$$

The coupling constants g and g' are related via the weak mixing angle θ_w:

$$\sin\theta_w = \frac{g'}{\sqrt{g^2+g'^2}}\,, \tag{2.22}$$

$$\cos\theta_w = \frac{g}{\sqrt{g^2+g'^2}}\,. \tag{2.23}$$

The weak mixing angle has to be measured since the SM does not predict a value for this quantity [13]

$$\sin^2\theta_w(M_z) = 0.23116 \pm 0.00013\,. \tag{2.24}$$

In analogy to the QED calculation the full electroweak Lagrangian is given by:

$$\mathcal{L}_{EW} = -\frac{1}{4}B_{\mu\nu}B^{\mu\nu} + \frac{1}{4}W_{\mu\nu}W^{\mu\nu} + \bar{\Psi}_L D_{\mu,L}\Psi_L + \bar{\Psi}_R\gamma^\mu D_{\mu,R}\Psi_R\,, \tag{2.25}$$

with $\frac{1}{2}\left(1-\gamma^5\right)\Psi = \Psi_L$ and $\frac{1}{2}\left(1+\gamma^5\right)\Psi = \Psi_R$. The terms containing the gauge fields in quadrature describe the self-coupling of the gauge fields, whereas the terms containing the covariant derivatives describe the interactions of left- and right-handed particles. In combination with the weak mixing angle the gauge fields provide the physical fields of the

particles mediating the electroweak interaction [13]:

$$Z_\mu = -\sin\theta_w B_\mu + \cos\theta_w W_\mu^3 \,, \tag{2.26}$$

$$A_\mu = \cos\theta_w B_\mu + \sin\theta_w W_\mu^3 \,, \tag{2.27}$$

$$W_\mu^\pm = \frac{1}{\sqrt{2}}\left(W_\mu^1 \pm i W_\mu^2\right) \,. \tag{2.28}$$

In this representation all four physical fields are massless, since also the gauge fields are massless. Gauge boson masses are introduced by electroweak symmetry breaking which is described by the Brout-Englert-Higgs (BEH) mechanism (see Section 2.1.3) [7], [8].

2.1.2 Quark Mixing

In the case of leptons the weak interaction is constrained to couplings within one generation, i.e. there is no cross generation coupling. The electroweak interaction of quarks can also occur between generations via a W-boson exchange (charged weak current). In 1963, Cabibbo suggested the introduction of the mixing angle θ_C for the weak charged current in order to reflect that the strangeness changing process is weaker than the strangeness conserving process. This leads to a vertex factor modification of $\sin\theta_C$ for the strangeness changing process and $\cos\theta_C$ for the strangeness conserving process (only the three lightest quarks were known at that point) [20]. The angle θ_C was measured experimentally to be $\theta_C = 13.5°$ [11, p. 325].

The limitation of this picture was soon shown as the theoretical decay amplitude of $K^0 \to \mu^+\mu^-$ was higher than the experimental limit [11, p. 326]. In 1970 Glashow, Iliopoulos and Maiani (GIM) postulated a fourth quark thus fixing the issue of the K^0 decay [21]. The GIM scheme suggests that the weak interaction eigenstates are used instead of the mass eigenstates of the quarks (representing the physical particles). The W-bosons therefore couple to Cabibbo rotated states [11, p. 328].

$$\begin{pmatrix} |d'\rangle \\ |s'\rangle \end{pmatrix} = \begin{pmatrix} \cos\theta_C & \sin\theta_C \\ -\sin\theta_C & \cos\theta_C \end{pmatrix} \begin{pmatrix} |d\rangle \\ |s\rangle \end{pmatrix} \tag{2.29}$$

The GIM scheme was then generalised to three generations of quarks by Kobayashi and Maskawa [22],[23], resulting in the Cabbibo-Kobayashi-Maskawa (CKM) matrix:

$$\begin{pmatrix} |d'\rangle \\ |s'\rangle \\ |b'\rangle \end{pmatrix} = \begin{pmatrix} V_{ud} & V_{us} & V_{ub} \\ V_{cd} & V_{cs} & V_{cb} \\ V_{td} & V_{ts} & V_{tb} \end{pmatrix} \begin{pmatrix} |d\rangle \\ |s\rangle \\ |b\rangle \end{pmatrix} \,. \tag{2.30}$$

The CKM matrix can be represented by four independent quantities, i.e. three Euler angles $\theta_{12}, \theta_{23}, \theta_{13}$ and a CP-violating phase:

$$V_{CKM} = \begin{pmatrix} c_{12}c_{13} & s_{12}c_{13} & s_{13}e^{i\delta} \\ -s_{12}c_{23} - c_{12}s_{23}s_{13}e^{i\delta} & c_{12}c_{23} - s_{12}s_{23}s_{13}e^{i\delta} & s_{23}c_{13} \\ s_{12}s_{23} - c_{12}c_{23}s_{13}e^{i\delta} & -c_{12}s_{23} - s_{12}c_{23}s_{13}e^{i\delta} & c_{23}c_{13} \end{pmatrix} \,, \tag{2.31}$$

with the identities $c_{ij} = \cos\theta_{ij}$ and $s_{ij} = \sin\theta_{ij}$. It is experimetally verified that $s_{13} \ll$

$s_{23} \ll s_{21} \ll 1$ therefore V_{CKM} can be written in the Wolfenstein parametrisation [13] by defining:

$$s_{12} = \quad \lambda = \quad \frac{|V_{us}|}{\sqrt{|V_{ud}|^2 + |V_{us}|^2}}\,, \tag{2.32}$$

$$s_{23} = \quad A\lambda^2 = \quad \lambda \left|\frac{V_{cb}}{V_{us}}\right|\,, \tag{2.33}$$

$$s_{13}e^{i\delta} = \quad V_{ub}^* = \quad A\lambda^3\left(\rho + i\eta\right) = \frac{A\lambda^3\left(\bar{\rho} - i\bar{\eta}\right)\sqrt{1 - A^2\lambda^4}}{\sqrt{1-\lambda^2}\left[1 - A^2\lambda^4\left(\bar{\rho} - i\bar{\eta}\right)\right]}\,. \tag{2.34}$$

with

$$\bar{\rho} - i\bar{\eta} = -\frac{V_{ud}V_{ub}^*}{V_{cd}V_{cb}^*}\,. \tag{2.35}$$

The CKM matrix written in terms of λ, A, ρ and η is then given as [13]:

$$V_{CKM} = \begin{pmatrix} 1 - \frac{\lambda^2}{2} & \lambda & A\lambda^3\left(\rho - i\eta\right) \\ -\lambda & 1 - \frac{\lambda^2}{2} & A\lambda^2 \\ A\lambda^3\left(1 - \rho - i\eta\right) & -A\lambda^2 & 1 \end{pmatrix} + \mathcal{O}\left(\lambda^4\right)\,. \tag{2.36}$$

Unitarity implies that there are six vanishing combinations of

$$\sum_i V_{ij}V_{ik}^* = \delta_{jk} \text{ and } \sum_j V_{ij}V_{kj}^* = \delta_{ik}\,. \tag{2.37}$$

These combinations can be represented as triangles in a complex plane. The quantities V_{ij} are free parameters in the SM and have to be measured experimentally. The most commonly used unitarity triangle is obtained from

$$\frac{V_{ud}V_{ub}^*}{V_{cd}V_{cb}^*} + 1 + \frac{V_{td}V_{tb}^*}{V_{cd}V_{cb}^*} = 0\,. \tag{2.38}$$

A sketch of the most common unitary triangle is shown in Figure 2.1. The representation of a combination of several measurements of CKM matrix elements is shown in Figure 2.2. The angles of the unitarity triangles shown are given by:

$$\alpha \quad = \phi_2 = \quad \arg\left(-\frac{V_{td}V_{tb}^*}{V_{ud}V_{ub}^*}\right)\,, \tag{2.39}$$

$$\beta \quad = \phi_1 = \quad \arg\left(-\frac{V_{cd}V_{cb}^*}{V_{td}V_{tb}^*}\right)\,, \tag{2.40}$$

$$\gamma \quad = \phi_3 = \quad \arg\left(-\frac{V_{ud}V_{ub}^*}{V_{cd}V_{cb}^*}\right)\,. \tag{2.41}$$

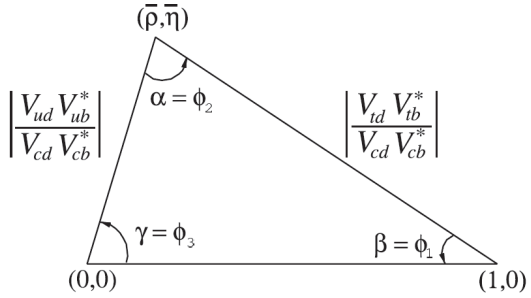

Figure 2.1.: A sketch of the most common unitarity triangle obtained from Equation 2.38, [13].

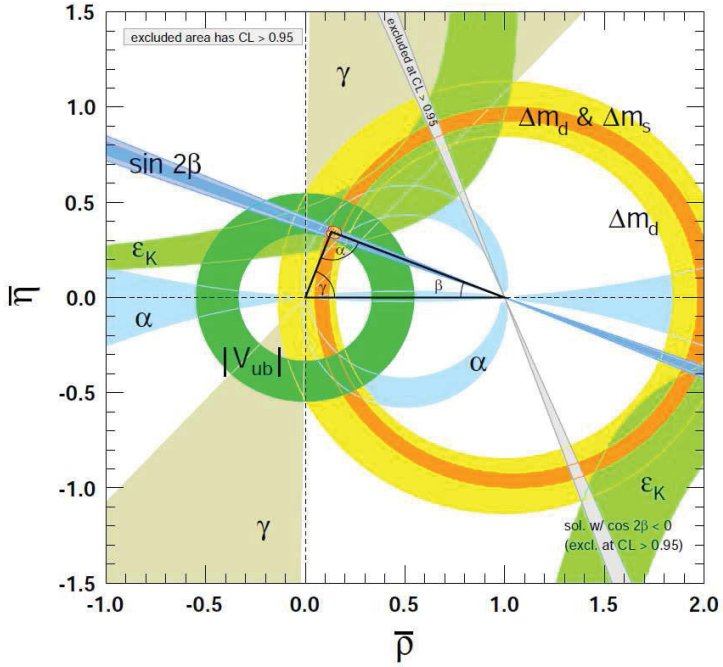

Figure 2.2.: A combination of measurements of CKM matrix elements of the unitarity triangle obtained from Equation 2.38. The shaded regions denote 95% confidence level (CL) of the corresponding measurement. The CL regions overlap consistently around the global fit region [13].

2.1.3 The Brout-Englert-Higgs Mechanism

As already mentioned in Section 2.1.1 the fields emerging from the requirement of local gauge invariance are massless. The solution to this problem is that the Lagrangian, that is derived in Equation 2.25, is not in the ground state. By re-expressing the Lagrangian in terms of its lowest energy state the initial symmetry of the Lagrangian is broken. This means that the ground state does not share the symmetries of the initial Lagrangian [11, p. 375]. The Brout-Englert-Higgs (BEH) mechanism introduces a self-interacting complex doublet of scalar fields. Three massless Goldstone bosons are generated, which give mass to the W- and Z-bosons. The second component of the doublet forms the Higgs-(scalar) boson. The masses of all fermions are generated via Yukawa couplings to the Higgs doublet

[13]. The Standard Model scalar potential is given by:

$$V(\phi) = \mu^2 \phi^\dagger \phi + \lambda \left(\phi^\dagger \phi\right)^2 , \tag{2.42}$$

where ϕ is a self interacting $SU(2)$ complex doublet with the weak hypercharge $Y = 1$ [13]:

$$\phi = \frac{1}{\sqrt{2}} \begin{pmatrix} \sqrt{2}\phi^+ \\ \phi^0 + ia^0 \end{pmatrix} , \tag{2.43}$$

where ϕ^+ and ϕ^0 are scalar fields. If the mass term μ^2 is negative the neutral component of the scalar doublet aquires a non-zero vacuum expectation value (VEV):

$$\langle \phi \rangle_0 = \begin{pmatrix} 0 \\ v \end{pmatrix} , \tag{2.44}$$

with $v = \sqrt{-\mu^2/\lambda}$. A VEV different from zero means that the symmetry is spontaneuosly (i.e. without external agency [11, p. 375]) broken. The Higgs field couples to the W_μ and the B_μ gauge fields of the electroweak theory. The Higgs Lagrangian is then given by [13]:

$$\mathcal{L}_{\text{Higgs}} = (D_\mu \phi)^\dagger (D^\mu \phi) - V(\phi) , \tag{2.45}$$

where D_μ is the covariant derivative:

$$D_\mu = \partial_\mu + i\frac{g}{2}\tau^a W_\mu^a + i\frac{g'}{2} Y B_\mu, \text{ with } a = 1, 2, 3 . \tag{2.46}$$

Here g and g' are the weak and electromagnetic coupling constants, τ^a are the Pauli matrices and Y is the weak hypercharge. This results in three 'broken' generators of the $SU(2)_L \times U(1)_Y$, the fourth generator remains unbroken since the electromagnetic $U(1)$ gauge symmetry is conserved [13]. Therefore, the photon, i.e. the corresponding gauge field, is still massless, as are the eight generators of the $SU(3)_C$ gauge symmetry (gluons, see Section 2.1.6). The gauge boson masses written in terms of the VEV are

$$M_W^2 = \frac{g^2 v^2}{4} \text{ and } M_Z^2 = \frac{\left(g'^2 + g^2\right) v^2}{4} . \tag{2.47}$$

From the fourth remaining degree of freedom of the Higgs doublet the physical Higgs-boson emerges. The Higgs boson carries no electrical charge (no coupling to photons) and transforms as a singlet under $SU(3)_C$ (no coupling to gluons). The mass of the Higgs-boson is given by $m_H = \sqrt{2\lambda} v$ where λ is the Higgs self coupling [13]. The quantity v is then determined by the Fermi coupling constant G_F

$$v = \left(\sqrt{2} G_F\right)^{\frac{1}{2}} \approx 246\,\text{GeV} . \tag{2.48}$$

The Fermi coupling constant is measured in the muon decay. If the particle discovered by ATLAS and CMS ([7], [8]) is the Higgs particle with a mass of $m_H \simeq 125\,\text{GeV}$, it would imply $\lambda \simeq 0.13$ and $|\mu| \simeq 88.8\,\text{GeV}$ [13].

2.1.4 The Yukawa Coupling

The masses of the SM fermions are generated via the interaction of the fermions with the Higgs field. This interaction is described by the Yukawa Lagrangian [13]:

$$\mathcal{L}_{\text{Yukawa}} = -\hat{h}_{d_{ij}} \bar{q}_{L_i} \phi \, d_{R_j} - \hat{h}_{u_{ij}} \bar{q}_{L_i} \tilde{\phi} \, u_{R_j} - \hat{h}_{l_{ij}} \bar{l}_{L_i} \phi \, e_{R_j} + \text{h.c.} \,. \tag{2.49}$$

The Yukawa Lagrangian does not transform with respect to the SM symmetries, but once the electroweak symmetry is broken it generates the fermion masses. In Equation 2.49 q_L (l_L), u_R, d_R (e_R) are quark (lepton) $SU(2)_L$ doublets and singlets, respectively, and $\tilde{\phi} = i\tau_2\phi^*$. Each term is parametrised by a 3×3 matrix in family space $\hat{h}_{d_{ij}}$ for down-type quarks, $\hat{h}_{u_{ij}}$ for up-type quarks and $\hat{h}_{l_{ij}}$ for leptons [13]. After electroweak symmetry breaking and the rotation of the fermions to the mass eigenstate basis the Higgs-fermion interactions $\hat{h}_{\text{f}_{ij}}$ are diagonalised

$$\hat{h}_{\text{f}_{ij}} \to h_{\text{f}} \mathbf{I} \,, \tag{2.50}$$

where $\mathbf{I}$ is the 3×3 identity matrix. Then all fermions acquire mass by:

$$m_{\text{f}} = h_{\text{f}} \frac{v}{\sqrt{2}} \,. \tag{2.51}$$

No mass predictions are made in the SM. The experimentally determined fermion masses are used to define the corresponding Yukawa couplings h_{f}. The Yukawa couplings of all fermions, but the top-quark's, are small compared to one. The exceptionally high top-quark mass of $(m_t = 173.34 \pm 0.27\,(\text{stat.}) \pm 0.71\,(\text{syst.}))\,\text{GeV}$ [24, p. 1]. results in $h_{\text{top}} \approx 1$. The presented Yukawa Lagrangian does not feature massive neutrinos but it can be expanded by adding a term similar to the up-type quark term for right handed neutrinos. Figure 2.3 shows the recent CMS results for the measurement of the Higgs-boson couplings.

2.1.5 Higgs-Boson Properties

The most recent result of the Higgs-boson mass measurement was published by the ATLAS collaboration in 2014. This measurement derives the Higgs-boson mass from a combined fit to the invariant mass spectra of the $H \to \gamma\gamma$ and $H \to ZZ^* \to 4l$ decay channels. The measured value of the Higgs-boson mass is given as [26, p. 1]

$$m_H = 125.36 \pm 0.37\,(\text{stat.}) \pm 0.18\,(\text{syst.})\,\text{GeV} \,. \tag{2.52}$$

The individual measurements used in the combination are shown in Figure 2.4. In the SM the dominant decay mode of the Higgs-boson is $H \to b\bar{b}$ for a mass of $m_H = 125\,\text{GeV}$ [27, p. 1]. The cross sections times branching ratios of the main Higgs-boson decay channels are illustrated in Figure 2.5.

The multijet background in the gluon fusion Higgs-boson production prevents the search for this decay. In the associated production of a Higgs-boson and a top-quark pair these multijet backgrounds can be significantly reduced due to the clear decay signatures of the top-quarks. Furthermore, the associated production allows for a direct measurement of the top-quarks Yukawa coupling. The results for the signal strength μ for the two decay channels of the associated production are shown in Figure 2.6.

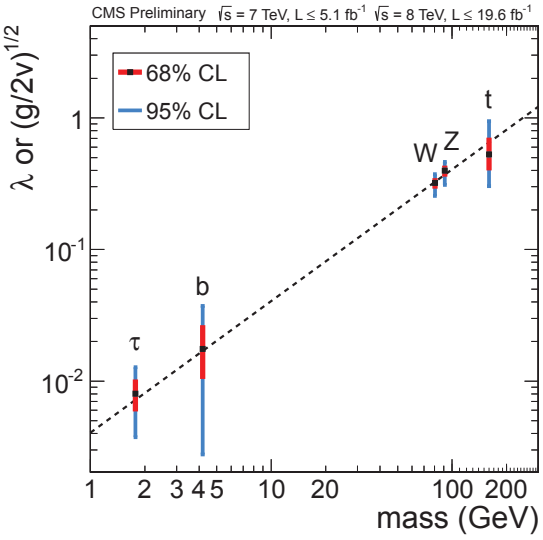

Figure 2.3.: Summary of the fits for deviations in the coupling for the generic five-parameter model not effective loop couplings, expressed as function of the particle mass [25]. For the fermions, the values of the fitted yukawa couplings $H \to ff$ are shown, while for vector bosons the square-root of the coupling for the $H \to VV$ vertex divided by twice the vacuum expectation value of the Higgs boson field is shown [25].

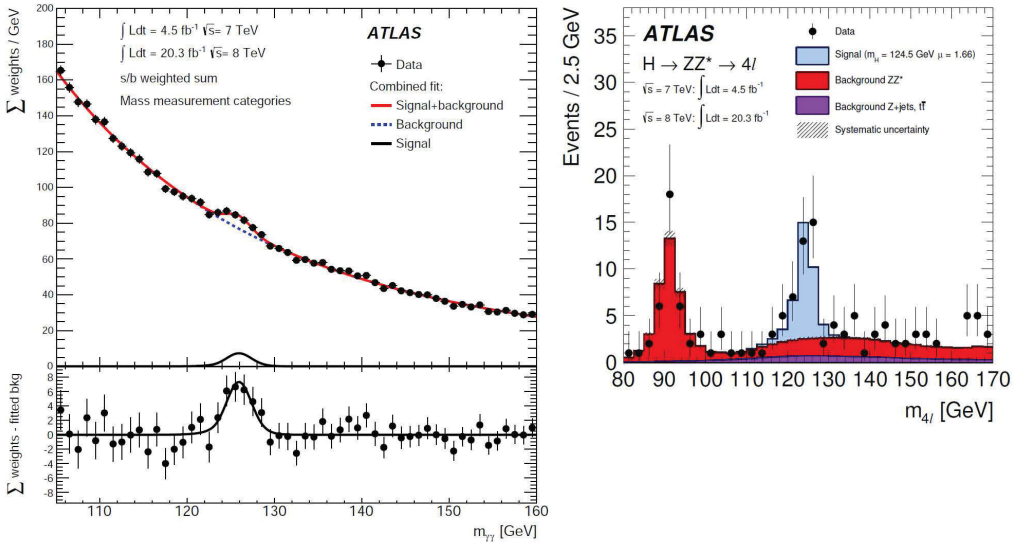

Figure 2.4.: The plot on the left-hand side shows the invariant mass distribution in the $H \to \gamma\gamma$ decay channel showing weighted data points. The fitted signal plus background and the background-only components of the fit are shown [26, p. 11]. The plot on the right-hand side shows the distribution of the four-lepton invariant mass for selected candidates. Superimposed are the expected distributions of a SM Higgs-boson signal for $m_H = 124.5\,\text{GeV}$ normalized to the measured signal strength, as well as the expected ZZ^* and reducible backgrounds [26, p. 18]. Both distributions feature a combined $\sqrt{s} = 7\,\text{TeV}$ and $\sqrt{s} = 8\,\text{TeV}$ dataset recorded using the ATLAS detector.

A recent measurement in the Higgs-boson associated production of top-quarks in the $H \to \gamma\gamma$ decay channel showed no significant excess over the background prediction of the $t\bar{t}H$ production cross section [28, p. 1]. The observed upper limit at 95% confidence level is 6.5 times the predicted SM value. The lower and upper limits at 95% confidence level on the Yukawa coupling strength parameter of the Higgs-boson to the top-quark are $\kappa_t^{\text{low}} = -1.3$ and $\kappa_t^{\text{up}} = 8.1$, where κ_t is the scale factor of the Yukawa coupling strength h_t (see Equation 2.51). A value of $\kappa_t \neq 1$ implies a modification in the BEH mechanism [28, p. 2]. Figure 2.7 illustrates the measurement of the upper and lower limits of the Yukawa coupling strength's scale factor κ_t.

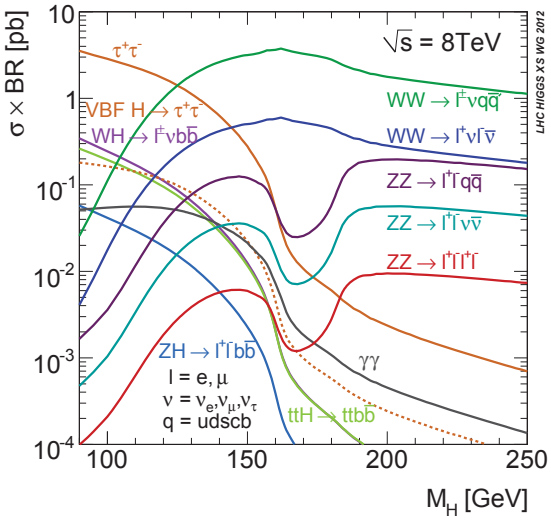

Figure 2.5.: The SM Higgs-boson production cross section times branching ratio at a centre of mass energy of 8 TeV for the main decay channels [29].

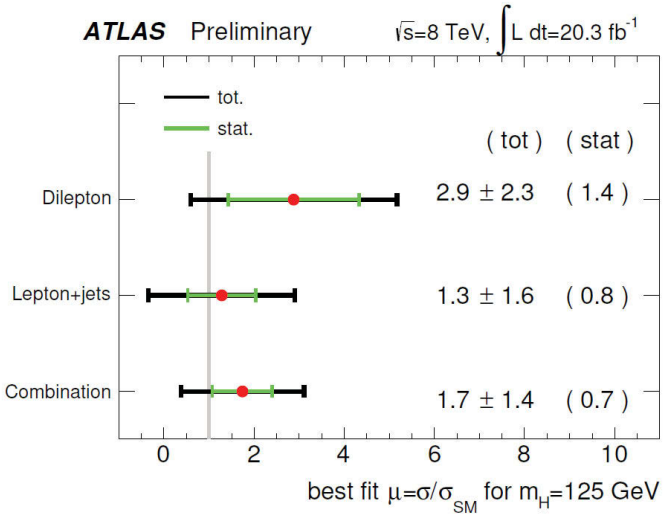

Figure 2.6.: The fitted value of the signal strength μ and the corresponding uncertainty in the individual channels, in the production of a $t\bar{t}$ event in association with a Higgs-boson. The Higgs-boson mass is assumed to be $m_H = 125\,\text{GeV}$ [27, p. 18].

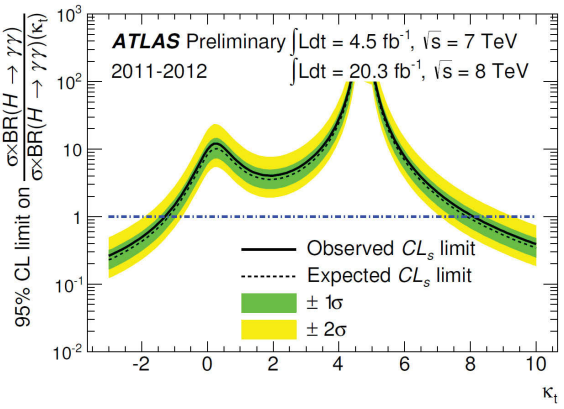

Figure 2.7.: The observed and expected upper limits on the inclusive Higgs production cross section w.r.t. the same cross section depending on the Yukava coupling strength scale κ_t. The Higgs mass is assumed to be $m_H = 125.4\,\text{GeV}$. The expected limits are calculated for $\kappa_t = 1$. All Higgs-boson production processes are taken into account for the inclusive cross section. The confidence level null hypothesis is given by continuous background-plus-SM Higgs boson production [28, p. 12].

2.1.6 Quantum Chromodynamics

Quantum chromodynamics (QCD) is the gauge field theory which describes strong interactions and denotes the $SU(3)_C$ part of the SM gauge symmetry group. While the masses of the quarks cover several orders of magnitudes ranging from few MeV to 173 GeV, the flavour itself is irrelevant in QCD [11, p. 284]. The important quantum number for the strong force is the colour. Quarks can carry one of three colours (red, green and blue) and anticolours, respectively. The mediator of the strong force is the massless gluon, which carries colour and anticolour. Following the colour $SU(3)$ symmetry the gluon exists as an colour octet. An additional colour singlet is possible (the colour symmetry group would then be $U(1)$), but it would imply a long ranged strong interaction mediated by the free gluon colour singlet [11, p. 285]. This has been experimentally excluded. The Lagrangian of QCD is given by [13]:

$$\mathcal{L}_{\text{QCD}} = \sum_q \bar{\Psi}_{q,a} \left(i\gamma^\mu \partial_\mu \delta_{ab} - g_s \gamma^\mu \frac{\lambda^C_{ab}}{2} \mathcal{A}^C_\mu - m_q \delta_{ab} \right) \Psi_{q,b} - \frac{1}{4} F^A_{\mu\nu} F^{A\,\mu\nu} \,, \tag{2.53}$$

where γ^μ are the Dirac γ-matrices, $\Psi_{q,a/b}$ are quark-field spinors for a quark of flavour q, mass m_q and colour index $a, b = 1, \ldots, N_C$ ($N_C = 3$). $\mathcal{A}^C_\mu$ correspond to gluon fields with C running from one to $N_c^2 - 1$, therefore eight different gluons exist. The λ^C_{ab} correspond to eight 3×3 matrices (Gell-Mann matrices), which are the generators of the $SU(3)$ group. The QCD coupling constant is denoted by g_s. A more common notation for the coupling constant is $\alpha_s = g_s^2/4\pi$. The field strength tensor is given by

$$F^A_{\mu\nu} = \partial_\mu \mathcal{A}^A_\nu - \partial_\nu \mathcal{A}^A_\mu - g_s f_{ABC} \mathcal{A}^B_\mu \mathcal{A}^C_\nu \,, \tag{2.54}$$

with

$$\left[\lambda^A, \lambda^B\right] = 2i f_{ABC} \lambda^C \,, \tag{2.55}$$

where f_{ABC} are the structure constants of the $SU(3)$ group.

In contrast to the electroweak force the coupling of the strong force increases with the distance between the interacting particles due to the fact that gluons are able to couple among themselves (antiscreening [11, p. 300]). This leads to two fundamental characteristics of QCD, the possibility of hadronisation and asymptotic freedom caused by the running coupling $\alpha_s(|Q^2|)$ (with Q being the transferred momentum). If the distance between two quarks increases to approximately the size of a hadron 10^{-15} m [11, p. 275], a new quark-antiquark pair is formed from the energy stored in the gluon flux between the two initial quarks. This process is called hadronisation. Due to the antiscreening effect the coupling constant for colour interaction decreases logarithmically as the momentum transfer $|Q^2|$ increases. The running coupling constant $\alpha_s(|Q^2|)$ is given by [11, p. 301])

$$\alpha_s(|Q^2|) = \frac{12\pi}{(11N_c - 2N_f)\ln(|Q^2|/\Lambda^2)}, \text{ with } |Q^2| \gg \Lambda^2 . \tag{2.56}$$

In this equation Λ marks the scale at which the coupling constant is large and therefore the perturbation theory for QCD breaks down. The QCD scale Λ_C is to be determined from experimental data and lies in the range of $(100 \leq \Lambda_C \leq 500)$ MeV [11, p. 301]. The quantity $N_c = 3$ is the number of colours and $N_f = 6$ the number of quark flavours. With increasing energy Q or decreasing distance the strong coupling runs asymptotically approaching zero (see Figure 2.8). The fact that asymptotic freedom occurs at high

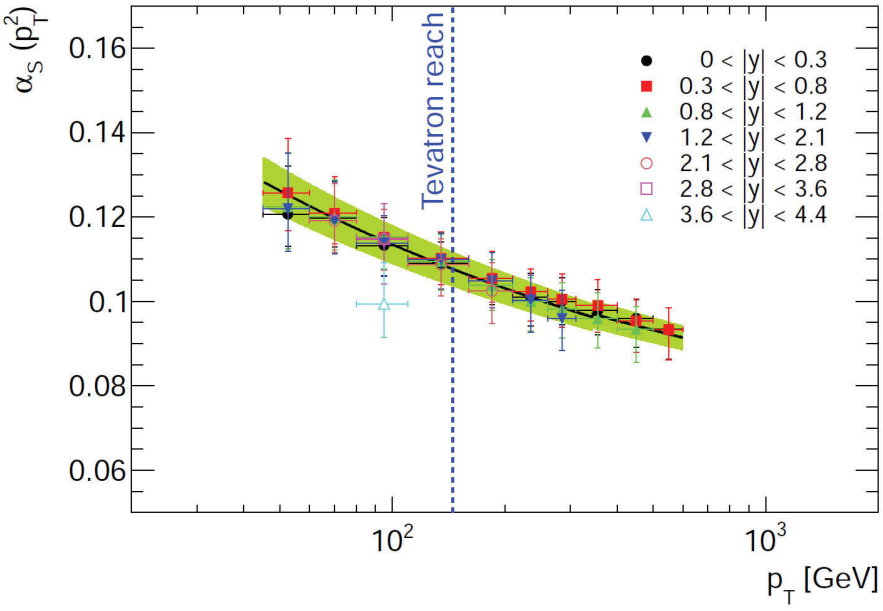

Figure 2.8.: The global weighted α_s average (green band) evolved to the corresponding scale of transverse momentum p_T together with the values derived in different bins of jet-pseudorapidity y. The blue line indicates the highest p_T value used in the Tevatron $\alpha_s(M_Z^2)$ determination from the inclusive jet cross section. The data points are derived by using proton-proton collision data taken with the ATLAS detector at a centre of mass energy of $\sqrt{s} = 7\,\text{TeV}$ [30, p. 13].

energies allows the application of perturbation theory, given the correct energy regime.

The strong coupling is usually measured at an energy corresponding to the Z-boson mass. The world average of the strong coupling constant is [31, p. 12]:

$$\alpha_s(M_Z^2) = 0.1186 \pm 0.0007\,. \tag{2.57}$$

2.2 The Top-Quark

In the 1970s, the discovery of the tau-lepton [32] and the Υ-Meson [33] (comprising a bottom and antibottom-quark) led to the conclusion that a sixth quark (the top-quark) could be discovered restoring the picture of a symmetry between the lepton and quark generations. The top-quark was then finally discovered in 1995 by the CDF and D0 collaborations at the Tevatron $p\bar{p}$ collider [2], [3].

The extraordinarily large (pole-) mass of the top-quark of $(173.07 \pm 0.52 \pm 0.72)\,\mathrm{GeV}$ [13] causes the top-quark to decay almost immediately. The lifetime of the top-quark is approximately $0.5 \times 10^{-24}\,\mathrm{s}$, which is why no bound states containing top-quarks are formed [34, p. 848]. The short lifetime of the top-quark grants the opportunity for measurements which are impossible to be performed on lighter quarks. Such as polarisation measurements. In bound states the spin of the quarks is depolarised by chromomagnetic interactions [34, p. 836]. Due to its high mass, and therefore large Yukawa coupling, the top-quark might play a special role in electroweak symmetry breaking. A comprehensive understanding of top-quark physics is also important for future physics beyond the SM since top-quark decays will be a large source of background for new physics processes.

2.2.1 Top-Quark Pair Production

At the Large Hadron Collider (LHC) two counter-circulating proton beams collide. The process responsible for the top-quark pair production does not occur between the protons, but between the constituents contained in them. The proton contains three valence quarks (up, up, down) and numerous gluons and quark-antiquark pairs originating from gluon splitting (sea quarks). The constituents of the proton each carry a fraction x of the full proton momentum.
The description of hadron-hadron interactions can be broken into a hard scattering partonic cross section, which can be calculated using perturbative QCD and non-perturbative QCD corrections which are factored into the parton longitudinal momentum distribution functions (i.e. parton density function) [34, p. 844]. The separation between short distance, hard scattering and long distance interactions is called factorisation. The hard scattering process between two partons i and j is denoted by σ^{ij} and the longitudinal momentum distribution functions as $f_i(x_i, \mu_f^2)$, where μ_F is the factorisation scale. An example of a momentum distribution function with $x\,f\left(x, Q^2\right)$ and $Q = \mu_f = 5\,\mathrm{GeV}$ is shown in Figure 2.9. In higher order calculations infinities from ultraviolet divergences appear and are removed by a renormalisation procedure. This introduces an arbitrary renormalisation scale μ_R^2 [34, p. 844]. Usually the renormalisation scale is chosen as $\mu_f^2 = \mu_R^2$. The total $t\bar{t}$ pair

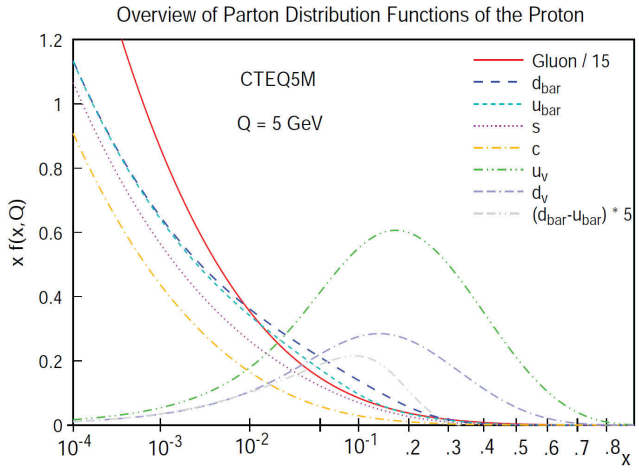

Figure 2.9.: The momentum distribution functions for (anti-)quarks and gluons as a function of longitudinal proton momentum from the CTEQ5M [35] parametrisation [36, p. 4].

production cross section at the centre of mass energy $\sqrt{s}$ is then given as [34, p. 844]:

$$\sigma_{t\bar{t}}\left(\sqrt{s}, m_t\right) = \sum_{i,j=q,\bar{q},g} \iint dx_i dx_j f_i\left(x_i, \mu^2\right) f_j\left(x_j, \mu^2\right) \sigma^{ij\to t\bar{t}}\left(\rho, m_t^2, x_i, x_j, \alpha_s(\mu^2), \mu^2\right) , \tag{2.58}$$

where the summation indices i and j run over all possible combinations of quarks and gluons, furthermore $\rho = 4m_t^2/\sqrt{\hat{s}}$ with the effective centre of mass energy $\hat{s} = x_i x_j s$. The Feynman diagrams of the tree level top-quark pair production are shown in Figure 2.10. The effective energy needs to be high enough to produce two top-quarks at rest $\hat{s} \geq (2m_t)^2$.

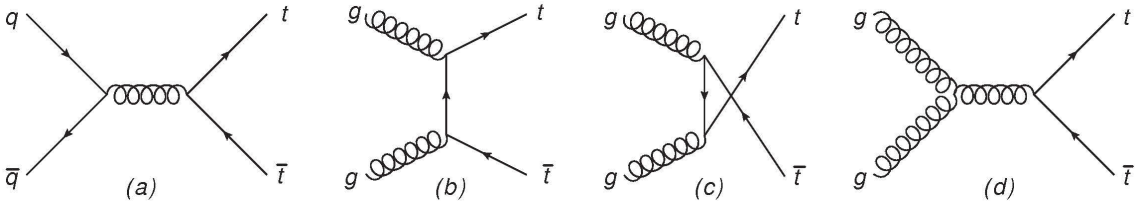

Figure 2.10.: The lowest order Feynman diagrams of top-quark pair production via the strong interaction. Diagram (a) shows the production via quark pair annihilation, the diagrams (b, c, d) the production via gluon fusion.

The typical momentum fraction $x_i \approx x_j$ at the pair production threshold is then given by

$$x \approx 2m_t/\sqrt{s}\,. \tag{2.59}$$

The typical value at the LHC is then 0.05 at a centre of mass energy of $\sqrt{s} = 7\,\text{TeV}$. At the LHC the top-quark pair production is dominated by the gluon fusion process. The $t\bar{t}$ cross section at approximate next-to-next-to leading order calculation for pp collisions at a centre-of-mass energy of $\sqrt{s} = 7\,\text{TeV}$ is $\sigma_{t\bar{t}} = 177^{+10}_{-11}\,\text{pb}$ for a top quark mass of $m_t = 172.5\,\text{GeV}$ and renormalisation and factorisation scale set to the top mass [37], [38]. For a full set of references on the top-quark pair production cross section refer to Appendix A.1. In 2012 the LHC collaborations determined the top-quark pair production

cross-section in good agreement with the SM prediction [39, p. 1]:

$$\sigma_{t\bar{t}} = 173.3 \pm 2.3\,(\text{stat.}) \pm 7.6\,(\text{syst.}) \pm 6.3\,(\text{lumi.})\,\text{pb}\,. \tag{2.60}$$

The values of the measurements, which are combined to the final value of $\sigma_{t\bar{t}}$, are illustrated in Figure 2.12. Figure 2.11 illustrates the theoretical predictions for the total hard scattering cross sections of several physics processes, which can occur at the Tevatron ($p\bar{p}$-collider) and the LHC (pp-collider). The top-quark production cross section is several orders of magnitude smaller than the cross section of e.g. W-boson or Z-boson production. In order to differentiate between these background processes and the signal process in the LHC environment an excellent theoretical understanding of both signal and background processes is necessary. Only then high precision measurements of SM properties related to the top-quark are possible. Figure 2.13 shows summary of the LHC and Tevatron measurements of the top-pair production cross section as a function of the centre of mass energy.

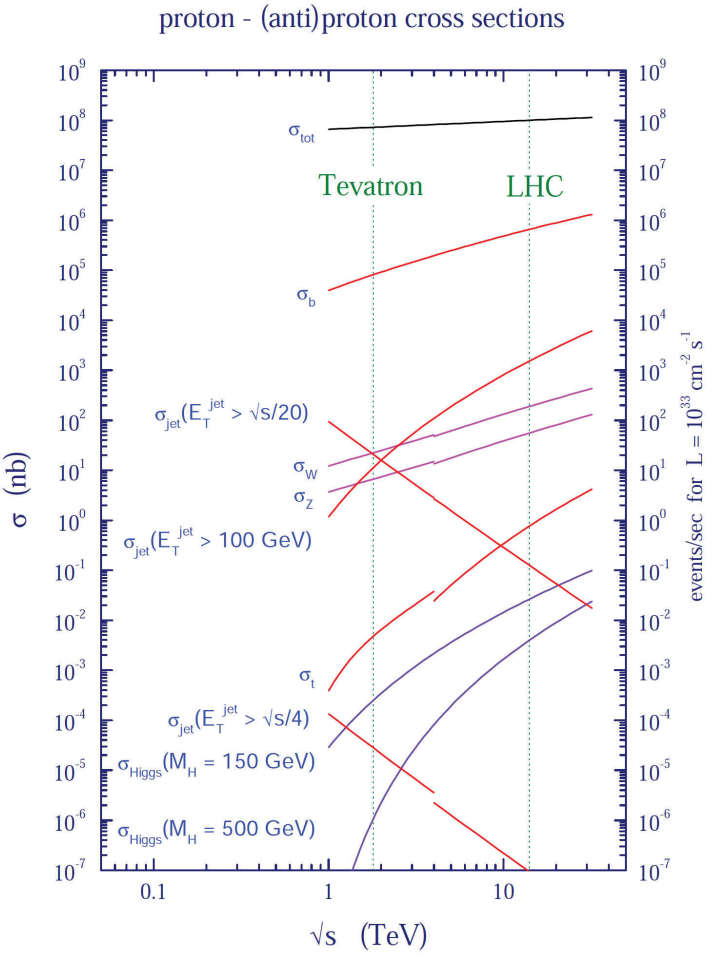

Figure 2.11.: Predictions of hard scattering cross sections of several different physics processes at the Tevatron and the LHC. The top-quark pair production cross section is denoted by σ_t. The discontinuity in the lines marks the change of the Tevatron $p\bar{p}$ production cross sections to the LHC pp production cross sections [36, p. 7].

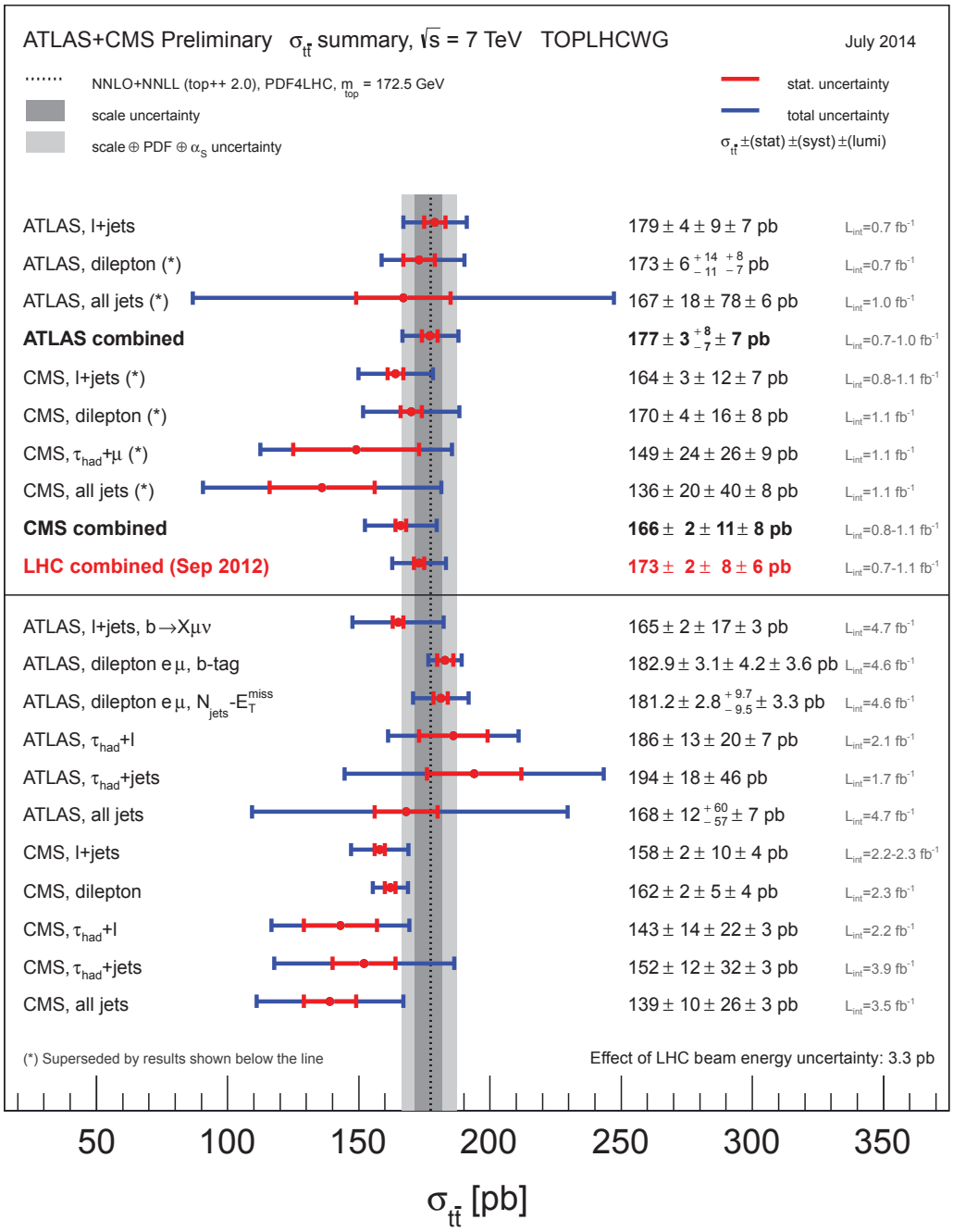

Figure 2.12.: The individual measurements of the LHC top-quark pair production cross section at $\sqrt{s} = 7\,\text{TeV}$. The grey band corresponds to the approximate NNLO QCD calculation. The upper part of the plot shows early LHC measurements and their combination. The lower part summarizes measurements performed after the LHC cross-section combination [40].

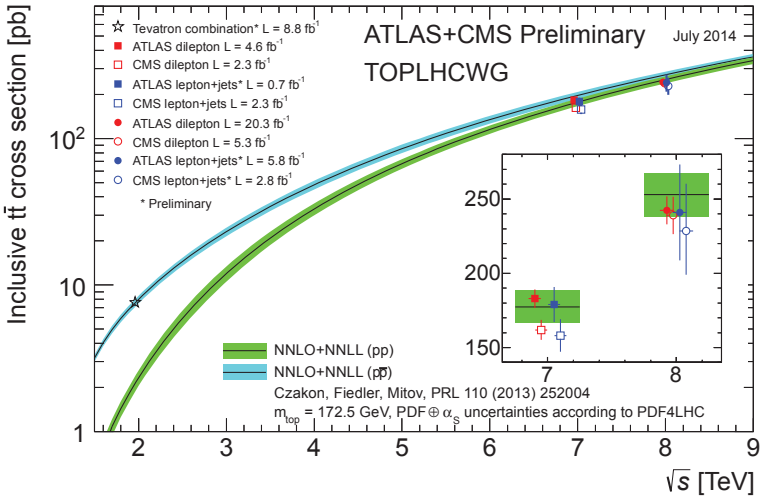

Figure 2.13.: LHC and Tevatron measurements of the top-quark pair production cross section compared to the next-to-next-to leading order QCD calculation. The bands around the theoretical prediction illustrate the uncertainties due to renormalisation/factorisation scales, parton density functions and the strong coupling. The theoretical calculation assumes $m_t = 172.5\,\text{GeV}$[40].

2.2.2 Single Top-Quark Production

Three different processes allow for the production of single top-quarks. The W-boson fusion, or t-channel process produces a single top-quark via a charged current deep inelastic scattering [41]. Furthermore there are the quark-antiquark annihilation (or s-channel production) [42] and the associated W-top production [43], [44]. The lowest order Feynman diagrams are shown in Figure 2.14. The single top-quark production processes occur via a charged current interaction, hence the corresponding cross sections are proportional to $|V_{tb}|^2\, g^2$, where V_{tb} is the CKM matrix element and g the weak coupling constant. A measurement of the cross section will offer insight on the $|V_{tb}|$ CKM matrix element as well as to the $V - A$ (vector-minus-axial-vector) structure of the top-quarks electroweak coupling. The single top-quark production is a source of background for other physics measurement e.g. some Higgs decay channels. Hence, detailed knowledge of the single top-quark production will also benefit other analyses.

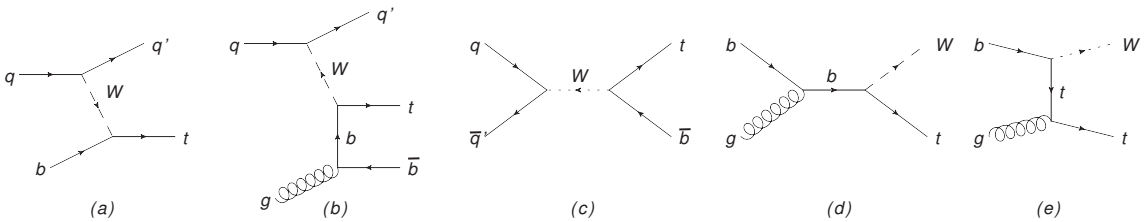

Figure 2.14.: The lowest order Feynman diagrams for single top-quark production: t-channel (a,b), s-channel (c) and W-top production (d,e).

The cross sections of the three single top-quark production processes are calculated with approximate next-to-leading order precision for $m_t = 173\,\text{GeV}$ and $\sqrt{s} = 7\,\text{TeV}$ at the

LHC. The t-channel values are taken from [45, pp. 7,8], the s-channel values from [46, pp. 6,8] and the value for the W-top production from [47, p. 6]. The associated W-top production cross section was calculated at approximate next-to-next-to-leading order. The s-channel cross section at the LHC is small compared to the t-channel cross section because the antiquarks needed in the initial state of this production channel are only provided by sea-quarks in the proton-proton collisions.

$$\sigma_t^{\text{t-channel}} = 41.7 \;{}^{+1.6}_{-0.2}\,(\text{scale}) \pm 0.8\,(\text{pdf})\,\text{pb}\,, \tag{2.61}$$

$$\sigma_{\bar{t}}^{\text{t-channel}} = 22.5 \pm 0.5\,(\text{scale}) \;{}^{+0.7}_{-0.9}\,(\text{pdf})\,\text{pb}\,, \tag{2.62}$$

$$\sigma_t^{\text{s-channel}} = 3.17 \pm 0.06\,(\text{scale}) \;{}^{+0.13}_{-0.10}\,(\text{pdf})\,\text{pb}\,, \tag{2.63}$$

$$\sigma_{\bar{t}}^{\text{s-channel}} = 1.42 \pm 0.01\,(\text{scale}) \;{}^{+0.06}_{-0.07}\,(\text{pdf})\,\text{pb}\,, \tag{2.64}$$

$$\sigma_{t,\bar{t}}^{\text{Wt-channel}} = 7.8 \pm 0.2\,(\text{scale}) \;{}^{+0.5}_{-0.6}\,(\text{pdf})\,\text{pb}\,. \tag{2.65}$$

In 2013 the ATLAS collaboration published the measurements of the t-channel [48, p. 1], the s-channel [49, p. 7] and the W-top cross section [50, p. 146]:

$$\sigma_t^{\text{t-channel}} = 41.9 \;{}^{+1.8}_{-0.8}\,\text{pb}\,, \tag{2.66}$$

$$\sigma_{\bar{t}}^{\text{t-channel}} = 22.7 \;{}^{+0.9}_{-1.0}\,\text{pb}\,, \tag{2.67}$$

$$\sigma_t^{\text{s-channel}} < 26.5\,\text{pb}\,, \tag{2.68}$$

$$\sigma_{t,\bar{t}}^{\text{Wt-channel}} = 16.8 \pm 2.9\,(\text{stat.}) \pm 4.9\,(\text{syst.})\,\text{pb}\,. \tag{2.69}$$

The t-channel measurement is in good agreement with the SM prediction. For the s-channel an upper limit was derived and for the associated W-top production a first evidence of $3.3\,\sigma$ has been found, the cross section agrees with the prediction.

2.2.3 The Top-Quark Decay

The decay width of the top quark is dominated by the decay $t \to W\,b$. The predicted SM width of the top quark is given by [34, p. 847]

$$\Gamma_t = \frac{G_F m_t^3}{8\pi\sqrt{2}} \left(1 - \frac{M_W^2}{m_t^2}\right)^2 \left(1 + 2\frac{M_W^2}{m_t^2}\right) \left[1 - \frac{2\alpha_s}{3\pi}\left(\frac{2\pi^2}{3} - \frac{5}{2}\right)\right], \tag{2.70}$$

where G_F is the Fermi constant, M_W the W-boson mass and α_s the strong coupling constant. In this equation higher order terms of $(m_b/m_t)^2$, α_s^2 and $(\alpha_s M_W^2)/(\pi m_t^2)$ are neglected. The SM predicted value for a top quark mass of $m_t = 172.5\,\text{GeV}$ is

$$\Gamma_t = 1.33\,\text{GeV}\,. \tag{2.71}$$

The top-quark decays $t \to W\,s\,(W\,d)$ are suppressed relative to the dominant $t \to W\,b$ decay by the square of the $|V_{ts}|$ and $|V_{td}|$ CKM matrix elements. This allows the measure-

ment of the $|V_{tb}|$ element via the branching ratio [34, p. 849]

$$R = \frac{B\,(t \to Wb)}{B\,(t \to Wq)} = \frac{|V_{tb}|^2}{|V_{td}|^2 + |V_{ts}|^2 + |V_{tb}|^2} = |V_{tb}|^2 \approx 1\,. \tag{2.72}$$

The denominator is equal to one under the assumption of three quark generations. In 2012, ATLAS collaboration published a result for the $|V_{tb}|$ CKM matrix element [51, p. 17]:

$$V_{tb} = 1.04^{+0.10}_{-0.11} \tag{2.73}$$

and a 95% confidence level lower limit $V_{tb} > 0.80$.

The decay of a top-quark pair is classified by the decay modes of the W-bosons. A W-boson can decay leptonically into a lepton and the corresponding neutrino or it can decay hadronically into two quarks. Hence there are three decay channels for a pair of top and antitop-quarks. Figure 2.15 illustrates the the branching fractions of a top-quark pair into the different final states.

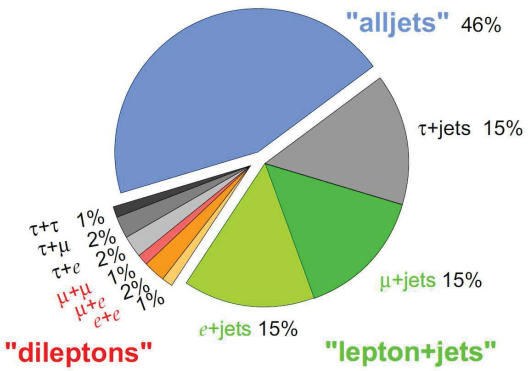

Figure 2.15.: The top-quark pair branching fractions into the three decay channels: alljets (= allhadronic), lepton+jets (= semileptonic) and dileptons (= dileptonic) [52].

- *Allhadronic final state* $t\bar{t} \to bW^+\bar{b}W^- \to bq_1\bar{q}_2\,\bar{b}q_3\bar{q}_4$: In this decay channel both W-bosons decay hadronically. This channel has the largest branching ratio of 46%, but physics analyses in the allhadronic final state suffer from the large irreducible background, since there is no clear signal signature which stands out in the QCD multijet environment of a hadron collider. The assignment of measured jets to decayed W-bosons is therefore difficult. A measurement of the $t\bar{t}$ cross section in the allhadronic channel was performed by the ATLAS collaboration in 2012 [53] using a kinematical fit exploiting the final states event topology.

- *Semileptonic final state* $t\bar{t} \to bW^+\bar{b}W^- \to bq_1\bar{q}_2\,\bar{b}l^-\bar{\nu}_l$ or $bl^+\nu_l\,\bar{b}q_1\bar{q}_2$: With one hadronically and one leptonically decaying W-boson this channels provides a large branching ratio of 45% (if the decay of a W-boson into a tau lepton is included) and a good detection signature with one high energetic lepton. This channel is often referred to as 'golden channel' in top-quark physics since it provides high statistics and a clear signature to be distinguished from the QCD multijet background.

- *Dileptonic final state* $t\bar{t} \rightarrow bW^+\bar{b}W^- \rightarrow bl_1^+\nu_{l_1}\,\bar{b}l_2^-\bar{\nu}_{l_2}$: In this channel both W-bosons decay leptonically. It provides the best detection signature of all three channels, due to the presence of two high energetic leptons. The branching ratio for the dileptonic final state is 9%, but since the signal to background ratio is large most top-quark analyses in this channel are not statistically limited. Due to the fact that tau-leptons are difficult to measure in ATLAS, combinations containing taus are not considered in analyses in the dileptonic decay channel.

2.3 Standard Model Properties of the Top-Quark

2.3.1 Top-Quark Mass

The mass of the top-quark is the largest of all quarks described in the SM, it is approximately 40 times heavier than the bottom quark. The experimentally measured top-quark mass (closely) corresponds the top-pole mass [54, p. 1] since it is usually derived from measurements of the invariant mass distribution. The pole mass is defined as the real part of the pole in the perturbative top-quark propagator. For a quark with a mass much larger than the energy scale of the strong interaction $\Lambda_{\mathrm{QCD}} = 200\,\mathrm{MeV}$ the pole mass is ambiguous by an amount proportional to the strong interaction scale [54, p. 1]. The LHC and Tevatron collaborations published in 2014 a combination of top-quark mass measurements [24, p. 1]:

$$m_t = 173.34 \pm 0.27\,(\mathrm{stat.}) \pm 0.71\,(\mathrm{syst.})\,\mathrm{GeV}\,. \tag{2.74}$$

In Figure 2.16 the different ATLAS and CMS measurements of the top-quark mass are shown.

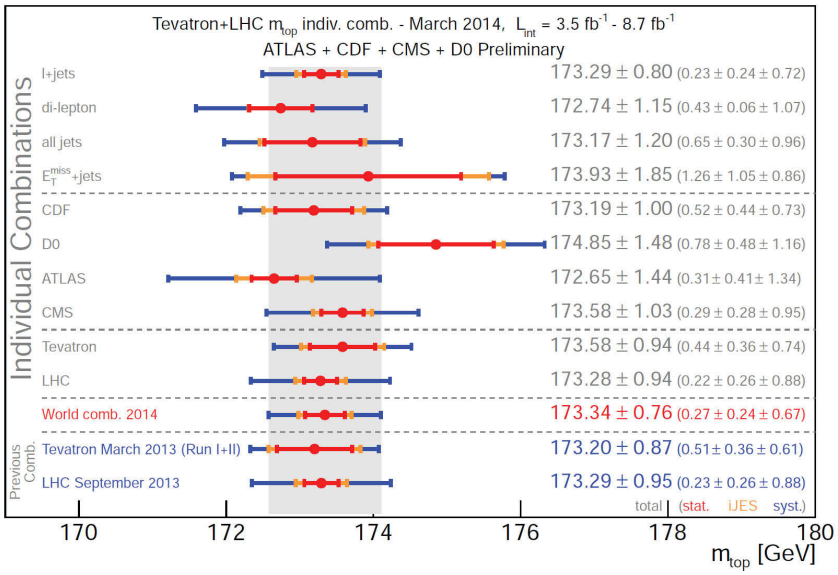

Figure 2.16.: The individual measurements and results of the LHC/Tevatron combination of top-quark mass measurements, the grey vertical band reflects the total uncertainty on the combined top-mass value [24, p. 17].

2.3.2 Electric Charge of the Top-Quark

The electric charge of a particle is a fundamental parameter. In case of the top-quark the SM assumes a value of $(2/3)\,e$, since here the top-quark is assumed to be the isospin partner of the bottom-quark. After the discovery of the top-quark at the Tevatron it was not ruled out that the measured particle could be in fact a different, heavy exotic quark Q_4 with an electric charge of $-(4/3)\,e$, which decays via $Q_4 \to W^- b$ [34, p. 851]. Direct measurements of the electric charge of the top-quark are possible in e^+e^- collisions via the cross section ratio $R = \sigma(e^+e^- \to \text{hadrons})/\sigma(e^+e^- \to \mu^+\mu^-)$ at (and beyond) the top-quark production threshold. In 2011 the ATLAS collaboration published a result for the indirect measurement of the top-quark charge [55]. Using data from semileptonic top-quark pair decays the charge of the W-boson is determined via the charge of the final state lepton. The charge of the corresponding bottom-quark is determined using a correlation between the charge of the bottom-quark and a weighted sum of the electric charges of the particles contained in the hadronisation cone (jet) of the bottom-quark. The scenario of an exotic quark Q_4 was excluded at a significance of more than $5\,\sigma$ [55, p. 14].

2.3.3 W-boson Polarisation

In the SM theory of the weak interaction the top quark can only couple to left-handed particles (at leading order). This is due to the $V - A$ charged current weak interaction which can be described by the vertex factor:

$$i\frac{g}{\sqrt{2}}V_{tb}\gamma^\mu\frac{1}{2}\left(1-\gamma^5\right)\,. \tag{2.75}$$

This means that the W-boson originating from a top-quark decay can only be left-handed (negative helicity) or longitudinal (zero helicity) [34, p. 851]. The theoretical predictions of the helicity fractions are at next-to-leading order and next-to-next-to leading order gluon radiation [56, p. 1] :

$$\mathcal{F}_L^{\text{SM}} = 0.3115\,, \tag{2.76}$$
$$\mathcal{F}_R^{\text{SM}} = 0.0017\,, \tag{2.77}$$
$$\mathcal{F}_0^{\text{SM}} = 0.6875\,. \tag{2.78}$$

The helicity fractions can be experimentally determined from measurements of the angular distribution of the top-quark decay products. The angle θ^* denotes the angle between the charged lepton (of the top-quark decay final state) momentum direction and the reversed momentum direction of the bottom quark (of the top-quark decay final state), after being boosted into the W-boson rest frame [57, p. 2]. The angular distribution is given by:

$$\frac{1}{\sigma}\frac{d\sigma}{d\cos\theta^*} = \frac{3}{4}\left(1-\cos^2\theta^*\right)\mathcal{F}_0 + \frac{3}{8}\left(1-\cos^2\theta^*\right)^2\mathcal{F}_L + \frac{3}{8}\left(1+\cos^2\theta^*\right)^2\mathcal{F}_R\,. \tag{2.79}$$

The LHC collaborations published a combined result of the W-boson polarisation measurement in top-quark decays in 2013 [58, p. 1]

$$\mathcal{F}_L^{\text{LHC}} = 0.359 \pm 0.021\,(\text{stat.}) \pm 0.028\,(\text{syst.})\,, \tag{2.80}$$
$$\mathcal{F}_R^{\text{LHC}} = 0.015 \pm 0.034\,, \tag{2.81}$$
$$\mathcal{F}_0^{\text{LHC}} = 0.626 \pm 0.034\,(\text{stat.}) \pm 0.048\,(\text{syst.})\,. \tag{2.82}$$

The results are in agreement with the SM next-to-next-to leading order theoretical predictions, the individual measurements are depicted in Figure 2.17.

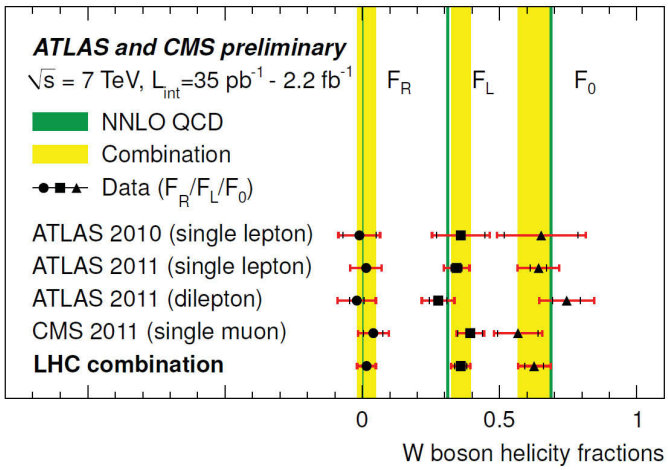

Figure 2.17.: The individual results of the W-boson polarisation measurement performed by the ATLAS and CMS collaborations. The green solid line indicates the predictions of next-to-next-to leading order QCD calculations [58, p. 13]

2.3.4 Top-Quark Spin Correlation

The lifetime of the top-quark is so short that it decays before bound states can be formed. The spin of the top-quark is therefore transferred to the decay products and can be measured via their angular distributions [59, p. 1]. The SM predicts small values for the polarisation of top- and antitop-quarks, but the degree of correlation A is suited as an observable. The spin correlation between the charged leptons of the dileptonic decay of a top-quark pair is given by [60, p. 5]

$$\frac{1}{\sigma}\frac{d\sigma}{d\cos\theta_+\, d\cos\theta_-} = \frac{1}{4}\left(1 + A\alpha_+\alpha_-\cos\theta_+\cos\theta_-\right)\,, \tag{2.83}$$

with the degree of correlation A and the angle between the lepton θ_- (antilepton θ_+) and the top- (antitop-) quark quantisation axis. The quantities $\alpha_\pm$ denote the spin analysing power which is predicted to be $\alpha_\pm = 0.999$ for the two final state leptons. The degree of correlation A is defined as the fractional difference between the number N of events where the top- and antitop-quark spin orientations are aligned ($\uparrow\uparrow, \downarrow\downarrow$) and those where the spins

have opposite alignment ($\downarrow\uparrow, \uparrow\downarrow$):

$$A = \frac{N(\uparrow\uparrow) + N(\downarrow\downarrow) - N(\uparrow\downarrow) - N(\downarrow\uparrow)}{N(\uparrow\uparrow) + N(\downarrow\downarrow) + N(\uparrow\downarrow) + N(\downarrow\uparrow)}, \tag{2.84}$$

where the arrows denote the spins of top- and antitop-quark with respect to a chosen quantisation axis. The standard model prediction of the correlation in the helicity basis is given as [60, p. 17]

$$A^{\mathrm{SM}}_{\mathrm{helicity}} = 0.31\,. \tag{2.85}$$

The degree of correlation was measured by the ATLAS collaboration in 2013 and is in agreement with the SM prediction [60, p. 16]

$$A^{\mathrm{ATLAS}}_{\mathrm{helicity}} = 0.27 \pm 0.03\,(\mathrm{stat.}) \pm 0.04\,(\mathrm{syst.})\,. \tag{2.86}$$

The zero spin correlation hypothesis was excluded with a significance of $5.1\,\sigma$ in 2012 [59, p. 5].

2.3.5 Top-quark Coupling to Gauge Bosons

As described in the beginning of the chapter the large top-quark mass suggests that it plays a special role in electroweak symmetry breaking. Therefore, the influence of new physics is likely to be seen first in the electroweak interactions of top-quarks, namely in deviations from SM predictions in $t\bar{t}\gamma$ and $t\bar{t}Z$-boson couplings. In e.g. technicolour or other models with a strongly coupled Higgs sector anomalies of up to 10% can be introduced [61, p. 1]. Hence a measurement of the coupling of top-quarks to gauge bosons provides the opportunity for a SM validation and the opportunity to discover new physics. The general function of the vertex of a top-quark pair and a neutral vector boson V is given by [61, p. 2]

$$\begin{aligned}\Gamma^{t\bar{t}V}_{\mu}\left(k^2, q, \bar{q}\right) &= -ie\{\gamma_\mu\left[F^V_{1V}(k^2) + \gamma_5 F^V_{1A}(k^2)\right] \\ &+ \frac{\sigma_{\mu\nu}}{2m_t}(q+\bar{q})\left[iF^V_{2V}(k^2) + \gamma_5 F^V_{2A}(k^2)\right]\}\end{aligned} \tag{2.87}$$

where e is the electrical charge, m_t is the top-quark mass, $q(\bar{q})$ is the outgoing top- (antitop-) quark four-momentum and $k^2 = (q+\bar{q})^2$. In the low energy limit $k^2 = 0$ the terms $F^V_{1V}(0)$ and F^V_{1A} are the $t\bar{t}V$ vector and axial-vector form factors. The coefficients $F^\gamma_{2V}(0)$ and $F^\gamma_{2A}(0)$ are given by [61, p. 2]

$$F^\gamma_{2V}(0) = Q_t\frac{g_t - 2}{2}\,, \tag{2.88}$$

$$F^\gamma_{2A}(0) = \frac{2m_t}{e}\,d^\gamma_t\,, \tag{2.89}$$

where $Q_t = 2/3$ is the electric charge of the top-quark, the magnetic form factor g_t and the electric dipole form factor d^γ_t. At leading order in the SM these form factors for neutral

gauge bosons are given by [61, p. 2]

$$F_{1V}^{\gamma,\mathrm{SM}} = -Q_t\,, \tag{2.90}$$

$$F_{1V}^{Z,\mathrm{SM}} = \frac{1}{4\sin\theta_w\cos\theta_w}\left(1-\frac{8}{3}\sin^2\theta_w\right)\,, \tag{2.91}$$

$$F_{1A}^{Z,\mathrm{SM}} = \frac{1}{4\sin\theta_w\cos\theta_w}\,, \tag{2.92}$$

$$F_{2V}^{\gamma,\mathrm{SM}} = F_{2V}^{Z,\mathrm{SM}} = F_{2A}^{\gamma,\mathrm{SM}} = F_{2A}^{Z,\mathrm{SM}} = F_{1A}^{\gamma,\mathrm{SM}} = F_{2V}^{\gamma,\mathrm{SM}} = 0\,, \tag{2.93}$$

where θ_w is the weak mixing angle. Besides a direct measurement of the top-quark electric charge using the F_{1V}^{γ} form factor new physics can be unveiled by comparing measured cross sections and kinematic distributions of $t\bar{t}V$ processes to the SM prediction. In 2013 CMS published a measurement of the $t\bar{t}$Z cross section yielding a significance of $3.3\,\sigma$. The cross section was measured to be [62, p. 3]

$$\sigma_{t\bar{t}Z}^{CMS} = 0.28^{+0.14}_{-0.11}\,(\mathrm{stat.})\,^{+0.06}_{-0.03}\,(\mathrm{syst.})\,\mathrm{pb}\,. \tag{2.94}$$

This result is compatible with the SM prediction [63, p. 7]

$$\sigma_{t\bar{t}Z}^{\mathrm{SM}} = 0.137^{+0.012}_{-0.016}\,\mathrm{pb}\,. \tag{2.95}$$

In 2011 the ATLAS collaboration published its first result of the $t\bar{t}\gamma$ cross-section times the branching ratio [64, p. 17], yielding a significance of $2.7\,\sigma$

$$\sigma_{t\bar{t}\gamma}^{\mathrm{ATLAS}} = 2.0 \pm 0.5\,(\mathrm{stat.})\ \pm 0.7\,(\mathrm{syst.})\ \pm 0.08\,(\mathrm{lumi.})\,\mathrm{pb}\,. \tag{2.96}$$

This measurement is also consistent with the SM prediction of [65], [64, p. 2]

$$\sigma_{t\bar{t}\gamma}^{\mathrm{SM}} = 2.1 \pm 0.4\,\mathrm{pb}\,. \tag{2.97}$$

2.3.6 Charge Asymmetry in Top-Quark Pair Production

As described in Section 2.2.1 top-quark pairs are produced via gluon fusion $gg \to t\bar{t}$ or quark pair annihilation $q\bar{q} \to t\bar{t}$. These lowest order Born processes do not distinguish between the top- and the antitop-quark and are therefore symmetric. The Born cross section for gluon fusion and quark annihilation are given by [66, p. 9]

$$\frac{d\sigma^{gg\to t\bar{t}}}{d\cos\hat{\theta}} = \alpha_s^2\frac{\pi\beta}{2\hat{s}}\left(\frac{1}{N_C(1-c^2)}-\frac{T_F}{2C_F}\right)\left(1+c^2+8m^2-\frac{32m^4}{1-c^2}\right)\,, \tag{2.98}$$

$$\frac{d\sigma^{q\bar{q}\to t\bar{t}}}{d\cos\hat{\theta}} = \alpha_s^2\frac{T_F C_F}{N_C}\frac{\pi\beta}{2\hat{s}}(1+c^2+4m^2)\,, \tag{2.99}$$

where $\hat{\theta}$ is the polar angle of the top-quark with respect to the incoming anti-quark in the centre-of-mass rest frame, $\beta = \sqrt{1-4m^2}$ is the velocity of the top-quark with $m = m_t/\sqrt{\hat{s}}$ [67, p. 8], $\sqrt{\hat{s}}$ is the effective partonic centre-of-mass energy, $c = \beta\cos\hat{\theta}$, and $N_C = 3$, $T_F = 1/2$, $C_F = 4/3$ are the colour factors. The Born cross sections for the top-quark pair production feature no term differentiating between top- and antitop. Hence, this is

also the case for the full $pp \to t\bar{t}$ cross section. Processes of higher order in the SM, which contain real or virtual gluon emission, introduce a difference in the differential top- and antitop-quark production processes and therefore a measureable charge asymmetry [66, p. 1]. Different interferences cause this asymmetry, radiative corrections to the quark annihilation process and heavy flavour production with interference terms contributing to gluon-quark scattering. Gluon quark scattering is a SM process of the order α_s^3 and therefore has (compared to the real and virtual gluon emissions) only a small contribution to the overall charge asymmetry.
The charge asymmetry is caused by an interference between amplitudes which are odd under the exchange of top- and antitop-quark [66, p. 1]. The largest positive contribution originates from the interference of box- (one-loop corrections) and Born processes. In Figure 2.18 the corresponding Feynman diagrams are shown. Gluon fusion processes do not contribute to the top-quark charge asymmetry.

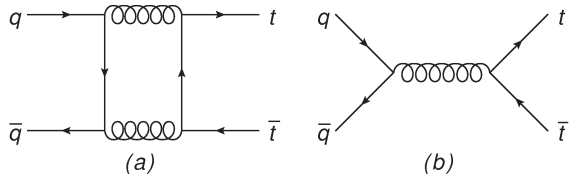

Figure 2.18.: The box (a) and Born (b) Feynman diagrams of top-quark pair production.

Interferences between initial and final state gluon bremsstrahlung add a negative contribution to the charge asymmetry, but the contribution is smaller than the of the Born/box interference. The Feynman diagram of the gluon initial and final state bremsstrahlung is shown in Figure 2.19. In Figure 2.20 the Feynman diagrams of the gluon quark scattering

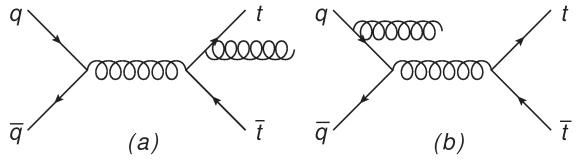

Figure 2.19.: The final (a) and initial (b) state gluon bremsstrahlung Feynman diagrams of top-quark pair production.

are shown. The dominant contribution to the charge asymmetry arises from the inter-

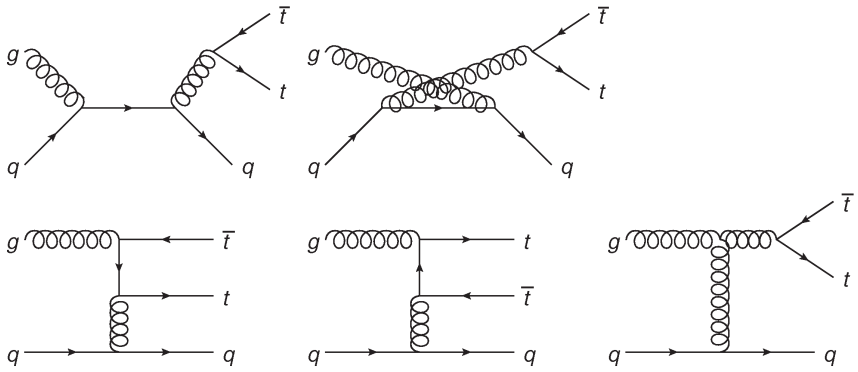

Figure 2.20.: The Feynman diagrams representing the contributions from quark gluon scattering.

ference of box and Born processes. The corresponding contribution is expressed by the absorptive contributions (cuts) of the Feynman diagrams shown in Figure 2.21. Only the dominant diagrams are shown. The line cutting two fermions in Figure 2.21 corresponds to the interference of the one loop box diagram with the Born level diagram. The three particle cut corresponds to the interference of Born diagrams with a $t\bar{t}$-gluon final state [68, p. 47]. The colour factors corresponding to the Feynman diagrams in Figure 2.21,

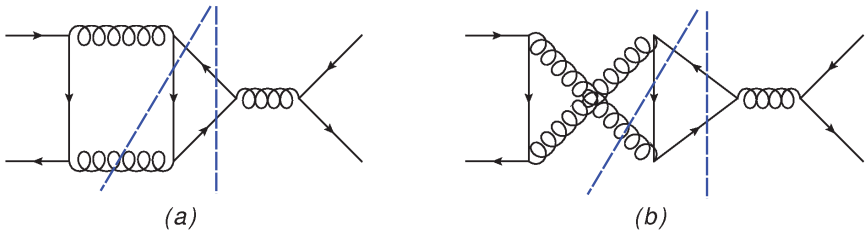

Figure 2.21.: The quark annihilation cut diagrams with the dominant contribution to the charge asymmetry in the top-quark pair production.

after averaging over initial and summing over final states are given by

$$C_{(a)} = \frac{1}{16N_C^2}\left(f_{abc}^2 + d_{abc}^2\right) , \tag{2.100}$$

$$C_{(b)} = \frac{1}{16N_C^2}\left(d_{abc}^2 - f_{abc}^2\right) , \tag{2.101}$$

where $f_{abc}^2 = \left(N_C^2 - 1\right) N_C$ and $d_{abc}^2 = \left(N_C^2 - 1\right)\left(N_C^2 - 4\right)/N_C$. Without the colour factors the interference in Diagram (a) and (b) in Figure 2.21 satisfies the relation [68, p. 47]

$$d\sigma_a^{p\bar{p}\to t\bar{t}} = -d\sigma_b^{p\bar{p}\to\bar{t}t} . \tag{2.102}$$

The cross sections are odd under $t\bar{t} \to \bar{t}t$ exchange. The charge asymmetry can be interpreted as a forward-backward (FB) asymmetry $A_{\mathrm{FB},t\bar{t}}$ for the top quark defined as

$$A_{\mathrm{FB},t\bar{t}} = \Delta\sigma_{\mathrm{FB}}/\sigma , \tag{2.103}$$

with the total cross section σ and $\Delta\sigma_{\mathrm{FB}}$ as the cross section difference between the forward and backward regions [68, p. 46]:

$$\Delta\sigma_{\mathrm{FB}} \equiv \int_{2m_t}^{\sqrt{s}} dM \left[\int_0^1 d\cos\hat{\theta}\,\frac{d^2\sigma^{p\bar{p}\to t\bar{t}}}{dM\,d\cos\hat{\theta}} - \int_{-1}^0 d\cos\hat{\theta}\,\frac{d^2\sigma^{p\bar{p}\to t\bar{t}}}{dM\,d\cos\hat{\theta}}\right] . \tag{2.104}$$

In this equation the charge symmetric parts of $\sigma^{p\bar{p}\to t\bar{t}}$ vanish and only the charge asymmetric components $\sigma_A^{xy\to t\bar{t}}$ contribute. These charge asymmetric contributions are given as functions of the scattering angle [66, p. 4]

$$\frac{d\sigma_A^{q\bar{q}\to t\bar{t}}}{d\cos\hat{\theta}} \equiv \frac{1}{2}\left(\frac{d\sigma(q\bar{q}\to t\bar{t})}{d\cos\hat{\theta}} - \frac{d\sigma(q\bar{q}\to \bar{t}t)}{d\cos\hat{\theta}}\right) , \tag{2.105}$$

$$\frac{d\sigma_A^{gq\to t\bar{t}}}{d\cos\hat{\theta}} \equiv \frac{1}{2}\left(\frac{d\sigma(gq\to t\bar{t})}{d\cos\hat{\theta}} - \frac{d\sigma(gq\to \bar{t}t)}{d\cos\hat{\theta}}\right) . \tag{2.106}$$

The individual contributions of the cross section for quark annihilation $\sigma^{q\bar{q}}$ and quark-gluon scattering σ^{qg} to the full process cross section $\sigma(p\bar{p} \to t\bar{t})$ are shown in Figure 2.22. In addition to this pure QCD amplitude also a mixed QCD/electroweak interference term

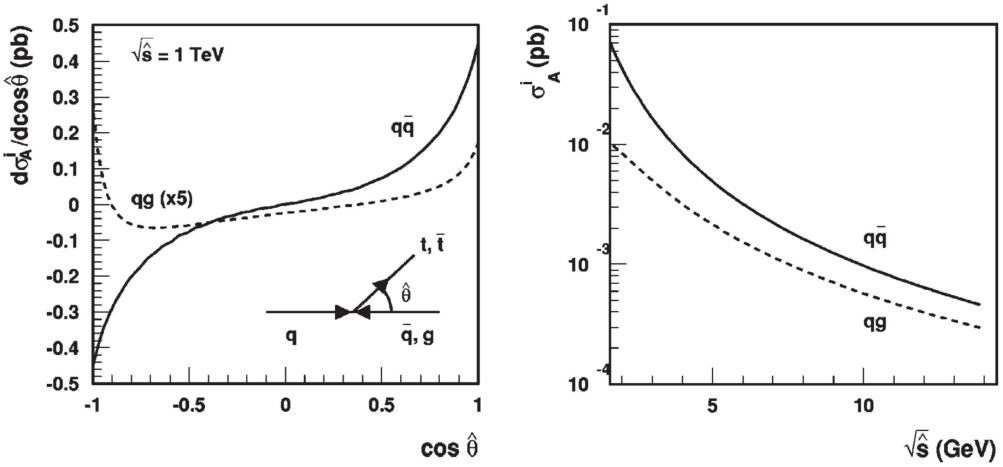

Figure 2.22.: The plot on the left-hand side shows the asymmetric parts of the differential top-quark pair production cross sections initiated by quark annihilation and quark-gluon scattering [66, p. 4]. The plot on the right-hand side shows the integrated charge asymmetric parts of the top-quark pair production cross section σ_A^i (where is is $q\bar{q}$ or qg) versus the effective centre of mass energy $\sqrt{\hat{s}}$ [66, p. 5].

contributes to the charge asymmetry. The QCD box diagram can produce a top- antitop-quark pair in a colour singlet configuration, which then interferes with the $t\bar{t}$ production through a photon or a Z-boson [66, p. 5]. The corresponding cut diagram is shown as (a) in Figure 2.23. The second electroweak contribution arises from the interference between the gluon-photon box, or the gluon-Z-boson box with the QCD Born diagram, an example of the corresponding cut diagram is shown as (b) in Figure 2.23. The charge asymmetry

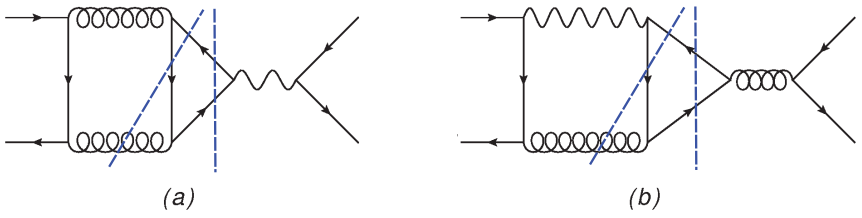

Figure 2.23.: The quark annihilation cut diagrams for the mixed QCD/electroweak contribution to the charge asymmetry in the top-quark pair production.

in the quark annihilation process in top-quark pair production implies that the top-quark is preferentially produced in the direction of the incoming quark and the antitop in the direction of the incoming antiquark [66, p. 7].

2.4 Observables in the Top-Quark Charge Asymmetry Measurement

The definition of the FB asymmetry in equation 2.103 suggests that the polar angle between the top-quark and the incoming parton of the hard scattering process is to be used

as an observable to measure the top-quark pair charge asymmetry. The differential charge asymmetry is given by [66, p. 3]

$$A_{\mathrm{FB},t\bar{t}}(\cos\hat{\theta}) = \frac{N_t(\cos\hat{\theta}) - N_{\bar{t}}(\cos\hat{\theta})}{N_{\bar{t}}(\cos\hat{\theta}) + N_{\bar{t}}(\cos\hat{\theta})}\,, \tag{2.107}$$

where $N(\cos\hat{\theta})$ is given as

$$N_{\bar{t}}(\cos\hat{\theta}) = \frac{d\sigma}{d\Omega}\left(\cos\hat{\theta}\right)\,, \tag{2.108}$$

with $N_{\bar{t}}(\cos\hat{\theta}) = N_t(-\cos\hat{\theta})$ as a consequence of charge conjugation symmetry. The integrated FB asymmetry is then defined as [66, p. 4]

$$A_{\mathrm{FB},t\bar{t}} = \frac{N_t(\cos\hat{\theta} \geq 0) - N_{\bar{t}}(\cos\hat{\theta} \geq 0)}{N_{\bar{t}}(\cos\hat{\theta} \geq 0) + N_{\bar{t}}(\cos\hat{\theta} \geq 0)}\,, \tag{2.109}$$

The value of $\cos\hat{\theta}$ cannot be measured directly, since the direction of the initial state parton is not known a priory. Therefore, the asymmetry has to be defined such that it does not rely on information on the directions of the particles in the hard scattering initial state. The rapidity of the top-quark y_t can replace $\cos\hat{\theta}$ since the sign of the rapidity directly reflects the sign of $\cos\hat{\theta}$. Figure 2.24 shows an illustration of the top- and antitop-quark rapidity distributions.

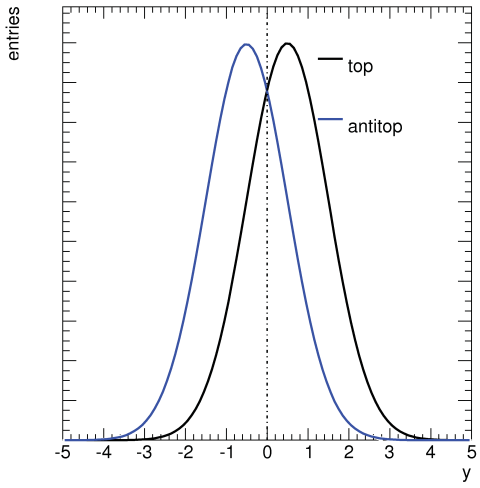

Figure 2.24.: Illustration of the top- and antitop-quark rapidity y distributions for a proton-antiproton collider.

Using the difference of the rapidity between top-and antitop-quark and the charge conjugation symmetry we find

$$\Delta y = y_t - y_{\bar{t}}\,, \tag{2.110}$$

therefore, the FB asymmetry in the $t\bar{t}$-rest-frame can be formulated in terms of the rapidity difference Δy:

$$A_{\mathrm{FB},t\bar{t}} = \frac{N(\Delta y > 0) - N(\Delta y < 0)}{N(\Delta y > 0) + N(\Delta y < 0)}\,, \tag{2.111}$$

where $N(\Delta y \gtrless 0)$ is the number of top-quark pair events measured with $\Delta y \gtrless 0$. The

theoretical prediction for the FB asymmetry at the Tevatron is $A_{\mathrm{FB},t\bar{t}}^{\mathrm{theory}} = 0.087 \pm 0.010$ (at $\sqrt{s} = 1.96\,\mathrm{GeV}$) [69, p. 10]. The most recent Tevatron measurements of the FB asymmetry provide values of

$$A_{\mathrm{FB},t\bar{t}}^{D0} = 0.106 \pm 0.03\,(\mathrm{stat.+syst.})\,, \tag{2.112}$$

for the D0 experiment [70, p. 15] and

$$A_{\mathrm{FB},t\bar{t}}^{CDF} = 0.164 \pm 0.047\,(\mathrm{stat.+syst.})\,, \tag{2.113}$$

for the CDF experiment [71, p. 21]. The charge asymmetry in the pair production of top-quarks causes the top-quark to be preferentially produced in the direction of the incoming quark and the antitop-quark in the direction of the incoming antiquark, respectively. The Tevatron is a proton-antiproton collider, hence the top-quark will preferably be produced in the direction of the proton and the antitop in the direction of the antiproton. This leads to a FB asymmetry which can be quantified using Equation 2.111.
The LHC provides a symmetric initial hadron state, since it is a proton-proton collider. Therefore, no FB asymmetry can be measured at the LHC. As a solution a central charge asymmetry $A_{C,t\bar{t}}$ is defined:

$$A_{C,t\bar{t}} = \frac{N(\Delta\,|y_{t\bar{t}}| > 0) - N(\Delta\,|y_{t\bar{t}}| < 0)}{N(\Delta\,|y_{t\bar{t}}| > 0) + N(\Delta\,|y_{t\bar{t}}| < 0)} = \frac{N_+ - N_-}{N_+ + N_-}\,, \tag{2.114}$$

where $\Delta\,|y_{t\bar{t}}|$ is defined as

$$\Delta\,|y_{t\bar{t}}| = |y_t| - |y_{\bar{t}}|\ . \tag{2.115}$$

This central asymmetry arises from the momentum difference between the quarks and antiquarks in the hard scattering process of a proton-proton collision. The valence quark, on average, carries a larger fraction of the proton momentum then the antiquark which is a sea quark generated via gluon splitting. This is then reflected in the transverse momenta of the generated top quark-pair, boosting the top-quark in the forward detector region, while the antitop-quark is (on average) produced in the central region of the detector. Figure 2.25 shows an illustration of the top- and antitop-quark rapidity distributions for a proton-proton collider. Theory predicts a value of $A_{C,t\bar{t}}^{\mathrm{theory}} = 0.0115 \pm 0.0006$ (at $\sqrt{s} = 7\,\mathrm{TeV}$) [69, p. 11]. The central asymmetry is not directly comparable to the FB asymmetry measured at Tevatron. The most recent central charge asymmetry value measured at the LHC is [6, p. 1]

$$A_{C,t\bar{t}}^{\mathrm{LHC}} = A_C = 0.005 \pm 0.007\,(\mathrm{stat.})\ \pm 0.006\,(\mathrm{syst.})\,. \tag{2.116}$$

This value is a combination of measurements from the ATLAS and the CMS experiment. The comprised individual measurements and a comparison to the SM value are shown in Figure 2.26.

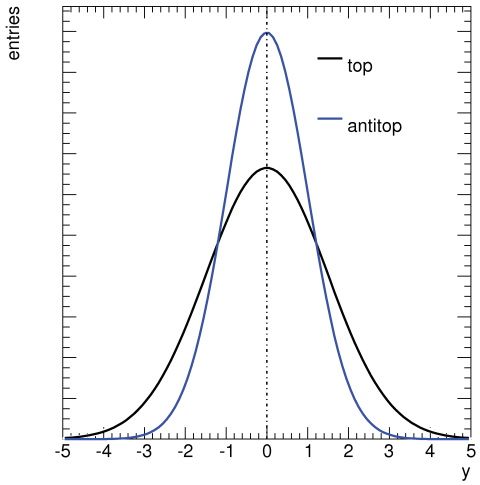

Figure 2.25.: Illustration of the top- and antitop-quark rapidity y distributions for a proton-proton collider.

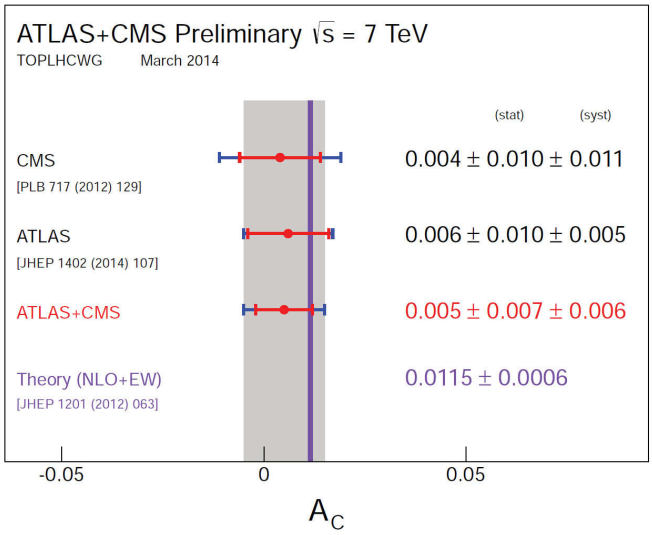

Figure 2.26.: The summary of the single measurements of the ATLAS and CMS experiments, as well as the LHC combination compared to the theory prediction. The inner red error bars indicate the statistical uncertainty, the blue outer error bars indicate the total uncertainty. The grey band illustrates the total uncertainty of the combined result [6, p. 7].

2.5 Top-Quark Charge Asymmetry Beyond the Standard Model

Beside the SM description a wide range of different models beyond the SM (BSM) exist, which would have an impact on the charge asymmetry in the production of top-quark pairs. In this section three different BSM theories with implications on the charge asymmetry are discussed, namely the exchange of massive gluons forming a colour octet as axigluons [67] or Kaluza Klein excitations [72] and the production of heavy Z-bosons [73].

2.5.1 Massive Colour Octet

A prominent example of a massive coloured octet is the axigluon and the most important model independent manifestation of an axigluon exchange is observable in the top-quark pair charge asymmetry at the LHC. Axigluons are heavy neutral gauge bosons which carry a colour charge and couple to quarks via an axial-vector current, which is of the same magnitude as the QCD coupling. The axigluon-gluon coupling is the same as the gluon-gluon coupling [67, p. 1]. The theoretical description of axigluons requires the strong interaction gauge group $SU(3)_L \times SU(3)_R$ to be spontaneously broken to the $SU(3)_{L+R}$ group under the assumption of the unifiable chiral colour model [74, p. 2]. Chiral colour models also require extra fermions and Higgs-bosons, additional to the minimal BEH mechanism. The extra fermions cancel anomalies and the additional Higgs-bosons are required to break the enlarged gauge symmetry [75, p. 3]. This results in an octet of massless gluons and an octet of massive axigluons with the axial-vector coupling

$$\frac{1}{2} g_s \gamma_\mu \gamma_5 \lambda^a \,, \tag{2.117}$$

where g_s is the strong coupling constant and λ^a are the Gell-Mann matrices. An axigluon contribution to charge asymmetry occurs via the interference between the gluon and the axigluon in the quark annihilation top-quark pair production process. The cross-section of the pair-production is unaffected by the gluon-axigluon interaction. The interference term is suppressed by the squared axigluon mass $1/m_{\mathrm{A}}^2$ [76, p. 4]. The square of the axigluon amplitude is symmetric and contributes to the total cross section. This leads to a resonance in the top-antitop-quark invariant mass distribution. The square of the axigluon amplitude is suppressed by a factor of $1/m_{\mathrm{A}}^4$, where m_{A} is the axigluon mass [76, p. 4]. The gluon fusion top-quark pair production process is not affected by the presence of axigluon interactions, since there are no direct gluon-axigluon vertices with an odd number of axigluons [76, p. 4]. The modified (w.r.t. Equation 2.99) Born cross section for the quark-annihilation in a model including axigluons is given by [67, p. 8]

$$\frac{d\sigma^{q\bar{q}\to t\bar{t}}}{d\cos\hat{\theta}} = \alpha_s^3 \frac{T_F C_F}{N_C} \frac{\pi\beta}{2\hat{s}} \left(1 + c^2 + 4m^2 + \frac{4c\hat{s}(\hat{s} - m_{\mathrm{A}}^2) + \hat{s}^2(\beta^2 + c^2)}{(\hat{s} - m_{\mathrm{A}}^2)^2 + m_{\mathrm{A}}^2 \Gamma_{\mathrm{A}}^2} \right) , \tag{2.118}$$

where terms which are odd in $c = \beta \cos\hat{\theta}$ (i.e. odd in the polar angle) contribute to the charge asymmetry. The decay width of the axigluon Γ_{A} is given by

$$\Gamma_{\mathrm{A}} = \sum_q \Gamma\left(\mathrm{A} \to q\bar{q}\right) \approx \frac{\alpha_s m_{\mathrm{A}} T_F}{3} \left[5 + \left(1 - \frac{4m_t^2}{m_A^2} \right)^{\frac{3}{2}} \right] . \tag{2.119}$$

ATLAS measurements have so far excluded axigluons affecting the top-quark pair charge asymmetry up to a particle mass of $\sim 3.7\,\text{TeV}$ [77, p. 4].
In the most general scenario of a colour-octet resonance G_μ^a the corresponding fields interact with quarks with arbitrary vector g_V^q and axial-vector g_A^q strengths relative to the strong coupling g_s [75, p. 4]. The Born cross section for quark annihilation in the top-quark pair production including the most general massive colour octet is given by [72, p. 13]:

$$\begin{aligned}\frac{d\sigma^{q\bar{q}\to t\bar{t}}}{d\cos\hat{\theta}} &= \alpha_s^2\frac{T_F C_F}{N_C}\frac{\pi\beta}{2\hat{s}}\left(1+c^2+4m^2+\frac{2\hat{s}(\hat{s}-m_G^2)}{(\hat{s}-m_G^2)^2+m_G^2\Gamma_G^2}\right. \\ &\times \left[g_V^q g_V^t(1+c^2+4m^2)+2g_A^q g_A^t c\right] \\ &+ \frac{\hat{s}^2}{(\hat{s}-m_G^2)^2+m_G^2\Gamma_G^2} \\ &\times \left[\left((g_V^q)^2+(g_A^q)^2\right)\left((g_V^t)^2(1+c^2+4m^2)\right.\right. \\ &\times \left.\left.(g_A^t)^2(1+c^2+4m^2)\right)8g_V^q g_A^q g_V^t g_A^t c\right]\Bigg),\end{aligned} \tag{2.120}$$

where m_G is the mass of the massive colour octet resonance. The two terms which are odd in c contribute to the charge asymmetry. The first term originates from the interference of the SM amplitude with the G_μ^a resonance amplitude and the second term arises from the squared resonance amplitude of G_μ^a [72, p. 13]. For large masses m_G the second term is suppressed and the charge asymmetry contribution is dominated by the value of the axial-vector coupling in the first term. The decay width is given by [72, p. 14]

$$\Gamma_G = \sum_q \Gamma(G\to q\bar{q}) \tag{2.121}$$

$$\begin{aligned}&\approx \frac{\alpha_s m_G T_F}{3}\left[\sum_q\left((g_V^q)^2+(g_A^q)^2\right)+\sqrt{1-\frac{4m_t^2}{m_G^2}}\right. \\ &\times \left.\left((g_V^t)^2\left(1+\frac{2m_t^2}{m_G^2}\right)(g_A^t)^2\left(1+\frac{4m_t^2}{m_G^2}\right)\right)\right].\end{aligned} \tag{2.122}$$

2.5.2 Coloured Scalars

Grand unified theories comprising large gauge groups can introduce new coloured scalar states [75, p. 4]. The unification of gauge interactions using the $SU(5)$ gauge group predicts scalar colour octets with an upper mass bound of $M_\Phi < 4.4\times 10^5\,\text{GeV}$, which can be produced at the LHC [78, p. 7]. A contribution to the top-quark charge asymmetry can be introduced by coloured scalars through flavour violating couplings in the t-channel. These coloured scalars can be singlets (e.g. [79]), triplets (e.g. [80]), sextets (e.g. [81, p. 5]) and octets. The description of an additional scalar particle ϕ after the electroweak symmetry breaking can be achieved by adding

$$\mathcal{L}_\phi = D_\mu\phi^\dagger D^\mu\phi - M_\phi^2|\phi|^2 + \phi^a\bar{\hat{t}}\,T_r^a(g_s+g_p\gamma_5)u + \text{h.c.} \tag{2.123}$$

to the SM Lagrangian [80, p. 2], which introduces a flavour violating coupling between top- and up-quark. Here D_μ is the covariant derivative, M_ϕ is the scalars mass, T_r^a are

Z' mass	expected limit, $\sigma_{Z'}$
100 GeV	< 2.0 pb
150 GeV	< 1.6 pb
200 GeV	< 1.4 pb

Table 2.4.: Observed upper limits for the low mass Z' cross sections $\sigma_{Z' \to tt}$ at 95% confidence level [85, p. 18]

the $SU(3)_C$ Clebsch-Gordon coefficients connecting ϕ^a of colour a to the two quarks and $\hat{t} = t$ for an octet or singlet case or $\hat{t} = i\gamma^0\gamma^2 t$ in the triplet or sextet case. The scalar and pseudoscalar coupling constants are denoted as g_s and g_p. Triplet and sextet coloured scalars agree with large charge asymmetries, but require large flavour violating couplings, singlet and octet scalars do not contribute to the top-quark pair production asymmetry [75, p. 5].

2.5.3 Extra Weak Gauge Bosons

Many theories beyond the standard model require additional gauge bosons, e.g. grand unified theory or topcolour models. The simplest way to extend the symmetry group of the SM is to include a second $U(1)$ group [82, p. 1]. Under the requirement of local gauge symmetry the Z' emerges as the corresponding gauge boson. The Z' is a spin one particle which carries no electric charge.
The amplitude for top-production through Z' exchange in the s-channel does not interfere with the SM amplitude at hadron colliders [75, p. 5]. Via the introduction of flavour violating couplings a large charge asymmetry is generated in the t-channel. These couplings are introduced to the SM Lagrangian via a $\mathcal{L}_{W',Z'}$ term

$$\mathcal{L}_{W',Z'} = \bar{t}\left(g_V^{Z'} + g_A^{Z'}\gamma_5\right)\gamma^\mu Z'_\mu\, u + \bar{t}\left(g_V^{W'} + g_A^{W'}\gamma_5\right)\gamma^\mu W'_\mu\, d\,. \tag{2.124}$$

The ATLAS collaboration found the measurement of the top-quark pair charge asymmetry in pp-collisions at $\sqrt{s} = 7\,\text{TeV}$ to be compatible with SM expectations. No evidence of a charge asymmetry excess beyond SM expectation was found, although the measurement is still statistically limited [83, p. 10]. A first limit on the production of real Z' particles was determined at the Tevatron in the search for like-sign top-quark production [84]. The upper limits on like-sign top-quark pair production (with heavy t-channel Z' exchange), derived by the ATLAS collaboration in 2012, are listed in Table 2.4.

2.5.4 Tevatron and LHC Predictions for BSM induced Charge Asymmetries

Figure 2.27 illustrates the theoretical predictions of different BSM contributions to the central charge asymmetry A_C^{new} for the LHC and the FB asymmetry $A_{\text{FB}}^{\text{new}}$ for the Tevatron. A measurement in agreement with the SM only hypothesis corresponds to values of $A_C^{\text{new}} = 0$ and $A_{\text{FB}}^{\text{new}} = 0$, respectively. The Tevatron predictions assume an invariant mass of the top-quark pair $m_{t\bar{t}} > 450\,\text{GeV}$, this enhances the value of the asymmetry. In Figure 2.27

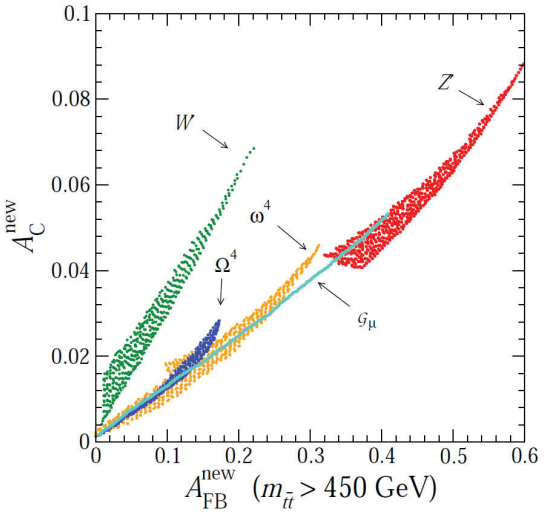

Figure 2.27.: The allowed regions for BSM physics contributions to the FB asymmetry at Tevatron $A_{\mathrm{FB}}^{\mathrm{new}}$ and the central charge asymmetry at the LHC A_C^{new} [86, p. 4].

the notations of the different BSM regions are:

- Z' represents a with an additional massive neutral vector boson with flavour violating couplings to top- and up-quarks.
- W shows a prediction for a massive charged boson with righthanded couplings contributing to the t-channel in top-quark pair production.
- ω^4 comprises a righthanded colour triplet scalar with flavour violating couplings to top- and up-quarks.
- Ω^4 contains a massive colour sextet (exchanged in the u-channel) with righthanded flavour violating couplings to top- and up-quarks.
- G_μ : A model assuming axigluon production only via $u\bar{u}$ and $d\bar{d}$ in the s-channel ($s\bar{s}$ is neglected). In this prediction the axigluon is too heavy to be produced on-shell.

BSM physics can explain a wide range of values for the charge asymmetry between no contribution to the SM prediction and excess of up to 10%.

Chapter 3

The Large Hadron Collider

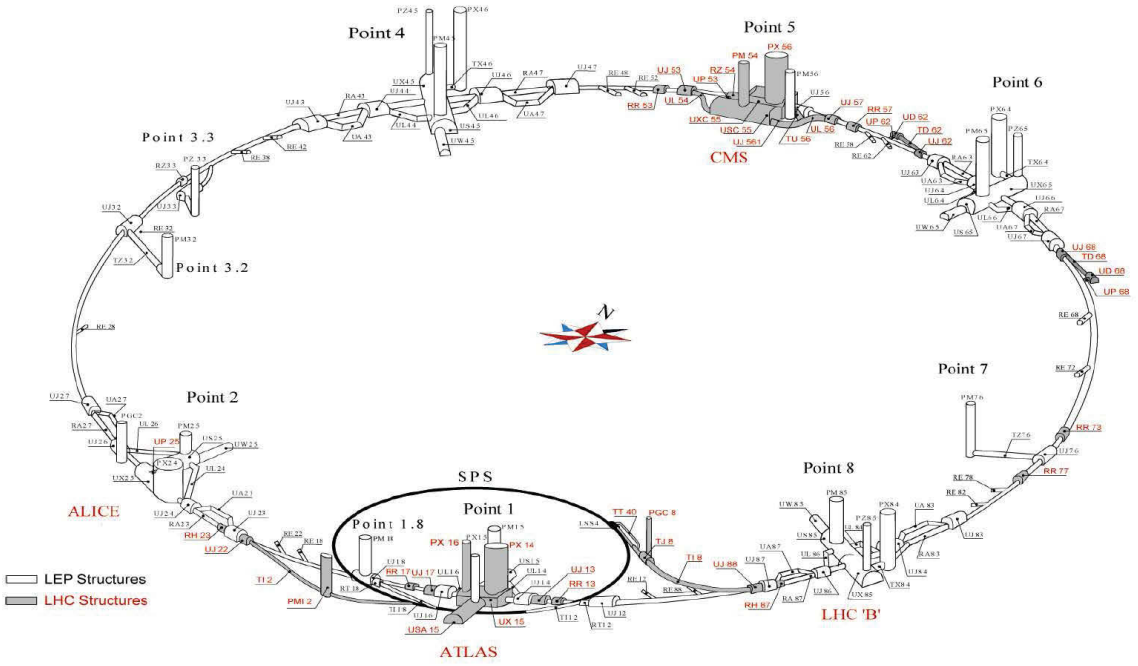

Figure 3.1.: Underground structure of the LHC. The main experiments are situated at points one, two, five and eight [87, p. 5].

The Large Hadron Collider (LHC) is a circular particle accelerator, it supports operation modes for proton and heavy ion acceleration. The LHC is located at CERN (Conseil Européen pour la Recherche Nucléaire), at the border between Switzerland and France near Geneva. At the LHC two counter circulating beams are stored and collide at four dedicated points at which four main experiments are located. A schematic view of the underground structures is provided in Figure 3.1. The design parameters of the LHC, its performance in 2011/2012 and its current status are discussed in Sections 3.1 and 3.2. A brief description of the main experiments is given in Section 3.3, other detectors located at the LHC are described in Section 3.4. The design parameters for the proton operation

mode are discussed in Section 3.1. A description of the heavy ion programme of the LHC lies beyond the scope of this thesis.

3.1 Design Parameters of the Large Hadron Collider

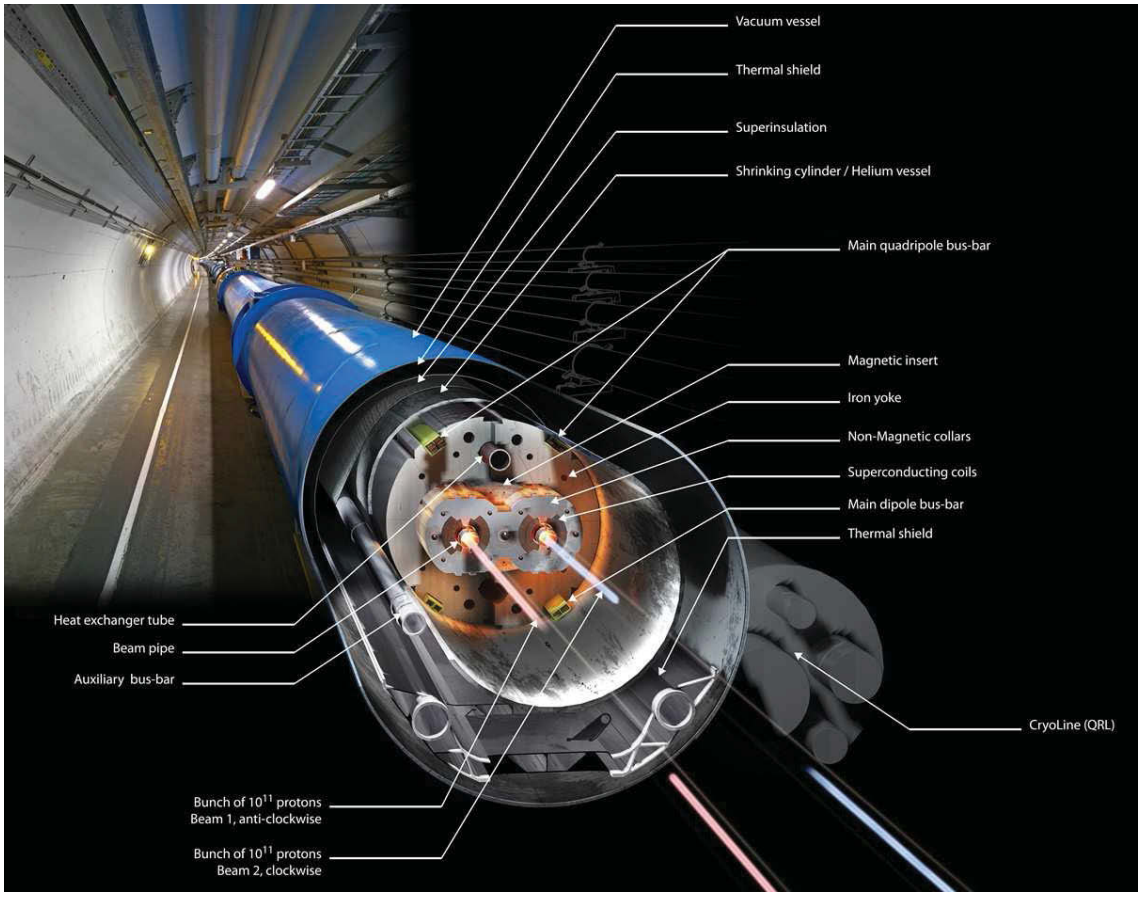

Figure 3.2.: Conceptional view of a LHC dipole magnet [88].

The storage ring of the LHC has a circumference of 26.66 km and is set up at a depth of 45 m to 170 m with a horizontal slope of 1.4 % down towards the Lake Geneva [87, p. 3]. The underground construction of the LHC reuses the tunnels of the former LEP (Large Electron Positron Collider) experiment. The LEP accelerator was operational from 1989 until 2000 (1989-1995 LEP1 and 1996-2000 LEP2) [89].
Two proton beams are accelerated in parallel running beam pipes with separate vacuum chambers and opposite magnetic fields. The maximum beam energy is limited by the peak dipole field of the storage ring. At 14 TeV the nominal magnetic flux density in a dipole is 8.33 T, which is reached by using superconducting magnets with super fluid Helium at a temperature of 1.9 K as coolant [90, pp. 22,155]. Due to space limitations in the tunnel there is no room for two rings of magnets, hence the LHC utilises twin bore magnets comprised of two sets of coils and vacuum chambers in the same supporting

structure, sharing one cryostat [90, pp. 21,22]. A schematic view of an LHC dipole is shown in Figure 3.2.

3.1.1 Injector Chain

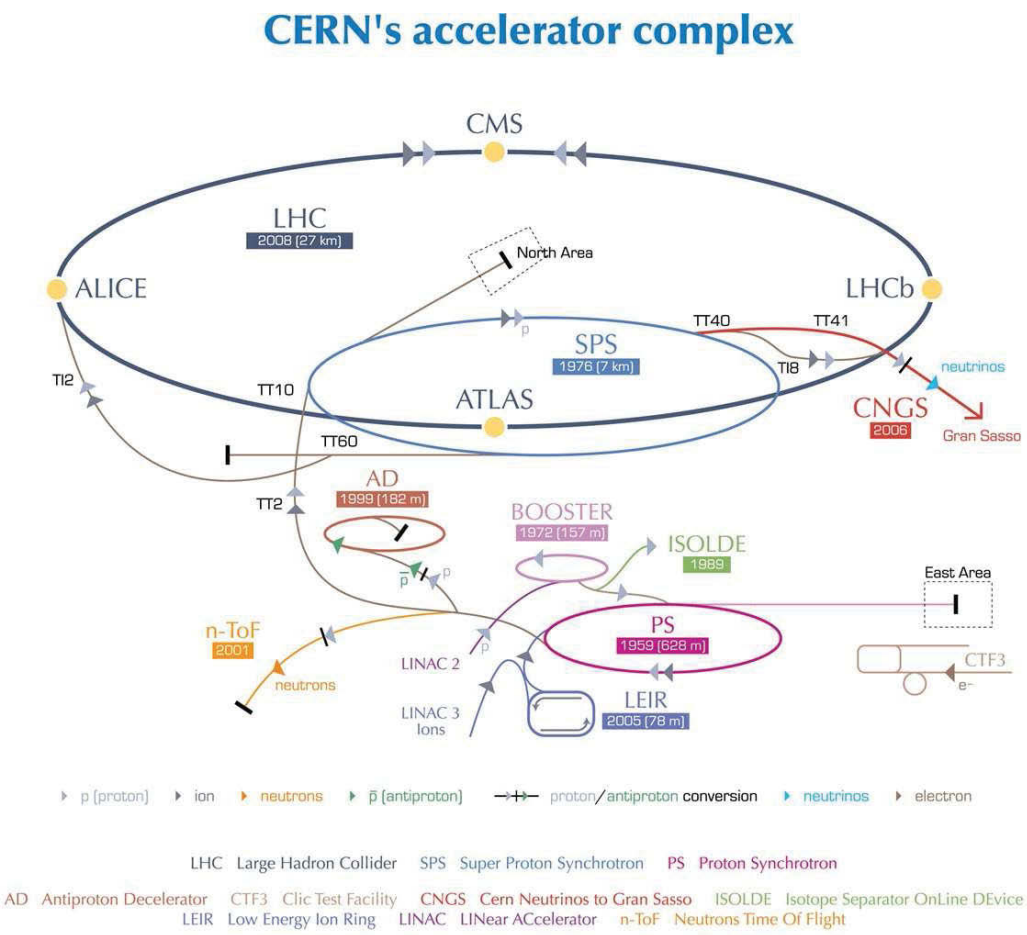

Figure 3.3.: The CERN accelerator complex, showing all particle accelerators situated at CERN. The LHC accelerator chain comprises (with increasing energy): Linac2 → Proton Synchrotron Booster → Proton Synchrotron Super Proton → Synchrotron LHC [91].

The protons circulating in the LHC storage ring are pre-accelerated before insertion. For pre-acceleration the retrofitted LEP injector chain is used. The injector chain is comprised of the Linac2 (Linear accelerator), the Proton Synchroton Booster (PSB), the Proton Synchrotron (PS) and the Super Proton Synchrotron (SPS).
The beam energy is increased in each step: 50 MeV (Linac2) → 1.4 GeV (PSB) → 25 GeV (PS) → 450 GeV (SPS) → 7 TeV (LHC). After the decommissioning of LEP the accelerators of the injector chain were upgraded to provide up to 2808 high intensity proton bunches per beam with small transverse and well defined longitudinal emittances. A schematic view of the CERN accelerator complex is shown in Figure 3.3.

3.1.2 Beam Properties and Limitations

The colliding proton beams provide a maximum centre of mass energy of 14 TeV and a peak luminosity of $\mathcal{L}_p = 10^{34}\,\mathrm{cm^2 s^{-1}}$ in the ATLAS (A Large Toroidal LHC Apparatus) and the CMS (Compact Muon Solenoid) experiments, $\mathcal{L}_{\mathrm{lhcb}} = 10^{32}\,\mathrm{cm^2 s^{-1}}$ in the LHCb (LHC Beauty) experiment, and $\mathcal{L}_{\mathrm{totem}} = 2 \times 10^{29}\,\mathrm{cm^2 s^{-1}}$ in the TOTEM (Total Elastic and Diffractive Cross Section Measurement) experiment (for description see Sections 3.3 and 3.4) [90, p. 21].
A beam is not a continuous stream of single protons, but it consists of up to 2808 bunches. These bunches contain $1.15 \cdot 10^{11}$ protons and circulate the LHC with a spacing of 25 ns. The particle density in one bunch is limited by non-linear beam-beam (BB) interactions, which are experienced by the particles in colliding bunches in the interaction regions [90, p. 22].
The beam-beam interactions can affect the performance of the LHC in different ways, such as decreased lifetime of the beams (incoherent BB effects), bunch to bunch variations (PACMAN effect), beam oscillations and instabilities (coherent BB effects). Bunches differing from the regular collision pattern are named PACMAN bunches. Those are e.g. bunches at the beginning and at the end of the bunch train [90, pp. 119,120]. Another limitation arises due to the mechanical aperture, which is given by the beam screen dimensions in the LHC arcs, leading to a peak nominal beam diameter of 1.2 mm [90, p. 22]. Combining the limitations of the BB interactions and the mechanical aperture leads to a maximum bunch intensity of 1.15×10^{11} protons per bunch.
Besides the maximum magnetic flux density of the dipoles the energy stored in the LHC is another limiting factor for the beam energy. The total energy stored adds up to approximately 1 GJ (362 MJ beam current, 600 MJ in the magnet system). This energy has to be absorbed not only in case of an emergency, but also at the end of each run (the definition of an ATLAS run can be found in Section 7). Hence the beam dumping system can be seen as an additional limit to the maximum beam energy. Other limiting effects are the heat load due to the synchrotron radiation, field quality errors affecting the beam stability and the interaction between the particles within one beam [90, pp. 22,23].

3.2 Status and Performance of the LHC

The LHC has performed remarkably well. During the 8 TeV physics run (04.04.2012 - 12.16.2012) a maximum number of 1374 bunches circulated, with a spacing of 25 ns, and an average bunch intensity of 1.5×10^{11}, thus exceeding the design parameters. The design bunch intensity was already met during the 7 TeV run in 2011 (03.13.2011 - 10.30.2011). A detailed description of the ATLAS dataset used in this thesis and a comparison of the properties of 2010 and 2011 data can be found in Section 7.

3.2.1 Integrated Luminosity as Performance Benchmark

A benchmark for the performance of the LHC is the delivered integrated luminosity, which is a measure of the amount of physics data taken by the corresponding experiment. The

integrated luminosity is the accumulated luminosity over a certain period of time. The luminosity is related to the observed event rate

$$\dot{N}_{\text{event}} = \mathcal{L}\,\sigma_{\text{event}}, \tag{3.1}$$

where σ_{event} is the cross section of the observed process. The luminosity only depends on the machine parameters and can be written as

$$\mathcal{L} = \frac{N_b^2\, n_b\, f_{\text{rev}} \gamma_r}{4\pi\, \epsilon_n\, \beta^*} F\,, \tag{3.2}$$

assuming a Gaussian beam distribution. Here N_b is the number of particles per bunch, n_b the number of bunches per beam, f_{rev} the revolution frequency, γ_r the relativistic gamma factor, ϵ_n the normalised beam emittance, β^* the beta function at the collision point and F the geometric luminosity reduction factor due to the crossing angle at the interaction point [90, p. 21]. F is given by

$$F = \left(1 + \left(\frac{\Theta_c \sigma_z}{2\sigma^*}\right)\right)^{-\frac{1}{2}}, \tag{3.3}$$

here is Θ_c the full crossing angle at the interaction point, σ_z the root mean square (RMS) bunch length and σ^* the transverse RMS beam size at the interaction point. These equations assume equal parameters for both beams [90, p. 21].

In 2011 ATLAS accumulated a total integrated luminosity of $5.5\,\text{fb}^{-1}$ at $\sqrt{s} = 7\,\text{TeV}$ [92, p. 2] and in 2012 a total integrated luminosity of $22.38\,\text{fb}^{-1}$ at $\sqrt{s} = 8\,\text{TeV}$ [93]. Figure 3.4 shows the evolution in time of the integrated luminosity for the ATLAS experiment for proton-proton collisions.

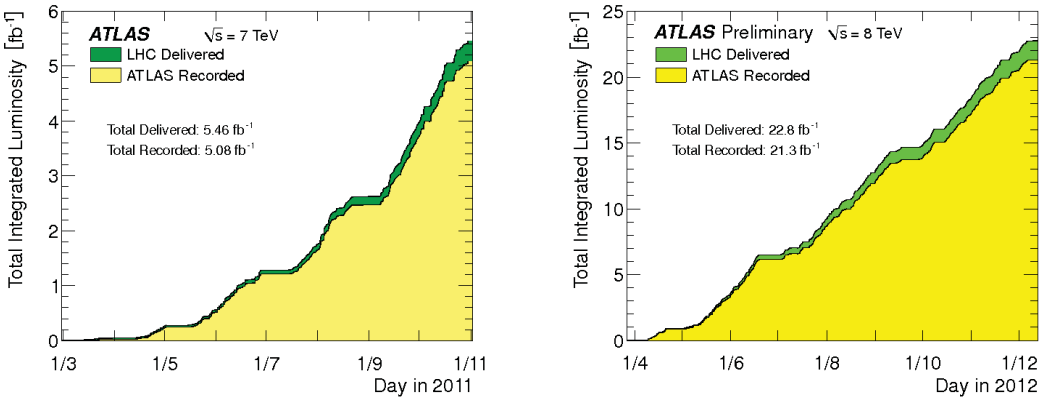

Figure 3.4.: Evolution of the integrated luminosity of ATLAS in 2011 and 2012 [93]

3.2.2 Pile-Up

At the energy and particle densities mentioned in Section 3.1 more than one proton-proton interaction per bunch crossing occurs at the designated interaction points. For ATLAS,

operating at design parameters, for each triggered event an average of $\langle n_P \rangle = 23$ additional interactions (minimum bias events) will be superimposed [94, p. 36]. The mean number of interactions per bunch crossing for the ATLAS 2011 data taking period is shown as $\langle \mu \rangle$ in Figure 3.5. The overall pile-up is intensified by the fact that the detector response is up to 500 ns long (e.g. in the Liquid Argon Calorimeter), leaving the detector sensitive to the effects of up to twenty consecutive bunch crossings. Pile-up is divided into two categories, event and detector pile-up [95].

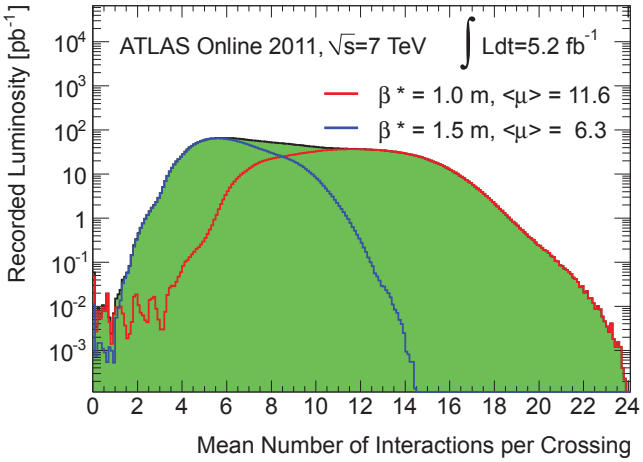

Figure 3.5.: The luminosity weighted distributions of the mean number of interactions per bunch crossing for the ATLAS 2011 data taking period. The blue line depicts the distribution for $\beta^* = 1.5\,\mathrm{m}$ and the red line for $\beta^* = 1.0\,\mathrm{m}$, where β^* is the bunch distance. The mean value for each β^* is given as $\langle \mu \rangle$ [93].

Event pile-up is the effect of additional minimum bias events in a single bunch crossing (also *in-time pile-up*). Minimum bias events from previous bunch crossings accumulating because of the long detector response, are called detector pile-up (also *out-of-time pile-up*). One model for the event pile-up [96, p. 1] assumes that the number of proton-proton collisions n follows a Poissonian distribution with the mean N_{mb}

$$P(n)_{mb} = \frac{(N_{mb})^n}{n!}\, e^{-N_{mb}}\,. \tag{3.4}$$

The number of particles per collision m is given by a Poissonian distribution with a mean of N_p

$$P(m)_{N_p} = \frac{(N_p)^m}{m!}\, e^{-N_p}\,. \tag{3.5}$$

The probability to produce N particles in one bunch crossing is then given by

$$P_N = \sum_{n=0}^{\infty} P(n)_{mb}\, e^{-n\,N_p}\, \frac{(n\,N_p)^N}{N!}\,. \tag{3.6}$$

The mean number of particles is given by the mean number of collisions multiplied by the mean number of particles generated by each collision [95, p. 17].
In general the detector pile-up is not treated as noise, because it is not purely random,

but due to the large number of collisions it essentially results in a continuous background. Under the assumption of uncorrelated bunch crossings the detector pile-up can be treated as noise. On average the measured signal should not be affected by adding minimum bias collisions in each crossing, but on an event by event basis large fluctuations, due to variances in the number of minimum bias collisions, are expected. This can lead to an increase of the width of the signal distribution [95, p. 18].
To reduce the noise due to detector pile-up topological clustering is introduced to preferentially select calorimeter cells with a high signal-to-noise ratio. The amount of noise depends on the luminosity, specified by the number of minimum bias collisions per bunch crossing and is calculated by a software tool in the ATLAS software and computing framework (Athena framework). Using this method a positive bias is added to the mean pile-up transverse energy E_T. This has an effect on the reconstruction of low E_T jets. Cutting on $|E_T|$ raises the significance of the positive tail of the E_T distributions by increasing the fraction of topoclusters from detector pile-up [95, p. 19].

3.3 Main Detectors at the LHC

To detect the particles produced in *pp*-collisions four different main detectors are integrated into the structure of the LHC. One of them is the ATLAS Detector, which will be described in detail in Chapter 4. The others are ALICE, CMS and LHCb.

The ALICE (A Large Ion Collider Experiment) detector is designed specifically for measurements of high energy interactions between two nuclei. Up to now lead ions are used. The data derived from these collisions provides an opportunity to study the phase transition from confined matter to a quark gluon plasma and allows the observation of hadronic matter under extreme temperature and density [97, p. 1].

CMS is a multi-purpose detector like ATLAS. It allows to probe a wide range of models in high energy particle physics. The foremost aim is to deliver new results concerning electroweak symmetry breaking, especially through the discovery of the Higgs-boson. The CMS detector is relatively small in size (21 m in length and 16 m in diameter), and features a strong solenoid magnet which provides a field of 4 T as well as a good muon identification over a wide range of momenta [98].

The LHCb experiment is designed to study charge/parity (CP) violation and other rare phenomena in B-meson decays with very high precision. This should provide a profound understanding of quark flavour physics in the framework of the Standard Model of particle physics and may hint to physics beyond the Standard Model. To achieve this goal, the detector features a high track reconstruction efficiency, a very good decay time resolution ($\approx$ 40 fs), and high trigger efficiencies for leptonic and hadronic final states [99, p. 1].

3.4 Other Detectors at the LHC

In addition to the main detectors the LHCf (Large Hadron Collider forward Experiment) and TOTEM (Total Elastic and Diffractive Cross-Section Measurement) experiments are situated at the LHC. LHCf investigates the energy distribution of particles emitted in the very forward region, which is important for the understanding of cosmic ray phenomena. LHCf shares point 1 with ATLAS. The TOTEM detector will measure the total proton-proton cross-section, study elastic scattering and diffractive dissociation at the LHC. The detector is installed in the forward region of the CMS detector [100, p. 1], [101, p. 1].

Chapter 4

The ATLAS Detector

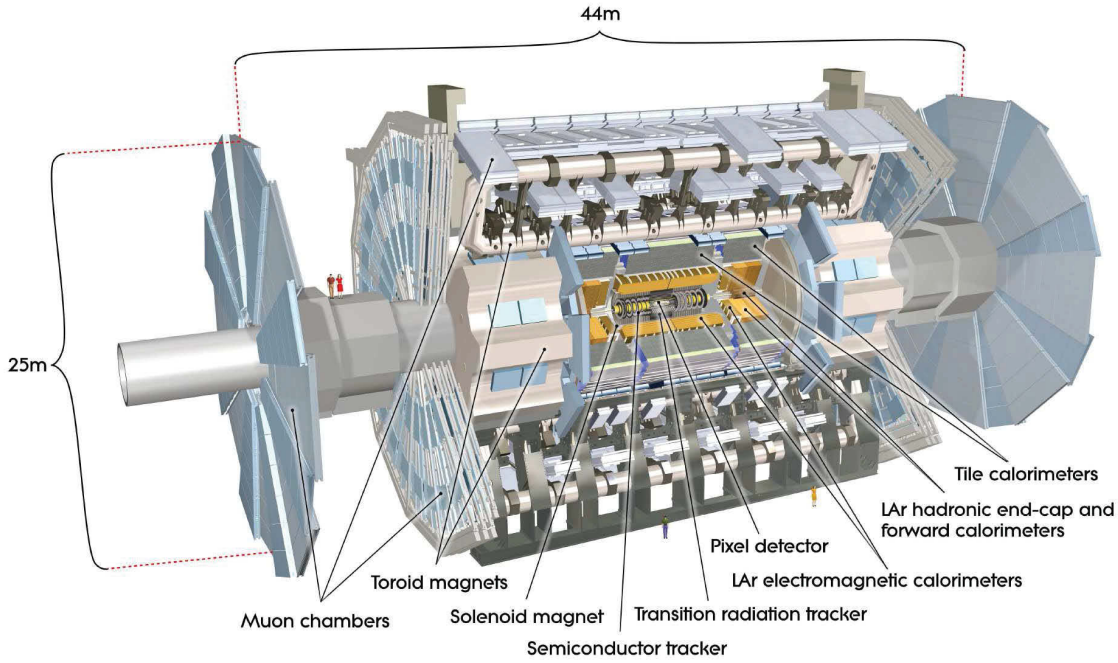

Figure 4.1.: Schematic view of the ATLAS detector [102, p. 4].

The ATLAS detector (A Large Toroidal LHC Aparatus) is a multipurpose particle detector. Data taken with this detector allows an extensive range of studies in the field of high energy particle physics. Its physics programme not only covers the investigation of proton-proton, but also heavy ion collisions. This includes tests and precision measurements of the Standard Model of particle physics (SM), physics beyond the SM, search for the Higgs boson and studies of the possible phase transition into a quark gluon plasma [102, p. 2].
The ATLAS detector measures 44 m in length and 22 m in diameter (without support structures) and weighs approximately 7000 t. It is built around interaction point one of the LHC beams (see Figure 3.1). A schematic view of the ATLAS detector is provided in

Figure 4.1. The detector is designed to meet the requirements of the physics programme and the harsh radiation environment of the LHC. It features fast, radiation hard sensors and electronics, large solid angle coverage around the interaction point, high momentum resolution and overall reconstruction efficiency for charged particles, efficient muon identification, electromagnetic and hadronic calorimetry and a trigger mechanism with good background suppression [102, p. 3].

4.1 ATLAS Coordinate System

The ATLAS coordinate system is right handed with its origin at the nominal interaction point. The z-axis is parallel to the beam direction and the $x-y$ plane is transverse to it. The x-direction is pointing towards the centre of the LHC ring. The y-direction is positive upwards, and the z-direction is positive in the counterclockwise circulation direction of the LHC ring. The azimuthal angle $\phi \in [0, 2\pi[$ is measured around the beam axis, starting with $\phi = 0$ in the x-direction and $\frac{\pi}{2}$ in the positive y-direction. The polar angle $\Theta \in \left[-\frac{\pi}{2}, \frac{\pi}{2}\right]$ is measured in the $y-z$-plane w.r.t. the positive y-axis [102, p. 1].
For a particle track the angles ϕ and Θ are calculated from the track momentum components p_x, p_y and p_z. Particle properties denoted with the subscript T are measured in the transverse $(x-y)$ plane. Properties measured in the transverse plane are momentum p_T, energy E_T, and missing energy $\not{E}_T$.

$$\tan\phi = \frac{p_y}{p_x} \tag{4.1}$$

$$\tan\Theta = \frac{p_T}{p_z} \tag{4.2}$$

The plain angles ϕ and Θ are not Lorentz invariant. Therefore the pseudorapidity $\eta \in [-\infty, \infty]$ is introduced, which commensurates the polar angle, but is Lorentz invariant for high energetic particles ($p \gg m$).

$$\eta \;=\; -\ln\left(\tan\frac{\Theta}{2}\right). \tag{4.3}$$

The rapidity $y \in [-\infty, \infty]$ is Lorentz invariant in any energy regime and is given by

$$y = \frac{1}{2}\ln\left(\frac{E+p_z}{E-p_z}\right). \tag{4.4}$$

The quantity ΔR denotes particle track distances in terms of pseudorapidity and azimuthal angle is defined as

$$\Delta R = \sqrt{\Delta\eta^2 + \Delta\phi^2}. \tag{4.5}$$

4.2 Inner Detector

The Inner Detector (ID) is comprised of three independent subdetectors installed in a hermetic encasement, offering a full ϕ acceptance and a pseudorapidity coverage of $|\eta| < 2.5$. Its construction and sensor assembly allow high precision track measurement of

charged particles with a transverse momentum above a threshold of $p_T = 0.5\,\text{GeV}$ [103, p. 53], resulting in an efficient primary and secondary vertex reconstruction [104, pp. 12-18]. The ID is enclosed by a cylindrical shell of 7.024 m length and 2.30 m diameter and is placed inside a 2 T solenoidal magnetic field [103, p. 7]. Figure 4.2 shows a schematic view of the three subdetectors, Pixel Detector, Semi Conductor Tracker (SCT) and Transition Radiation Tracker (TRT).

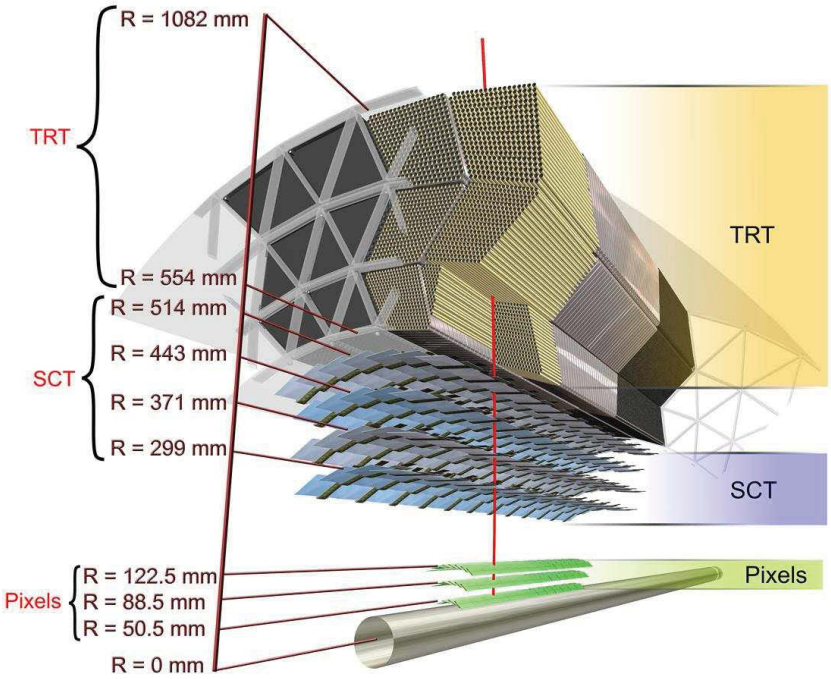

Figure 4.2.: Schematic view of the Pixel Detector, the Semiconductor Tracker and the Transition Radiation Tracker [105].

4.2.1 Pixel Detector

The innermost subdetector of the ID is a silicon pixel detector. It consists of three cylindrical (barrel) layers of identical sensor modules parallel to the beam axis and in the forward and backward region three disks perpendicular to the beam axis. These disks are equipped with the same type of sensors as the barrel section. The innermost pixel detector layer is referred to as the b-layer, because the reconstruction of the secondary decay vertices of long lived B-mesons relies mostly on the information from this layer. The other layers are denoted as layer one and layer two. Overall, there are 1744 sensor modules installed. Each module has $6.08\,\text{cm} \times 1.64\,\text{cm}$ of sensitive surface subdivided in 47232 pixels (40680 readout channels), of which 89% have a size of $400\,\mu\text{m} \times 50\,\mu\text{m}$ and 11% have a size of $600\,\mu\text{m} \times 50\,\mu\text{m}$ [106, p. 33]

The pixel detector can measure up to three space points for charged particle tracks in the barrel region, in the forward region it is possible to measure more space points. It offers an pseudorapidity range of $|\eta| < 2.5$ with an $|\eta|$-averaged resolution of 12 µm in R/ϕ and 100 μm in z-direction [104, p. 18], and a transverse impact parameter resolution better than 15 µm. Thus it allows a primary vertex reconstruction with a resolution $\sigma(z) < 1$ mm and three dimensional vertexing capability. To reduce multiple scattering and secondary interactions a minimum of passive material was used for supporting structures (mainly carbon fibre and Aluminum) [106, pp. 3,4]. The pixel detector was designed to work in a high radiation environment, withstanding an estimated lifetime dose of 500 kG (or $10^{15}_{\text{neq}}\text{cm}^{-2}$) over 10 years [106, p. 4].

4.2.2 Semi Conductor Tracker

The Semi Conductor Tracker (SCT) is a silicon microstrip detector and is located between the Pixel Detector and the Transition Radiation Tracker. Like the Pixel Detector the SCT is designed for high precision track measurement and three dimensional vertex reconstruction.
It consists of four concentric barrel layers parallel to the beam axis and nine discs, perpendicular to the beam axis, in the forward and backward region. The SCT is comprised of 4088 modules [103, p. 64] equipped with silicon strip sensors. For charged particles these sensors contribute four space points (eight strip crossings) per track with a space point resolution of 16 µm in R/ϕ and 580 µm in z-direction, in the range $|\eta| < 2.5$. The SCT features 6.2 million readout channels in total [107, p. 9].
Each module consists of four sensors in two layers. Each sensor in the first module layer is wirebonded to its twin in the second layer. The modules are glued back to back on a carbon fibre support structure and are aligned in a stereo angle of 40 mrad. One sensor features 786 readout strips with a constant pitch of 80 µm and a length of 6.4 cm [107, p. 8].

4.2.3 Transition Radiation Tracker

The Transition Radiation Tracker (TRT) provides position measurements of charged particles and information for electron identification using high and low detection thresholds. The TRT is comprised of layers of straw tubes. A straw tube is a small gas-drift detector with a diameter of 4 mm. The measurement principle of the TRT is based on the detection of transition radiation emitted by charged particles during the transition between two media with different dielectric constants. The TRT comprises gas filled straw tubes in 73 layers interleaved with fibres in the barrel region and 160 straw planes interleaved with foils in the forward and backward region (end-cap region). The fibres and the foils provide the material from which the transition radiation originates [103, p. 68]. The gas filling is a mixture of 70% Xe, 27% CO_2 and 3% O_2 [103, p. 59].
A charged track with $p_T = 0.5$ GeV and $|\eta| < 2.0$ is expected to traverse ≥ 36 straws in the barrel. In the transition region between barrel and end-cap ($0.8 < |\eta| < 1.0$) at least 22 straws are expected to be hit [103, p. 68]. Each straw measures the hit position with an intrinsic accuracy of approximately 130 µm in the R/ϕ-plane [103, p. 57].

4.3 Calorimeter System

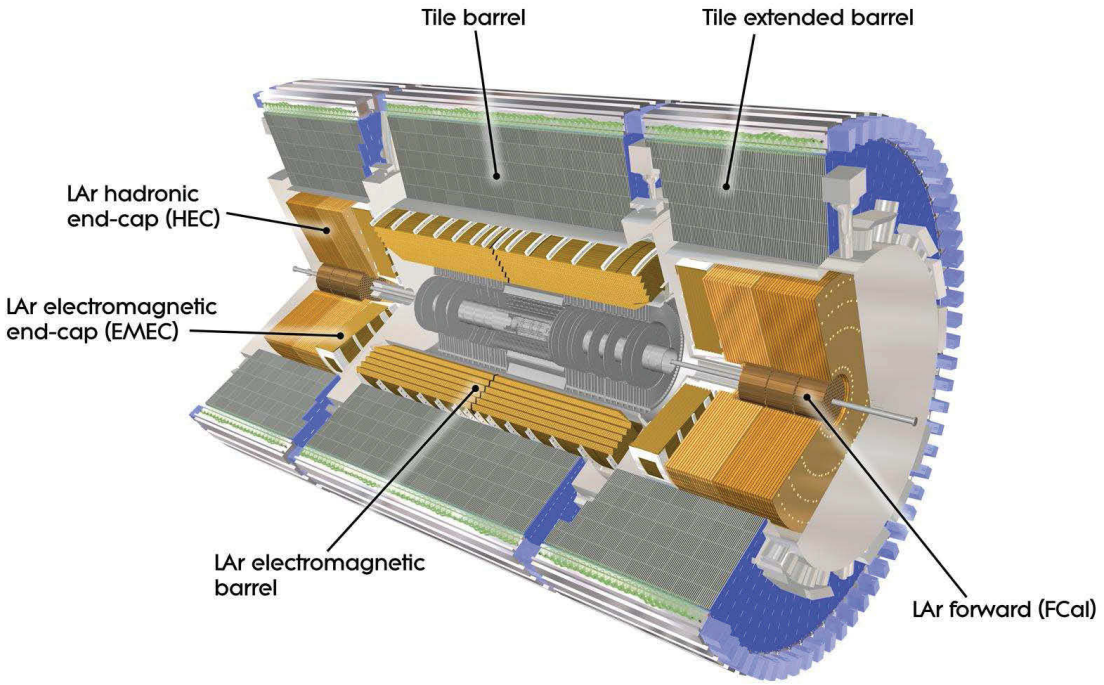

Figure 4.3.: Schematic view of the ATLAS calorimeter system [108].

The calorimeter system is used to measure the energy of the traversing particles. A schematic view of the ATLAS calorimeters is shown in Figure 4.3. All subcalorimeters combined cover a range of $|\eta| < 4.9$ [103, p. 7]. All subcalorimeters use sampling technology featuring alternating passive high density absorber and active detector material [103, p. 7]. When a particle (primary) traverses the passive material it produces a cascade of secondary particles (referred to as shower), which are detected in the active material. The energy and coarse track information of the primary particle can be derived from dimensions and shape of the corresponding shower.
The ATLAS calorimeter system features an electromagnetic (EM) calorimeter and a hadronic (HAD) calorimeter to measure the energy and the position for particles which are mainly subjected to electromagnetic (EM) and strong (HAD) interactions. Detailed information on the different calorimeters is provided in the following sections.

4.3.1 Electromagnetic Calorimeter

The EM calorimeter is a sampling calorimeter, utilising lead as passive and LAr as active material, with accordeon shaped polyamide electrodes to provide full ϕ coverage and fast signal extraction at the rear or front of the electrodes [103, p. 112]. The EM calorimeter is structured into three subsystems, each providing full azimuthal coverage: a barrel part covering a range of $|\eta| < 1.475$ and two end-cap parts covering a range of $1.375 < |\eta| <$

3.2. Each subsystem is located in its own cryostat [103, p. 110]. The barrel part of the EM calorimeter consists of two half barrels separated by a gap of 4 mm at $z = 0$. Each end-cap consists of two coaxial wheels. The inner wheel covers a range of $1.375 < |\eta| < 2.5$ and the outer wheel a range of $2.5 < |\eta| < 3.2$. In the region of $|\eta| < 1.8$ a presampler detector is used to correct for the energy lost by electrons and photons upstream of the calorimeter. The presampler consists of an active liquid Argon (LAr) layer with a thickness of 1.1 cm (0.5 cm) in the barrel (end-cap) region [103, pp. 7,8,10].
In the region dedicated to high precision measurements ($|\eta| < 2.5$) the calorimeter is structured into three depth levels, and for the remaining acceptance in two levels with coarser lateral granularity [103, p. 9]. The thickness of the calorimeter in terms of radiation lenghts X_0 increases from $22X_0$ in the very center of the barrel ($|\eta| = 0.0$) to $38X_0$ in the outer end-cap region ($|\eta| = 3.2$) [103, p. 111].

4.3.2 Hadronic Calorimeter

The hadronic calorimeter covers a range of $|\eta| < 4.9$ featuring three hadronic subcalorimeters [103, p. 10].

The tile calorimeter is placed next to the EM calorimeter containment, divided into three cylindrical shells, the tile barrel and extended tile barrel, as shown in Figure 4.3. The (extended) tile barrel covers a region of $|\eta| < 1.0$ ($0.8 < |\eta| < 1.7$), extending from an inner radius of 2.28 m to an outer radius of 4.25 m. Featuring steel as absorber and scintillating tiles as detector material, both the centre and the extended barrel are azimuthally divided in 64 modules. In depth the barrel sections are segmented into three layers with a thickness of approximately 1.5, 4.1 and 1.8 interaction lengths λ ($3.3\,\lambda$ for the extended barrel) [103, p. 10]. The gap regions between the centre and the extended shells are equipped with modules of steel-scintillator sandwiches, partially recovering the energy, which would otherwise be lost in the detector crack regions [103, p. 121]. The positioning between the muon system and the EM calorimeter reduces the punch-through of hadronic particles to an acceptable rate [103, p. 8]. The scintillating tiles are read out on two sides using wavelength shifting fibres, which feed the signals into two separate photomultiplier tubes [103, p. 10].

The hadronic end-cap calorimeter (HEC) is placed behind the end-cap EM calorimeter and shares the same liquid Argon cryostat. The HEC spans the region $1.5 < |\eta| < 3.2$ and overlaps with the tile calorimeter (at $|\eta| \approx 1.7$) and the forward calorimeter (at $|\eta| \approx 3.1$). The overlap reduces the material density drop in the transition region between the different calorimeter subsystems [103, p. 10]. The HEC consists of two wheels per end-cap with each comprised of 32 wedge-shaped modules and is placed perpendicular to the beam axis. Each wheel is divided into two layers in depth. The inner wheels utilise 25 mm parallel copper plates as absorber, while in the outer wheels copper absorbers with a thickness of 50 mm are used (for all wheels the first plate has half of the thickness). The copper absorber plates alternate with 8.5 mm gaps, which are filled with liquid Argon, providing the active medium for the HEC [103, p. 10]. The size of the readout cells is $\Delta\eta \times \Delta\phi = 0.1 \times 0.1$ in the region of $|\eta| < 2.5$ and 0.2×0.2 for larger values of η [103, p. 127].

The forward calorimeter (FCal) consists of two high density hadronic ($91.3\,X_0$ and $89.2\,X_0$) and an EM calorimeter ($27.6\,X_0$). The EM calorimeter faces the interaction point followed by the two hadronic elements at the outer positions. The FCal is integrated into the end-cap calorimeter cryostats positively affecting both the uniformity of detector coverage and radiation background in the muon spectrometer [103, p. 10]. The front of the FCal is recessed by 1.2 m w.r.t. the EM calorimeter, at a distance of about 4.7 m from the interaction point. This reduces the neutron albedo in the ID containment. The FCal covers a range of $3.1 < |\eta| < 4.9$ [103, p. 129]. The EM module utilises copper-liquid Argon sampling, which provides optimal resolution and heat removal, while the hadronic modules use tungsten-liquid Argon sampling. The liquid Argon layer has a depth of 0.269 mm in the EM calorimeter and 0.376 mm and 0.508 mm for the first and second hadronic calorimeter [103, p. 130]. This small size minimises problems due to ion build-up and helps to maintain fast signal transport [103, p. 10]. A copper alloy shielding is placed between the third module and the muon spectrometer to further reduce background radiation in the end-cap muon system.

4.4 Muon System

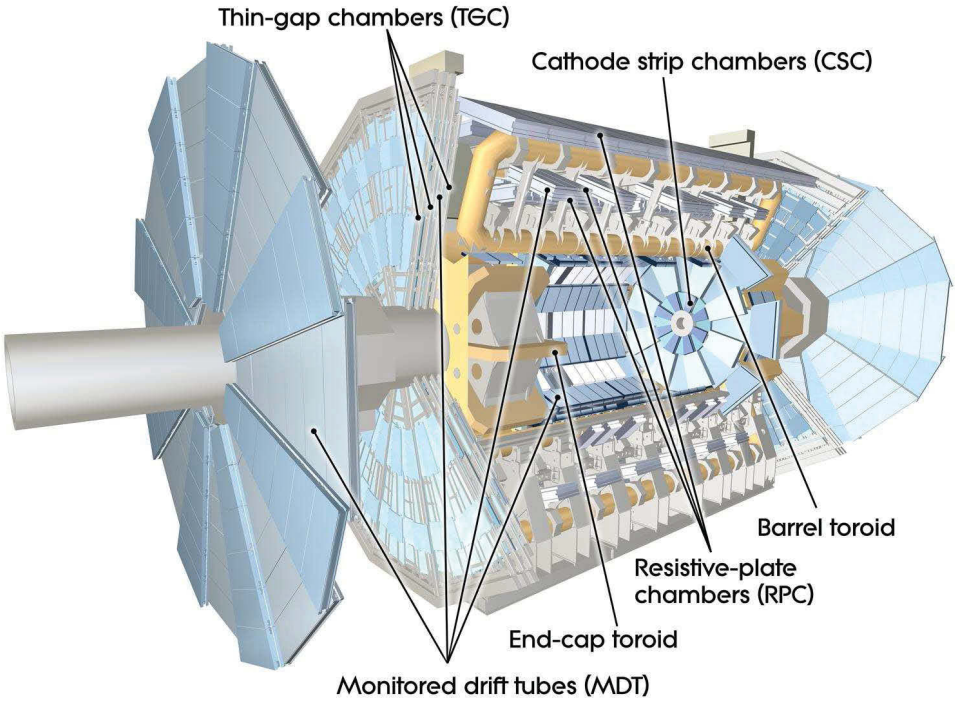

Figure 4.4.: Schematic view of the ATLAS muon system [109].

The muon spectrometer is the outermost detector layer of the ATLAS detector and is instrumented with separate trigger and high-precision tracking chambers [103, p. 10]. The muon spectrometer features different subdetectors, i.e. Monitored Drift Tubes (MDTs), Cathode Strip Chambers (CSCs), Resistive Plate Chambers (RPCs) and Thin Gap Chambers (TGCs).

The barrel part of the ATLAS muon spectrometer is comprised of three concentric layers placed around the hadronic calorimeter at radii of 5.0 m, 7.5 m and 10.0 m, covering a range of $|\eta| < 1.0$ in pseudorapidity. In the transition and end-cap regions the muon spectrometer consists of four wheels perpendicular to the beam axis, located at distances of 7 m, 10 m, 14 m and 21 m − 23 m from the interaction point, covering a range of $1.0 < |\eta| < 2.7$ [103, p. 164].

The muon spectrometer provides track measurements in the range $|\eta| < 2.7$ and Level1 trigger information (see Section 4.6) in $|\eta| < 2.4$ for charged particles leaving the ID and calorimeter section [103, p. 11]. The track measurements in the muon system provide increased precision in the total energy reconstruction, thus enhancing the accuracy of the missing energy determination of an event. A schematic view of the muon spectrometer is shown in Figure 4.4. The magnetic field for the deflection of the muon tracks within $|\eta| < 1.4$ is provided by large superconducting air-core toroid magnets, in the range of $1.6 < |\eta| < 2.7$ and by two smaller end-cap toroid magnets, which are inserted into both ends of the barrel toroid. The region $1.4 < |\eta| < 1.6$ is covered by a combination of the barrel and end-cap fields. This magnet configuration allows for a field which is orthogonal to the muon trajectories and minimises resolution degradation due to multiple scattering [103, p. 11].

The muon spectrometer is designed for a momentum resolution of $\Delta p_{\mathrm{T}} < 1 \times 10^{-4}\,\mathrm{GeV}$, for $p_{\mathrm{T}} > 300\,\mathrm{GeV}$. At smaller momenta, the resolution is limited to a few percent by multiple scattering in the magnet and detector structures, and by energy loss fluctuations in the calorimeters [110, p. 8].

4.4.1 Monitored Drift Tubes and Cathode Strip Chambers

The track measurement is provided by the MDT over most of the pseudorapidity range ($|\eta| < 2.7$ outer layer and $|\eta| < 2.0$ inner end-cap layer). In a range of $2.0 < |\eta| < 2.7$ and close to the interaction point CSCs with higher granularity are utilised [103, p. 165]. MDT chambers are comprised of eight layers of single wire drift chambers made of Aluminium tubes with a diameter of 30 mm, a wall thickness of 0.4 mm and a central WolframRhenium wire. The baseline MDT gas is a non-flammable mixture of 91% Ar, 4% N_2, and 5% CH_4, operated at an absolute pressure of 3 bar [110, p. 10]. MDTs provide an average resolution of 80 µm per tube and approximately 30 µm − 50 µm per chamber [103, p. 165]. The MDTs and the CSCs are controlled by an optical alignment system to ensure the accuracy of the chamber positioning, which is directly related to the tracking precision.

The cathode strip chambers (CSC) are multiwire proportional chambers, located in the first layer of the end-cap. The CSCs cover the region with $|\eta| > 2$, because the counting rates in this pseudorapidity region exceed the limit of safe oparation for the MDTs [103, p. 178]. The CSC symmetry axis are oriented radially. There are two segmented cathodes, one parallel and the other one perpendicular to the anode wires. The cathodes are segmented in strips. This setup provides a transverse coordinate and a precision coordinate.

The track position is measured via interpolation between the charges induced on neighbouring cathode strips [103, p. 179]. The CSC reaches a resolution of 60 µm per plane. A resolution of 5 mm is achieved in a region perpendicular to the plane in which the charged particle tracks bend in the magnetic field due to a coarser cathode segmentation [103, p. 179]. The gas mixture (80% Ar and 20% CO_2) and the small gas volume result in a low neutron sensitivity and a timing resolution of approximately 7 ns per plane [103, p. 179].

4.4.2 Resistive Plate Chambers and Thin Gap Chambers

The task of the resistive plate chambers and thin gap chambers is to provide fast and coarse tracking information, bunch crossing identification and discrimination in muon transverse momentum for high level trigger functionality. In the barrel region ($|\eta| \leq 1.5$) RPCs are used, while in the end-cap regions ($1.05 < |\eta| < 2.40$) TGCs are utilised [103, p. 192].
An RPC is a gas based parallel electrode-plate detector, in which two resistive plates made of phenolic-melaminic plastic laminate are held parallel to each other. The gap is filled with a mixture of $C_2H_2F_4$ (94.7%), Iso $- C_4H_{10}$ (5.0%) and SF_6 (0.3%) [103, p. 194].

TGCs are multi-wire proportional chambers with a design similar to the CSCs. The distance between wire and cathode (1.4 mm) is smaller than the distance between the wires (1.8 mm). Combined with a high quenching gas filling of CO_2 and n-C_5H_{12} this geometry allows for operation in a quasi-saturated mode. These features lead to a very good time resolution for a large majority of the tracks and an efficiency $\geq$ 99 % for tagging of the beam crossing [103, p. 199].
TGCs provide two functions, muon trigger capability and determination of the second azimuthal coordinate to supplement the MDT measurement in the radial direction. In the end-cap the MDT is accompanied by seven layers of TGCs, while the inner MDT layer features only two layers of TGCs. The inner layer is segmented radially into two non-overlapping regions (end-cap and forward small wheel). The end-cap TGCs are mounted on support structures of the barrel toroid coils [103, p. 198].

4.5 Magnet System

The ATLAS Detector features a hybrid system of four superconducting magnets. Overall the magnet system measures 22 m in diameter and 26 m in length. The four superconducting magnets provide a magnetic field over a volume of roughly 12000 m^3 (region with a magnetic field strength $\geq$ 50 mT). The magnetic field is necessary to bend the tracks of charged particles in order to reconstruct their momenta from the bending radii. The layout of the magnet system is shown in Figure 4.5, depicting the eight barrel toroids, two end-cap coils and the barrel solenoid. The barrel toroid and the two end-cap toroids, provide a magnetic field of approximately 0.5 T and 1 T for the muon detectors in the central and end-cap regions, respectively. The volume of the barrel toroid encloses the calorimeters and both end-cap toroids. The barrel toroid consists of eight coils in a racetrack-shaped vacuum casing. Their overall size is 25.3 m in length with an inner and outer diameter of 9.4 m and 20.1 m, respectively.
The cylindrical solenoid is concentrically aligned with the beam axis and provides a 2 T

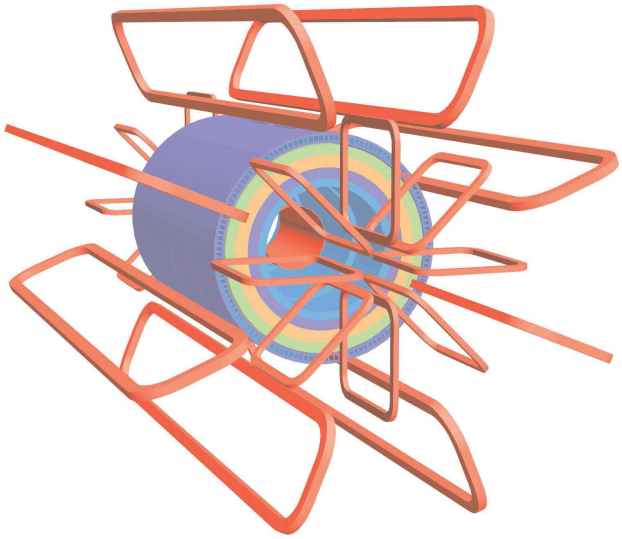

Figure 4.5.: Schematic view of the ATLAS magnet layout [103, p. 20].

axial magnetic field for the Inner Detector. It is a single layer coil, with optimised thickness, achieving high field strength. The coil measures a length of 5.8 m and an inner and outer diameter of 2.46 m and 2.56 m, respectively [103, p. 20].

4.6 Trigger System

The trigger system of the ATLAS detector incorporates a three level structure, Level1, Level2 and event filter (EF), whereas Level2 and EF are referred to as the high level trigger. Each trigger level reduces the event rate and refines the event selection from the previous level. The first level reduces the event rate from 40 MHz to about 75 kHz and only accesses limited detector information in order to make a fast decision whether to use the event or not. The higher the trigger level, the more detector information is used. The EF features an output at a rate of up to 200 Hz [103, p. 14]. A block diagram of the trigger and data acquisition is shown in Figure 4.6. The instantaneous luminosity increases further during the 8 TeV run. Since the data storage and networking capacities are limited all triggers can be prescaled. This means that only a certain amount of events can pass the trigger selection. More detailed information on the trigger settings recommended by the top work group can be found in Chapter 5.

4.6.1 Level1 Trigger

The Level1 trigger searches for signatures from muons with high transverse momentum (p_T), electrons/photons, jets and hadronically decaying tau leptons and provides the initial event selection. Besides high p_T muons the Level1 trigger selects events with large missing transverse Energy ($\not{E}_T$) and large total transverse energy. The Level1 trigger utilises low granularity information from RPCs and TGCs for high p_T muons and information from

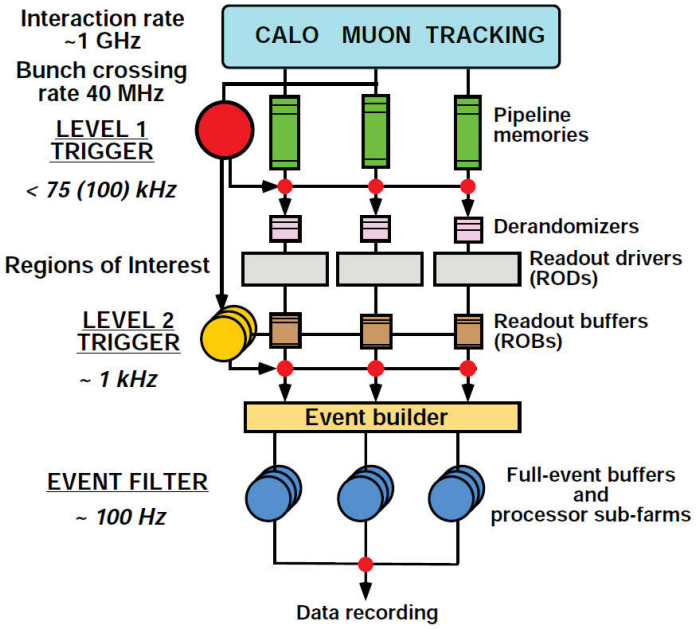

Figure 4.6.: Block diagram of the ATLAS trigger and the data acquisition system [94, p. 24].

the calorimeter for electromagnetic clusters, $\not{E}_T$ and hadronic objects. The trigger decision is formed within a 2.5 µs window after the associated bunch crossing [103, p. 218]. A block diagram of the Level1 trigger structure is shown in Figure 4.7. For electron/photon and tau triggers a minimum angular separation from significant energy deposits can be required (isolation criteria). The Level1 muon trigger decision is based on fast signals from RPCs and TGCs. The trigger algorithm searches for pattern of hits consistent with high p_T muons originating from the interaction region [103, p. 220].
Upon the trigger decision information of the geometric location of the trigger objects is sent as to the Level2 trigger. This information describes a Region of Interest (RoI). The Level1 trigger allows for unambiguous bunch crossing identification, which presents a challenge especially for the calorimeter triggers, since the width of the calorimeter trigger extends over several (on average four) bunch crossings [103, p. 221].

4.6.2 Level2 Trigger

Information about RoIs is passed to the Level2 trigger from the Level1 trigger. The RoIs are generated using Level1 trigger information to identify regions of the detector in which possible trigger objects are tagged. RoIs provide the seed for the Level2 trigger decision. The Level2 trigger utilises coordinates, transverse momentum of selected objects, energy, and signature type information of the RoIs. This limits the amount of information which has to be processed. The Level2 trigger has access to the complete event data with full precision and granularity if needed. The Level2 trigger further reduces the event rate to below 3.5 kHz and has a processing time of approximately 40 ms [103, p. 218].
The Level2 muon trigger rejects events by raising the p_T threshold compared to Level1

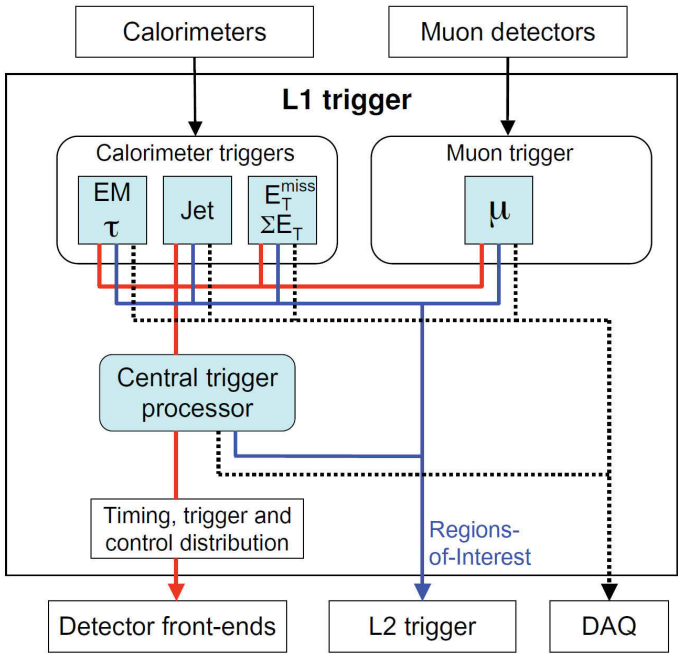

Figure 4.7.: Block diagram of the ATLAS Level1 Trigger [103, p. 220].

and applying isolation requirements. This is possible because the Level2 trigger utilises information from the precision muon chambers in the Inner Detector.
To reject electrons the Level2 the full granularity of the calorimeter and matching to high p_T charged tracks in the Inner Detector is used [94, p. 25]. It provides less rejection power for photons compared to electrons, because of the high probability of photon conversion in the material of the Inner Detector. Because high precision/granularity information of the calorimeter is used, the rejection power for photons of the Level2 trigger is improved compared to the Level1 trigger. The Level2 rejection for hadron and tau triggers is achieved by utilising full granularity information of the calorimeter and the Inner Detector. The Level2 trigger requires a localised, isolated cluster in the hadronic calorimeter and a matching high p_T Inner Detector track [94, p. 26].

4.6.3 Event Filter

The last stage of the online event selection is performed by the EF. It uses offline analysis algorithms on completely reconstructed events. Up to date calibration, alignment information and magnetic field maps are used. The EF makes the final selection of physics events which are written to permanent storage for full offline reconstruction. The output rate of the EF is approximately 100 Hz resulting in an output of roughly 100 MByte/s.
The EF confirms the results of the Level2 trigger decision and utilises the output of the former trigger as seed. The rejection power of the EF is based on refined algorithms and higher p_T thresholds compared to Level2. The availability of previously tagged RoIs and Level2 information and a larger time window for event processing (up to four seconds) further improves the rejection power of the EF [94, p. 26].

4.7 Data Storage

The operation of the ATLAS detector produces a vast amount of data to be processed. Hence it is vital to decentralise and share computing resources. The primary data processing takes place at CERN, referred to as Tier-0 facility. The raw data is archived at CERN and then distributed to the national Tier-1 facilities. These facilities not only provide reprocessing capabilities, but also allow physics analysis groups to access various versions of processed data for analysis purposes. Datasets derived by the physics groups are then copied to Tier-2 facilities for further analysis. These facilities not only provide the computing power for data analysis but also for the processing of simulated data stored at Tier-1 facilities. Furthermore the Tier-2 facilities have the capacity to produce the offline calibrations based on processing of raw data. The automatic distribution and processing of data on the Tier-1, 2, 3 facilities is managed by the LHC Computing Grid (LCG) environment [111, pp. 1,2].

Chapter 5

Object Definitions

The signals provided by the different systems of ATLAS comprise timing, position and energy information. These signals have to be translated, or reconstructed, into physics objects which can be used in various physics analyses. This chapter describes the reconstruction and selection of the objects relevant for the analysis presented in this thesis. Unless stated otherwise all criteria are applied to data and Monte Carlo (MC) simulation likewise.

5.1 Electrons

5.1.1 Trigger

ATLAS features a three-staged trigger system (see Section 4.6) to reduce the initial event rate of 40 MHz to approximately 100 Hz and to refine the event selection [103, p. 14]. The trigger utilises information on electromagnetic objects, which are the basis for the electron reconstruction. At the first stage (Level1) electromagnetic (EM) objects (e.g. photons, electrons) are selected if the transverse energy deposited in the EM calorimeter in two neighbouring towers of $\Delta\eta \times \Delta\phi = 0.1 \times 0.1$ is above a certain threshold. At the second stage the Level2 trigger utilises a special tracking algorithm (optimised in terms of response time) to serve the need for a fast trigger feedback. In the final stage the event filter (EF) uses similar algorithms as the final offline EM object reconstruction but with looser cuts [112, p. 3]. For more detailed information on the performance of the electron trigger refer to [113, pp. 1-2].

In order to control the overall output rates of events triggered by the single electron trigger, owing to the instantaneous luminosity increase in 2011, three different sets of selection thresholds were used. The details of the trigger menus can be found in [113, p. 3]. A short description is given in Table 5.1.

Period (2011)	Trigger Signature	Lumi Range (cm^{-2})	L1 Rate (Hz)	L2 Rate (Hz)	EF Rate (Hz)
B-J	e20_medium	up to 2×10^{33}	7300	273	50
K	e22_medium	$2 - 2.3 \times 10^{33}$	5700	273	45
L-M	e22vh_medium	$> 2.3 \times 10^{33}$	3600	150	22

Table 5.1.: The lowest threshold single electron triggers (without prescaling) are shown. The columns list the data period in which the triggers are applied, the trigger signature, the luminosity range and trigger rates at all three levels [113, p. 5]. The meaning of the signature is the following. A single e is the signature of a single electron trigger, the number following is the threshold of the transverse energy of the electron in GeV, while *medium* tags the reconstruction requirement of the electron. The additional tag *vh* means that instead of raising the trigger threshold (at the expense of reduced acceptance for physics) a hadronic leakage requirement was applied [113, p. 3].

5.1.2 Reconstruction

The offline reconstruction of electrons as physics objects involves the matching of clusters above a certain energy in the electromagnetic (EM) calorimeter to tracks of charged particles reconstructed in the inner detector (ID). Reconstructing the electrons using both the EM calorimeter and ID information helps to minimise the background levels. For details refer to [114, pp. 7-8].
The first step in the reconstruction is the creation of seed clusters with energies above 2.5 GeV in the middle layer EM cell units by using a sliding window algorithm (window size 3×5 cell units, which corresponds to $\eta \times \phi = 0.025 \times 0.025$) [114, p. 7]. After performing an energy comparison between the seed clusters possible duplicate clusters are removed from neighbouring seed clusters.
The detector region with $|\eta| < 2.5$ provides full tracking detector coverage, where an electron is defined by the existence of more than one reconstructed tracks matching a seed cluster. The matching is achieved by extrapolating the last measured space point in the ID to the middle layer of the EM calorimeter. Then the η and ϕ coordinates of the extrapolated impact point are compared to those of the corresponding seed cluster. If the difference is below a certain threshold the track is considered a match. In cases of tracks with no hits in the Pixel- and Silicon Strip Detectors the matching is restricted to the ϕ coordinate due to the limited η resolution of the Transition Radiation Tracker. In case of multiple track matches to one seed cluster the tracks are ordered by their matching quality (smallest $\Delta R = \sqrt{\Delta\eta^2 + \Delta\phi^2}$). Tracks with hits in the silicon detectors always have a priority over tracks with TRT hits only.

The reconstruction strategy inherits an ambiguity between prompt electrons and photons converted to e^+e^- pairs since both have to satisfy the same criteria in matching a track to a cluster in the EM calorimeter. This results in a significant contribution of misidentified photons in the electron candidate collection. This ambiguity is resolved by the particle identification criteria (Section 5.1.3), which allows for high electron reconstruction efficiency and purity of the final electron selection. Using MC simulations the

efficiency is estimated from W and Z decays to be $\sim 95\%$ at $E_T = 5\,\text{GeV}$ and $\sim 100\%$ with $E_T > 15\,\text{GeV}$ [112, p. 3]. The objects created by matching tracks to the seed clusters are treated as electron candidates. The EM clusters of the candidates are then re-evaluated using a sliding window algorithm (window size: 3×7 cells in the barrel and 5×5 cells in the end caps). Then several corrections are applied to the reconstructed cluster energy and the electron four-momentum is calculated from the best matched track. These corrections are necessary because there can be energy deposits in material in front of the EM calorimeter (lateral leakage) and also beyond (longitudinal leakage) [112, p. 4]. The energy of the physics object is the result of the weighted average between recalculated cluster energy and track momentum.
In the very forward region $2.5 < |\eta| < 4.9$ no tracking information is available. Here the electron candidates are reconstructed solely by grouping neighbouring calorimeter cells in three dimensions [112, p. 4]. These topological clusters are variable in size. The direction of an electron in the forward region is defined by the barycentre of the cluster cells. The energy is determined by the energy of the cluster corrected for lateral and longitudinal leakage [112, p. 4]. A forward electron candidate is only reconstructed if it has a small hadronic energy component and $E_T < 5\,\text{GeV}$.
The condition of the EM calorimeter dictates the quality of the electron energy measurement. At the analysis level three issues arising from the calorimeter condition have to be addressed:

- A few percent (1.2%) of the calorimeter cells cannot be read out because of electronics failure [115, p. 15]. Some of the front-end boards are inoperable because the optical transmitter failed. If a part of a cluster (seed or recalculated) lies in a region with dead front-end boards the cluster is rejected. If the dead region is in the back layer of the calorimeter or in the pre-sampler the object is reconstructed nonetheless.
- Approximately 6.1% of the readout cells are operating with reduced high voltage supply [115, p. 14]. If a cluster is recorded in such a region the cluster is rejected. The low voltage supply in those cells only adds to the noise in the energy measured but does not need special treatment in the reconstruction procedure [112, p. 4].
- Some cells produce a high noise signal or no signal at all. These cells are masked in the reconstruction software. If a noisy cell is in the outliers of a recalculated cluster its energy is set to the average of its neighbouring cells. If however a noisy cell is in the core of a cluster, the cluster is rejected [112, p. 4]. The non-functioning front-end boards are the dominating cause of acceptance losses.

5.1.3 Identification

After the offline reconstruction the candidate electron objects are filtered (identified) based on three different quality criteria. The electron identification is achieved by a cut based selection on calorimeter, tracking and isolation variables (or combinations thereof). Table 5.2 describes the different variables used in loose, medium and tight selections for electron identification.

Variable	Name	Description	l.	m.	t.
Detector acceptance	–	$\lvert\eta\rvert < 2.47$, excluding the region: $1.37 < \lvert\eta\rvert < 1.52$	✓	✓	✓
Transverse energy	E_T	$E_T = \frac{E_{\text{cluster}}}{\cosh(\eta_{\text{track}})} > 25\,\text{GeV}$	✓	✓	✓
Electron/jet overlap	–	Reject electrons with $\Delta R\,(\text{electron, jet}) > 0.4$ only for jets with $p_T > 20\,\text{GeV}$	✓	✓	✓
Hadronic leakage	R_{had1}	Ratio of E_T in the first sampling of the hadronic calorimeter to E_T of the EM cluster (range: $\lvert\eta\rvert < 0.8$ and $\lvert\eta\rvert > 1.37$)	✓	✓	✓
	R_{had}	Ratio of E_T in the the hadronic calorimeter and E_T of the EM cluster (range: $\lvert\eta\rvert > 0.8$ and $\lvert\eta\rvert < 1.37$)	✓	✓	✓
Middle layer of the EM	R_η	Ratio in η of cell energies in 3×7 versus 7×7 cells	✓	✓	✓
Calorimeter	$\omega_{\eta 2}$	Lateral width of the shower	✓	✓	✓
Strip layer of the EM	ω_{stat}	Total lateral shower width (20 strips)	×	✓	✓
Calorimeter	E_{ratio}	Ratio of the energy difference between the largest and second largest energy deposits over the sum of these energies	×	✓	✓
Track quality	n_{pixel}	Number of hits in the Pixel Detector (≥ 1)	×	✓	✓
	n_{Si}	Number of hits in the Semi Conductor Tracker (SCT) and the Pixel detector (≥ 7)	×	✓	✓
	d_0	Transverse impact parameter with respect to primary vertex ($< 5\,\text{mm}$)	×	✓	✓
B-layer	n_{BL}	Number of hits in the B-layer (≥ 1)	×	×	✓
Transition Radiation Tracker	n_{TRT}	Total number of hits in the TRT (for $\lvert\eta\rvert < 2.0$)	×	×	✓
	f_{HT}	Ratio of the number of high threshold hits to the total number of TRT hits (for $\lvert\eta\rvert < 2.0$)	×	×	✓
Track matching	$\delta\eta$	$\lvert\Delta\eta\rvert < 0.01$ between the cluster and the track in the strip layer of the EM calorimeter	×	✓	✓

Table 5.2.: Definitions of variables used for electron identification [116], [117], [113, p. 4] for loose (l.), medium (m.) and tight (t.) selection criteria.

Variable	Name	Description	l.	m.	t.
	$\Delta\phi_2$	$\lvert\Delta\phi\rvert < 0.02$ between the cluster and the track in the middle layers of the EM calorimeter	×	×	✓
	E/p	Ratio of the cluster energy to the track momentum	×	×	✓
Calorimeter isolation	etcone20	Total transverse energy collected in the calorimeter in a cone with $\Delta R = 0.2$ around an electron/photon object	×	✓	✓
		etcone20 $< 6\,\text{GeV}$	✓	×	×
Track isolation	ptcone30	Total transverse momentum of all tracks in a cone with $\Delta R = 0.3$ around an electron/photon object	×	✓	✓
		ptcone30 $< 6\,\text{GeV}$	✓	×	×

Table 5.2.: Definitions of variables used for electron identification [116], [117], [113, p. 4] for loose (l.), medium (m.) and tight (t.) selection criteria.

5.1.4 Scale Factors

The data and Monte Carlo (MC) show slightly different efficiencies for trigger, reconstruction, selection and isolation-cuts. Scale factors of the form $\epsilon_{\text{data}}/\epsilon_{\text{MC}}$ are applied to each event with a selected electron in its final state. Electron reconstruction and trigger efficiencies are evaluated using a tag and probe method [118, p. 16] and $Z \to ee$ samples. The derived scale factors are calculated for 9 (18) η bins for the reconstruction (trigger) efficiencies. The discrimination into different bins is necessary because the efficiencies vary in different detector regions, e.g. due to support structures. For the trigger reconstruction efficiencies there are additional corrections in 6 bins of E_T for $E_T > 6\,\text{GeV}$ [119, p. 9]. Selection efficiencies are derived from combined measurements of $Z \to ee$ and $W \to e\nu$ samples and are binned in 9 η bins with corrections in 6 E_T bins [119, p. 9]. Isolation-cut efficiencies with respect to the tight electron selection are measured using $Z \to ee$ samples. The efficiencies are derived directly from a two dimensional histogram with $(8\,\text{bins}\,E_T) \times (9\,\text{bins}\,\eta)$ [119, p. 9].

5.2 Muons

5.2.1 Trigger

The muon trigger corresponds to the three level structure of the ATLAS trigger system. There are three types of triggers available at Level2, standalone-, combined- and isolated-trigger [120, p. 3]. In the barrel region three layers of resistive plate chambers and thin

gap chambers provide the Level1 muon trigger signal. The Level1 muon trigger is a hardware trigger. It selects muon candidates based on a coincidence signal from the trigger chambers. The hit pattern along the trajectory of the candidate is used to determine the transverse momentum of the muon [120, p. 2].
The Level2 stage of the muon trigger selects Regions of Interest, based on the Level1 position information. At this second stage a muon (standalone) algorithm constructs tracks from the data of the muon system within the Regions of Interest seeded by the Level1 information [120, p. 2]. Then reconstructed tracks from the standalone algorithm are combined with ID tracks to improve the quality of the measured track parameters. A third (isolated) muon algorithm uses the result of the combined algorithm as a starting point, but incorporates calorimetric information to find isolated muons.

At the event filter (EF) stage the full event data is accessible. There are two strategies employed by the EF muon trigger. The *outside-in* strategy starts from a Level2 region of interest, utilising the precision tracking data. These candidates only rely on muon system data and form the EF standalone trigger. The standalone candidates are then combined with ID tracking information, thus forming the EF muon combined trigger. The *inside-out* strategy starts with the ID tracks and extrapolates them to the muon system. Both strategies were used in parallel during the 2011 data taking [120, p. 3]. As in case of the electrons, different muon trigger menus were chosen for different data periods. The corresponding features and descriptions can be found in Table 5.3.

Period	Trigger Signature	Lumi Range (cm^{-2})	L1 Rate (Hz)
B-I	mu18	$< 1.9 \times 10^{33}$	15000 (L1_MU10)
J-M	mu18_medium	$> 1.9 \times 10^{33}$	8000 (L1_MU11)

Table 5.3.: The lowest threshold single muon triggers are shown, without pre-scaling, the data period at which they are applied, the luminosity range where they are used as main triggers and trigger rates at Level1. The L1_MU10 trigger is composed of coincidences of hits from a two station trigger in the barrel region and three hits in the endcap region, the L1_MU11 trigger uses three stations in both regions. The term medium does not denote the object quality but only points to a change in the trigger requirements [120, pp. 3-4].

5.2.2 Reconstruction

The muon offline reconstruction also features two different algorithms, namely standalone and combined. The standalone algorithm solely uses information provided by the ATLAS muon system. Muon properties are derived by extrapolating the particle tracks measured in the muon spectrometer back to the beam line, taking into account the energy loss in the calorimeter section. For details see [120, pp. 7-8].
The combined reconstruction is performed separately in the ID and in the muon system. The track is then formed by calculating a weighted average of the ID and muon system

track parameters. Muons reconstructed by the combined algorithm must feature a minimum number of hits in the silicon detector and in the TRT along the found track (see Table 5.4). The cuts on the number of hits in the ID are used to suppress fake tracks and to discriminate against muons from secondary hadronisation processes. In ATLAS top-quark analyses only combined muons (Muid) are used for physics analyses.

5.2.3 Identification

The muon identification criteria are summarised in Table 5.4. Analyses using dilepton final states use additional cuts to reject events triggered by muons from cosmic rays. The criteria for cosmics rejection are summarised in Table 5.5.

Type	Name	Description	loose	tight
Reconstruction algorithm	Muid	Combined algorithm as described in Sections 5.2.1 and 5.2.2	✓	✓
Transverse momentum	p_T	$p_T > 20\,\text{GeV}$	✓	✓
Acceptance	η	$\lvert\eta\rvert < 2.5$	✓	✓
ID hit requirements	n_{BL}	Number of b-layer hits $n_{\text{BL}} > 0$	✓	✓
	n_{P}	Number of pixel hits and number of dead pixels on track, $n_{\text{P}} = n_{\text{Pix}} + n_{\text{DeadPix}} > 1$	✓	✓
	n_{S}	Number of SCT hits and number of dead SCT sensors on track, $n_{\text{S}} = n_{\text{SCT}} + n_{\text{DeadSCT}} \geq 6$	✓	✓
	n_{H}	Number of pixel holes and number of SCT holes, $n_{\text{H}} < 3$	✓	✓
	n	Combined number of TRT hits and TRT outliers $n_{\text{TRT}} + n_{\text{TRToutlier}}$. Accepted if:		
		$n > 5$ and $n_{\text{TRToutlier}}/n < 0.9$ for $\lvert\eta\rvert \geq 1.9$	✓	✓
		$n > 5$ and $n_{\text{TRToutlier}}/n < 0.9$ for $\lvert\eta\rvert < 1.9$	✓	✓
		no additional cut for $n \leq 5$ and $\lvert\eta\rvert \geq 1.9$		
Longitudinal impact parameter	z_0	$z_0 < 2\,\text{mm}$	✓	✓
Muon/jet overlap	–	Reject muons with $\Delta R\,(\text{muon,jet}) < 0.4$ only for jets with $p_T > 25\,\text{GeV}$ and jet vertex fraction $\lvert\text{JVF}\rvert > 0.75$	✓	✓
Calorimeter isolation	etcone20	Total transverse energy in a cone of $\Delta R = 0.2$ around a muon object, etcone20 $< 4\,\text{GeV}$	×	✓

Table 5.4.: Definition of variables used for muon identification [117] .

Type	Name	Description	loose	tight
Track isolation	ptcone30	Total transverse momentum of all tracks in a cone of $\Delta R = 0.3$ around a muon object, ptcone30 $< 2.5\,\text{GeV}$	✗	✓

Table 5.4.: Definition of variables used for muon identification [117] .

Type	Name	Description
Transverse impact parameter	d_0	Like sign of the d_0 variable from both muons and $\lvert d_0\rvert < 0.5\,\text{mm}$
Muon pair azimuth distance	$\Delta\phi$	$\Delta\phi > 3.1$

Table 5.5.: Criteria for cosmics rejection [117] .

5.2.4 Scale Factors

As in case of the electrons, muons show slightly different efficiencies in data and MC [121, p. 5]. These differences in muon identification- and trigger efficiencies have to be corrected using scale factors. Similar to the electron scale factors, the muon counterparts are measured in $Z \to \mu\mu$ events using a tag and probe method. The resulting scale factors are evaluated separately in the B-I, J-K and L-M data periods. Their values are within 1% of unity for the identification type scale factor. The trigger efficiencies vary due to hardware issues in individual trigger chambers and hence they are parametrised in η and ϕ. They are separate for three data sets B-I, J-K and L-M [121, p. 5]. The muon scale factors are taken into account for every event containing a selected muon.

5.3 Jets

5.3.1 Reconstruction

The ATLAS top physics working group uses jet objects reconstructed by the anti-k_t jet clustering algorithm, which is IRC (infrared and collinear) safe and soft resilient [117], [122, p. 2]. Particles subject to the strong interaction can radiate low energy (soft) gluons or gluons which are collinear to the mother particle track. IRC safe and soft resilient means that the jet algorithm must ensure that the presence of soft or collinear radiation does not change the structure of higher energy jets in the event [123, p. 3]. The anti-k_t algorithm guarantees that by employing the sequential recombination algorithms, k_t and Cambridge/Aachen.
The underlying principle is to introduce two measures of distances: d_{ij} between particles

i (entities) and pseudojets j, and d_{iB} between an entity i and the beam B. An entity i is added to a cluster of a pseudojet if d_{ij} is the smallest of both distances. If, however, d_{iB} is the smallest distance, the corresponding entity i is deleted from the list of entities. Then all distances are recalculated and the procedure is repeated until no entity is left [122, p. 2]. The extension of the anti-k_t algorithm lies in the definition of d_{ij} and d_{iB}.

$$d_{ij} = \min\left(k_{ti}^{2p}, k_{tj}^{2p}\right) \frac{\Delta_{ij}^2}{R^2}, \tag{5.1}$$

$$d_{iB} = k_{ti}^{2p}, \tag{5.2}$$

where k_{ti} is the transverse momentum of the entity i, $\Delta_{ij}^2 = (y_i - y_j)^2 + (\phi_i - \phi_j)^2$, y_i and ϕ_i are rapidity and azimuth of particle i, and R is the radius parameter of the cone. The parameter p regulates the relative power of the energy versus the geometrical scales [122, p. 2]. Different values of p recover different behaviours of the clustering algorithm: $p = 1$ recovers the inclusive k_t, $p = 0$ the Cambridge/Aachen and $p = -1$ the anti-k_t jet clustering algorithm. The parameter d_{ij} between a hard and a soft particle is in general smaller than the d_{ij} between similarly separated soft particles, because

$$d_{ij} = \min\left(k_{ti}^{-2}, k_{tj}^{-2}\right) \Delta_{ij}^2 / R^2 \tag{5.3}$$

is dominated by the transverse momentum of the hard particle. This means that soft particles tend to cluster to high p_T particles before clusters of soft particles are formed [122, p. 3]. For the analysis presented the anti-k_t algorithm is implemented with a radius parameter $R = 0.4$ and uses topological calorimeter clusters as entities [124, p. 8].

In order to reconstruct jets topological clusters are formed from seed cells, which are required to have a signal to noise ratio of $r_s > 4$. The neighbouring cells with $r_s > 2$ are included iteratively. The algorithm stops if no nearby cells fulfill the r_s criteria. After the clusters are formed all cells contained in a cluster are searched for local maxima in energy content. In case of a local maximum $> 500\,\text{GeV}$ this cell is used as a new seed cell and the cluster is split [124, p. 9]. The energy of the jet is measured at the EM scale from the energy depositions in the topological clusters, while the jet four-momentum is reconstructed from the corrected energy and angles with respect to the primary vertex. The energy correction is part of the application of the EM+JES calibration (electromagnetic, jet energy scale) scheme. This calibration is added as a function of the jet energy and pseudorapidity, and corrects for different effects such as [124, p. 12]:

- Pile-up: Energy of additional secondary pp-collisions is subtracted. This correction is calculated from MC and parametrised in bins of jet η according to the number of primary vertices in the event and the number of average interactions per luminosity block.
- Vertex mismatching: Track parameters are corrected if they point to the geometrical detector centre and not to the primary vertex.
- Jet energy and direction correction: Energy and direction of jets are corrected using constants derived from reconstructed and truth jets in MC.

The energy correction is derived from the jet calibration, which balances out different detector effects: incomplete measurement of deposited energy, energy loss in dead detector

material, particle leakage outside the calorimeter, signal losses in the calorimeter clustering and jet reconstruction [124, p. 5].

5.3.2 Jet Quality

The jets are comprised of many particles. Therefore the reconstruction is sensitive to out-of-time energy depositions, calorimeter hardware problems, LHC beam gas interactions and cosmic ray induced showers. These falsely reconstructed jets are referred to as fake jets or bad jets. By application of several quality criteria these fake jets are removed from the jet candidate list. There are several sources of fake jets: calorimeter noise, cosmic rays, beam induced background and pile-up.

Calorimeter noise is a source for bad jets and can be categorised in two main types. Sporadic noise bursts in the hadronic endcap calorimeter and coherent noise in the EM calorimeter [125, p. 3]. Noise bursts originate in a few noisy calorimeter cells, which contribute almost all of the jet energy. One noisy cell in the endcap calorimeter results in reconstructed jets with a large energy fraction in the endcap calorimeter and a large fraction of energy reconstructed in cells with poor signal shape quality. As a result of the capacitive coupling between channels, the cells in the vicinity of noisy cells will have negative energy. Hence a cut on negative energy and large energy fraction from the hadronic endcap calorimeter is used to reject these jets. Similar bad jets originate from coherent noise and are characterised by a large EM energy fraction.

The fake jets due to cosmic rays and beam induced background can be rejected by applying a cut on the jet time. The jet time is the time in which energy is deposited in the calorimeter cells (weighted by the squared energy) relative to the collision time. Cuts on the EM energy fraction and on the maximum energy fraction deposited in any calorimeter layer are employed to further reduce the non collision background [125, p. 3].

Another source of bad jets is the in-time pile-up (Section 3.2.2). In order to reduce the influence of in-time pile-up a cut on the jet vertex fraction (JVF) is employed. The cut on JVF $> 75\%$ means that 75% of all tracks associated to the jet at hand originate from the primary vertex [121, p. 12].

5.3.3 Identification

For the analysis presented in this thesis only jets reconstructed using the anti-k_t algorithm (with a cone size of $\Delta R = 0.4$) are considered. The input for the anti-k_t algorithm are topoclusters and for the energy calculation the EM+JES calibration scheme is used. A selected jet is required to be reconstructed in an acceptance range of $|\eta| < 2.5$, to have a transverse momentum of $p_T > 25\,\text{GeV}$, and has to fulfill the jet vertex fraction requirement JVF > 0.75.
The jet reconstruction relies on calorimeter information as does the electron reconstruction. Due to that all electrons (causing energy deposits in the calorimeter) are treated as jet candidates. In order to remove these electron-jet duplicates a cut on the $\Delta R\,(\text{jet,electron}) <$

0.2 between all accepted electrons fulfilling the tight selection criteria and all energy corrected jets is applied. If a jet fails this cut it is removed from the jet collection [117].

5.3.4 b-Tagging

The top-quark mainly decays into a W-boson and a bottom-quark (Section 2). Hence the identification of jets originating from bottom-quarks is important for top-quark analyses and boosts the purity of the final event selection. The ATLAS top physics working group recommends the use of the MV1 tagger at the 70% working point [117]. The MV1 algorithm is a neural-network based algorithm that uses the output weights of three tagging algorithms (IP3D, SV1 and JetFitterCombNN) as inputs.

The IP3D tagging algorithm is impact parameter based and uses a likelihood technique in which input variables are compared to pre-defined smoothed and normalised MC distributions for b- and light-jet hypotheses [126, p. 7]. The distributions are two dimensional representations of the signed impact parameter significance d_0/σ_{d_0} and the longitudinal impact parameter significance z_0/σ_{z_0}. The impact parameters are computed with respect to the primary vertex. Since the decay point of the bottom-quark has to lie along its flight path the impact parameter is signed to discriminate bottom-quark tracks from other tracks originating from the primary vertex. The sign of the impact parameter is calculated using

$$\text{sign}\,(d_0) = \left(\vec{P}_j \times \vec{P}_t\right) \cdot \left(\vec{P}_t \times \left(\vec{X}_{\text{pv}} - \vec{X}_t\right)\right) . \tag{5.4}$$

The impact parameter is the distance of closest approach of the track to the primary vertex. With $\vec{P}_j$ denoting jet direction as measured in the calorimeter, the direction or the track $\vec{P}_t$, the position of the track at the point of closest approach to the primary vertex $\vec{X}_t$ and the position of the primary vertex $\vec{X}_{\text{pv}}$. Tracks from the primary vertex generate a random sign, while tracks from the bottom (charm)-quark decay tend to have a positive sign. The impact parameter significances of all the tracks in the jet, combined with the correlation to the longitudinal impact parameter, provide the basis for the IP3D tagger [127, pp. 406-407].

The SV1 tagging algorithm is a secondary vertex based algorithm. A secondary vertex is formed whenever a particle hadronises outside the primary vertex. The secondary vertex algorithm starts by searching for all track pairs forming a good vertex only using tracks which are far enough from the primary vertex. The requirement is formulated in the following way

$$\frac{L_{D3}}{\sigma_{L_{D3}}} > 2,\ L_{D3} = \left|\vec{X}_{\text{pv}} - \vec{X}_t\right| . \tag{5.5}$$

Using an iterative method the track pairs are combined into a single vertex, always dismissing those track pairs with the worst χ^2 in the vertex fit. The SV1 tagger relies on a two dimensional distribution between the invariant mass of all tracks associated to the vertex and the ratio of the sum of energies of all tracks (of the vertex) to the sum of energies of all tracks in the jet. Additionally, a one dimensional distribution of the number of track pair vertices is used [127, p. 407].

The JetFitterCombNN combines the IP3D and the JetFitter algorithm using a neural network. The JetFitter exploits the topological structure of weak bottom- and charm-

quark decays within a jet. It utilises a Kalman fitter to find a common line between the primary vertex and the bottom- and charm-quark vertices. Light jets, bottom- and charm-quarks are discriminated using a likelihood expression based on similar variables as the SV1 tagger [127, p. 407].
If a jet passes the selection criteria mentioned in Section 5.3.3 and features an MV1 weight of $\omega_{\mathrm{MV1}} > 0.601713$ ($\sim 70\%$ working point) it is considered to be a jet originating from a hadronising bottom-quark. As in case of the electrons and muons, also for jets a scaling factor needs to be applied in order to match MC and data b-tagging efficiencies. The scale factor is the ratio of the data b-tagging efficiency and the MC b-tagging efficiency. These efficiencies are measured in ten regions of transverse momentum between 25 GeV to 300 GeV [128, p. 1]. Additionally a mistag scale factor is computed to correct for jets tagged as b-jets but originating from light-quarks or a charm-quark. It is determined in analogy to the b-tagging efficiency scale factor.

5.4 Missing Transverse Energy

The missing transverse energy $\not{E}_T$ in a collider experiment is defined as the momentum imbalance in the transverse detector plane. It provides a measure for the presence of undetectable particles, such as neutrinos. The momentum imbalance is obtained from the negative vector sum of the momenta of all particles detected in a collision event [129, p. 1]. The missing energy is estimated using energy deposits in the calorimeters (EM-scale calibrated topoclusters) and muons reconstructed in the muon spectrometer.

$$\not{E}_{x(y)} = \not{E}^{\mathrm{calo}}_{x(y)} + \not{E}^{\mu}_{x(y)}. \tag{5.6}$$

Also tracks of low transverse momentum are considered in order to recover particles which are not detected by the calorimeters due to their low transverse momentum. Muons only reconstructed by the ID are used because some regions are not covered by the muon spectrometer. The values of $\not{E}_T$ and its azimuthal coordinate are then calculated as

$$\not{E}_T = \sqrt{(\not{E}_x)^2 + (\not{E}_y)^2}, \tag{5.7}$$

$$\phi^{\mathrm{miss}} = \arctan\left(\not{E}_y, \not{E}_x\right). \tag{5.8}$$

The calorimeter term of the $\not{E}_{x(y)}$ part is reconstructed using calorimeter cells, which are calibrated according to an associated high transverse momentum object, increasing the precision of the measurement. Cells without an associated object are taken into account as the $\not{E}_T^{\mathrm{CellOut}}$ contribution. The calorimeter term is then calculated as

$$\not{E}^{\mathrm{calo}}_{x(y)} = \not{E}^{e}_{x(y)} + \not{E}^{\gamma}_{x(y)} + \not{E}^{\tau}_{x(y)} + \not{E}^{\mathrm{jets}}_{x(y)} + \not{E}^{\mathrm{softjets}}_{x(y)} \left(+\not{E}^{\mathrm{calo},\mu}_{x(y)}\right) + \not{E}^{\mathrm{CellOut}}_{x(y)}, \tag{5.9}$$

with each term calculated from the negative sum of calibrated cell energies inside the corresponding objects in a pseudorapidity range of $|\eta| < 4.5$. A jet is considered a soft jet if its transverse momentum is between 7 GeV and 20 GeV. All jets are calculated according to the EM scale. The muon term is calculated from the momenta of muon tracks reconstructed with $|\eta| < 2.7$

$$\not{E}^{\mu}_{x(y)} = -\sum_{\mathrm{muons}} p^{\mu}_{x(y)}, \tag{5.10}$$

where the muon term is summed for selected muons and is calculated differently for isolated and non-isolated muons. A muon is considered non-isolated if a reconstructed jet is found within a distance of $\Delta R < 0.3$ [129, pp. 3-4].

Chapter 6

Signal and Background Simulation

Analyses in high energy physics rely on the comparison between detector data and simulated physics processes. Only by comparing simulated events and real detector data underlying physics processes can be identified and verified. These processes are simulated in the perturbative theory of the Standard Model (SM) to both leading order (LO) and next-to-leading order (NLO) approximation. For the production of the samples used in this analysis different general-purpose Monte Carlo generators and showering algorithms are used, MC@NLO [130], Alpgen [131], Acer MC [132], HERWIG [133] and PYTHIA [134]. These generators are briefly described in Sections 6.3 and 6.4. All samples used in this thesis are part of the ATLAS MC11 production campaign. A list of the MC samples can be found in Appendix A.

Tree level matrix element calculations with parton shower matching are used to simulate several processes. These LO calculations are then normalised to the NLO cross-section. Final states with different parton multiplicities (e.g. $Z \rightarrow ee + n$ additional partons) are simulated for predefined shower matching cuts. The sum of the exclusive cross-sections is then normalised to the result of higher order calculations. However, large uncertainties are expected in the absolute cross-section predictions in extreme phase space regions, such as final states with high jet multiplicities [127, p. 4].

Different MC models are used for the production of main signal and background samples. In this analysis a central model, recommended by the ATLAS top working group, is used. The central sample is completely simulated (using the full detector model). It allows for for precision measurements and provides the baseline sample for top-quark physics analyses. Fast simulations are used for the calculation MC modelling systematic uncertainties [121, p. 70]. The background due to fake leptons originating in quantum chromodynamic (QCD) processes is estimated by a data driven technique requiring a special event and object selection and is hence described separately in Chapter 7.2.

6.1 Production of Monte Carlo Samples in ATLAS

The current ATLAS MC production chain can be split up into five general steps. The first step is the event generation, in which the hard process is simulated using LO or NLO MC generators. The output of this step contains four-vector information of the initial-, intermediate- and final-state particles.
The final state particles are then passed to a second MC generator, which handles the non-perturbative evolution, especially hadronisation and the up-following parton showering. ATLAS mainly uses PYTHIA and HERWIG for this production step, hence incorporating two different hadronisation models, namely the Lund-string model in the case of PYTHIA and the cluster model for HERWIG. The Lund model is a string fragmentation model in which the long range confinement forces can distribute the energies and flavours of an interacting parton configuration in a way that forms additional primary hadrons between the interacting pair. These new primary hadrons can decay subsequently [134, p. 12]. The cluster model used in HERWIG forms colour singlet clusters of light quark-antiquark (diquark-antidiquark) pairs. These clusters have a small spatial size, a small mass, and are asymptotically independent of the hard sub-process type and scale. If a cluster is too light to be fragmented into two hadrons it is assumed to be the lightest single hadron of its flavour. If a cluster has enough mass to decay into a hadron pair the cluster is fragmented [133, p. 23]. HERWIG is linked to JIMMY [135] which handles the simulation of underlying events. Both PYTHIA and HERWIG are connected to the PHOTOS [136] package which improves the applied quantum electrodynamic (QED) corrections [136, pp. 1-2].
After simulation of the hard process and subsequent showering the detector simulation added as the third step. It simulates the interactions of particles with the structure of the ATLAS detector. This not only includes particle interactions with the active and passive detector material, but also the effects of the magnetic field as the particle traverses through the ATLAS detector. The ATLAS detector simulation is handled by Geant4 [137]. Geant4 is a simulation tool kit which provides tracking, geometry description and navigation, material specification, abstract interfaces to physics processes, event management and tools for the calculation of the detector response [137, p. 1].
The fourth and fifth step in the production of simulated samples are the simulation of pile-up and the digitisation. For the pile-up simulation additional proton interactions are overlaid with the hard process. The digitisation step transforms the Geant4 simulation into the expected detector response, taking into account e.g. the response of the readout electronics. After digitisation the simulated event data is comparable to real events taken from proton-proton collisions [138, pp. 2-4].

6.2 File Formats

The raw data processing results in a number of event formats, decreasing the event size in each processing level. However, not all formats are suitable for the end user analysis. Raw detector and raw simulated data is processed in the same way. The different file formats in order of derivation are, raw data in byte-stream format, Simulated Event Data (SIM), Event Summary Data (ESD), Analysis Object Data (AOD) and Derived Physics Data (DPD).
The output of the event filter (EF) is called the raw data and has an event size of approximately 1.6 MB. It has a byte stream format representing the data as delivered from the detector. Hence, it features no object oriented representation. Each file contains events

from a single run. These are not consecutive or ordered. SIM refers to a range of data types starting with generator events (e.g. Pythia), over Geant4 hit simulations or direct detector response (events after digitisation). The only difference (file format wise) between SIM and Raw data is the presence of Monte Carlo truth information increasing the file size [111, pp. 7-8]. The ESD files are derived from the raw data. They store the output of the reconstruction process. ESDs have a size of roughly 500 kB per event and feature an object oriented representation stored in ROOT [139] files. The ESD file format is not designed as end user format. The AODs feature a reduced event representation derived from the ESD. They contain physics objects in an object-oriented representation with an average event size of 100 kB. AODs are also stored in ROOT files.
The DPD file format provides a standardised format covering all variables needed for standard analysis in an n-tuple style representation [111, p. 7]. D3PDs are derived by further slimming of DPDs and have the same features as DPDs. It is easily accessible with standard analysis tools (ROOT etc.). Except D3PD files all other file formats feature a more complex structure than flat n-tuples [140, p. 1].

6.3 Top-Quark Pair Production Sample

The inclusive $t\bar{t}$ signal sample is generated using the MC@NLO generator (version 4.01) incorporating a set of parton density distribution functions from CT10 [141]. The MC@NLO generator matches next to leading order perturbative calculations of a given QCD process with a parton shower Monte Carlo simulation. The total exclusive rates are accurate to NLO. Hard emissions are treated as in NLO computations while soft/collinear emissions are handled by the MC simulation with smooth matching between the hard and soft/collinear regions [130, p. 2].
The MC@NLO generator produces weighted events allowing for negative weights ($\omega = \pm 1$). The negative weights do not originate in the negative contributions of NLO computations, they appear because MC@NLO is not required to be positive definite. The weight distributions are separately definite, which is not true for NLO computations [130, p. 5].
The combination of NLO calculation and MC simulations results in double counting (in the soft and collinear regions) of the one particle emission phase space, since MC and NLO results coincide when only leading terms are considered. This double counting is resolved internally and is of no concern to the end user [130, p. 5].
Parton showering, fragmentation and underlying events have been modelled using HERWIG (version 6.520) [133] and JIMMY (version 4.31) for multi-parton interactions, using the CT10 HERWIG and JIMMY ATLAS AUET2 tune [142, p. 30]. The $t\bar{t}$ cross-section is normalised to the approximate next-to-next-to leading order predictions of $166.78^{+16.5}_{-17.8}$ pb [121, p. 70]. For the calculation of the cross-section the HATHOR [143] tool was used. The sample statistics of the described central $t\bar{t}$ sample corresponds to an integrated luminosity of approximately 150 fb^{-1}[121, p. 70].

6.4 Background Simulation

Several different processes contribute to the background (non signal processes with a similar dileptonic final state) of top quark pair production. These processes are simulated with different MC generators and showering algorithms as described in the following sections.

6.4.1 Single Top

The main samples for single top production in the s-channel and $Wt \rightarrow$ X were created using the same MC generator (MC@NLO version 4.01), parton showering tools (HERWIG version 6.520) and tunes as the $t\bar{t}$ signal sample described in Section 6.3 [121, p. 70]. The t-channel single top samples were produced using the AcerMC generator (version 3.8) [132] interfaced with PYTHIA [134] with the MRST LO** [144] PDF set and the ATLAS AUET2b [145] tune.
The AcerMC generator is used because of modelling deficiencies of the initial MC@NLO and HERWIG setup [121, p. 70]. The MC@NLO and HERWIG setup resulted in additional unphysical jets from the HERWIG shower [146]. The AcerMC generator is optimised for the modelling of SM background processes at 14 TeV in the LHC environment but also works at LHC energies of 7 TeV and 8 TeV. The program provides a library of matrix elements and phase space modules for the generation of selected processes [132, p. 5]. The matrix elements have been coded by the MadGraph/HELAS [147] package, the phase-space generation is based on the multi-channel self-optimising approach using the modified Kajantie-Byckling formalism [148] for phase space construction and further smoothing of the phase space was obtained by using a modified ac-VEGAS algorithm [132, p. 1].
The single top cross-sections are normalised to next-to-next-to leading order predicted values of $64.6^{+2.7}_{-2.0}$ pb [45] for the t-channel, 4.6 ± 0.2 pb [46] for the s-channel and 15.7 ± 1.1 pb [47] for the Wt-channel. For each of the electron-, muon- and tau- s-channel leptonic decay samples ~ 300 k events are available. For the corresponding t-channel decay samples ~ 1 M events are available. The $Wt \rightarrow$ incl. decay sample features ~ 900 k events.

6.4.2 Z-Boson Production with Additional Partons

The vector boson production uses ALPGEN interfaced with HERWIG and JIMMY that in turn uses the CTEQ6.1 PDF [35], as well as the AUET2 [142] tune. ALPGEN is a LO MC generator and was developed for the study of multi-parton hard processes in hadronic interactions, specifically those expected at the Tevatron and the LHC. At LO full matrix elements are calculated for a large set of parton level processes. These processes comprise a colour and flavour structure, allowing for the evolution into fully hadronised final states [131, p. 1]. The inclusive Z-boson production samples originate from the full set of parton multiplicity sub-samples and belong to the same production process as the $Z +$ jets and the $Z +$heavy quark+jets processes [121, p. 71]. ALPGEN does not match matrix element partons and jets from the parton shower. The same heavy flavour final states can occur in multiple samples, therefore the heavy flavour overlap removal tool is used to prevent double counting [149].
The production cross-sections are normalised to the next-to-next-to leading order cross-sections (details can be found in [150]). The parton multiplicity sub-samples are produced for an equivalent of $\sim 10\,\text{fb}^{-1}$ [121, p. 71].

6.4.3 Diboson

The diboson processes are simulated using HERWIG, creating separate samples for WW, ZZ and WZ processes. These samples are filtered for one lepton with $p_T > 10$ GeV and $\eta < 2.8$ [151]. This ensures that at least one boson is decaying leptonically. The k-factors

(provided in the Appendix A.3) are such that the unfiltered HERWIG cross-sections agree with the numbers in [150] and are calculated with the Monte Carlo for Femtobarn Processes (MCFM) code [152].

6.4.4 Monte Carlo Weighting

The baseline MC weight is given by the MC generator itself. Most MC generators feature positive event weights of 1. Of the generators used only MC@NLO has an output of a weight of -1 for approximately ten percent of the simulated events. The MC and data do not always feature same efficiencies for identification and reconstruction. Hence additional weights are used to correct for these deficiencies. These individual scale factors are explained in the Sections 5.1.4, 5.2.4 and 5.3.4.
The influence of pile-up has to be considered separately, although pile-up is also taken into account in the simulation before the digitisation stage. This is because MC samples are usually produced with conditions similar to those of a given data taking period. Pile-up conditions of the data run can differ from those of the simulation. To correct for deviations a pile-up reweighting scheme is implemented on analysis level. The analysis presented in this thesis uses pile-up weights as described in [153].

For data taken in 2011 in-time and out-of-time pile-up has to be considered. The average number of pile-up interactions $\langle\mu\rangle$ has been introduced as a measure for both pile-up quantities and is used to calculate the reweighting factor. The variable $\langle\mu\rangle$ is directly correlated to the instantaneous luminosity and is taken as average over one lumiblock, since this is the smallest amount of data. The event weight is calculated using the $\langle\mu\rangle$ distributions of data and MC

$$\omega_{\text{pileup}} = \frac{\langle\mu\rangle^{\text{data}}}{\sum_i \langle\mu\rangle_i^{\text{data}}} \left(\frac{\langle\mu\rangle^{\text{MC}}}{\sum_i \langle\mu\rangle_i^{\text{MC}}} \right)^{-1}. \tag{6.1}$$

The overall event weight is then the accumulation of electron, muon, b-tagging and pile-up scale factors (weights) and is applied to each event in each selection step. The total weight is given by

$$\begin{aligned} \omega_{\text{event}} &= \omega_{\text{MC}} \\ &\times \prod_{\text{el}} s^e_{\text{trigger}}\, s^e_{\text{reco}}\, s^e_{\text{ID}}\, s^e_{\text{isolation}} \\ &\times \prod_{\text{mu}} s^\mu_{\text{trigger}}\, s^\mu_{\text{reco}}\, s^\mu_{\text{isolation}} \\ &\times \prod_{\text{tb}} s^b_{\text{tagging}} \\ &\times \prod_{\text{mb}} s^b_{\text{mis-id}} \\ &\times \omega_{\text{pileup}}, \end{aligned} \tag{6.2}$$

where *tb* means true b-jets and *mb* means misidentified b-jets.

Chapter 7

Data Description

The LHC has performed well in terms of stability and the amount of recorded data. In this thesis a dataset corresponding to an integrated luminosity of $4.71\,\mathrm{fb}^{-1}$ of pp-collision data at $\sqrt{s} = 7\,\mathrm{TeV}$ is used. Figure 7.1 shows the cumulative luminosity delivered (green) by the LHC and recorded (yellow) by ATLAS during stable beams, for pp-collisions at $\sqrt{s} = 7\,\mathrm{TeV}$. The offline luminosity determined for data taken in 2010 is 3.6% lower than the online luminosity shown here [154, p. 1]. The data was recorded by the ATLAS experiment over the course of the year 2011. For comparison, in 2010 the LHC delivered data equivalent to $47\,\mathrm{pb}^{-1}$ at $\sqrt{s} = 7\,\mathrm{TeV}$ and in 2012 $21.3\,\mathrm{fb}^{-1}$ at $\sqrt{s} = 8\,\mathrm{TeV}$ [93].

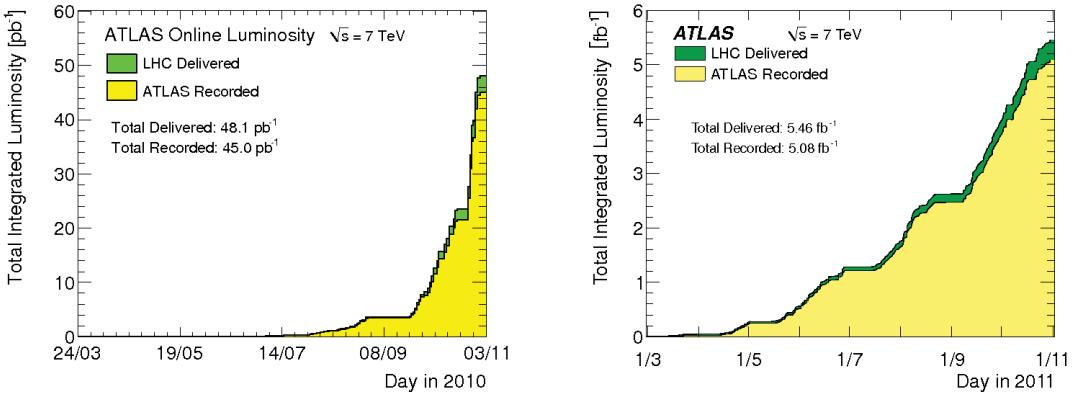

Figure 7.1.: Cumulative luminosity as a function of time (2010-2011) for ATLAS and the LHC [93].

Table 7.1 shows a comparison of selected LHC parameters in 2010 and 2011 [92, p. 2]. The average data taking efficiency of ATLAS is $\sim 93\%$ (see Figure 7.2). The data taking efficiency is the ratio of recorded to delivered luminosity. The instantaneous luminosity was increased by a factor of 18 by increasing the bunch population, decreasing the bunch spacing and a tighter focus of the proton beams (see Figure 7.3).

Parameter	2010	2011
Max. number of bunch pairs colliding	348	1331
Min. bunch spacing (ns)	150	50
Typical bunch population (10^{11} protons)	0.9	1.2
Peak luminosity $\left(10^{33}\mathrm{cm}^{-2}s^{-1}\right)$	0.2	3.6
Max. inelastic interactions per crossings	~ 5	~ 20
Total integrated Luminosity delivered $\left(\mathrm{fb}^{-1}\right)$	0.047	5.5

Table 7.1.: Selected LHC run parameters [93].

In general the time period of an LHC fill during which the ATLAS detector is taking data is defined as an ATLAS run. The run is then subdivided into intervals of approximately one minute which are referred to as luminosity blocks. If a run has to be stopped and restarted, e.g., due to problems with a subdetector, one fill can correspond to multiple runs. Runs are grouped in periods with similar data taking conditions. For 2011 twelve periods are available (B-M).

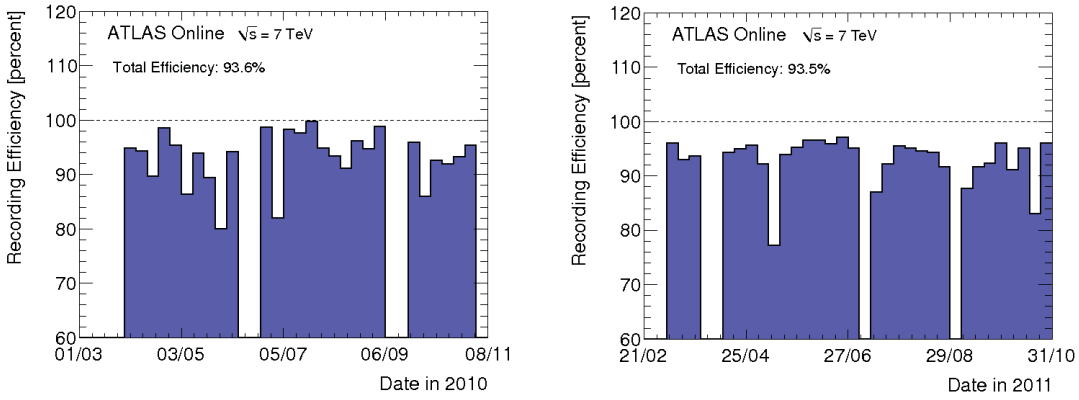

Figure 7.2.: The data taking efficiency in 2010 and 2011 is shown. The denominator for the calculation of the data taking efficiency is the luminosity delivered between the declaration of stable beams and the LHC request to turn the sensitive detectors off in order to allow a beam dump or beam studies. The numerator is the luminosity recorded by ATLAS. Each bin represents one week. The empty bins are due to weeks in which no stable beams were delivered by the LHC [93].

The quality of the data is checked online and offline, this ensures that no damaged or otherwise irregular data is passed to the distributed storage centres. The feedback on the data quality is given in form of status tags and key histograms, which are then automatically compared with a reference. The status tags and results of the histogram comparisons are monitored and in case of problems on-call experts are notified [155, p. 1].
Table 7.2 gives an overview of the data periods used. For information on individual runs refer to [156].

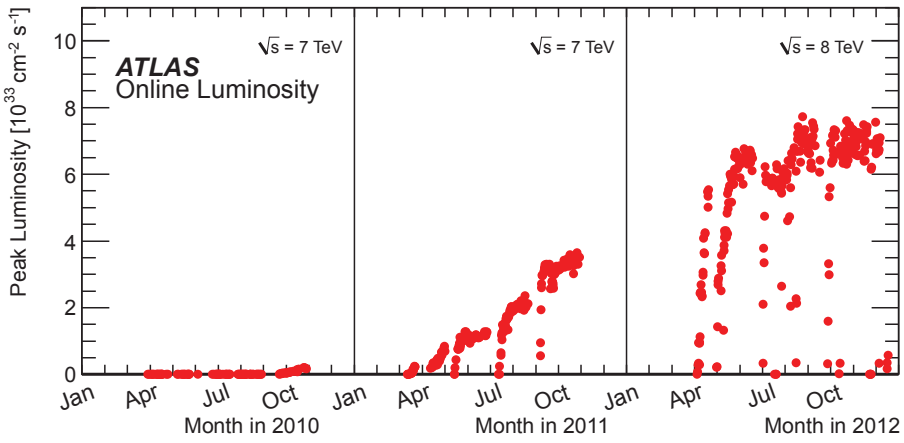

Figure 7.3.: Peak instantaneous luminosity in ATLAS *pp*-runs [93].

Period	Run-Range	$\mathcal{L}_{\text{int}}$ $\left[\text{pb}^{-1}\right]$
B-D	177986 - 180481	173.80
E-H	180614 - 184169	924.67
I	185353 - 186493	328.61
J	186516 - 186755	220.38
K	186873 - 187815	575.16
L-M	188902 - 191933	2368.38

Table 7.2.: Delivered luminosity per data taking period [156].

The ATLAS top quark physics working group has introduced three different event filters (see Table 7.3). These filters provide a low level skim of the data and allow for faster data processing. The collected output of these filters is referred to as streams. The first two filters introduce quality criteria which have to be satisfied by at least one lepton in an event. The third filter is used for analyses in the $t\bar{t}$-allhadronic channel and is not used in this thesis. The definitions of the reconstructed objects referred to as electron, muon and jet can be found in Chapter 5.

To ensure that only data taken during stable beam and detector conditions is used for physics analyses lists of usable runs are created. These GoodRunLists take into account online and offline data quality information, as well as feedback from the individual data quality shift crews. Only runs listed in the GoodRunList are considered for analysis. For details on the top working group GoodRunLists see [157].

Stream	Criteria
EGamma	≥ 1 electron with: $p_T > 20\,\text{GeV}$, *or* ≥ 1 electron with $p_T > 13\,\text{GeV}$ and $\not{E} > 20\,\text{GeV}$, *and* ≥ 2 leptons (electron or muon) with $p_T > 13\,\text{GeV}$.
Muon	≥ 1 muon with $p_T > 18\,\text{GeV}$, *or* ≥ 1 muon with: $p_T > 13\,\text{GeV}$ and $\not{E} > 20\,\text{GeV}$, *and* ≥ 2 leptons (electron or muon) with $p_T > 13\,\text{GeV}$.
Jet	≥ 4 jets with $p_T > 20\,\text{GeV}$ and ≥ 2 jets with $p_T > 40\,\text{GeV}$, *or* ≥ 5 jets with $p_T > 20\,\text{GeV}$.

Table 7.3.: Data stream quality criteria [158].

7.1 Event Selection

The event selection is based on the selection used for the measurement of the $t\bar{t}$-production cross-section at $\sqrt{s} = 7\,\text{TeV}$ in dilepton final states [159, p. 3]. The event selection consists of seventeen subsequent cuts, each introducing higher quality criteria. If not stated otherwise all criteria are applied to each decay channel in data and MC.

1. *Application of GoodRunList on Data, True Dilepton Events in Signal MC*
   In data, only events with stable beam- and detector- conditions are considered for analyses. A cut on true dilepton events in the MC@NLO signal MC sample is applied, because the signal sample is not specifically dedicated to dilepton analyses and otherwise no meaningful selection efficiencies can be quoted.

2. *Minimum Trigger Requirement*
   Events have to be triggered by an inclusive single lepton trigger. The trigger requirements for the single electron trigger can be found in Table 5.1, the single muon trigger is described in Table 5.3.

3. *Primary Vertex*
   At least five tracks have to originate from the primary vertex. This criterion is introduced to reject non collision background.

4. *Cosmics Rejection*
   The event is rejected if a muon pair fulfils the requirements of cosmic muons. The requirements are listed in Table 5.5.

5. *Lepton Requirement a)*
   The event is required to have at least two selected (tight criteria as described in Chapter 5) leptons. The dielectron channel requires two selected electrons, the

dimuon channel two selected muons and the mixed channel at least one selected lepton of each type.

6. *Trigger Matching*
   In order to ensure that one of the selected leptons triggered the event a ΔR matching between the lepton and the trigger object is performed. The event is accepted if $\Delta R \leq 0.15$ between the lepton and the trigger object.

7. *Electron Muon Overlap*
   If a selected electron and a muon share the same track, the event is rejected. This is achieved by requiring $\Delta R\,(e_{\text{track}},\, \mu_{\text{track}}) > 0$ for the event.

8. *Jet Cleaning*
   If an event contains a jet which is classified as bad the event is rejected. The definition of bad jets is given in Section 5.3.2. In addition to these criteria a jet is considered bad if $p_T^{\text{jet}} \leq 20\,\text{GeV}$ or the energy of the jet is negative.

9. *$\not{E}_T$, H_T*
   In the dielectron and dimuon channels an event is rejected if $\not{E}_T \leq 60\,\text{GeV}$. In the electron-muon channel an event is rejected if $H_T \leq 130\,\text{GeV}$, where H_T is the scalar sum of the transverse momenta of all selected jets and leptons. The threshold for $\not{E}_T$ is introduced to reduce QCD multijet background faking signal-like leptons.

10. *Minimum Jet Requirement*
    The event is rejected if there are less than two jets with a $p_T > 25\,\text{GeV}$ and $|\eta| < 2.5$ and if the jet vertex fraction is below 0.75.

11. *Lepton Requirement b)*
    The event is required to contain exactly two selected leptons. The lepton types have to match the decay channel.

12. *Lepton Requirement c)*
    Both selected leptons are required to have opposite electric charge.

13. *Lepton Pair Mass a)*
    The invariant dilepton mass in the dielectron and dimuon decay channels is required to fulfill $M_{l\bar{l}} > 15\,\text{GeV}$. This criterion is introduced to reject backgrounds from bottom-quark production and vector meson decays.

14. *Lepton Pair Mass b)*
    The invariant dilepton mass in the dielectron and dimuon decay channel is required to be $|M_{l\bar{l}} - 91\,\text{GeV}| > 10\,\text{GeV}$. This criterion strongly suppresses the dominant background from Z-boson decays.

15. *Prompt Leptons*
    For MC samples both selected leptons are required to match truth leptons. This ensures that the selected lepton is a prompt lepton, regardless if it originated from a top-quark, Z- or W-boson decay. This criterion prevents double counting of fake events from MC and from QCD multijet backgrounds. A lepton is considered truth matched, if its track can be matched to the track of a truth lepton originating from a top-quark, Z- or W-Boson.

16. *LAr Error*
    Events with flagged noise bursts in the calorimeter (see Section 5.3.2) are rejected.

17. *b-Tagging*
    At least one selected jet is required to have an MV1 jet weight of $\omega_{\mathrm{MV1}} > 0.601713$.

Table 7.4 contains the event yields for each cut for collision data. The event yields and cut efficiencies for the MC@NLO signal sample are shown in Table 7.5 (and TableB.2 including the dilepton selection efficiency explicitly). The MC event yields without luminosity scaling but with applied MC scale factors (as described in Section 6.4.4) can be found in Appendix B.1. In this thesis the term *pretag* event selection refers to a selection from cut 1 through 16 and the term *tagged* refers to an event selection to a selection from cut 1 through 17.

Cut	Description	ee-Channel	$\mu\mu$-Channel	$e\mu$-Channel
1	GoodRunList	219386480	209389520	219386480
2	Minimum Trigger Requirement	165150864	170476192	165872304
3	Primary Vertex	164432096	169580432	165151632
4	Cosmics Rejection	164432096	169580304	165151632
5	Lepton Requirement a)	683248	1818383	12920
6	Trigger Matching	683224	1818330	12917
7	Electron Muon Overlap	683224	1818330	12917
8	Jet Cleaning	680235	1809089	12863
9	$\not{E}_T$, H_T	1732	5209	7529
10	Minimum Jet Requirement	982	2775	5410
11	Lepton Requirement b)	977	2763	5393
12	Lepton Requirement c)	965	2740	5287
13	Lepton Pair Mass a)	942	2718	5287
14	Lepton Pair Mass b)	742	2015	5287
15	Prompt Leptons	742	2015	5287
16	LAr Error	740	2004	5272
17	b-Tagging	567	1555	4302

Table 7.4.: Event yields, ATLAS 2011, corresponding to an integrated luminosity of $\mathcal{L}_{\mathrm{int}} = 4.71\,\mathrm{fb}^{-1}$.

Cut	ee-Channel Event Yield	Eff.	$\mu\mu$-Channel Event Yield	Eff.	$e\mu$-Channel Event Yield	Eff.
0	453635.1 ± 445.5	100.0%	453635.1 ± 445.5	100.00%	453635.1 ± 445.5	100.00%
1	12885.5 ± 25.6	2.84%	13474.7 ± 26.2	2.97%	26317.2 ± 36.6	5.80%
2	10485.5 ± 23.1	2.31%	10817.6 ± 23.4	2.38%	21431.8 ± 33.0	4.72%
3	10477.8 ± 23.1	2.31%	10812.1 ± 23.4	2.38%	21417.2 ± 33.0	4.72%
4	10477.8 ± 23.1	2.31%	10812.1 ± 23.4	2.38%	21417.2 ± 33.0	4.72%
5	1719.9 ± 9.3	0.38%	4863.2 ± 15.7	1.07%	5886.5 ± 17.2	1.30%
6	1719.9 ± 9.3	0.38%	4851.6 ± 15.7	1.07%	5885.7 ± 17.2	1.30%
7	1719.9 ± 9.3	0.38%	4851.6 ± 15.7	1.07%	5885.7 ± 17.2	1.30%
8	1701.0 ± 9.3	0.37%	4794.2 ± 15.6	1.06%	5815.7 ± 17.1	1.28%
9	888.9 ± 6.7	0.20%	2670.6 ± 11.6	0.59%	5520.3 ± 16.6	1.22%
10	696.8 ± 5.9	0.15%	2101.3 ± 10.3	0.46%	4524.5 ± 15.1	1.00%
11	696.6 ± 5.9	0.15%	2101.1 ± 10.3	0.46%	4523.8 ± 15.1	1.00%
12	691.5 ± 5.9	0.15%	2100.9 ± 10.3	0.46%	4504.2 ± 15.1	0.99%
13	687.8 ± 5.9	0.15%	2082.9 ± 10.3	0.46%	4504.2 ± 15.1	0.99%
14	578.1 ± 5.4	0.13%	1767.2 ± 9.5	0.39%	4504.2 ± 15.1	0.99%
15	572.7 ± 5.4	0.13%	1767.2 ± 9.5	0.39%	4486.5 ± 15.1	0.99%
16	572.7 ± 5.4	0.13%	1767.2 ± 9.5	0.39%	4486.5 ± 15.1	0.99%
17	485.6 ± 5.0	0.11%	1491.8 ± 8.7	0.33%	3796.4 ± 13.8	0.84%

Table 7.5.: Event yields with statistical errors and selection efficiencies for the $t\bar{t}$ non full hadronic signal MC as described in Section 6.3. The event yields take into account the scaling factors described in Section 6.4.4. The event yields are scaled to an integrated luminosity of $\mathcal{L}_{\text{int}} = 4.71\,\text{fb}^{-1}$.

7.2 Data Driven Lepton Fake Estimate

The event selection for dileptonic $t\bar{t}$-decays encompasses the identification of two leptons with large transverse momentum. The dominant background of electroweak Z-boson decays is suppressed by cuts on the dilepton invariant mass in the channels with two leptons of the same type. However, there are additional background components from events with mis-identified or non-isolated leptons. These are called fake leptons.
The fake leptons mostly stem from semi-leptonically decaying bottom-quarks, long-lived weakly decaying hadrons ($\pi^{\pm}$ or K-mesons), π^0 showers reconstructed as electrons, mis-identified photons or electrons from photon conversion. The quality and rate of the simulation of multijet events producing fake leptons strongly depends on details of the detector simulation. Especially for high jet multiplicities the simulation differs from the data taken with the detector. Hence a data driven method is applied to estimate the fake lepton background contribution. The chosen method is the matrix method [119, pp. 24-26].

Two different categories of events are selected for the matrix method. These are defined as loose and tight. The tight-event selection is described in Section 7.1. The loose-event selection uses the same basic event selection cuts but uses the loose lepton definition. The yield of background events is then the yield of events with two well defined lepton candidates containing at least one fake lepton [159, p. 4]. Control regions, enriched with fake

or real leptons, are selected. The probability for real leptons is measured in $Z \to ee\,(\mu\mu)$ events, while the probability of fake leptons is measured in a dijet enriched data sample. The matrix method then calculates the yield of selected events with different lepton criteria:

$$\begin{pmatrix} N^{\mathrm{tt}} \\ N^{\mathrm{tl}} \\ N^{\mathrm{lt}} \\ N^{\mathrm{ll}} \end{pmatrix} = M \begin{pmatrix} N^{\mathrm{tt}}_{\mathrm{rr}} \\ N^{\mathrm{tl}}_{\mathrm{rf}} \\ N^{\mathrm{lt}}_{\mathrm{fr}} \\ N^{\mathrm{ll}}_{\mathrm{ff}} \end{pmatrix}, \tag{7.1}$$

with

$$M = \begin{pmatrix} r_1 r_2 & r_1 f_2 & f_1 r_2 & f_1 f_2 \\ r_1\,(1-r_2) & r_1\,(1-f_2) & f_1\,(1-r_2) & f_1\,(1-f_2) \\ (1-r_1)\,r_2 & (1-r_1)\,f_2 & (1-f_1)\,r_2 & (1-f_1)\,f_2 \\ (1-r_1)\,(1-r_2) & (1-r_1)\,(1-f_2) & (1-f_1)\,(1-r_2) & (1-f_1)\,(1-f_2) \end{pmatrix}, \tag{7.2}$$

where N^{tt} denotes the number of events with two tight leptons and N^{ll} the number of events with two loose leptons. The variable $N^{\mathrm{tt}}_{\mathrm{rr}}$ is then the number of events with two selected tight leptons containing two real leptons. The real (r) and fake (f) event rates are measured in the control regions and are defined as

$$r = \frac{N^{\mathrm{tight}}_{\mathrm{real}}}{N^{\mathrm{loose}}_{\mathrm{real}}} \;\text{ and }\; f = \frac{N^{\mathrm{tight}}_{\mathrm{fake}}}{N^{\mathrm{loose}}_{\mathrm{fake}}}\,. \tag{7.3}$$

By inverting the matrix M and solving the equation for $N^{\mathrm{tt}}_{\mathrm{fake}}$ the fake contribution can be estimated:

$$\begin{aligned} N^{\mathrm{tt}}_{\mathrm{fake}} &= N^{\mathrm{tt}}_{\mathrm{rf}} + N^{\mathrm{tt}}_{\mathrm{fr}} + N^{\mathrm{tt}}_{\mathrm{ff}} \\ &= r_1 f_2 N^{\mathrm{ll}}_{\mathrm{rf}} + f_1 r_2 N^{\mathrm{ll}}_{\mathrm{fr}} + f_1 f_2 N^{\mathrm{ll}}_{\mathrm{ff}} \\ &= \alpha r_1 f_2 \left[(f_1 - 1)\,(1-r_2)\,N^{\mathrm{tt}} + (1-f_1)\,r_2 N^{\mathrm{tl}} + f_1\,(1-r_2)\,N^{\mathrm{lt}} - f_1 r_2 N^{\mathrm{ll}} \right] \\ &+ \alpha f_1 r_2 \left[(r_1 - 1)\,(1-f_2)\,N^{\mathrm{tt}} + (1-r_1)\,f_2 N^{\mathrm{tl}} + r_1\,(1-f_2)\,N^{\mathrm{lt}} - r_1 f_2 N^{\mathrm{ll}} \right] \\ &+ \alpha f_1 f_2 \left[(1-r_1)\,(1-r_2)\,N^{\mathrm{tt}} + (r_1 - 1)\,r_2 N^{\mathrm{tl}} + r_1\,(r_2 - 1)\,N^{\mathrm{lt}} - r_1 r_2 N^{\mathrm{ll}} \right], \end{aligned} \tag{7.4}$$

with

$$\alpha = \frac{1}{(r_1 - f_1)\,(r_2 - f_2)}\,. \tag{7.5}$$

A detailed list of MC event yields, fake lepton background event yields, data event yields and a complete collection of control plots comparing data with MC and lepton fake background can be found in the Appendix B.2 for the pretag event selection and in Appendix B.3 for the tagged event selection.

Chapter 8

Kinematic Reconstruction of the $t\bar{t}$-System

The full reconstruction of the top-quark pair four-momenta is necessary for the calculation of the top-quark charge asymmetry. The final state of the dileptonic decay of a top-quark pair consists of two charged leptons, two bottom-quarks and two neutrinos. When recorded with the ATLAS detector, these events typically contain two leptons with large transverse momenta, two jets originating from the heavy flavour hadronisation and missing transverse energy.
The events selected using the dilepton event selection (see Section 7.1) can comprise jet multiplicities with higher values than two (e.g. see Figure B.2). These jets cannot be assigned uniquely to the bottom-quarks originating from the top-quark pair decay [160, p. 1]. Even for an event with only two selected jets there are two possible assignments of jets to the bottom-quarks, because it is not possible to decide if ajet originated from a bottom- or antibottom-quark. Therefore, reconstruction algorithms have to be applied to identify the two jets originating from those bottom-quarks.

It is possible (after the identification of the correct jet pair) to calculate the four-momenta of the initial top-quark pair from the four-momenta of all final state particles. However, the presence of two neutrinos in the final state results in various problems. Although the missing energy provides a measure of the energy of the neutrinos, it can only be quantified in a plane transverse to the beam direction (see Section 5.4). Therefore the reconstructed kinematic system of the top-quark pair decay final state is underconstrained by one degree of freedom (DOF). Here the term DOF corresponds to unknowns in the kinematic equations which are used to reconstruct the four-momenta of the initial top-quark pair. Some of the unknowns can be measured (e.g. particle momenta) and others are known from previous experiments (e.g. particle masses). These measurements and known properties can be combined to calculate the missing neutrino momenta. The corresponding equations are referred to as constraints. If it is possible to match the number of constraints to the number of degrees of freedom the resulting system of equations is solvable and hence the top-quark pair four-momenta can be reconstructed. For details on the kinematic equations see [161, pp. 85-87].

There are 6 particles in the final state of a dileptonic top-quark pair decay, each providing 4 DOF (the corresponding four-momenta), resulting in a total of 24 DOF. The masses of the final state particles are known (the neutrino masses are neglected) and the momenta of the charged leptons and jets are measured. This corresponds to 18 constraints. The estimation of the missing energy in the transverse plane adds 2 constraints. The decays of the $W^{\pm}$-bosons add 2 constraints:

$$m^2_{W^{\pm}} = \left(E_{(\bar{\nu})} + E_{l^{\pm}} \right)^2 - \left(\vec{p}_{(\bar{\nu})} + \vec{p}_{l^{\pm}} \right)^2 . \tag{8.1}$$

The top-quark pair decay adds 1 constraint similar to those of the W-boson decays. This adds up to a total of 23 constraints. In order to solve the still under constrained kinematic system a neutrino weighting approach is used [161, p. 45]. A short description of the neutrino weighting approach is given in Section 8.1. The solution to the kinematic equations is presented in the Appendix C.1.

In this analysis a likelihood based reconstruction algorithm is used to reconstruct the properties of the top-quark pair before the decay. This reconstruction is achieved by the determination of the best possible assignment of selected jets to the bottom-quarks of the $t\bar{t}$ decay final state and by the estimation of the momenta of the neutrino and anti-neutrino.
For the analysis presented in this thesis the dilepton likelihood is calculated for each of the permutations of the seven leading (in p_T) selected jets in an event. The restriction to seven leading jets is chosen to conserve the CPU processing time. Increasing the accepted jet multiplicity leads to no significant increase in the reconstruction efficiency, but to a dramatic increase in CPU time consumed. The reconstruction algorithm used is part of the Kinematic Likelihood Fitter (KLFitter) framework (version 00-05-21) [160].

8.1 Kinematic Likelihood Fitter

The basis of the reconstruction algorithm provided by the KLFitter is the likelihood function (Equation 8.3) for the dilepton decay channel of a top-quark pair. For the selected events the KLFitter dilepton likelihood is calculated for every possible permutation of two jets out of the given jet multiplicity. The likelihood is then maximised according to the neutrino momenta that have been calculated according to the kinematic equations. The jet permutation which provides the largest likelihood is then assumed to have the correct assignment of the jets to the bottom-quarks from the top-quark pair decay final state.

8.1.1 Neutrino Weighting Approach

A neutrino weighting scheme is introduced in the KLFitter to solve the kinematic equations of the $t\bar{t}$ decay. In the neutrino weighting scheme a top-quark mass hypothesis and a neutrino rapidity distribution according to Standard Model expectation is assumed. The measured missing energy is not explicitly used as a constraint, but it is introduced to test the validity of the assumptions made [161, p. 45], [162]. The neutrino rapidity distribution is described by a Gaussian model where the width depends on the top-quark mass hypothesis. The parametrisation of the width of the Gaussian model is given by

Equation C.1 in the Appendix. For each neutrino and antineutrino momentum up to two mathematical solutions exist [161, pp. 85-87]. For every combination of these momenta solutions one neutrino weight (ω_ν) [161, p. 46] is calculated. The neutrino weight is used as a measure of the most probable (anti-) neutrino momentum solution combination. The sum of these weights is included in the dilepton likelihood function (see Equation 8.3) [162]. The neutrino weight for one combination of (anti-) neutrino momentum solutions is given by

$$\omega_\nu = \exp\left[\frac{-\left(\not{E}_x^{\text{calc}} - \not{E}_x^{\text{obs}}\right)^2}{2\left(\sigma_x^{\text{miss}}\right)^2}\right] \times \exp\left[\frac{-\left(\not{E}_y^{\text{calc}} - \not{E}_y^{\text{obs}}\right)^2}{2\left(\sigma_y^{\text{miss}}\right)^2}\right], \tag{8.2}$$

where $\not{E}_i^{\text{calc}}$ is the missing energy in direction i expected for the given (anti-) neutrino momentum solutions. $\not{E}_i^{\text{calc}}$ is a function of the given pair of neutrino and antineutrino momentum solutions p_i^ν and $p_i^{\bar{\nu}}$, the top-quark mass m_{top} and the assumed neutrino and antineutrino rapidity distributions η^ν and $\eta^{\bar{\nu}}$. Furthermore, $\not{E}_i^{\text{obs}}$ is the missing energy observed in direction i and σ_i^{miss} the Gaussian resolution of the missing energy. The parametrisation of the Gaussian resolution of the missing energy is given in Equation C.4. The selected leptons are ensured to pair (according to their charge) correctly to the neutrinos [162].

8.1.2 KLFitter Dilepton Likelihood Function

The dilepton likelihood is determined for every possible permutation of two jets out of the selected collection. In the jet permutation with the maximum likelihood, the combination of neutrino momentum solutions with the highest neutrino weight is assumed to comprise the best estimate for the neutrino momenta. These neutrino properties are then used to calculate the top-quark pair four-momenta. The dilepton likelihood for one jet permutation normalised to the sum of all dilepton likelihoods, for the event at hand, is referred to as event probability. Distributions of the event probability and the neutrino weight are shown in Section C.2 (e.g. Figure C.2). The full dilepton $t\bar{t}$-likelihood function [162] is defined as

$$\begin{aligned} L \;=\; & \prod_{i=x,y} G\left(\not{E}_T \mid p_i^\nu,\, p_i^{\bar{\nu}},\, \sigma_i^{\text{miss}}\left(m_{\text{top}}, m_W,\, \eta^\nu,\, \eta^{\bar{\nu}}\right)\right) \\ \times\; & G\left(\eta^\nu \mid m_{\text{top}}\right) G\left(\eta^{\bar{\nu}} \mid m_{\text{top}}\right) \left[m\left(l_1, j_1\right) + m\left(l_2, j_2\right)\right]^\alpha \\ \times\; & W\left(\tilde{E}_{j_1} \mid E_{b_1}\right) W\left(\tilde{E}_{j_2} \mid E_{b_2}\right) \\ \times\; & \begin{cases} W\left(\tilde{E}_{l_1} \mid E_{l_1}\right)\; W\left(\tilde{E}_{l_2} \mid E_{l_2}\right) & \text{for } ee\text{-channel,} \\ W\left(\tilde{p}_{T,l_1} \mid p_{T,l_1}\right) W\left(\tilde{p}_{T,l_2} \mid p_{T,l_2}\right) & \text{for } \mu\mu\text{-channel,} \\ W\left(\tilde{E}_{l_1} \mid E_{l_1}\right)\; W\left(\tilde{p}_{T,l_2} \mid p_{T,l_2}\right) & \text{for } e\mu\text{-channel.} \end{cases} \end{aligned} \tag{8.3}$$

The function

$$\prod_{i=x,y} G\left(\not{E}_T \mid p_i^\nu,\, p_i^{\bar{\nu}},\, \sigma_i^{\text{miss}}\left(m_{\text{top}}, m_W,\, \eta^\nu,\, \eta^{\bar{\nu}}\right)\right) \tag{8.4}$$

denotes the neutrino weighting likelihood component. G is a Gaussian distribution which compares the assumed (anti-) neutrino momentum (p_i^ν and $p_i^{\bar{\nu}}$) and the measured missing

transverse energy ($\not\!\!E_T$) in the x and y direction. This comparison uses a sharp Gaussian prior for the top-quark pole mass. The top-quark mass is fixed to a value of $m_{\text{top}} = (172.5 \pm 1.4)$ GeV, the W-boson mass is fixed to $m_{\text{W}} = 80.4\,\text{GeV}$. The (anti-) neutrino pseudorapidity value ($\eta^{(\bar{\nu},\nu)}$) is assumed according to Standard Model expectation. By fixing the (anti) top-quark mass and the assumption of the neutrino pseudorapidity three constraints are introduced. This allows to ignore the two constraints of missing energy but still keeps the kinematic system solvable [161, p. 45]. Equation 8.4 can be written in terms of the neutrino weight introduced in Equation 8.2 as:

$$\prod_{i=x,y} G\left(\not\!\!E_T \mid p_i^{\nu},\, p_i^{\bar{\nu}},\, \sigma_i^{\text{miss}}\right) = \sum_s \omega_{\nu,s}\,, \tag{8.5}$$

where the index s runs over all possible combinations of solutions for neutrino and antineutrino momenta. The product of Gaussian functions

$$G\left(\eta^{\nu} \mid m_{\text{top}}\right)\, G\left(\eta^{\bar{\nu}} \mid m_{\text{top}}\right) \tag{8.6}$$

returns the Standard Model probability for the calculated value of (anti-) neutrino pseudorapidity. The width ($\sigma_{\eta^{\bar{\nu},\nu}}$) of the Gaussian distributions weakly depends on the top-quark mass. This dependency is assumed to be linear

$$\sigma_{\eta^{\bar{\nu},\nu}} = a + b\, m_{\text{top}}. \tag{8.7}$$

The values for a and b are given in Table C.1. The likelihood component

$$\left[m\left(l_1, j_1\right) + m\left(l_2, j_2\right)\right]^{\alpha} \tag{8.8}$$

is proportional to the invariant mass of each pairing of leptons to jets. The tuning factor $\alpha = -2$ was chosen to maximise the reconstruction efficiency. The indices l_1 and l_2 stand for the selected leptons, j_1 and j_2 stand for the two selected jets in the given permutation.

The functions denoted with $W\left(\tilde{x} \mid x\right)$ are transfer functions [163]. In general a transfer function is the relation between the input and the output of a system. They provide a mapping of measured values $\tilde{x}$ to the assumed true values x. Here, the transfer functions are defined as the conditional probability to obtain a certain response after reconstruction of a value $\tilde{x}$, given a true value x [163]. The indices b_1 and b_2 in the transfer functions contained in Equation 8.3 stand for the bottom-quarks, since the given jet is assumed to originate from a bottom quark decay. The transfer functions are parametrised by double-Gaussian functions

$$W\left(\tilde{x} \mid x\right) = \frac{1}{\sqrt{2\pi}\left(m_2 + m_3 m_5\right)} \left(\exp\left[-\frac{\left(\Delta x - m_1\right)^2}{2m_2^2}\right]\, m_3 \exp\left[-\frac{\left(\Delta x - m_4\right)^2}{2m_5^2}\right]\right). \tag{8.9}$$

The parameters m_i $(i = 1 \ldots 5)$ are functions of the true energy of the particle, Δx is the difference between the reconstructed and the true value divided by the true value. The parameters m_i for the different particle types (leptons in this analysis) are derived in five regions of η, in which Δx is derived from MC simulations. The parametrisations m_i can be found in Section C (see Equations C.2 and C.3). Figure 8.1 shows two examples of transfer functions for b-jets and light jets.

The transfer functions (Equation 8.9) are normalised to unity, i.e.:

$$\int W\left(\tilde{x} \mid x\right) d\tilde{x} = 1\,. \tag{8.10}$$

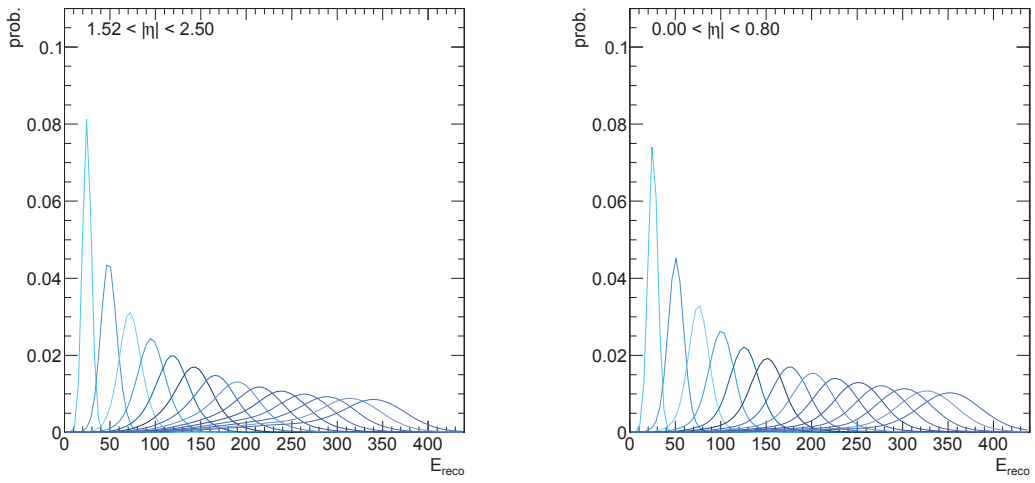

Figure 8.1.: Normalised transfer functions (Equation 8.9) according to [163], for bottom quark induced jets (left) and light quark induced jets (right). The y-axis depicts the probability of the reconstructed value to correspond to the true value. The different curves correspond to different truth values for the energy. The peak value of each individual function is the truth value for which the function was calculated. The functions are normalised to unity and are valid in the acceptance regions denoted in the plots.

8.2 Minimisation Algorithm

The minimisation algorithm for the optimisation of the likelihood is taken from the Bayesian Analysis Toolkit (BAT) library [164] (version BAT-0.9). The BAT library offers different methods of minimisation: Marcov Chain MC, Minuit and Simulated Annealing. The Simulated Annealing algorithm is chosen for this analysis because it provides approximately 100 times faster processing than Marcov Chain MC or Minuit with a comparable efficiency and precision.
Simulated Annealing is based on the modified Metropolis algorithm [165]. The main feature of the Simulated Annealing method is that there is only a slow decrease in the probability to accept solutions worse than the solution of the present state. This allows the algorithm to discard local extrema [166, p. 10].

8.3 Use of Heavy Flavour-Tagging Information

The information of heavy flavour- (b-)tagging is taken into account. There are several options available in the KLFitter, of which the following were tested in this analysis:

kVeto(noFit)
Vetoes the jet permutations in which a non-tagged jet is in the position of a bottom quark. If the *noFit* option is used the vetoed permutation is removed. Without this option the permutation is allowed, but the event probability is set to zero. The removal of a vetoed jet permutation conserves processing time.

kVeto(noFit)Light
Vetoes the jet permutations in which a tagged jet is in the position of a model light quark.

Using the *noFit* option reduces the CPU load, but it is possible that every permutation is vetoed. In the reconstruction of the dileptonic decay channel the veto options of the KLFitter show no significant difference in the reconstruction efficiencies, quality or the CPU-time consumption. The reconstruction and matching efficiencies are shown in Table 8.1 and in Figures 8.2 and 8.4. In this thesis the *kVeto* option is chosen for the reconstruction of the events selected using the tagged event selection.

8.4 Efficiency and Quality of the Reconstruction of the $t\bar{t}$-System

The quality of the reconstruction of the $t\bar{t}$-system can be judged by comparing the top-quark properties reconstructed using the KLFitter to the underlying truth information of the simulated MC@NLO $t\bar{t}$-signal sample.
Figures 8.3 and 8.5 show a comparison of the KLFitter reconstructed top-quark transverse momentum and truth top-quark transverse momentum in the $t\bar{t}$ MC signal sample. In general, the distributions of the top-quark properties are in good agreement. Compared to the truth values the (anti-) top-quarks are reconstructed with a slightly higher transverse momentum and the rapidity distributions have a slightly smaller width.
Figures 8.2 and 8.4 and Table 8.1 show the reconstruction efficiency of the KLFitter. All efficiencies are calculated between the truth particles and the KLFitter output for the best jet permutation and neutrino solution. The errorbars show statistical errors only. A pairing of reconstructed and truth particle is considered a match for the following conditions:

- in case of leptons: $\Delta R\left(l^{\pm}_{\text{reco}} \mid l^{\pm}_{\text{truth}}\right) < 0.1$,
- in case of jets: $\Delta R\left(j^{(\text{i})}_{\text{reco}} \mid \overline{b}_{\text{truth}}\right) < 0.3$.

For the efficiency calculation only events are considered that are truth matched. The percentage of matched events is listed in the Appendix in Table C.2. The terminology for the different efficiencies is the following:

- *KLFitter efficiency* denotes the overall reconstruction efficiency of the KLFitter, i.e. that at least one neutrino momentum solution has been found.

- *Full match* is the efficiency in correctly matching all input particles (charged leptons and jets).
- *Lepton match* describes the efficiency to correctly match both charged leptons.
- *Bottom-quark, i jets* is the probability that the KLFitter chooses the correct bottom-quark to jet assignment from the collection of selected jets (for the given jet multiplicity i).
- *Stat. only* shows the probability to randomly choose the correct jet pairing from the given jet multiplicity.

Event Selection	Type	Efficiency ee-Channel [%]	Efficiency $\mu\mu$-Channel [%]	Efficiency $e\mu$-Channel [%]
Pretag	KLFitter reco.	93.2 ± 1.3	94.7 ± 0.8	95.0 ± 0.5
	Full Match	59.6 ± 1.1	56.6 ± 0.6	57.6 ± 0.4
Tagged ($kVeto$)	KLFitter reco.	94.2 ± 1.4	95.3 ± 0.8	95.6 ± 0.5
	Full Match	58.3 ± 1.1	57.3 ± 0.6	57.4 ± 0.4

Table 8.1.: Reconstruction efficiencies of the KLFitter in different dilepton decay modes of top-quark pairs. Values are derived from the MC@NLO $t\bar{t}$-signal MC. The errors shown are statistical errors.

As seen in Figures 8.2 and 8.4 the jet matching efficiency is significantly higher than the probability to randomly choose the correct jet pair. Since high jet multiplicities of up to seven jets are allowed, the overall probability for a full match of the event is lower compared to the pure reconstruction efficiency. A complete compilation of reconstructed top-quark and KLFitter properties compared to the underlying truth distributions is shown in Sections C.2 and C.3.

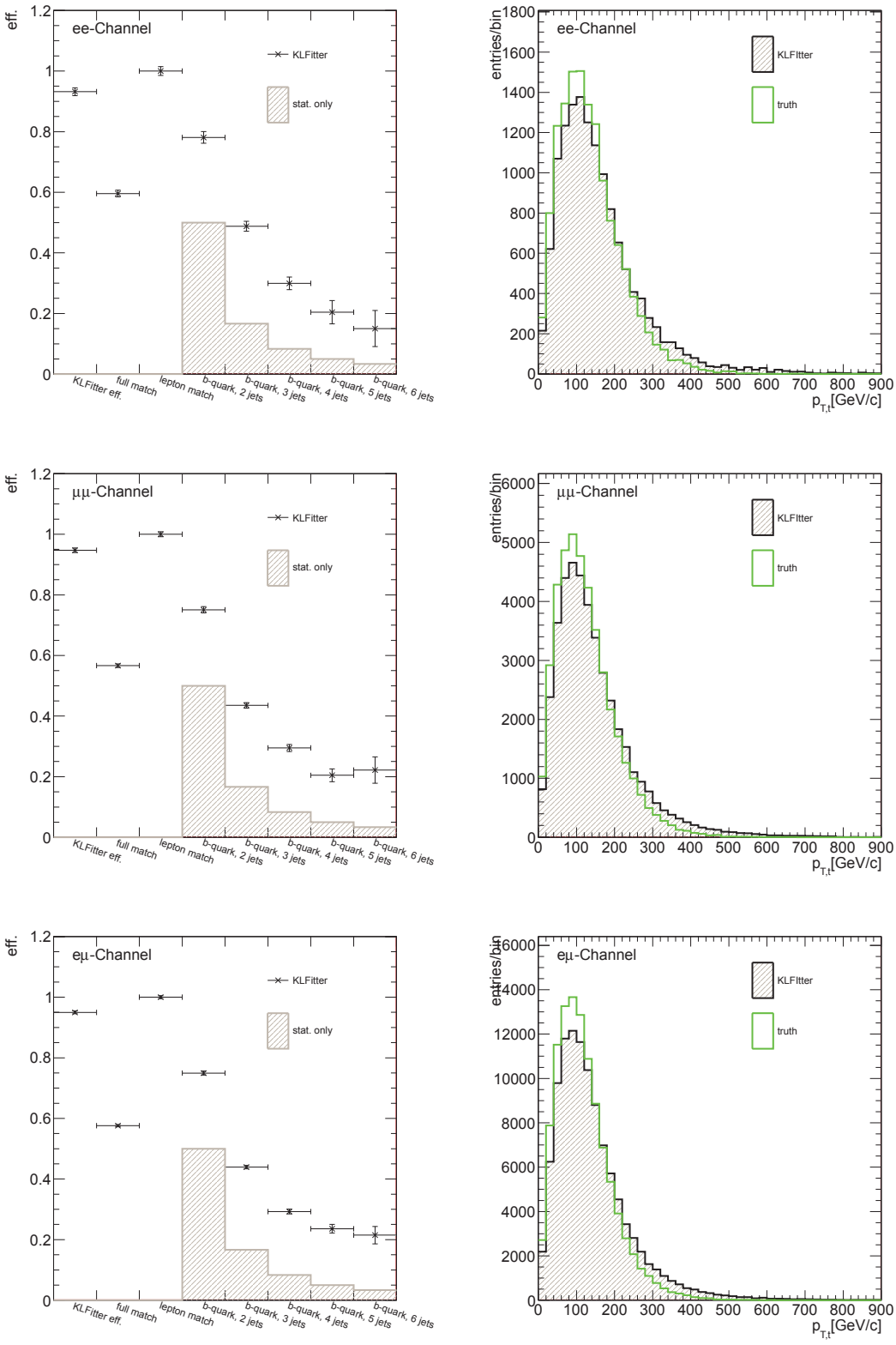

Figure 8.2.: Left: Shown is the KLFitter reconstruction efficiency estimated for the $t\bar{t}$-signal sample and the statistical probability to randomly select the correct jet pair from a given multiplicity (depicted in grey). Right: Shown is the transverse momentum of the top-quark. Truth information is depicted in green and the KLFitter reconstructed information black. All scale factors are applied except luminosity scaling. Events are selected according to the pretag selection.

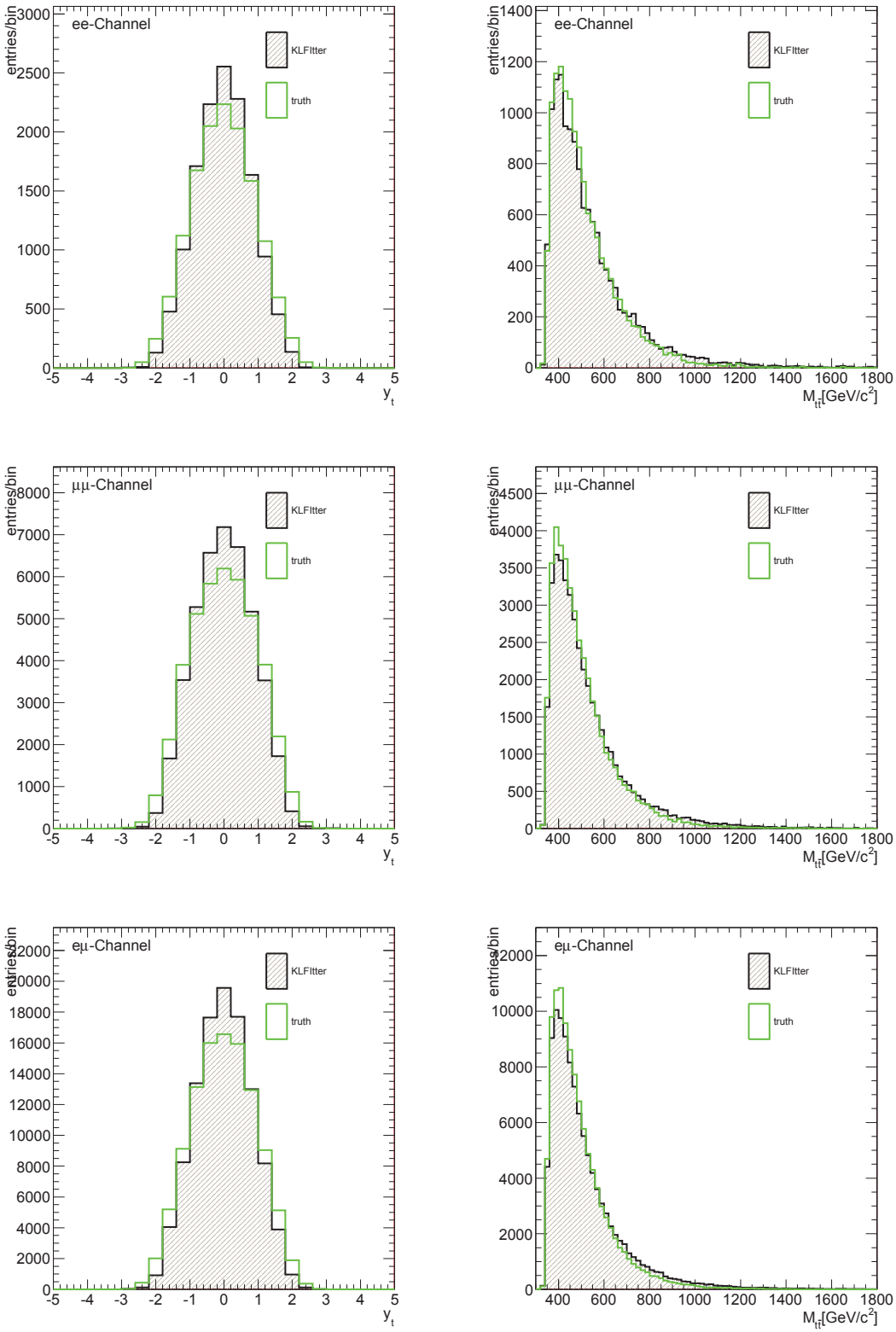

Figure 8.3.: The top-quark rapidity distributions (left) and the invariant $t\bar{t}$-pair mass (right). Truth information is depicted in green and the KLFitter reconstructed information in black. All scale factors are applied except luminosity scaling. Events are selected according to the pretag selection.

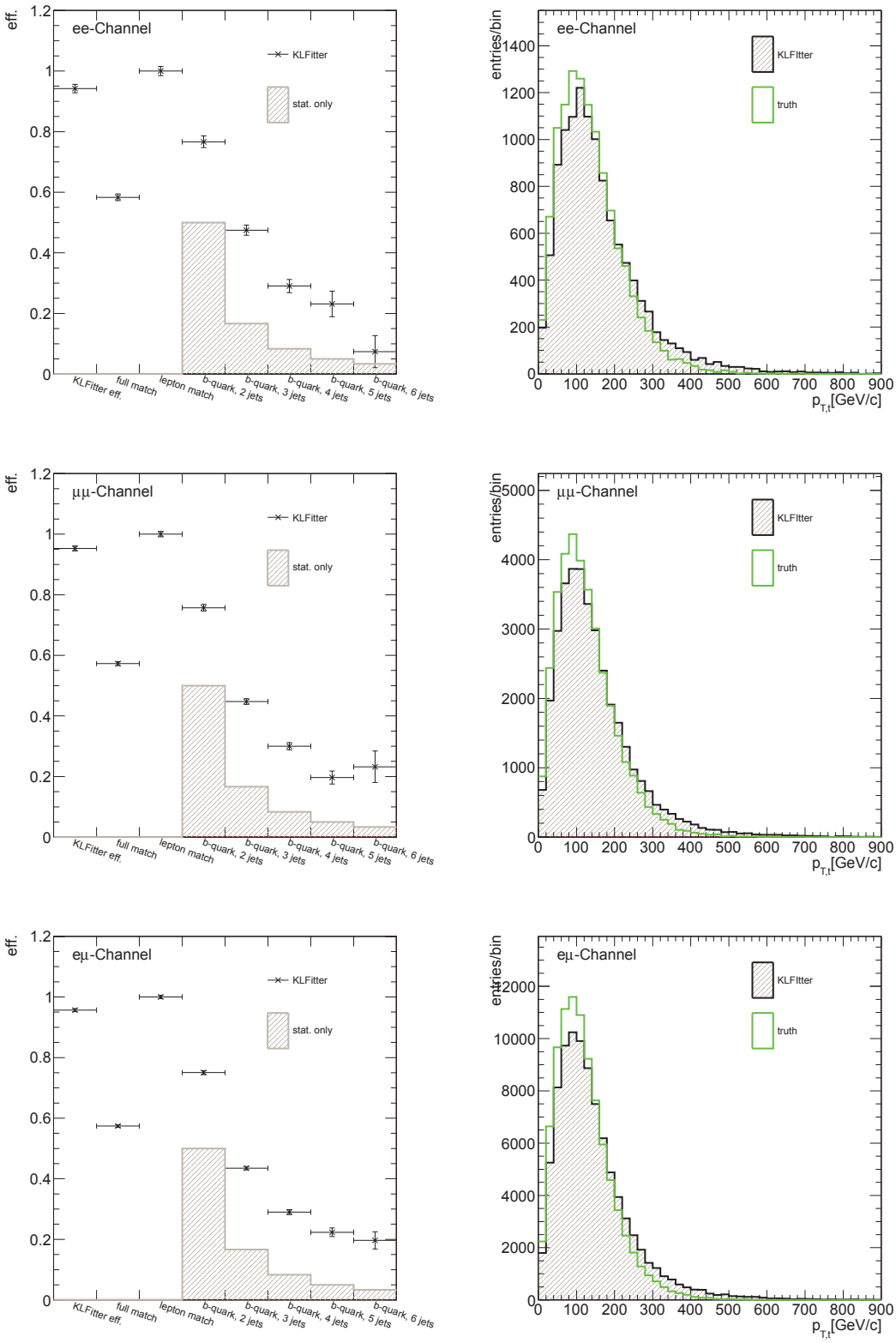

Figure 8.4.: Left: KLFitter reconstruction efficiency estimated for the $t\bar{t}$-signal sample and the statistical probability to randomly select the correct jet pair from a given multiplicity (depicted in grey). Right: Transverse momentum of the top-quark. Truth information is depicted in green and the KLFitter reconstructed information in black. All scale factors are applied except luminosity scaling. Events are selected according to the tagged selection.

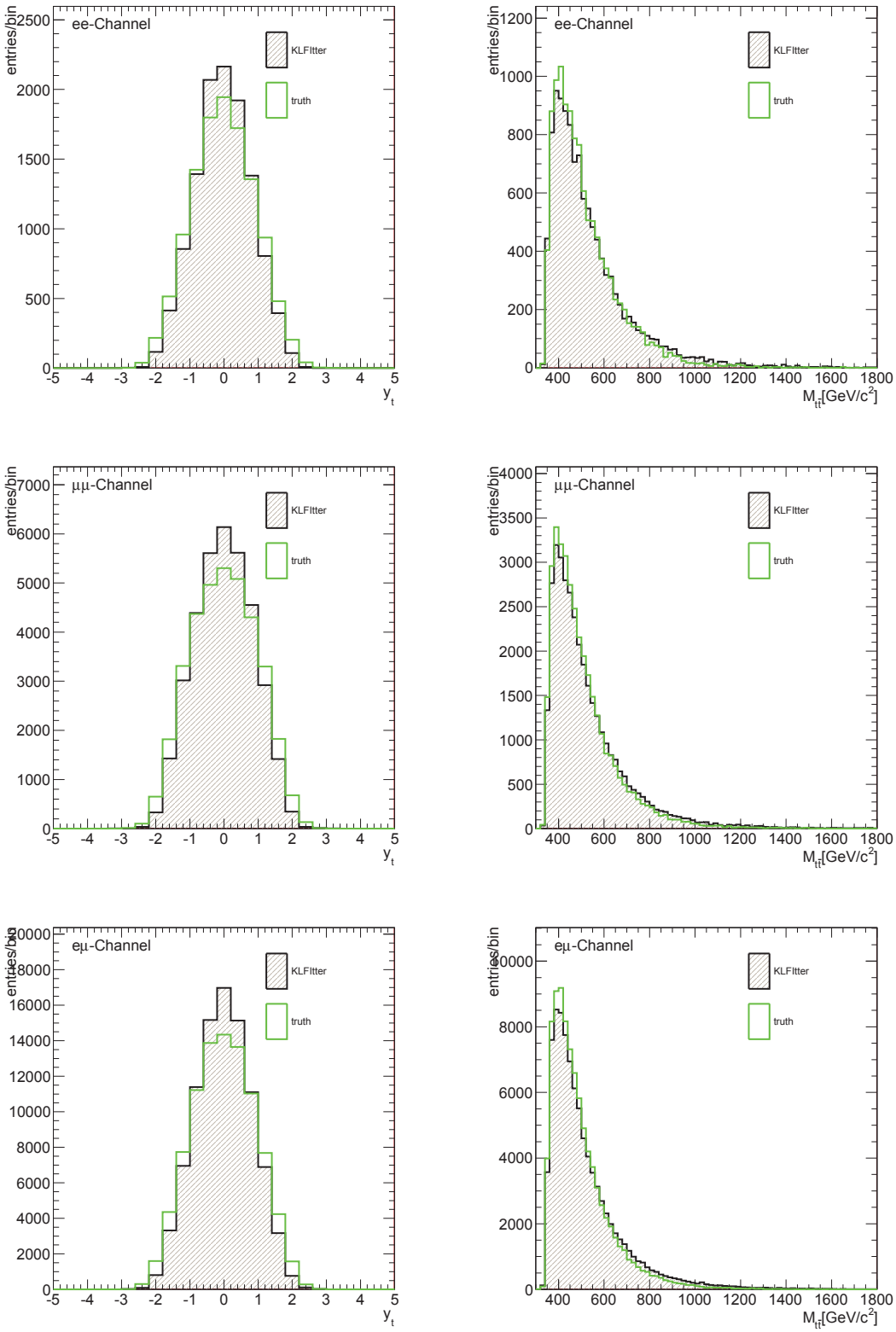

Figure 8.5.: The top-quark rapidity distributions (left) and the invariant $t\bar{t}$ pair mass (right). Truth information is depicted in green and the KLFitter reconstructed information in black. All scale factors are applied except luminosity scaling. Events are selected according to the tagged selection.

8.5 Reconstructed Top-Quark Charge Asymmetry

The reconstructed and truth top-quark charge asymmetries, derived from the MC@NLO $t\bar{t}$-signal sample, are listed in Table 8.2, separately for each of the top-quark pair decay channels. The top-quark charge asymmetry $A_{C,t\bar{t}}$ is calculated using Equation 2.114. For details on the calculation of the top-quark charge asymmetry refer to Section 2.4. The values reconstructed using the KLFitter are (within the statistical errors) in good agreement with the underlying true values. The charge asymmetries derived for the 2011 7 TeV dataset are listed in Table 8.3 separately for each of the top-quark pair decay channels. Within the statistical limitations the charge asymmetry derived from data is in good agreement with the value expected from MC and lepton fake background. This holds for both the pretag and the tagged event selection. A complete collection of control plots is shown in Sections C.4 (pretag) and C.5 (tagged).

$A_{C,t\bar{t}}$	ee-Channel [%]	$\mu\mu$-Channel [%]	$e\mu$-Channel [%]
Truth before sel.	0.456 ± 0.001	0.457 ± 0.001	0.457 ± 0.001
Truth after sel. cut 1	0.474 ± 0.153	0.565 ± 0.150	0.771 ± 0.107
	Pretag:		
Truth sel. events	1.000 ± 0.755	0.773 ± 0.429	0.383 ± 0.268
Reconstructed	-0.062 ± 0.755	-0.049 ± 0.429	0.072 ± 0.268
	≥ 1 b-tagged jet:		
Truth sel. events	1.355 ± 0.819	1.334 ± 0.466	0.597 ± 0.291
Reconstructed *kVeto*	0.563 ± 0.819	0.740 ± 0.466	0.493 ± 0.291

Table 8.2.: The top-quark charge asymmetry $A_{C,t\bar{t}}$ is shown comparing true and (KLFitter) reconstructed values for the MC@NLO $t\bar{t}$-signal sample (see Section 6.3). The row *truth before sel.* shows the true $A_{C,t\bar{t}}$ before the event selection. The row *truth after sel. cut 1* shows the true $A_{C,t\bar{t}}$ after the first event selection cut (dileptonic top-quark pair decays only). The rows *truth sel. events* show the true $A_{C,t\bar{t}}$ after the pretag and tagged event selection cut, for events which were also reconstructed using the KLFitter. The rows denoted *reconstructed* show the KLFitter reconstructed $A_{C,t\bar{t}}$ after the pretag and tagged event selection cut, respectively. The given results include statistical errors only.

$A_{C,t\bar{t}}$	ee-Channel [%]	$\mu\mu$-Channel [%]	$e\mu$-Channel [%]
	Pretag:		
MC Signal + Bkg.	0.917 ± 0.729	0.756 ± 0.420	0.290 ± 0.263
Data	0.448 ± 3.866	0.759 ± 2.329	2.326 ± 1.422
MC Signal	-0.062 ± 0.755	-0.049 ± 0.429	0.072 ± 0.268
Data - Bkg.	2.371 ± 4.238	1.190 ± 2.479	4.939 ± 1.517
	≥ 1 b-tagged jet:		
MC Signal + Bkg.	1.280 ± 0.793	1.326 ± 0.461	0.536 ± 0.286
Data	0.000 ± 4.327	-0.475 ± 2.606	2.677 ± 1.567
MC Signal	0.563 ± 0.819	0.741 ± 0.466	0.597 ± 0.291
Data - Bkg.	1.691 ± 4.775	-0.385 ± 2.682	4.404 ± 1.641

Table 8.3.: The top-quark charge asymmetry $A_{C,t\bar{t}}$ measured after the KLFitter reconstruction is performed. The row *MC Signal + Bkg.* shows the reconstructed $A_{C,t\bar{t}}$ from the MC@NLO $t\bar{t}$-signal sample with added background contributions. The row *Data* shows the charge asymmetry derived from the ATLAS 2011 7 TeV dataset. The values in the row *MC Signal* are derived from the MC@NLO $t\bar{t}$ MC signal sample. The charge asymmetry shown in the row *Data - Bkg.* is derived from data after subtraction of MC and fake lepton background contributions. The errors shown are purely statistical errors.

Chapter 9

Unfolding

The measurement of the top-quark charge asymmetry is achieved by the reconstruction of the initial top-quark pair properties using the final state particles measured with the ATLAS detector. The reconstructed properties of the top-quark pair are subject to undesirable characteristics and limitations of the ATLAS detector. Measured particle distributions are limited by detector acceptance, finite resolution and reconstruction efficiency. The reconstruction efficiency not only refers to the reconstruction of the physics objects using the ATLAS offline software framework, but also to the efficiency of the kinematic reconstruction of the KLFitter. For example, Figure 9.1 shows the true absolute top and anti-top-quark rapidity difference for dileptonic events before application of any event selection for the dielectron channel. Also shown are the distributions after the event selection and the distribution after reconstruction with the KLFitter. There are large differences between the true distribution and the KLFitter reconstructed distribution. This is due to the efficiency of the event selection and the reconstruction efficiency of the KLFitter. In order to correct for these selection and reconstruction effects an unfolding procedure is applied. Two unfolding methods are employed, the Bayesian iterative unfolding and unfolding using singular value decomposition. The latter is used as a cross-check. The calculations shown in this chapter adopt the following notational conventions: bold uppercase letters denote matrices and bold lowercase letters denote vectors.

Formally, the process of measuring an observable using a detector can be expressed as the folding integral:

$$\hat{g}(y) = \int_a^b A(y,x)\, f(x) dx + b(y) + \epsilon(y)\,, \tag{9.1}$$

where $\hat{g}(y)$ is the probability distribution of the measured variable y. The function $f(x)$ denotes the distribution of the underlying true values of the measured variable and the interval $[a,b]$ denotes the domain of the variable x. The kernel function $A(x,y)$ describes the probability to measure the value y if the true value is x. In the case of a measurement with ATLAS the kernel describes the detector response. The functions $b(y)$ and $\epsilon(y)$ denote a possible background contribution and the statistical error. If the sample size of the measured quantity is small the statistical error dominates.

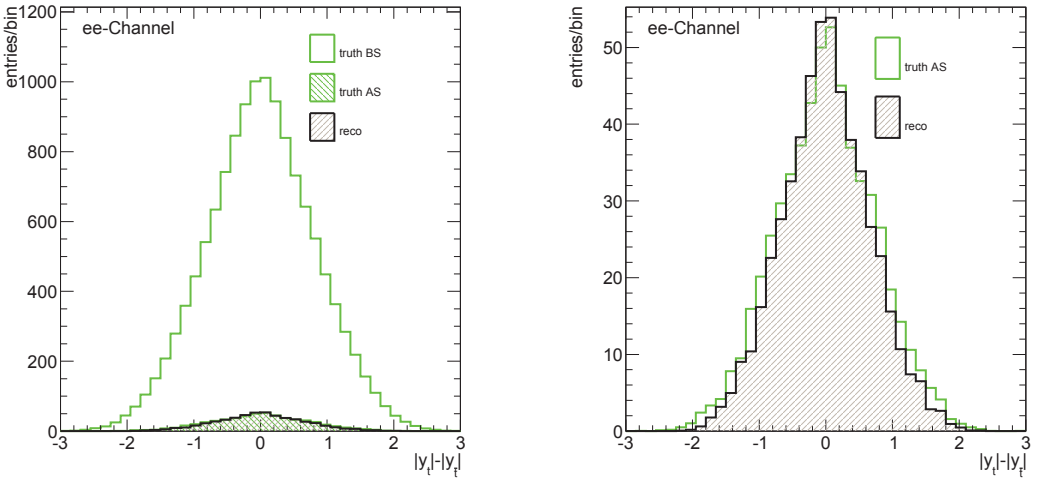

Figure 9.1.: Left: The distribution of the absolute top- and anti-top-quark rapidity difference shown for the true values before application of the pretag event selection *truth BS* (event selection cut 1, true dilepton events only), after application of the pretag event selection, *truth AS*, and the KLFitter reconstructed values *reco*. Right: The same variable is shown as on the left side. Shown is a comparison of the distributions for the true value after the pretag event selection *truth AS* and the KLFitter reconstructed values *reco*. All distributions are derived from the MC@NLO signal sample, all MC scale factors are applied. The distributions are scaled to an integrated luminosity of $\int L\,dt = 4.71\,\mathrm{fb}^{-1}$.

Equation 9.1 is called Fredholm integral equation of the first kind [167, p. 330]. If a specific expectation $f_{\mathrm{th}}(x)$ exists for the function $f(x)$ the expected distribution g_{th} can be calculated from Equation 9.2.

$$g_{\mathrm{th}}(y) = \int_a^b A(y,x)\, f_{\mathrm{th}}(x) dx\,. \tag{9.2}$$

If g_{th} agrees (within statistical errors) with the measured distribution $\hat{g}$, then the theoretical distribution f_{th} is compatible with f [167, p. 331]. If however the expectation is not compatible with the measurement, or no expected distribution is available, $f(x)$ has to be reconstructed from the measured distribution $\hat{g}(y)$. This reconstruction process is called unfolding.
The distributions of physics quantities measured by any experiment are subject to different limitations and biases. Figure 9.2 shows a comparison of a simulated measured and the corresponding true distribution of an arbitrary quantity. The measured distribution in this figure is affected by the following statistical and systematic effects, which are common for measurements in high energy particle physics [168, p. 188]:

- *Statistical Fluctuations:* In all measured bins there are statistical fluctuations from Poisson statistics (for independent bins).
- *Migration:* Finite resolution of the detector causes migrations between bins.
- *Acceptance:* A limited detector acceptance and reconstruction efficiency leads to missing potential entries.

- *Non Linear Response:* Systematic effects as a non-linear detector response lead to a shift in a certain direction.

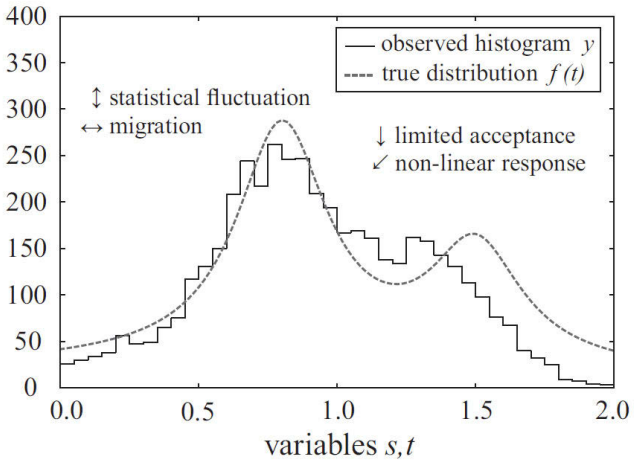

Figure 9.2.: Illustration of the unfolding problem, f is the true distribution and y ($\hat{=}g$) is the corresponding simulated measurement in a typical particle physics experiment [168, p. 188].

If the variables x and y in Equation 9.1 are discrete the integral has to be substituted by a sum. If the variables are continuous the equation has to be discretised to allow for a numerical solution [167, p. 331]. The most common approach to discretise the equation is to integrate the distributions in short equidistant intervals, resulting in histograms [168, p. 189]. Two histograms of the values of $f(x)$ and $\hat{g}(y)$ are a simple representation of a discretised Fredholm integral equation. Given the case of discrete variables the variables x and y are integer numbers in an interval of $1 \dots m$ and $1 \dots n$. Instead of the functions $f(x)$ and $\hat{g}(y)$ there are now vectors with the elements f_j where $j = 1 \dots m$ and g_i where $i = 1 \dots n$. The unfolding integral is then transformed into

$$\hat{\mathbf{g}} = \mathbf{A}\,\mathbf{f} + \mathbf{b} + \boldsymbol{\epsilon}\,, \tag{9.3}$$

where $\mathbf{f}$ is a vector of size m, $\hat{\mathbf{g}}$, $\mathbf{b}$ and $\boldsymbol{\epsilon}$ are vectors of size n and $\mathbf{A}$ is an $n \times m$ matrix referred to as the response matrix [167, p. 331]. Equation 9.3 can be rearranged, assuming the statistical error $\boldsymbol{\epsilon}$ is small, in order to estimate $\hat{\mathbf{f}}$

$$\hat{\mathbf{f}} = \mathbf{A}^{-1}\left(\hat{\mathbf{g}} - \mathbf{b}\right)\,, \tag{9.4}$$

where $\mathbf{A}^{-1}$ is the inverse matrix corresponding to $\mathbf{A}$. In the following $\mathbf{b} = 0$ is assumed. The expectation value $E\left(\hat{\mathbf{f}}\right)$ equals the true value $\mathbf{f}$ if the measured distribution $\hat{\mathbf{g}}$ is not distorted. Standard error propagation results in

$$\mathbf{V}\left[\hat{\mathbf{f}}\right] = \mathbf{A}^{-1}\mathbf{V}\left[\hat{\mathbf{g}}\right]\left(\mathbf{A}^{-1}\right)^{T}\,, \tag{9.5}$$

where $\mathbf{V}\left[\hat{\mathbf{f}}\right]$ represents the covariance matrix calculated from the covariance matrix $\mathbf{V}\left[\hat{\mathbf{g}}\right]$ of the measured distribution.

This relatively straight forward way of unfolding often delivers widely oscillating negative correlation coefficients between neighbouring points and large positive correlation coefficients between next to nearest neighbours [168, p. 191]. Regularisation methods have to be implemented in order to reduce these oscillations to a minimum. Regularisation is an estimation of the smooth development of the true solution $\mathbf{f}$ [167, p. 332]. This can introduce a distortion and hence the regularisation has to be controlled in order to keep its influence small in comparison to the statistical error. For details on the regularisations used refer to the Sections 9.2 and 9.1.

9.1 Bayesian Iterative Unfolding

The Bayesian iterative unfolding (BIU) uses an iterative approach, based on the Bayes theorem, to invert the response matrix [169, p. 3]. The Bayes formula for a finite amount of independent causes C_i (with $i = 1, 2, \ldots, n_c$) which can produce an effect E is then given by

$$P(C_i \mid E) = \frac{P(E \mid C_i)\, P(C_i)}{\sum_{l=1}^{n_c} P(E \mid C_l)\, P(C_l)}\,. \tag{9.6}$$

If a single effect E is observed, the probability that it has been due to the i-th cause is proportional to the probability of the cause $P(C_i)$ times the probability of the cause to produce the effect $P(E \mid C_i)$ [169, p. 3]. Transferred to the case of a measurement which observes $n(E)$ events with the effect E, the expected number of events $\hat{n}(C_i)$ assignable to each cause is given by [169, p. 4]:

$$\hat{n}(C_i) = P(C_i \mid E)\, n(E)\ , \tag{9.7}$$

where $P(C_i \mid E)$ is the posterior probability

$$P(C_i \mid E_j) = \frac{P(E_j \mid C_i)\, P_0(C_i)}{\sum_{l=1}^{n_c} P(E_j \mid C_l)\, P_0(C_l)}\,, \tag{9.8}$$

in which $P_0(C_l)$ is the initial probability of the cause. This prior knowledge is obtained from Monte Carlo using a training sample. Equation 9.8 written in terms of the notation used in the SVD unfolding is

$$P(f_i \mid g_j) = \frac{P(g_j \mid f_i)\, P_0(f_i)}{\sum_{l=1}^{n_c} P(g_j \mid f_l)\, P_0(f_l)}\,, \tag{9.9}$$

where $P(g_j \mid f_i)$ represents the response matrix element A_{ji}. The final probability distribution $\hat{P}(C_i)$ is given by

$$\hat{P}(C_i) \equiv \frac{\hat{n}(C_i)}{\sum_{i=1}^{n_c} \hat{n}(C_i)}\,. \tag{9.10}$$

If the initial probability distribution $P_0(C_i)$ is not consistent with the data, it will not agree with the final probability distribution $\hat{P}(C_i)$, but the final probability distribution $\hat{P}(C_i)$ always lies between $P_0(C_i)$ and the true distribution (see [169, p. 5] for details). This suggests that this method can be used iteratively when the obtained posterior probability distribution $P(f_i \mid g_j)$ is used as a prior for subsequent iterative steps.

The regularisation in the BIU is achieved by limiting the number of iterative steps. The

number of iterative steps depends on the discretisation of the measured distribution, bin migration effects in the response matrix and the choice of the prior. While different discretisations can easily be tested, migration effects in the response matrix, which are represented by the magnitude of the off-diagonal elements, cannot be controlled since the response matrix is obtained from the MC@NLO $t\bar{t}$-signal MC.

9.2 Singular Value Decomposition

The singular value decomposition (SVD) is a simple, effective way to invert the response matrix in order to unfold a given discretised distribution. It offers full error propagation and the complete covariance matrix [170, p. 1]. The SVD of a real $m \times n$ matrix $\mathbf{A}$ is its factorisation of the form

$$\mathbf{A} = \mathbf{L}\,\mathbf{S}\,\mathbf{R}^T\,, \tag{9.11}$$

where $\mathbf{L}$ is an $m \times m$ orthogonal matrix, $\mathbf{R}$ is an $n \times n$ orthogonal matrix and $\mathbf{S}$ is an $m \times n$ diagonal matrix with non-negative diagonal elements [170, p. 4]. The quantities of Equation 9.11 have to fulfill

$$\mathbf{L}\mathbf{L}^T = \mathbf{L}^T\mathbf{L} = \mathbf{I},\ \mathbf{R}\mathbf{R}^T = \mathbf{R}^T\mathbf{R} = \mathbf{I}\,, \tag{9.12}$$

$$S_{ij} = 0 \ \text{ for } \ i \neq j,\ S_{ii} \equiv s_i \geq 0\,, \tag{9.13}$$

where $\mathbf{I}$ is the identity matrix. The quantities s_i are called singular values of the matrix $\mathbf{A}$, and columns of $\mathbf{L}$ and $\mathbf{R}$ are called left and right singular vectors [170, p. 4]. Comprehensive descriptions of how to implement the SVD itself can be found in literature, see e.g. [171] or [172]. Matrix inversion using SVD can be explained using a simplified representation of a measurement similar to Equation 9.3:

$$\mathbf{A}\mathbf{f} = \mathbf{g}\,, \tag{9.14}$$

where $\mathbf{A}$ is then decomposed as shown in Equation 9.11. In order to solve this linear equation system $\mathbf{L}$, $\mathbf{R}$ and $\mathbf{S}$ are used to rotate the unknown vector $\mathbf{f}$ and the measured vector $\mathbf{g}$

$$\mathbf{z} = \mathbf{R}^T\mathbf{f} \ \text{ and } \ \mathbf{d} = \mathbf{L}^T\mathbf{g}\,. \tag{9.15}$$

Then a diagonal system of equations is formed

$$\mathbf{S}\mathbf{z} = \mathbf{d} \ \Leftrightarrow \ \mathbf{z} = \mathbf{S}^{-1}\mathbf{d}\,. \tag{9.16}$$

The unknown vector $\mathbf{f}$ can be obtained by rotating $\mathbf{z}$ back

$$\mathbf{f} = \mathbf{R}\mathbf{z} = \mathbf{R}\mathbf{S}^{-1}\mathbf{U}^T\mathbf{b} = \mathbf{A}^{-1}\mathbf{g}\,. \tag{9.17}$$

From Equation 9.17 the identity

$$\mathbf{A}^{-1} = \mathbf{R}\mathbf{S}^{-1}\mathbf{L}^T \tag{9.18}$$

can be obtained. Since the matrix $\mathbf{S}$ is diagonal it can be inverted by inverting the matrix entries s_i. Going back to Equation 9.14 the problem presented can be expressed as a

solution of the following least squared problem

$$\sum_{i=1}^{n_g} \sum_{j=1}^{n_f} \left(A_{ij} f_j - g_i\right)^2 = \min . \tag{9.19}$$

Regularisation of the given Equation 9.19 can be achieved by addition of a regularisation (or stabilisation term):

$$\left(\mathbf{Af} - \mathbf{g}\right)^T \left(\mathbf{Af} - \mathbf{g}\right) + \tau \left(\mathbf{Cf}\right)^T \left(\mathbf{Cf}\right) = \min , \tag{9.20}$$

where the matrix $\mathbf{C}$ defines the a priory condition on the solution and the regularisation parameter τ the relative weight of this condition [170, p. 11].

9.3 Unfolding Studies on Monte Carlo

Before the unfolding procedure is performed on the (KLFitter reconstructed) ATLAS 2011 7 TeV dataset studies on MC are necessary in order to determine the best combination of discretisation (i.e. the binning) and the regularisation parameter. The unfolding is performed using the RooUnfold package (version 1.1.1) [173]. It is applied separately for each of the top-quark pair decay channels. In order to conduct studies on unfolding two samples are necessary. One sample for the training of the response matrix and a second sample to which the unfolding procedure is applied. The sample used for the creation of the response matrix is referred to as *training sample* and the sample to which the unfolding procedure is applied is referred to as *unfolding sample*. In this analysis the MC@NLO $t\bar{t}$-signal sample was used as the training sample (all MC scaling factors, but no luminosity scaling is applied). The MC signal sample is also used as the unfolding sample after reweighting it to different asymmetries

$$A_{C,t\bar{t}}^{\text{rew}} \in \{-0.1, -0.05, -0.025, 0.0, 0.025, 0.05, 0.1\} ,$$

and scaling the number of MC events to the statistics of the ATLAS 2011 7 TeV dataset (for the corresponding channel). An example of the reweighted distributions is shown in Figure 9.3. The statistical error of the unfolding sample is set to the statistical error expected from the 2011 dataset. This ensures that the unfolding studies are performed under the same conditions as the unfolding of the 2011 dataset. The reweighted asymmetries are (for the positive values) chosen to cover a range of possible asymmetries which could originate from new physics (see Section 2.5.4). The negative values of $A_{C,t\bar{t}}^{\text{rew}}$ are added in order to perform a linear scaling check of the unfolding procedure.
The reweighting of the unfolding sample is performed by the application of an additional event weight $\omega_{\pm}$. This asymmetry weight is determined for each channel separately and comprises two values ($\pm$) for each value of reweighted top-quark charge asymmetry ($A_{C,t\bar{t}}^{\text{rew}}$). For details on the determination of the asymmetry weights see Appendix D.1. The asymmetry weight is applied to all MC events. The usage of ω_+ and ω_- depends on the true absolute rapidity difference $\Delta\left|y_{t\bar{t}}\right| = \left|y_t\right| - \left|y_{\bar{t}}\right|$ between top and antitop-quark:

- if $\Delta\left|y_{t\bar{t}}^{\text{truth}}\right| < 0$, apply ω_-,
- if $\Delta\left|y_{t\bar{t}}^{\text{truth}}\right| > 0$, apply ω_+.

In order to choose the ideal combination of discretisation and regularisation ensemble, tests of the unfolding procedure are performed. N_P ensembles of pseudo data are created by varying each bin of the distribution to which the unfolding is applied, assuming a Poissonian uncertainty around the expectation. This was performed for combinations of discretisation, regularisation parameters and different reweighted asymmetries. The tested binnings of the $\Delta|y_{t\bar{t}}|$ distribution are:

- *4 bins:* $[-3.0, -1.5, 0.0, 1.5, 3.0[$,
- *6 bins a):* $[-3.0, -1.0, -0.5, 0.0, 0.5, 1.0, 3.0[$,
- *6 bins b):* $[-3.0, -1.2, -0.6, 0.0, 0.6, 1.2, 3.0[$,
- *6 bins c):* $[-3.0, -2.0, -1.0, 0.0, 1.0, 2.0, 3.0[$,
- *8 bins a):* $[-3.0, -1.5, -1.0, -0.5, 0.0, 0.5, 1.0, 1.5, 3.0[$,
- *8 bins b):* $[-3.0, -2.25, -1.5, -0.75, 0.0, 0.75, 1.5, 2.25, 3.0[$.

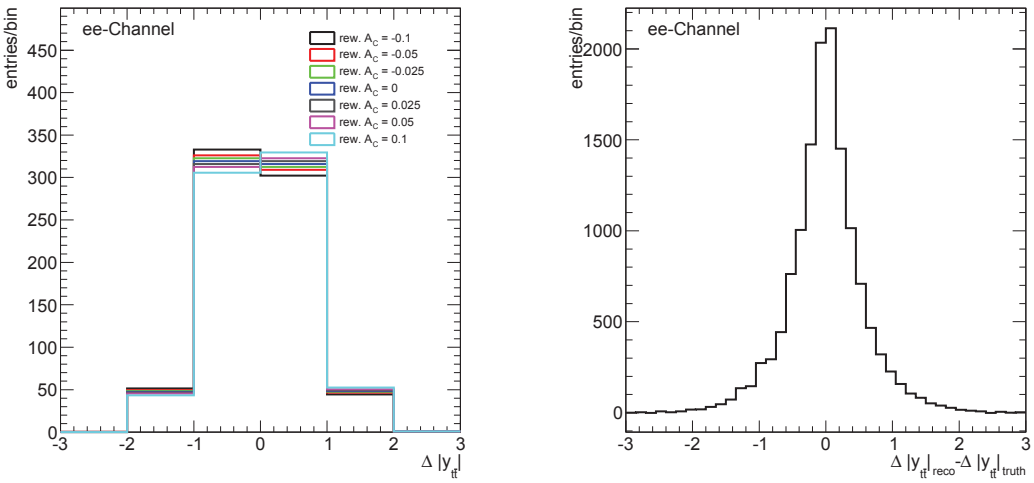

Figure 9.3.: The reweighted $\Delta|y_{t\bar{t}}|$ distributions of the unfolding sample for different asymmetries (left) and the KLFitter reconstruction resolution distribution (right). Events are selected according to the pretag selection.

The binning of the $\Delta|y_{t\bar{t}}|$ distribution is chosen such as keeping as few bins as possible to preserve the statistical significance. In order to compute the top-quark charge asymmetry two bins are sufficient. The corresponding 2×2 response matrix has large off-diagonal elements leading to strong bin migration effects. This causes large fluctuations in the charge asymmetry derived from the unfolded $\Delta|y_{t\bar{t}}|$ distribution. Hence the minimum number of bins is chosen to be four. Bin migration only affects the derived charge asymmetry if the number of entries in the positive and negative sides of the $\Delta|y_{t\bar{t}}|$ distribution change. Hence the unfolding was tested additionally for six and eight bins in order to check if increasing the number of bins would minimise the migration between the positive and negative sides of the distribution. The minimum bin width is defined as the full width at half maximum of the $\Delta|y_{t\bar{t}}|_{\text{reco}} - \Delta|y_{t\bar{t}}|_{\text{truth}}$ distribution, which corresponds to the resolution of the KLFitter reconstruction (see Figure 9.3). The minimum width of one bin is determined to be 0.5.

The regularisation of the BIU is achieved by increasing the number of iterations N_{it}. For the SVD unfolding method, regularisation is achieved by introducing the regularisation parameter $\tau = 2, 3, \ldots, N_{\text{bins}}$, where τ cannot exceed the number of bins in the distribution which is unfolded. The SVD unfolding was performed as a cross-check to the BIU. Details on the SVD unfolding can be found in Appendix F.

The settings used for the unfolding of the ATLAS 2011 7 TeV dataset are derived by combining different discretisations and regularisations. For each combination $N_p = 5000$ sets of pseudo-data are generated and the unfolding is applied. The regularisation is chosen so that the change in the error $\Delta\sigma_{A_C} = \left|\sigma_n^{A_C} - \sigma_{n-1}^{A_C}\right|$ in the subsequent number of iterations n is small. Additionally, the convergence of the unfolded property is checked. This means that for each unfolded pseudo-data set the top-quark charge asymmetry is derived. The distribution of these values is then fitted using a Gaussian model. The mean of the Gaussian is then taken as the average value of the charge asymmetry $\langle A_{C,t\bar{t}}^{\text{unf}} \rangle$ while the width of the distribution is used as an estimate of the statistical error. The convergence for different unfolding settings is then checked by subtracting the true value of the unfolded distribution with the averaged value from the pseudo data. The proper estimation of the statistical error is checked using pull distributions. The pull is defined as

$$\text{pull} = \frac{A_{C,t\bar{t}}^{\text{unf}} - A_{C,t\bar{t}}^{\text{truth}}}{\sigma_{A_C^{\text{unf}}}} \,. \tag{9.21}$$

It is calculated for each set of pseudo-data, and the corresponding distribution is fitted using a Gaussian model. If the unfolded property is derived correctly, the mean of the pull distribution is at zero and the width of the pull distribution is one.

Finally, the linear scaling (LS) of the different unfolding settings is checked. This ensures that the settings chosen deliver proper results for different reweighted asymmetries. The LS is checked by plotting the averaged unfolded asymmetries (derived from N_P sets of pseudo-data) versus the true asymmetry of the unfolded sample. Then a linear fit is applied which delivers a slope p_s and an axis intercept p_a value. An example of this fit is shown in Figure 9.7. A slope value of one and an axis intercept value of zero ensure that the unfolded asymmetry equals the true charge asymmetry. The values of p_s and p_a for the chosen unfolding settings are listed in Table 9.1. The settings used for the unfolding of the 2011 7 TeV dataset are the same for each channel and for the pretag and tagged event selection. The chosen discretisation is *4 bins* and the optimal regularisation for the BIU is achieved by using $N_{it} = 40$ iterations.

Parameter	ee-Channel	$\mu\mu$-Channel	$e\mu$-Channel
		Pretag:	
p_s	1.0 ± 0.5	1.0 ± 0.4	1.0 ± 0.2
p_a	0.00 ± 0.03	0.00 ± 0.02	0.00 ± 0.01

Table 9.1.: Results of the linear fit performed on a distribution of average unfolded an asymmetry, derived from a Gaussian fit to the charge asymmetry distribution of $N_P = 5000$ ensembles of pseudo-data, versus the true charge asymmetry of the unfolding sample. The results are derived for the *4 bins* discretisation and $N_{it} = 40$ iteration steps of BIU.

Parameter	ee-Channel	$\mu\mu$-Channel	$e\mu$-Channel
	≥ 1 b-tagged jet:		
p_s	1.0 ± 0.5	1.0 ± 0.3	1.0 ± 0.2
p_a	0.00 ± 0.03	0.00 ± 0.02	0.00 ± 0.01

Table 9.1.: Results of the linear fit performed on a distribution of average unfolded an asymmetry, derived from a Gaussian fit to the charge asymmetry distribution of $N_P = 5000$ ensembles of pseudo-data, versus the true charge asymmetry of the unfolding sample. The results are derived for the *4 bins* discretisation and $N_{it} = 40$ iteration steps of BIU.

9.4 Estimation of the Settings for the Bayesian Iterative Unfolding

The settings for the Bayesian iterative unfolding (BIU) concerning the regularisation strength (i.e. the number of iterations N_{it}) and the discretisation (i.e. the binning of the $\Delta|y_{t\bar{t}}|$) are derived by checking the evolution of the error of the unfolded charge asymmetry, the convergence, the pull and the linear scaling. These studies are performed on $N_P = 5000$ ensembles of pseudo-data for each combination of unfolding settings. The tested settings comprise all binnings listed in Section 9.3 and $N_{it} \epsilon [1, 5, 10, \ldots, 100]$ numbers of iterations. Only the results of the checks performed on the *4 bins* and *6 bins c)* discretisations are shown, since the remaining discretisations do not reach a stable statistical error within $N_{it} = 100$ iterations. The plots shown in this section are exemplary for the pretag event selection. The plots featuring the tagged event selection are given in the Appendix D.2.

The evolution of the estimated error of the unfolded charge asymmetry for different regularisations (i.e. number of iterations) and discretisations is shown in Figure 9.4. The evolution of the error for increasing regularisation strength is the main benchmark to identify the optimal unfolding setting for BIU. An optimal number of iterations is found if the estimated error of the unfolded charge asymmetry only fluctuates within its uncertainty for higher numbers of iterations. If the number of iterations is small the unfolded result is biased by the prior, which is the truth $\Delta|y_{t\bar{t}}|$ distribution of the MC training sample. If too many iterative steps are performed, large fluctuations in the statistical errors can appear.
For each datapoint shown in Figure 9.4 the number of iterations is increased in steps of five (or ten for larger N_{it}) to a maximum of $N_{it} = 100$ iterations. This is then repeated for different discretisations. For the *4 bins* and *6 bins c)* discretisations a stable statistical error (with only small variations for subsequent numbers of iterations) is reached after $N_{it} = 40$ iteration steps. The error of the unfolded charge asymmetry is estimated using the following procedure:
The $\Delta|y_{t\bar{t}}|$ distribution of each ensemble of pseudo-data is unfolded and the corresponding charge asymmetry is calculated. This results in a distribution of unfolded charge asymmetries, which is then fitted using a Gaussian model. The mean of the Gaussian is then

the averaged unfolded charge asymmetry $\langle A_{C,t\bar{t}}^{\mathrm{unf}} \rangle$ and the width of the Gaussian is the expected statistical error σ_{A_C}, which is then shown in Figure 9.4.

The evolution of the convergence of the unfolded averaged charge asymmetry is shown in Figure 9.5 for different unfolding settings. The convergence is reached when the difference between the true asymmetry of the unfolding sample and the averaged unfolded charge asymmetry is zero, within the bounds of statistical errors. Depending on the discretisation convergence is reached within $N_{it} \approx 20$. Again the discretisations *4 bins* and *6 bins c)* show the best results in terms of fast convergence and stability for different reweighted asymmetries.

The evolution of the pull of the unfolded charge asymmetry for different unfolding settings is shown in Figure 9.6. The pull is defined in Equation 9.21 and it provides an estimate of the validity of the derived statistical error. The pull is calculated for each ensemble of pseudo-data. The resulting distribution is described by a Gaussian model. The mean of the Gaussian is used as the average pull and the width of the distribution as the error of the average pull. The mean value of the pull converges to zero within $N_{it} = 10$ in the dielectron channel and $N_{it} = 25$ in the electron-muon channel. This means that no bias from the training sample is present in the unfolded distributions. However, the estimated error of the pull is larger than one if the number of iterations exceeds $N_{it} = 5$ for the dielectron channel and $N_{it} = 10$ for the electron-muon channel. This means that the statistical error of the unfolded distribution is underestimated since it is smaller than the average difference between the true and the unfolded asymmetry value. This is fixed by the introduction of the linear scaling uncertainty (LSU). For details on the LSU refer to Section 9.5.

Figure 9.7 shows examples of the linear fit performed on a distribution of an average unfolded asymmetry, derived from a Gaussian fit to the charge asymmetry distribution of $N_P = 5000$ ensembles of pseudo-data, versus the true charge asymmetry of the unfolding sample. Figure 9.8 shows the result of the LS test. The slope (p_s) of the linear fit is one and the axis intercept (p_a) zero for the chosen unfolding settings. This shows that the unfolded charge asymmetry is unbiased by the training sample and the unfolding provides stable results over the whole range of expected charge asymmetries. Figures 9.7 and 9.8 show that the LS of the unfolding procedure is ensured for $N_{it} = 10$ iterations.

The estimation of the unfolding settings is performed using the pretag and the tagged event selection. Performing these checks on the events selected using the tagged selection shows that the same unfolding settings can be applied to both event selections. For the tagged selection only the figures for the *4 bins* and *6 bins c)* discretisations are shown since the other discretisations do not reach a stable statistical error within $N_{it} = 100$. The results for the three dileptonic top-quark pair decay channels are shown in Figures D.1, D.2 and D.3. A summary of the LS tests for all three channels is shown in Figures D.4 and D.5. The result of the LS test for $N_{it} = 40$ and the *4 bins* discretisation is summarised in Table 9.1.

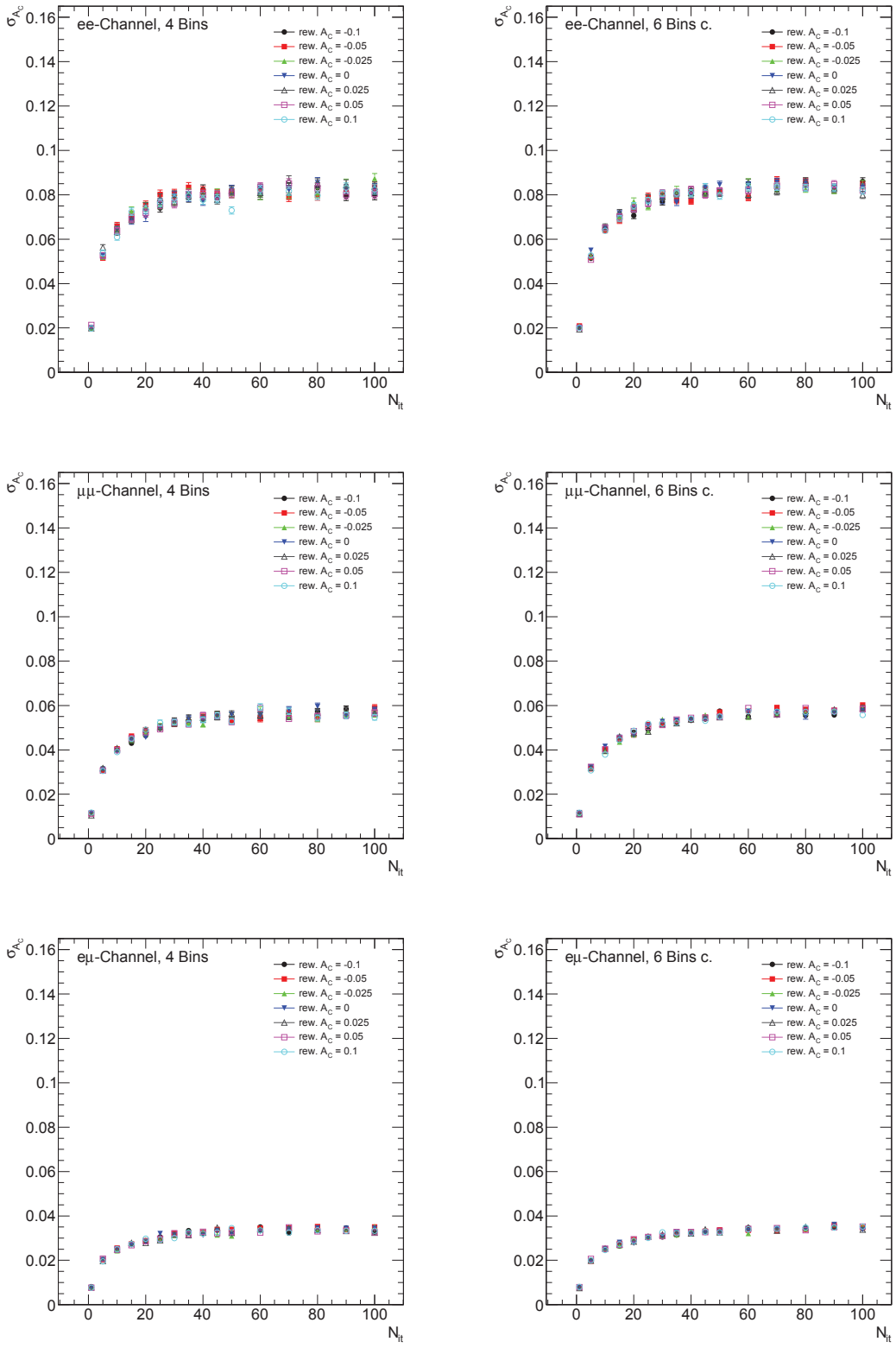

Figure 9.4.: The expected statistical error σ_{A_C} of the charge asymmetry versus the regularisation strength N_{it} for different reweighted charge asymmetries *rew* A_C of the unfolding sample. The data points are derived for $N_P = 5000$ ensembles of pseudo-data. The pretag selection is used. Top, middle and bottom row show the three dileptonic decay channels, using the *4 bins* (left) and the *6 bins c)* (right) discretisations. The errors are statistical errors.

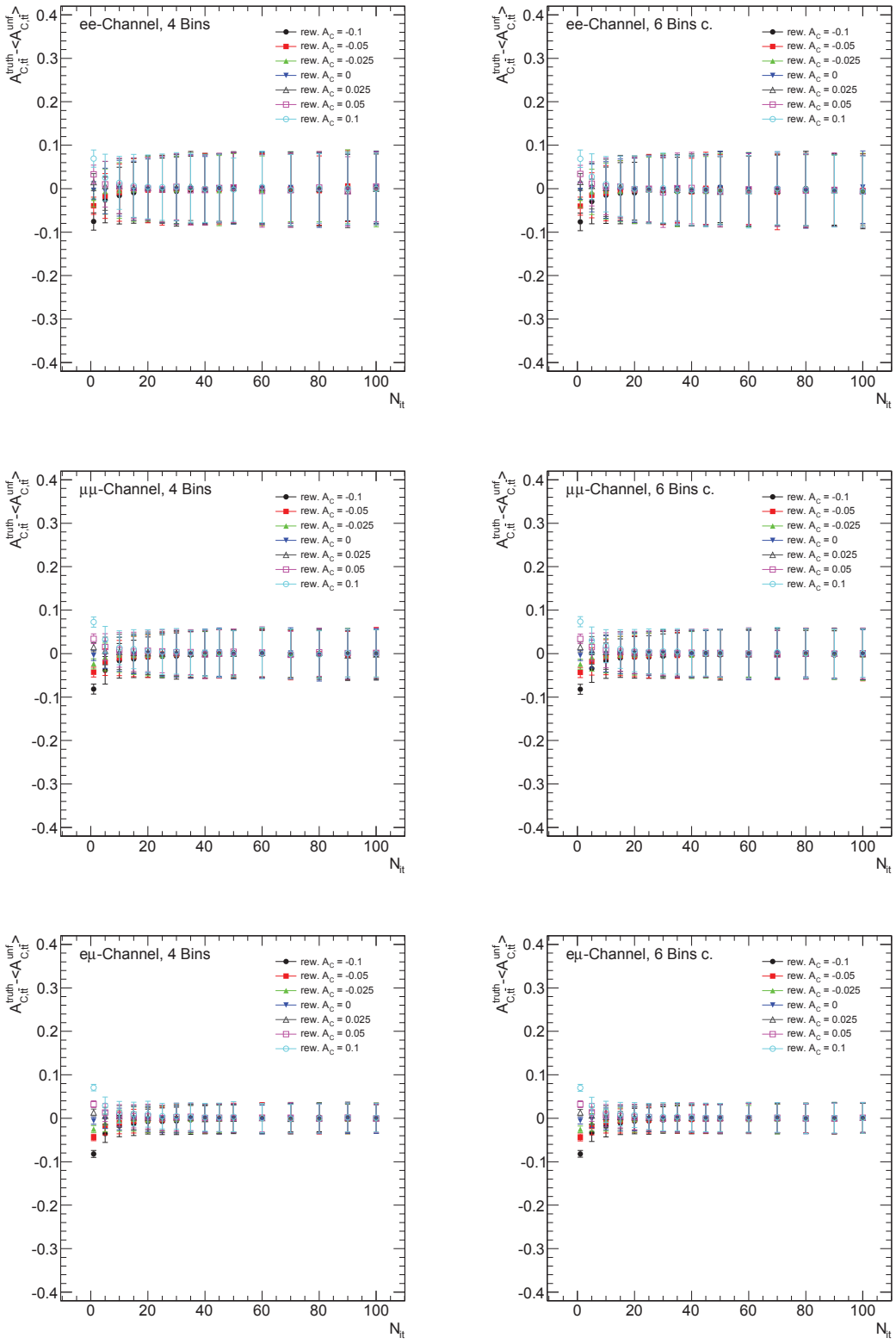

Figure 9.5.: The convergence $A_{C,t\bar{t}}^{\text{truth}} - \langle A_{C,t\bar{t}}^{\text{unf}} \rangle$ of the charge asymmetry versus the regularisation strength N_{it} for different reweighted charge asymmetries *rew* A_C of the unfolding sample. The data points are derived for $N_P = 5000$ ensembles of pseudo-data. The pretag selection is used. Top, middle and bottom row show the three dileptonic decay channels, using the *4 bins* (left) and the *6 bins c)* (right) discretisations. The errors are statistical errors.

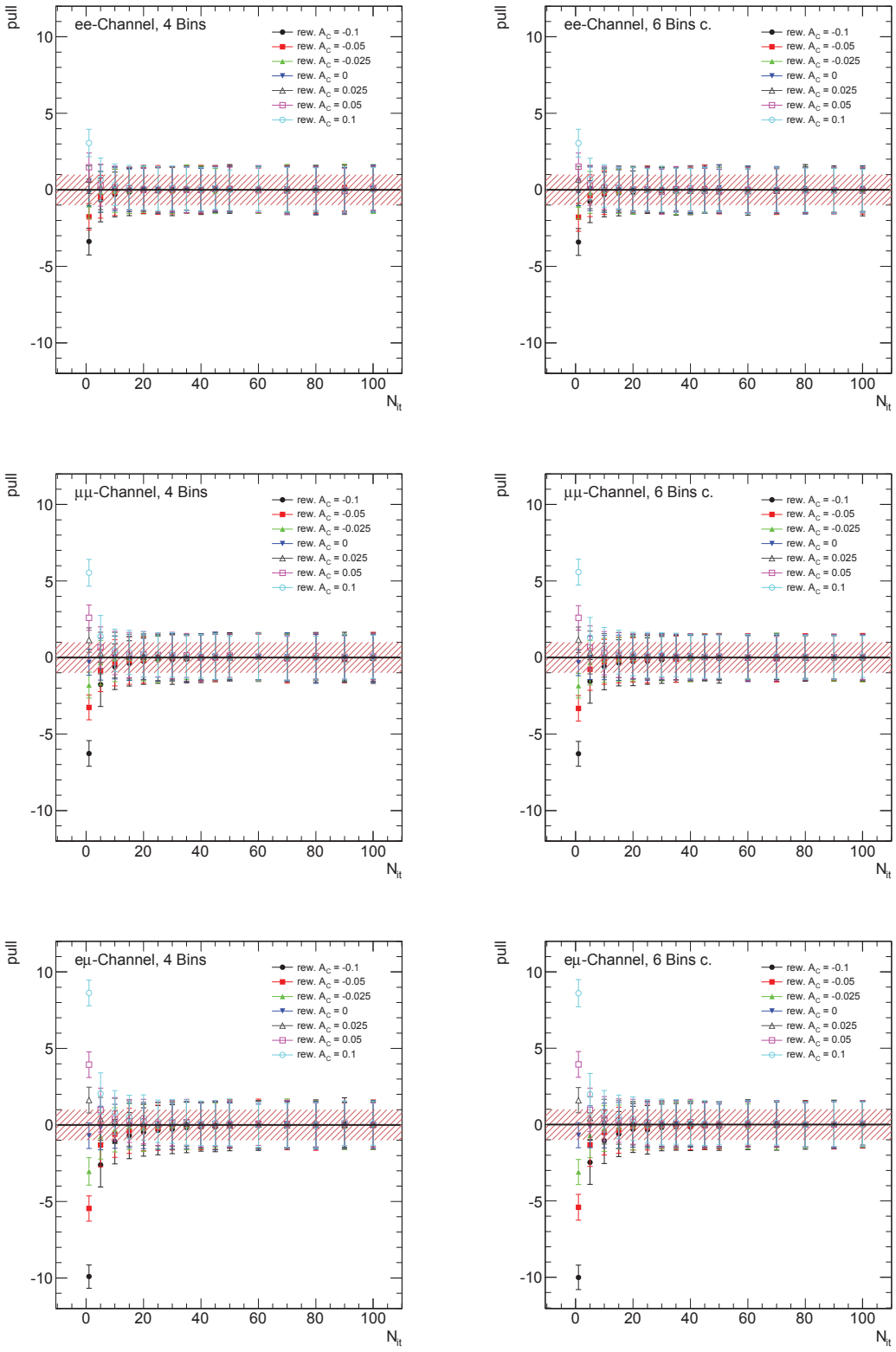

Figure 9.6.: The averaged pull versus the regularisation strength N_{it} for different reweighted charge asymmetries *rew* A_C of the unfolding sample. The data points are derived for $N_P = 5000$ ensembles of pseudo-data. The pretag selection is used. Top, middle and bottom row show the three dileptonic decay channels, using the *4 bins* (left) and the *6 bins c)* (right) discretisations. The errors are statistical errors.

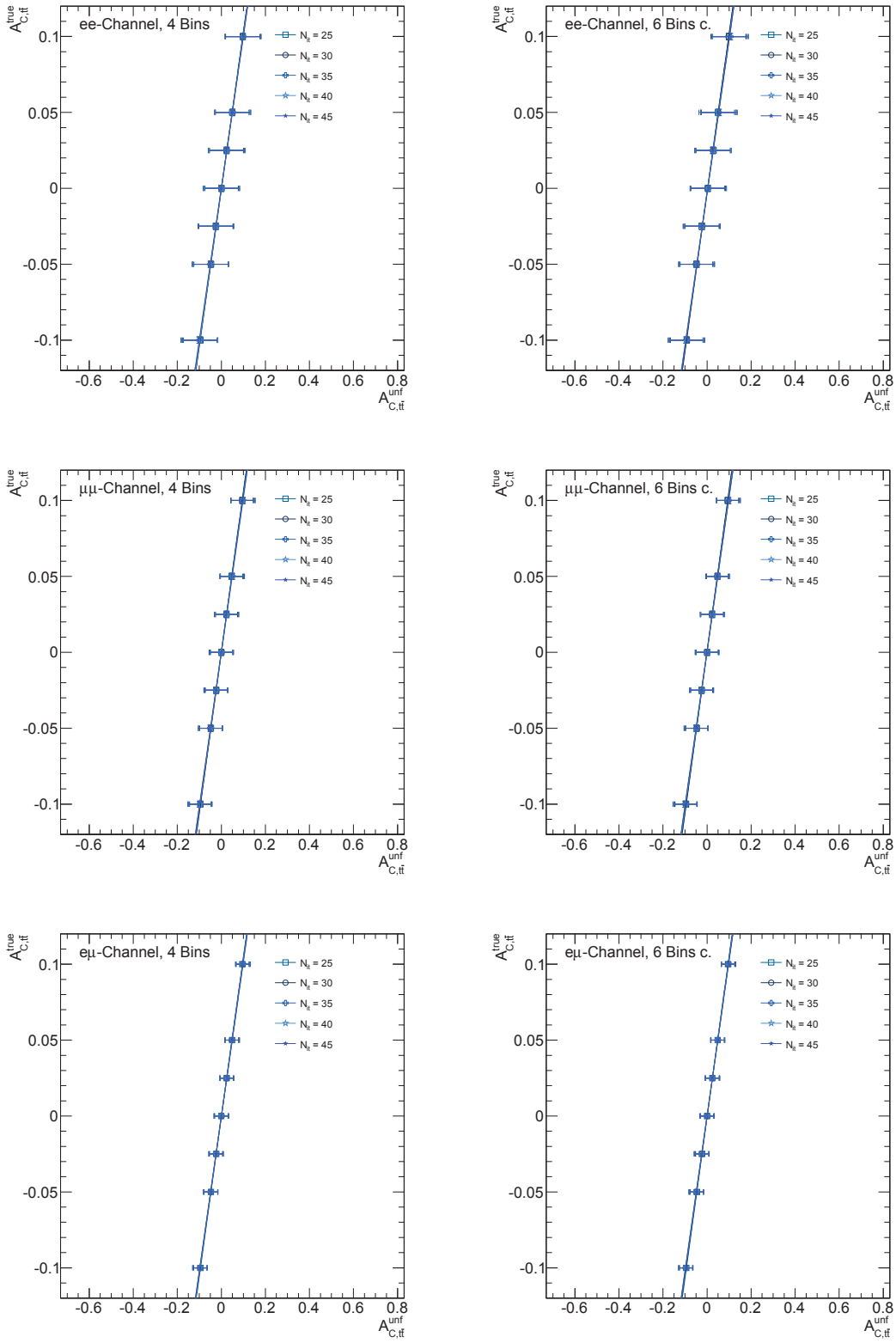

Figure 9.7.: Compilation of linear fits of the $A^{\mathrm{unf}}_{c,t\bar{t}}$ versus $A^{\mathrm{true}}_{c,t\bar{t}}$ distribution for different regularisation strengths N_{it}. The fit is described in Section D.2. Top, middle and bottom row show the three dileptonic decay channels, using the *4 bins* (left) and the *6 bins c)* (right) discretisations. Shown errors are statistical errors and the pretag selection is used.

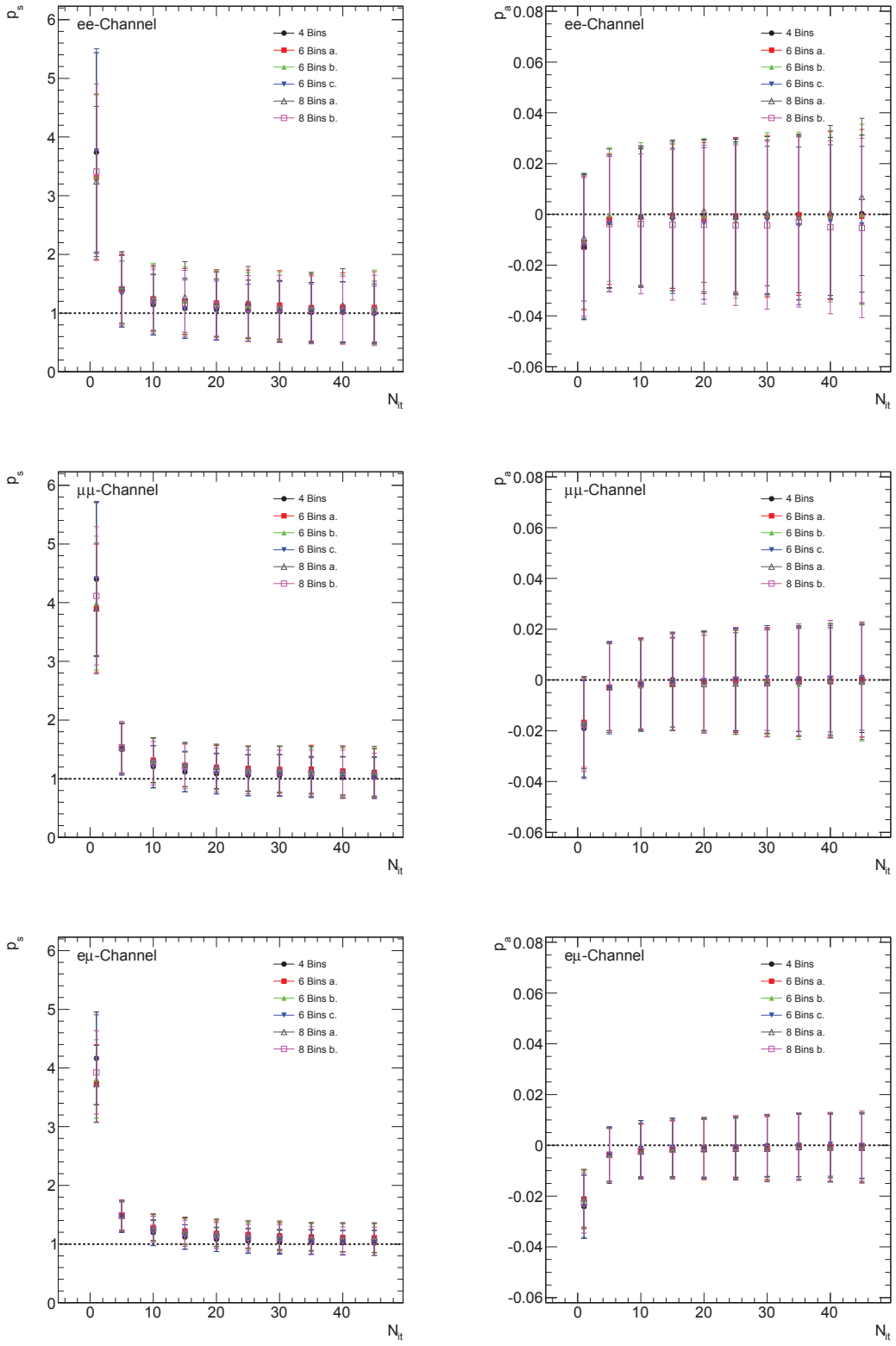

Figure 9.8.: The slopes (left) and the axis intercepts (right) of linear fits versus the regularisation strength N_{it}. The fit is described in Section D.2. Each plot features the results for different discretisations. Top, middle and bottom row show the results for the three top-quark pair decay channels. The errors are statistical errors and the pretag selection is used.

9.5 Data Unfolding

The response matrices used for the data unfolding are created from the MC@NLO $t\bar{t}$-signal sample. The unfolding of the $\Delta|y_{t\bar{t}}|$ distribution for the ATLAS 2011 7 TeV dataset is performed separately for each dileptonic top-quark pair decay channel. The Bayesian iterative unfolding (BIU) is applied once using the settings derived from MC studies. The charge asymmetry calculated from this unfolded distribution is then used as the central value of the top-quark charge asymmetry. Then the unfolding is applied to $N_p = 100000$ ensembles of pseudo-data, creating a posterior distribution of asymmetry values. The width of the posterior distribution (calculated from a fit using a Gaussian model) is used as an estimate of the statistical error. The asymmetry value calculated after the application of the unfolding $A_{C,t\bar{t}}^{\text{meas}}$ has to take into account the linear scaling of the unfolding procedure and the corresponding uncertainty (linear scaling uncertainty LSU):

$$A_{C,t\bar{t}}^{\text{meas}} = A_{C,t\bar{t}}^{\text{unf}} \; p_s + p_a \,. \tag{9.22}$$

Since the parameter $p_s = 1$ and the parameter $p_a = 0$ for the chosen unfolding settings (within the error) the central value of $A_{C,t\bar{t}}^{\text{meas}}$ and $A_{C,t\bar{t}}^{\text{unf}}$ are the same, but the uncertainty of p_s and p_a has to be taken into account in the calculation of the error of the unfolded asymmetry. The calculation of the parameters p_s and p_a is described in detail in Appendix D.2. For the values and errors of p_s and p_a see Table 9.1. The uncertainty σ_{lin} originating from the limited unfolding LS is calculated using Gaussian error propagation for Equation 9.22 and is added in quadrature to the statistical error derived from the asymmetry posterior distribution. For details on the calculation of the linear scaling uncertainty refer to Section D.3.

The data contains background events in addition to the signal events. In order to apply the unfolding only to the $t\bar{t}$-signal, the background contribution has to be subtracted from the data. In order to show the effect of the background the unfolding has also been performed without subtracting the background. The unfolding results for $N_{it} = 40$ and the *4 bins* discretisation are summarised in Table 9.2. The table presents two different results for the pretag and the tagged selection, namely with and without background subtraction. The background subtraction is performed bin-wise for the $\Delta|y_{t\bar{t}}|$ data distribution before the unfolding is applied. The resulting distribution is then unfolded and the top-quark charge asymmetry is calculated. The background was estimated using MC for the $Z \to ee, (\mu\mu, \tau\tau)$, single top and diboson contributions and a data driven technique for the fake lepton contribution, a description of the background contributions is given in Section 6.4. For additional information on the calculation of the unfolded charge asymmetry (including the full covariance matrices) and the corresponding errors see Appendix E.

Figure 9.9 shows $\Delta|y_{t\bar{t}}|$ distributions for the ATLAS 2011 7 TeV dataset, the MC@NLO signal MC and the background contributions, for the pretag event selection. The data distribution shown is the input for the calculation of the central unfolded charge asymmetry value which is listed in Table 9.2. In addition the distribution of the data after bin-wise background subtraction is shown. The unfolded $\Delta|y_{t\bar{t}}|$ distributions (with and without background subtraction) are shown in Figure 9.10. The width of the posterior distribution of $A_{C,t\bar{t}}^{\text{meas}}$ is taken as statistical error on the central charge asymmetry value. The posterior distributions are shown in Figure 9.11 for $N_P = 100000$ ensembles of pseudo-data. The

width is determined by fitting a Gaussian model to the posterior distribution. The width of the Gaussian is then σ_{A_C}. For the distributions using the tagged event selection refer to Appendix E.1.

ee-Channel [%]	$\mu\mu$-Channel [%]	$e\mu$-Channel [%]	Bkg. subtraction
	Pretag:		
(1.8 ± 10.1)	(2.1 ± 6.6)	(5.7 ± 4.0)	✗
(6.2 ± 12.8)	(3.0 ± 7.2)	(11.3 ± 4.9)	✓
	≥ 1 b-tagged jet:		
(0.1 ± 11.1)	(-2.4 ± 7.1)	(5.6 ± 4.4)	✗
(3.4 ± 15.1)	(-2.3 ± 7.4)	(9.4 ± 5.1)	✓

Table 9.2.: The unfolded top-quark charge asymmetries $A_{C,t\bar{t}}^{\text{meas}}$, derived from the ATLAS 2011 7 TeV dataset. Bayesian iterative unfolding is applied using $N_{it} = 40$ and the *4 bins* discretisation. The error is the quadratic sum of the statistical error derived from the posterior distribution for $N_P = 100000$ ensembles of pseudo-data and the LSU. The top-quark charge asymmetry $A_{C,t\bar{t}}$ is calculated using Equation 2.114. For details on the calculation of the top-quark charge asymmetry refer to Section 2.4.

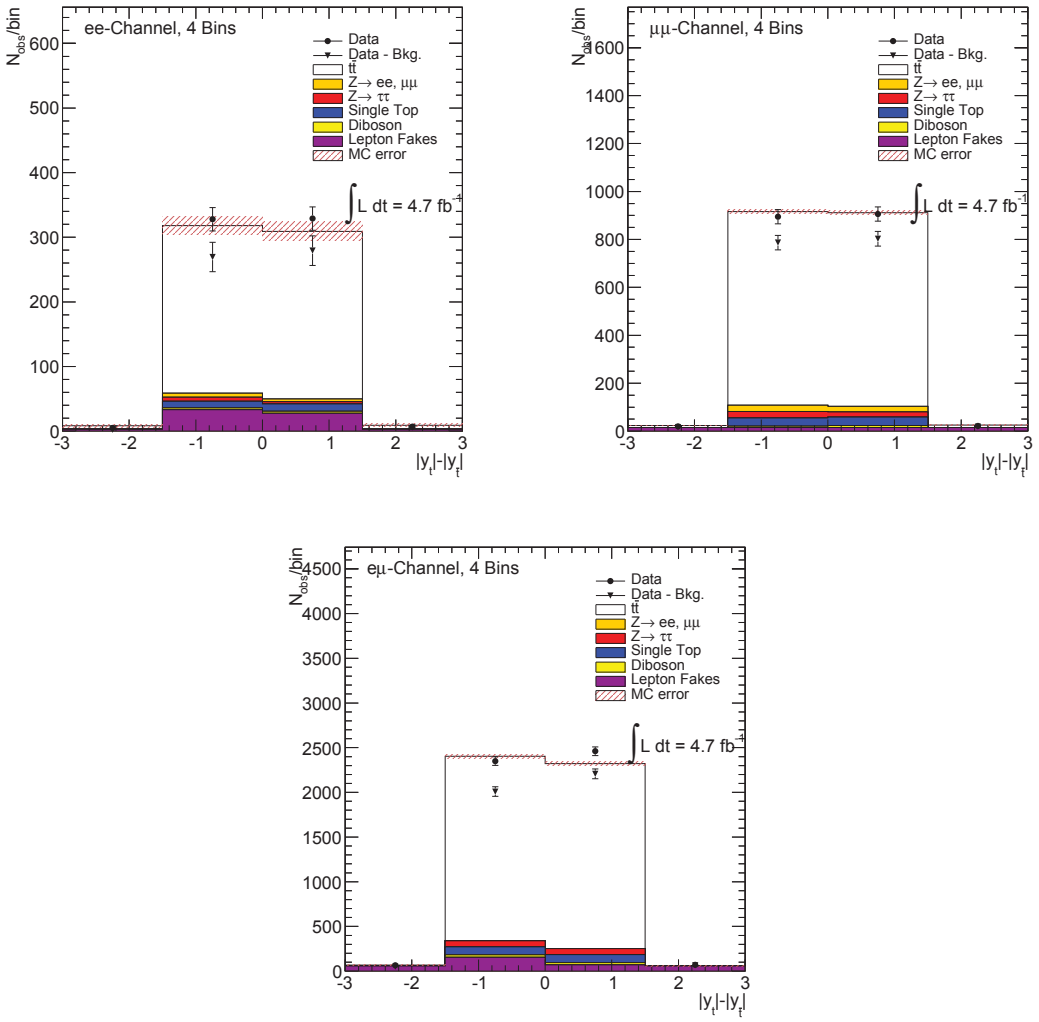

Figure 9.9.: The $\Delta\,|y_{t\bar{t}}| = |y_t| - |y_{\bar{t}}|$ distributions for the ATLAS 2011 7 TeV dataset (with and without bin-wise background subtraction), the MC@NLO signal MC and the background contributions ($Z \to (ee, \mu\mu, \tau\tau)$, single top, diboson and lepton fakes). The MC contributions are scaled to an integrated luminosity of $\int L\,dt = 4.71\,\mathrm{fb}^{-1}$. The events are selected according to the pretag event selection. The errors shown are statistical errors.

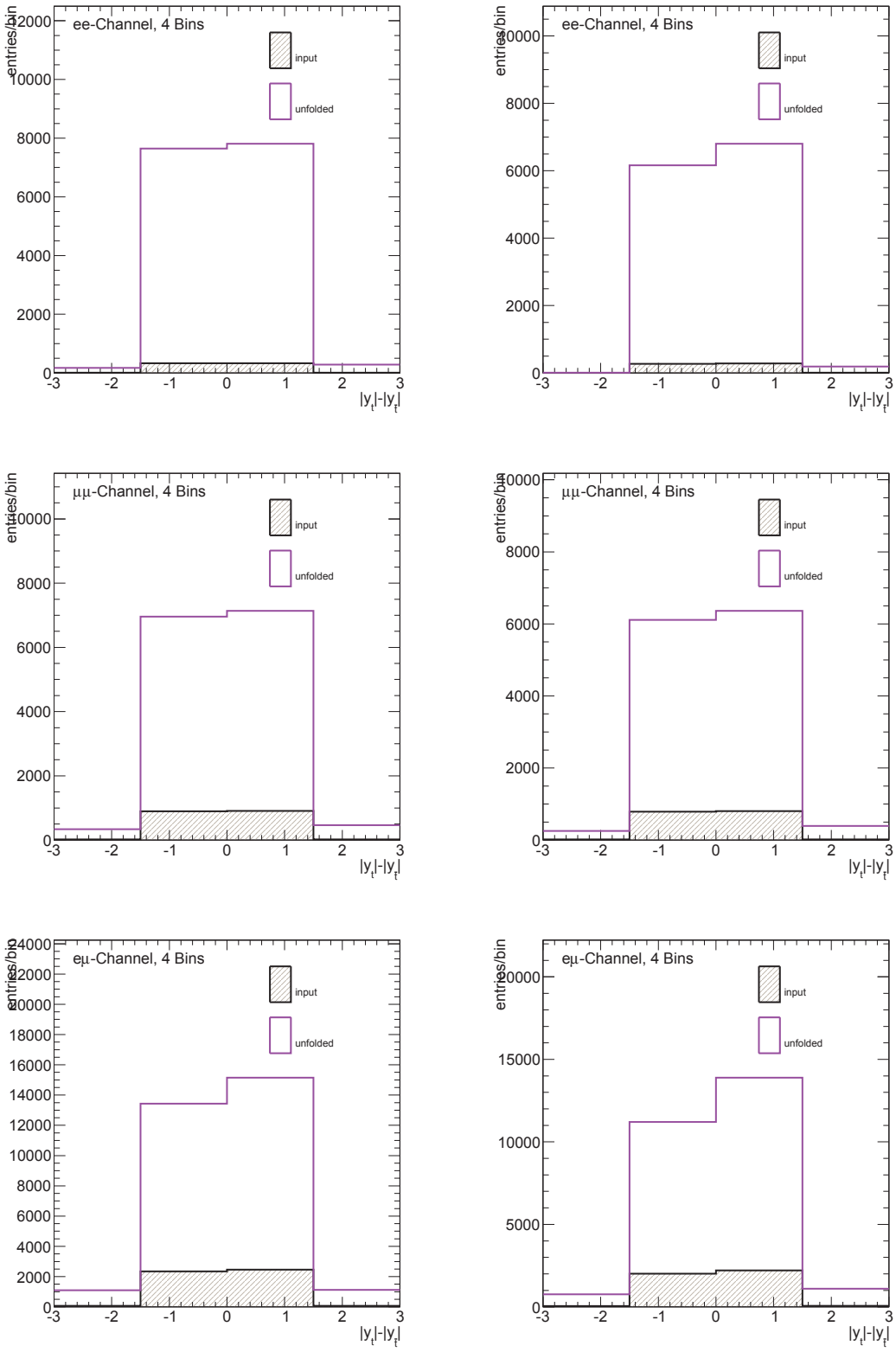

Figure 9.10.: The unfolded $\Delta|y_{t\bar{t}}| = |y_t| - |y_{\bar{t}}|$ distributions for the ATLAS 2011 7 TeV dataset with (left) and without (right) bin-wise background subtraction. The top, middle and bottom rows show the distributions for the dielectron, dimuon and electron-muon top-quark pair decay channels. The events are selected according to the pretag event selection.

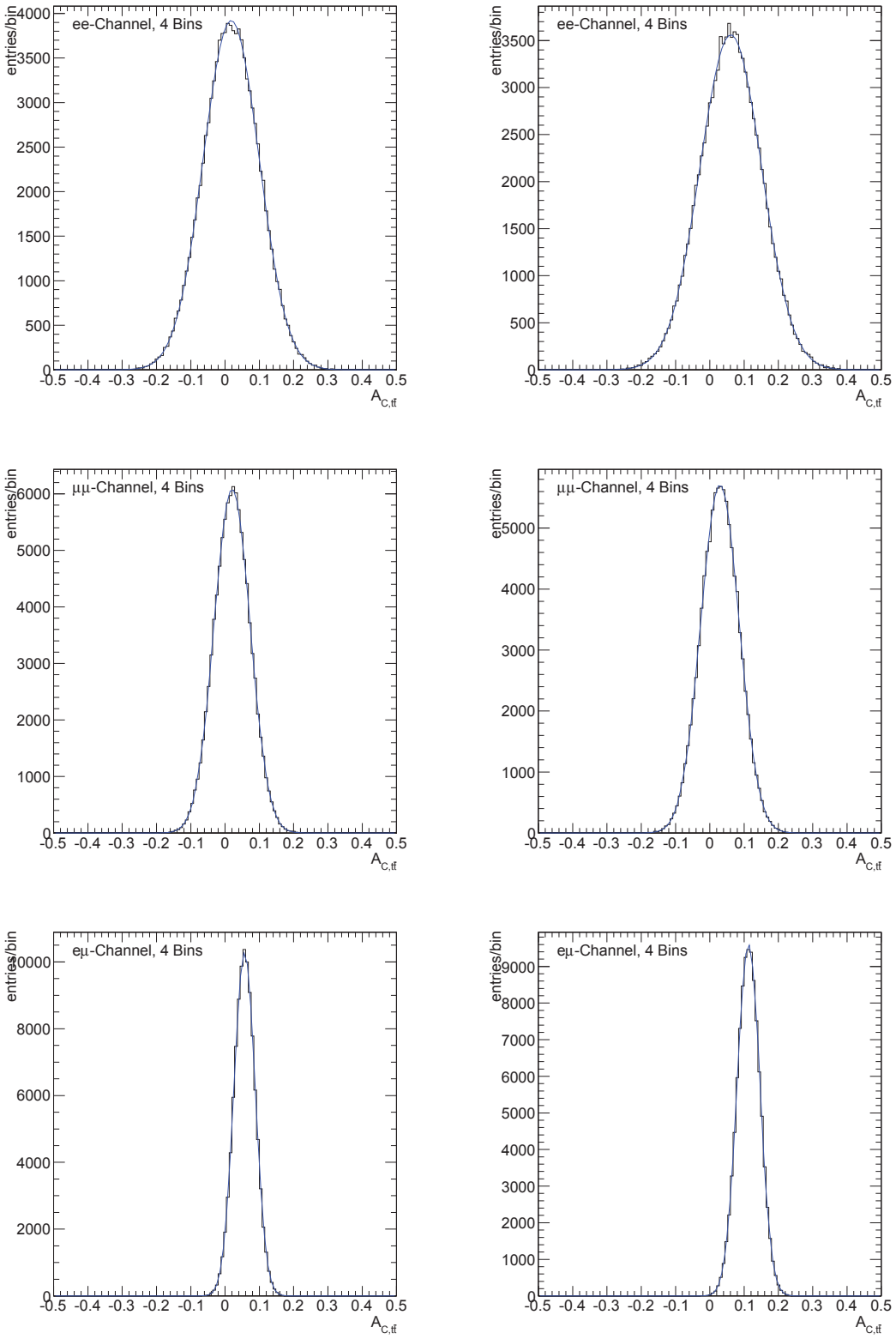

Figure 9.11.: The posterior distributions of $A_{C,t\bar{t}}^{\text{meas}}$ for $N_P = 100000$ ensembles of pseudo-data for the ATLAS 2011 7 TeV dataset with (left) and without (right) bin-wise background subtraction. The top, middle and bottom rows show the distributions for the dielectron, dimuon and electron-muon top-quark pair decay channels. The events are selected according to the pretag event selection. The errors shown are statistical errors.

Chapter 10

Systematic Uncertainties

In addition to the uncertainty arising from limited data statistics the measurement of the top-quark charge asymmetry is influenced by various systematic effects causing systematic errors. These effects are studied individually and separately for each channel and the pretag/tagged event selections. The corresponding systematic uncertainties on the top-quark charge asymmetry measurement are determined. The systematic uncertainties can be categorised in three categories.

- Generator modelling systematics.
- Detector modelling systematics.
- Background and luminosity systematics.

Depending on the modelled effect the analysis (described in Chapters 8 and 9) is performed using a modified (or different) training sample as input for the derivation of the detector response matrix and linear scaling (LS) correction. The modifications made on the training sample range from shifting one or more parameters within their uncertainties (e.g. jet energy resolution) before the object/event selection is applied to an event by event reweighting according to the uncertainty of the parton density function used. All uncertainties are derived for data with subtracted background. For the evaluation of systematic uncertainties related to generator modelling different $t\bar{t}$ samples are used as training input. These samples feature e.g. enhanced underlying event or varied initial and final state radiation contributions. In this chapter short descriptions of the systematic effects and the methods used to estimate the corresponding systematic uncertainties are given. All uncertainties are evaluated following the prescription of the ATLAS top working group for the analysis of data taken in 2011 [174].

10.1 Generator Modelling Systematics

Generator modelling systematics refer to uncertainties arising from e.g. the use of different MC generators or detector simulations. These systematics affect the $t\bar{t}$ Monte Carlo (MC) and therefore have an impact on the response matrix (and the linear scaling correction) used for the data unfolding process. In order to assess these uncertainties the analysis (KLFitter reconstruction, estimation of the LS and data unfolding) is repeated for different

$t\bar{t}$ training input samples. This results in one value of the unfolded top-quark charge asymmetry for each systematic. In contrast to the nominal data unfolding the unfolded charge asymmetry is determined by the mean of the posterior distribution for 100000 ensembles of pseudo data for the systematics evaluation. The linear scaling parameters, derived for the samples used, are shown in the Appendix G.4 in the Figures G.1 to G.5. A complete list of the different $t\bar{t}$ training input samples is given in the Appendix G.1. In the following details on the evaluation of the individual generator modelling systematics are presented. Table 10.1 lists the systematic uncertainties originating from generator modelling.

10.1.1 Monte Carlo Generator

This uncertainty describes the influence of the choice of the MC generator and parton showering algorithm. In order to obtain this uncertainty the analysis is performed using response matrices and LS corrections determined using different $t\bar{t}$ training input samples. The training input samples used are simulated with different MC generators, showering- and detector reconstruction algorithms. For details on the individual MC generators and algorithms refer to Chapter 6. The effect of the usage of different MC generators is determined by using the largest of the following three differences of the individually evaluated unfolded top-quark charge asymmetries as symmetric systematic uncertainty:

1. Difference between the FULLSIM POWHEG/PYTHIA and the MC@NLO $t\bar{t}$ signal sample.
2. Difference between the FULLSIM POWHEG/PYTHIA and the FULLSIM Alpgen sample.
3. Difference between the ATLFAST2 POWHEG/PYTHIA and the ATLFAST2 POWHEG/HERWIG + JIMMY sample.

The values of the three differences described above are listed in Table G.7.

10.1.2 Parton Shower and Fragmentation Model

The uncertainty originating from the use of different parton shower models is determined by the comparison of the measured top-quark charge asymmetry derived from ATLFAST2 POWHEG/PYTHIA and the ATLFAST2 POWHEG/HERWIG + JIMMY samples. This is equal to the evaluation of the third difference described in the previous section.

10.1.3 Initial and Final State Radiation Variation

Initial and final state radiation (ISR/FSR) describes jets induced by gluons which are radiated from the initial (final) state particles of the process under observation. Increased ISR/FSR leads to a greater amount of soft jets in the event. This can influence the event selection efficiency. More events pass the event selection due to a higher jet multiplicity. Furthermore, the initial radiation of gluons decreases the energy available for the top-quark pair production. In order to evaluate the uncertainty arising from ISR/FSR the analysis is performed using response matrices and LS corrections derived from samples with different

levels of ISR/FSR. The samples used are listed in the Appendix G. The uncertainty is then taken as half of the largest difference of the unfolded top-quark charge asymmetry between the nominal Alpgen sample and Alpgen samples with in- and decreased ISR/FSR (*radHi* and *radLo*). The absolute of the largest difference is then taken as symmetrical systematic uncertainty for ISR/FSR variation. The corresponding values of the differences of the unfolded top-quark charge asymmetries are listed in Table G.8.

10.1.4 Renormalisation and Factorisation

The effects of varied renormalisation and factorisation scales (RFSs) are studied by performing the analysis using response matrices and LS corrections derived from samples in which the RFSs are varied by a factor of 0.5 (2.0) of the default generator value. The uncertainty is then derived as the difference of the unfolded charge asymmetry between samples with RFSs shifted upwards (muup) and downwards (mudown). The differences determined using the muup and mudown samples are listed in Table G.9.

10.1.5 Colour Reconnection and Underlying Event

The uncertainty originating from colour reconnection (CR) is studied by using detector response matrices and LS corrections from two different POWHEG samples. One sample is simulated using the nominal PYTHIA setup and one sample using the Perugia2011 NO CR tune [175, p. 15] in which the CR is switched off [119, p. 75]. The CR related systematic uncertainty is determined as the difference between the unfolded charge asymmetry derived for the nominal sample and the sample without CR.
The systematic uncertainty arising from varying underlying event (UE) is determined analogously to the CR uncertainty using the nominal POWHEG sample and a sample with increased UE (*mpiHi*) (see Appendix G). The chosen variations in UE result in approximately 10% more or less activity w.r.t. the nominal values. For details see [119, p. 75]

10.1.6 Top-Quark Mass Variation

The KLFitter assumes a sharp prior for the top-quark pole mass ($m_t = 172.5\,\text{GeV}$). Hence, the influence of different top-quark masses on KLFitter reconstruction and unfolding has to be studied. The expected uncertainty is determined for five POWHEG/-PYTHIA samples featuring each a different top-quark mass in the range of $m_t = 167.5\,\text{GeV}$ to $m_t = 177.5\,\text{GeV}$. As described before a value of the unfolded top quark charge asymmetry is derived for each of these samples (using the corresponding response matrices and LS corrections). Then the differences of these values to the nominal unfolded top-quark charge asymmetry derived from the MC@NLO $t\bar{t}$-signal sample are calculated. These results are then scaled to the expected top-quark mass uncertainty of $0.8\,\text{GeV}$ ($m_t = 173.34 \pm 0.27\,(\text{stat}) \pm 0.71\,(\text{syst})$ GeV [176, p. 1]). The scaled results are used as symmetric systematic uncertainties. The differences between the unfolded top-quark charge asymmetry for the nominal top-quark mass $A_{C,t\bar{t}}^{\text{nom}}$ and the individual unfolded asymmetries derived for varied masses $A_{C,t\bar{t}}^{x}$ are listed in Table G.10.

10.1.7 Parton Density Function

The parton density function (PDF) determines the momentum fraction carried by the constituents of the colliding protons and hence the energy provided for the top-quark pair generation. The choice of the PDF and the corresponding uncertainty therefore has an impact on the top-quark charge asymmetry measurement [177], [178].
The influence of the choice of different PDFs on the analysis is determined by reweighting the nominal MC@NLO $t\bar{t}$-signal sample according to three different PDF sets. The reweighting is done on an event by event basis. The weights are calculated to simulate the impact of the three different PDF sets, CT10 [141], MWST2008nlo68cl [179] and NNPDF-20_100 [180]. Files containing the weights for different $t\bar{t}$-input samples are provided by the top working group [181].
The PDF event weight ω_{PDF} is calculated using the nominal momentum fractions of both initial state constituents $f_0\left(x_1, Q^2\right)$ and $f_0\left(x_2, Q^2\right)$ and the momentum fractions calculated using the new PDF set $f_1\left(x_1, Q^2\right)$ and $f_1\left(x_2, Q^2\right)$:

$$\omega_{\mathrm{PDF}} = \frac{f_1\left(x_1, Q^2\right)\ f_1\left(x_2, Q^2\right)}{f_0\left(x_1, Q^2\right)\ f_0\left(x_2, Q^2\right)}. \tag{10.1}$$

For each PDF a set of error PDFs is available to estimate the intra-PDF uncertainty [177], [178].

The overall PDF uncertainty is calculated according to the PDF4LHC working group [178] recommendation. For each of the PDF and error PDF sets a reweighted detector response matrix and the corresponding LS correction is determined. The analysis is then repeated using the modified response matrix (and LS correction) and the corresponding unfolded top-quark charge asymmetry is calculated. Then the upper and lower spread is determined. The upper (lower) spread is defined as the central asymmetry value with added (subtracted) half of the RMS of the asymmetry value distribution created using the results obtained from the error PDF sets. The distance between minimum and maximum of the spreads of all three PDF sets is called the envelope. The overall PDF uncertainty is defined as half of the envelope.

10.1.8 Summary of Generator Modelling Uncertainties

Table 10.1 summarises the results of the estimation of the generator related systematic uncertainties for the pretag and the tagged event selection. The MC generator uncertainty is determined by using the largest of the three differences listed in Table G.7 as systematic error. The uncertainty originating from ISR/FSR is taken as the largest value listed in Table G.8 and is then symmetrised. The RFS uncertainty is determined analogously to the ISR/FSR uncertainty, the corresponding values are taken from Table G.9. The scaled values σ_m stated in Table G.10 are used as the top-quark mass variation uncertainty. The systematic uncertainties are assumed to be uncorrelated and are therefore added in quadrature for the total estimate. Uncertainties smaller than 0.001 are neglected for the total uncertainty.

Systematic	ee-Channel	$\mu\mu$-Channel	$e\mu$-Channel
	Pretag:		
MC Generator	± 0.044	± 0.016	± 0.006
Parton Shower	± 0.003	± 0.016	± 0.005
ISR/FSR	± 0.003	± 0.002	± 0.002
RFS	± 0.015	± 0.003	± 0.001
CR	± 0.002	± 0.007	± 0.003
UE	± 0.002	± 0.004	<0.001
Mass variation	± 0.001	<0.001	± 0.001
PDF	± 0.001	± 0.004	± 0.003
Total	± 0.047	± 0.025	± 0.009
	≥ 1 b-tagged jet:		
MC Generator	± 0.023	± 0.016	± 0.005
Parton Shower	± 0.002	± 0.016	± 0.005
ISR/FSR	± 0.007	± 0.002	± 0.003
RFS	± 0.013	± 0.005	± 0.002
CR	± 0.004	± 0.005	± 0.001
UE	± 0.009	± 0.004	± 0.001
Mass variation	± 0.001	± 0.001	± 0.001
PDF	± 0.005	± 0.007	± 0.003
Total	± 0.030	± 0.025	± 0.009

Table 10.1.: Shown are the MC modelling systematics. The values are derived as described in Sections 10.1.1 through 10.1.7. The total MC modelling systematic is calculated as the quadratic sum of the systematics separately for each channel.

10.2 Detector Modelling Systematics

The detector description used in the simulation of ATLAS events deviates slightly from the real ATLAS detector. Therefore, corrections have to be applied to the reconstructed physics objects (as described in Chapter 5). The uncertainties of these corrections have to be taken into account as detector modelling systematic uncertainties.
The systematics related to the lepton physics objects are divided into trigger (reconstruction, identification) efficiency and momentum scale (resolution). The jet object uncertainties due to detector mis-modelling are divided into jet energy scale (JES), jet energy resolution (JER), jet reconstruction efficiency (JEFF) and jet vertex fraction uncertainties (JVF). Furthermore the effects of different pile-up conditions, different amounts of soft/cell-out jets and variations in the b-tagging scale factors are studied. The determination of the detector modelling systematics is done accordingly to the top working group recommendations [119].
The baseline method for the determination of detector modelling systematics is the following:

1. Shift the parameter, corresponding to the systematic under investigation, up- and downwards within its inherent uncertainty in the training sample and reconstruct the $t\bar{t}$-system using the KLFitter.

2. Create the response matrix and calculate the linear scaling correction separately for the up- and down-shift of the parameter. The plots G.6 to G.10 show the corresponding linear scaling corrections.

3. Perform the data unfolding using the response matrix and linear scaling correction determined in step two for $N_p = 100000$ ensembles of pseudodata.

4. Calculate the difference between the mean of the posterior distribution and the nominal measured top-quark charge asymmetry separately for the parameter shift up- and downwards.

5. Use the larger of both differences as symmetric systematic uncertainty.

The results for the up- and downwards-shift are symmetrised since the deviations to the nominal value for the upwards shifted parameter are not necessarily positive and the difference for the downwards shifted parameter negative, respectively. So the symmetrisation provides a conservative estimation of the systematic uncertainty. Details on the evaluation of the individual uncertainties are given in the following sections.

10.2.1 Jet Systematics

The jet systematics comprise a variety of different uncertainties. The corresponding uncertainties are listed in Tables G.11 and G.12.

- *Jet Energy Scale:* The JES uncertainty is evaluated by balancing the transverse momenta of dijets in proton-proton collisions at $\sqrt{s} = 7\,\text{TeV}$ using $34 \pm 4\,\text{pb}^{-1}$ of integrated luminosity. The deviations between data and MC are depending on the transverse momentum and the η region of the jet at hand. The differences range between 2% for jets with $p_T > 60\,\text{GeV}$ ($|\eta| < 2.8$) and 12% for jets is the extreme forward region $3.6 < |\eta| < 4.4$ [182, p. 1].

- *Jet Energy Resolution:* The JER agrees in data and MC [119, p. 12]. Hence no smearing is applied to the central values. For the determination of the systematic uncertainty the jets are smeared according to the systematic uncertainties derived from the resolution measurement in the full ATLAS 2011 dataset [119, p. 14].

- *Jet Reconstruction Efficiency:* The JEFF is derived using a tag and probe method. It is defined as the fraction of probe track-jets matched to a calorimeter jet. The difference between data and MC is accounted for by discarding a fraction of randomly selected jets within the inefficiency range [119, p. 14].

- *Jet Vertex Fraction:* To determine the JVF scale factors for efficiency and inefficiency are applied per event. The efficiency for a jet to satisfy the JVF requirement in the jet object selection (see Section 5.3.2) is measured in $Z\,(\rightarrow l^+l^- + \text{one add. parton})$ events in data and simulation. These events are divided into events enriched with hard-scatter jets and events enriched with pile-up jets. Efficiency and inefficiency scale factors are then calculated for both kinds of selected events [183, p. 27].

10.2.2 Lepton Systematics

The lepton related systematics comprise a range of different uncertainties. The corresponding uncertainties are listed in Tables G.13 and G.14.

- *Lepton Reconstruction Efficiency:* The mis-modelling of lepton trigger, reconstruction and selection efficiencies is corrected using scale factors. These scale factors are derived from efficiency measurements in data. The scale factors are derived according to the kinematics of leptons in $Z \rightarrow \mu\mu$ (ee) and $W \rightarrow e\nu$ events. The corresponding uncertainties are determined by variation of the lepton and signal selections. The uncertainties are of the order of 1% [119, pp. 75,76]. The corresponding uncertainty values are listed as EL_RECO (electrons) and MU_RECO (muons).

- *Lepton Identification and Trigger:* The lepton reconstruction, identification and trigger efficiency are corrected by scale factors in order to match data and MC efficiencies (see Section 6.4.4). The scale factors are estimated using a tag and probe method on $Z \rightarrow \mu\mu$ (ee) data and MC. The differences in the efficiencies between data and MC are in the order of a few percent. [183, p. 27]. For the estimation of the systematic uncertainty the corresponding scale factor is shifted within its uncertainty. The results are listed as EL_TRIGGER_SF (electrons) and MU_TRIGGER_SF (muons).

- *Electron Energy Scale and Resolution:* The electron energy scale and resolution is corrected in both data and MC, hence the systematic uncertainties originating from the applied scaling and resolution smearing have to be studied. The uncertainties are measured in $Z \rightarrow ee$ and $J/\Psi \rightarrow ee$ events of the 2010 ATLAS dataset [112, p. 7]. The ratio between the reconstructed and the true electron energy is found to be in the range of 1% of unity, while the energy resolution ranges from 2% to 3% depending on the η-region [112, p. 7]. The results are listed as EL_ENERGY_SC and EL_ENERGY_RES.

- *Muon Momentum Scale and Resolution:* The lepton momentum scale and resolution is measured in $Z \rightarrow l^+l^-$ events. Scale factors and uncertainties are derived to match MC to the measured distributions in data [119, p. 76]. The corresponding difference

is listed as MU_SCALE. For muons the momentum resolution is measured separately in the inner detector and the muon spectrometer. The systematic uncertainty is then derived by varying the inner detector and muon spectrometer components separately up- and downwards. The uncertainty is half of the difference between the maximum and minimum unfolded top-quark charge asymmetry derived for the varied components [174]. These differences are listed as MU_MS (spectrometer component variation) and MU_ID (inner detector component variation).

10.2.3 Miscellaneous Detector Modelling Systematics

Deviations in the detector modelling also affect the measurement of missing energy and the bottom-quark tagging performance. The corresponding uncertainties are listed in Table G.15.

- *Missing Energy:* The measurement of the missing energy is influenced by the uncertainties propagated from the pile-up corrections. The pile-up uncertainty accounts for a missing energy uncertainty of 6.6% [174]. Furthermore, uncertainties originating from contributions of calorimeter cells which are not associated to any jets and contributions from soft jets are estimated (CELL_OUT/SOFTJET). Soft jets are jets in a p_T range of $(7 \leq p_T \leq 20)$ GeV.
- *Bottom-Quark Tagging:* The bottom-quark tagging efficiencies and fake rates are measured in single- and dileptonic top-quark pair decays. The efficiencies are measured by application of a kinematic fit or cut and count methods. These measurements are used to create tagging scale factors, which are applied on an event by event basis (see Section 6.4.4). The total uncertainties on the scale factors range from 5% to 15% for a jet p_T in the range of $(25 \leq p_T \leq 300)$ GeV [184, p. 1].

10.2.4 Summary Detector Modelling Systematics

The Tables 10.2 and 10.3 summarise the results of the estimation of the systematic uncertainties related to detector modelling effects for the pretag and the tagged event selection, respectively. The systematic uncertainties are assumed to be uncorrelated and are therefore added in quadrature for the total estimate. Uncertainties smaller than 0.001 are neglected for the total uncertainty.

Systematic	ee-Channel	$\mu\mu$-Channel	$e\mu$-Channel
	Pretag:		
JES	±0.002	±0.002	±0.001
JER	±0.001	±0.002	±0.003
JEFF	±0.005	±0.001	<0.001
JVF	±0.003	±0.001	±0.001
EL_ENERGY_RES	±0.007	±0.002	±0.001
EL_ENERGY_SC	±0.005	±0.001	-0.001
EL_RECO	±0.003	±0.002	±0.001
EL_TRIGGER_SF	±0.003	±0.002	±0.001
MU_MS/MU_ID	<0.001	±0.002	±0.001
MU_SCALE	±0.003	±0.003	±0.002
MU_RECO_SF	±0.004	±0.001	±0.001
MU_TRIGGER_SF	±0.004	±0.001	<0.001
PILEUP	±0.009	±0.002	±0.004
CELL_OUT/SOFTJET	±0.035	±0.019	±0.003
BTAG_SF	±0.003	±0.002	±0.001
Total	±0.039	±0.020	±0.006

Table 10.2.: Shown are the detector modelling systematics. The values are derived as described in Sections 10.2.1 to 10.2.3. The total detector modelling systematic is calculated as the quadratic sum of the systematics separately for each channel.

Systematic	ee-Channel	$\mu\mu$-Channel	$e\mu$-Channel
	≥ 1 b-tagged jet:		
JES	±0.014	±0.001	±0.004
JER	±0.011	±0.001	±0.003
JEFF	±0.016	±0.002	±0.003
JVF	±0.014	±0.007	±0.003
EL_ENERGY_RES	±0.015	±-0.007	±0.004
EL_ENERGY_SC	±0.013	±-0.007	±0.003
EL_RECO	±0.014	±-0.007	±0.003
EL_TRIGGER_SF	±0.014	±-0.007	±0.003
MU_MS/MU_ID	±0.001	±-0.002	±0.002
MU_SCALE	±0.014	±0.001	±0.003
MU_RECO_SF	±0.014	±0.007	±0.003
MU_TRIGGER_SF	±0.015	±0.007	±0.003
PILEUP	±0.018	±0.003	±0.004
CELL_OUT/SOFTJET	±0.050	±0.019	±0.003
BTAG_SF	±0.015	±-0.007	±0.004
Total	±0.072	±0.028	±0.013

Table 10.3.: Shown are the detector modelling systematics. The values are derived as described in Sections 10.2.1 to 10.2.3. The total detector modelling systematic is calculated as the quadratic sum of the systematics separately for each channel.

10.3 Background and Luminosity Systematics

The background estimation in this analysis heavily relies on MC, since only the fake lepton contribution can be determined using a data driven method (see Section 7.2). The MC backgrounds are normalised to the corresponding theoretical cross sections (see Chapter 6). Hence the uncertainty of the theoretical prediction has to be taken into account as systematic uncertainty on the MC normalisation. The shape of the MC backgrounds is not varied. For the estimation of the fake lepton background uncertainty the real and fake efficiency rates (see Equation 7.4) are separately varied within their uncertainties. Then the fake lepton background is derived separately for each of the varied real and fake efficiencies. The systematic uncertainty on the luminosity of the ATLAS 2011 dataset measurement is 1.8%. It is determined using van der Meer scans [185], [186], [187]. The systematic luminosity uncertainty is found to be < 0.001 and is therefore not stated in the summary tables.

10.3.1 Monte Carlo Background Normalisation Uncertainty

In order to obtain the systematic error originating from the MC background the normalisation of the MC backgrounds is varied. This is done separately according to the uncertainty on the theoretical prediction of the cross section. These varied backgrounds are then (bin-by-bin) subtracted from the data and the unfolding procedure is applied. Then the mean of the posterior distribution is derived. The largest absolute difference of the mean of the posterior distribution and the nominal top-quark charge asymmetry value (for one normalisation shifted up- and downwards) is then used as the symmetric systematic uncertainty.

- *Single Top:* The single top background is normalised to the NNLO order cross section. The uncertainty on the prediction is 7%, [174], [45], [46], [47].
- *Z-Boson:* The background originating from Z-boson production with additional partons is normalised to the NNLO cross section. The uncertainty at the inclusive level is 4%. For each required jet another 24% are added in quadrature to the inclusive uncertainty. The event selection used in this analysis requires two jets. Hence the uncertainty for the Z-boson background normalisation is 34% [174], [188].
- *Diboson:* The diboson MC background is normalised to NLO. The normalisation of the diboson background comprises an inclusive uncertainty of 5% with an additional 24% for each jet required in the event selection. This leads to a total normalisation uncertainty of 34% [174].

The detailed results for the estimation of the MC background normalisation uncertainty are listed in Tables G.16 and G.17, the results are summarised in Tables 10.4 and 10.5.

10.3.2 Fake Lepton Background Uncertainty

The fake lepton background uncertainty is derived by variation of the real and fake efficiency rates in the data driven background estimation method. The real and fake efficiencies are modified separately for muons and electrons. The unfolding procedure is then applied to data with subtracted modified lepton fake background. The difference of the posterior distribution to the nominal charge asymmetry value is calculated for each systematic efficiency shift (up- and downwards). The largest difference determined for an up-/downwards shift of the efficiencies is then taken as symmetric systematic uncertainty. The correlation between real and fake efficiencies is negligible [189], hence the contributions of fake and real efficiency variations are added in quadrature for the full fake lepton background uncertainty. Tables G.18 and G.19 list the detailed differences. Tables 10.4 and 10.5 show the systematic uncertainties originating from the fake lepton background variation.

10.3.3 Summary Background and Luminosity Systematics

The Tables 10.4 and 10.5 summarise the results of the estimation of the systematic uncertainties related to MC- and fake-lepton background normalisation uncertainties for the pretag and the tagged event selection, respectively. The systematic uncertainties are assumed to be uncorrelated and are therefore added in quadrature for the total estimate.

Uncertainties smaller than 0.001 are neglected for the total uncertainty.

Systematic	ee-Channel	$\mu\mu$-Channel	$e\mu$-Channel
	Pretag:		
ST_NORM	± 0.001	± 0.001	± 0.002
DB_NORM	± 0.001	< 0.001	± 0.003
ZJETS_NORM	± 0.007	± 0.005	± 0.004
MU_REAL_EFF	± 0.009	± 0.005	± 0.004
MU_FAKE_EFF	± 0.015	± 0.005	± 0.020
EL_REAL_EFF	± 0.011	± 0.002	± 0.011
EL_FAKE_EFF	± 0.007	± 0.002	± 0.003
Total	± 0.023	± 0.010	± 0.025

Table 10.4.: Shown are the systematic uncertainties originating from Monte Carlo and fake-lepton normalisation uncertainties. The values are derived according to Section 10.3.1. The total background systematic is calculated as the quadratic sum of the systematics separately for each channel.

Systematic	ee-Channel	$\mu\mu$-Channel	$e\mu$-Channel
	≥ 1 b-tagged jet:		
ST_NORM	± 0.007	± 0.001	± 0.002
DB_NORM	± 0.007	< 0.001	± 0.001
ZJETS_NORM	± 0.008	± 0.002	± 0.002
MU_REAL_EFF	± 0.003	± 0.002	± 0.016
MU_FAKE_EFF	± 0.008	<0.001	± 0.010
EL_REAL_EFF	± 0.026	± 0.003	± 0.009
EL_FAKE_EFF	± 0.005	± 0.004	± 0.019
Total	± 0.031	± 0.006	± 0.028

Table 10.5.: Shown are the systematic uncertainties originating from Monte Carlo and fake-lepton normalisation uncertainties. The values are derived according to Section 10.3.1. The total background systematic is calculated as the quadratic sum of the systematics separately for each channel.

10.4 Summary Systematic Uncertainties

A summary of the systematic uncertainties for the top-quark charge asymmetry measurement is shown in Tables 10.6 and 10.7. The individual uncertainties are added in quadrature to obtain the total systematic error. The largest contributions to the total systematic error are given by the MC generator uncertainty, the renormalisation and factorisation scale (dielectron channel) and the variation of the soft jet and cell out ratios (CELL_OUT/SOFTJET). The variation of the cell out term leads to changes in the calculation of the missing transverse energy and therefore migrates to the KLFitter reconstruction of the top-quark kinematic system. The KLFitter assumes a sharp prior for the top-quark mass in order to calculate the solutions for the unknown neutrino momenta. Hence variations of the top-quark mass influence the result of the reconstruction process.

Systematic	ee-Channel	$\mu\mu$-Channel	$e\mu$-Channel
MC Generator	±0.044	±0.016	±0.006
Parton Shower	±0.003	±0.016	±0.005
ISR/FSR	±0.003	±0.002	±0.002
RFS	±0.015	±0.003	±0.001
CR	±0.002	±0.007	±0.003
UE	±0.002	±0.004	<0.001
Mass variation	±0.001	<0.001	±0.001
PDF	±0.001	±0.004	±0.003
JES	±0.002	±0.002	±0.001
JER	±0.001	±0.002	±0.003
JEFF	±0.005	±0.001	<0.001
JVF	±0.003	±0.001	±0.001
EL_ENERGY_RES	±0.007	±0.002	±0.001
EL_ENERGY_SC	±0.005	±0.001	±0.001
EL_RECO	±0.003	±0.002	±0.001
EL_TRIGGER_SF	±0.003	±0.002	±0.001
MU_MS/MU_ID	<0.001	±0.002	±0.001
MU_SCALE	±0.003	±0.003	±0.002
MU_RECO_SF	±0.004	±0.001	±0.001
MU_TRIGGER_SF	±0.004	±0.001	<0.001
PILEUP	±0.009	±0.002	±0.004
CELL_OUT/SOFTJET	±0.035	±0.019	±0.003
BTAG_SF	±0.003	±0.002	±0.001
ST_NORM	±0.001	±0.001	±0.002
DB_NORM	±0.001	< 0.001	±0.003
ZJETS_NORM	±0.007	±0.005	±0.004
MU_REAL_EFF	±0.009	±0.005	±0.004
MU_FAKE_EFF	±0.015	±0.005	±0.020
EL_REAL_EFF	±0.011	±0.002	±0.011
EL_FAKE_EFF	±0.007	±0.002	±0.003
Total	±0.067	±0.034	±0.027

Table 10.6.: Shown are the systematic uncertainties derived for the top-quark charge asymmetry measurement for the pretag event selection. The total systematic uncertainty is calculated as the quadratic sum of the systematics separately for each channel.

Systematic	ee-Channel	$\mu\mu$-Channel	$e\mu$-Channel
MC Generator	± 0.023	± 0.016	± 0.005
Parton Shower	± 0.002	± 0.016	± 0.005
ISR/FSR	± 0.007	± 0.002	± 0.003
RFS	± 0.013	± 0.005	± 0.002
CR	± 0.004	± 0.005	± 0.001
UE	± 0.009	± 0.004	± 0.001
Mass variation	± 0.001	± 0.001	<0.001
PDF	± 0.005	± 0.007	± 0.003
JES	± 0.014	± 0.001	± 0.004
JER	± 0.011	± 0.001	± 0.003
JEFF	± 0.016	± 0.002	± 0.003
JVF	± 0.014	± 0.007	± 0.003
EL_ENERGY_RES	± 0.015	± 0.007	± 0.004
EL_ENERGY_SC	± 0.013	± 0.007	± 0.003
EL_RECO	± 0.014	± 0.007	± 0.003
EL_TRIGGER_SF	± 0.014	± 0.007	± 0.003
MU_MS/MU_ID	± 0.001	± 0.002	± 0.002
MU_SCALE	± 0.014	± 0.001	± 0.003
MU_RECO_SF	± 0.014	± 0.007	± 0.003
MU_TRIGGER_SF	± 0.015	± 0.007	± 0.003
PILEUP	± 0.018	± 0.003	± 0.004
CELL_OUT/SOFTJET	± 0.050	± 0.019	± 0.003
BTAG_SF	± 0.015	± 0.007	± 0.004
ST_NORM	± 0.007	± 0.001	± 0.002
DB_NORM	± 0.007	< 0.001	± 0.001
ZJETS_NORM	± 0.008	± 0.002	± 0.002
MU_REAL_EFF	± 0.003	± 0.002	± 0.016
MU_FAKE_EFF	± 0.008	<0.001	± 0.010
EL_REAL_EFF	± 0.026	± 0.003	± 0.009
EL_FAKE_EFF	± 0.005	± 0.004	± 0.019
Total	± 0.084	± 0.038	± 0.032

Table 10.7.: Shown are the systematic uncertainties derived for the top-quark charge asymmetry measurement for the tagged event selection. The total systematic uncertainty is calculated as the quadratic sum of the systematics separately for each channel.

Chapter 11

Summary and Outlook

A measurement of the top-quark charge asymmetry $A_{C,t\bar{t}}$ is presented in this thesis. The measurement was performed on the ATLAS dataset which was recorded in 2011 at a centre of mass energy of $\sqrt{s} = 7\,\text{TeV}$. The amount of data analysed corresponds to an integrated luminosity of $\mathcal{L}_{\text{int}} = 4.71\,\text{fb}^{-1}$. The measurement is performed separately for the three $t\bar{t}$ dileptonic decay channels.

In order to enhance the signal an event selection scheme is employed requiring exactly two leptons, at least two jets and a large amount of missing transverse energy. An additional selection stage requires that at least one of the selected jets is tagged by the MV1 tagging algorithm. The results of the pretag and tagged event selection are presented separately. The kinematic system of the top-quark pair is reconstructed using a kinematic likelihood fitter (KLFitter). The resulting distribution of the absolute rapidity difference of the top- and antitop-quark, $\Delta\,|y_{t\bar{t}}| = |y_t| - |y_{\bar{t}}|$, is corrected for background contributions using Monte Carlo and data driven background estimates. The background subtracted $\Delta\,|y_{t\bar{t}}|$ distribution is then unfolded using Bayesian iterative unfolding to correct for detector and acceptance effects. After the application of the unfolding procedure the top-quark charge asymmetry is derived from the $\Delta\,|y_{t\bar{t}}|$ distribution. The results for the measured top-quark charge asymmetry are cross-checked using a different unfolding technique (singular value decomposition). The measured top-quark charge asymmetries for the three decay channels are combined using the best linear unbiased estimator (BLUE). For details on the application of the BLUE method refer to Appendix H. The individual values of the top-quark charge asymmetries for the three channels are listed in Tables 11.1 and 11.2.

Channel	$A_{C,t\bar{t}}^{\text{pretag}}$
ee	$0.062 \pm 0.128\,(\text{stat.}) \pm 0.067\,(\text{syst.})$
$\mu\mu$	$0.030 \pm 0.072\,(\text{stat.}) \pm 0.034\,(\text{syst.})$
$e\mu$	$0.113 \pm 0.049\,(\text{stat.}) \pm 0.027\,(\text{syst.})$

Table 11.1.: Listed are the top-quark charge asymmetry measurements for the pretag event selection and their statistical and systematic uncertainties.

Channel	$A_{C,t\bar{t}}^{\text{tagged}}$
ee	$0.034 \pm 0.151\,(\text{stat.}) \pm 0.084\,(\text{syst.})$
$\mu\mu$	$-0.023 \pm 0.074\,(\text{stat.}) \pm 0.038\,(\text{syst.})$
$e\mu$	$0.094 \pm 0.051\,(\text{stat.}) \pm 0.032\,(\text{syst.})$

Table 11.2.: Listed are the top-quark charge asymmetry measurements for the tagged event selection and their statistical and systematic uncertainties.

After the combination of the measurements from the three separate dileptonic $t\bar{t}$-decay channels the top-quark charge asymmetry (for the pretag event selection) is determined to be

$$A_{C,t\bar{t}}^{\text{pretag}} = 0.085 \pm 0.039\,(\text{stat.}) \pm 0.025\,(\text{syst.}). \tag{11.1}$$

The combined top-quark charge asymmetry for the tagged event selection is calculated to be

$$A_{C,t\bar{t}}^{\text{tagged}} = 0.055 \pm 0.041\,(\text{stat.}) \pm 0.029\,(\text{syst.}). \tag{11.2}$$

The measurements agree with the Standard Model prediction [1, p. 11] of

$$A_{C,t\bar{t}}^{\text{theory}} = 0.0123 \pm 0.0005. \tag{11.3}$$

The obtained results are dominated by the corresponding statistical errors. The statistical uncertainties are more than a factor three larger than the SM predicted value of the top-quark charge asymmetry. For an observation of the charge asymmetry a much larger dataset is needed. Further improvements to harden the analysis w.r.t. systematic effects can be achieved by improving the background estimation techniques. The requirement of an additional bottom-tagged jet shifts the central value of the charge asymmetry to lower values (compared to the pretag selection). This is due to the fact that the tagging requirement further suppresses the background contribution of the non fake lepton background. The subtraction of the background MC and fake lepton background introduces a large shift in the central value of the reconstructed charge asymmetry in all three decay channels (see Table 8.3). The difference between the statistical error in the two event selections is marginal so that the inclusion of a b-tagging requirement improves measurements of the top-quark charge asymmetry. The recent measurement could be used to exclude models that predict a much larger asymmetry than the SM expectation.

The dileptonic $t\bar{t}$ decay channel is a promising channel for the top-quark charge asymmetry measurement. The ATLAS 8 TeV dataset recorded in 2012 features a significantly larger statistic of approximately $\mathcal{L}_{\text{int}} = 20.3\,\text{fb}^{-1}$ and a 1.4 times larger cross section of $\sigma_{t\bar{t}} = 252.89^{+13.30}_{-14.52}$ pb [37], [38]. This increases the amount of data which can be used for this analysis by a factor of six. With larger statistics differential measurements and measurements in different top-quark pair mass bins are also possible for the dileptonic decay channel.
Another factor that can improve the measurement is the unfolding method. Fully Bayesian unfolding (FBU) [190] was recently successfully implemented in the measurement of the top-quark charge asymmetry in the single lepton decay channel [191, p. 7] and can be

adopted for use in the dilepton charge asymmetry measurement. In FBU regularisation is achieved by the choice of a regularisation function and a regularisation strength. For the Bayesian iterative approach chosen in this analysis regularisation is achieved by limiting the number of iterative steps. If too few iterations are performed the unfolded result is biased by the prior, which in this case is the truth $\Delta|y_{t\bar{t}}|$ distribution of the MC training sample. If too many iterative steps are performed, fluctuations in the statistical errors may appear. In FBU, a regularisation function can be chosen in a way that smooth distributions are favoured while the strength of the regularisation is handled separately. In the analysis of the single lepton decay channel a curvature function is used [191, p. 9]. An improvement in the unfolding method can also influence the statistical error since it is derived as the width of the posterior distribution from a number of ensembles of pseudo data. An unfolding method with a less wide posterior distribution would therefore improve the statistical error as well.

Appendices

Appendix A

Monte Carlo Samples

Both signal and background processes use a consistent set of cross-sections for SM processes and higher order Quantum Chromodynamics (QCD) corrections, which are expressed as k-factors [127, p. 3].

A.1 Top Quark Samples

The $t\bar{t}$ cross section for pp collisions at a centre-of-mass energy of $\sqrt{s} = 7\,\text{TeV}$ is $\sigma_{t\bar{t}} = 177^{+10}_{-11}$ pb for a top quark mass of $172.5\,\text{TeV}/c^2$. It has been calculated at next-to-next-to leading order (NNLO) in QCD including resummation of next-to-next-to-leading logarithmic (NNLL) soft gluon terms with top++2.0 [37], [38], [192], [193], [194], [195].
The PDF and α_S uncertainties were calculated using the PDF4LHC prescription [177] with the MSTW2008 68% CL NNLO [196], [197], CT10 NNLO [141], [198] and NNPDF2.3 5f FFN [199] PDF sets, added in quadrature to the scale uncertainty. The NNLO+NNLL value, as implemented in Hathor 1.5 [143], is about 3% larger than the exact NNLO prediction.

DSID	Description	Matrix Element	Parton Shower	XSec [pb]	k-factor
105200	$t\bar{t}$ No Full Hadronic (e, μ, τ)	MC@NLO	HERWIG	79.01	1.219
117360	t-channel $\rightarrow e\nu$	ACERMC	PYTHIA	8.06	0.865
117361	t-channel $\rightarrow \mu\nu$	ACERMC	PYTHIA	8.06	0.865
117362	t-channel $\rightarrow \tau\nu$	ACERMC	PYTHIA	8.06	0.865
108343	s-channel $\rightarrow e\nu$	MC@NLO	HERWIG/JIMMY	0.47	1.064
108344	s-channel $\rightarrow \mu\nu$	MC@NLO	HERWIG/JIMMY	0.47	1.064
108345	s-channel $\rightarrow \tau\nu$	MC@NLO	HERWIG/JIMMY	0.47	1.064
108346	$Wt \rightarrow$ incl.	MC@NLO	HERWIG	14.59	1.079

A.2 Z Boson Production samples with Additional Partons

These Z+jets samples have been generated with dileptons in the invariant mass range of $40\,\text{GeV} < \text{M}_{ll} < 2000\,\text{GeV}$, These Z+jets cross sections are normalised to the next-to-

next-to leading order production cross section value passed in [150] in the $40\,\text{GeV} < M_{ll} < 2000\,\text{GeV}$ [200].

DSID	Description	Matrix Element	Parton Shower	XSec [pb]	k-factor
107650	$Zee + \text{Np0}$	ALPGEN	HERWIG/JIMMY	668.32	1.25
107651	$Zee + \text{Np1}$	ALPGEN	HERWIG/JIMMY	134.36	1.25
107652	$Zee + \text{Np2}$	ALPGEN	HERWIG/JIMMY	40.54	1.25
107653	$Zee + \text{Np3}$	ALPGEN	HERWIG/JIMMY	11.16	1.25
107654	$Zee + \text{Np4}$	ALPGEN	HERWIG/JIMMY	2.88	1.25
107655	$Zee + \text{Np5}$	ALPGEN	HERWIG/JIMMY	0.83	1.25
107660	$Z\mu\mu + \text{Np0}$	ALPGEN	HERWIG/JIMMY	668.68	1.25
107661	$Z\mu\mu + \text{Np1}$	ALPGEN	HERWIG/JIMMY	134.14	1.25
107662	$Z\mu\mu + \text{Np2}$	ALPGEN	HERWIG/JIMMY	40.33	1.25
107663	$Z\mu\mu + \text{Np3}$	ALPGEN	HERWIG/JIMMY	11.19	1.25
107664	$Z\mu\mu + \text{Np4}$	ALPGEN	HERWIG/JIMMY	2.75	1.25
107665	$Z\mu\mu + \text{Np5}$	ALPGEN	HERWIG/JIMMY	0.77	1.25
107670	$Z\tau\tau + \text{Np0}$	ALPGEN	HERWIG/JIMMY	668.40	1.25
107671	$Z\tau\tau + \text{Np1}$	ALPGEN	HERWIG/JIMMY	134.81	1.25
107672	$Z\tau\tau + \text{Np2}$	ALPGEN	HERWIG/JIMMY	40.36	1.25
107673	$Z\tau\tau + \text{Np3}$	ALPGEN	HERWIG/JIMMY	11.25	1.25
107674	$Z\tau\tau + \text{Np4}$	ALPGEN	HERWIG/JIMMY	2.79	1.25
107675	$Z\tau\tau + \text{Np5}$	ALPGEN	HERWIG/JIMMY	0.77	1.25

These Z+jets samples have been generated with dileptons in the invariant mass range of $10\,\text{GeV} < M_{ll} < 40\,\text{GeV}$ (LM) [200].

DSID	Description	Matrix Element	Parton Shower	XSec [pb]	k-factor
116250	$Zee + \text{Np0}\,(\text{LM})$	ALPGEN	HERWIG/JIMMY	3055.20	1.25
116251	$Zee + \text{Np1}\,(\text{LM})$	ALPGEN	HERWIG/JIMMY	84.92	1.25
116252	$Zee + \text{Np2}\,(\text{LM})$	ALPGEN	HERWIG/JIMMY	41.40	1.25
116253	$Zee + \text{Np3}\,(\text{LM})$	ALPGEN	HERWIG/JIMMY	8.38	1.25
116254	$Zee + \text{Np4}\,(\text{LM})$	ALPGEN	HERWIG/JIMMY	1.85	1.25
116255	$Zee + \text{Np5}\,(\text{LM})$	ALPGEN	HERWIG/JIMMY	0.46	1.25
116260	$Z\mu\mu + \text{Np0}\,(\text{LM})$	ALPGEN	HERWIG/JIMMY	3054.90	1.25
116261	$Z\mu\mu + \text{Np1}\,(\text{LM})$	ALPGEN	HERWIG/JIMMY	84.87	1.25
116262	$Z\mu\mu + \text{Np2}\,(\text{LM})$	ALPGEN	HERWIG/JIMMY	41.45	1.25
116263	$Z\mu\mu + \text{Np3}\,(\text{LM})$	ALPGEN	HERWIG/JIMMY	8.38	1.25
116264	$Z\mu\mu + \text{Np4}\,(\text{LM})$	ALPGEN	HERWIG/JIMMY	1.85	1.25
116265	$Z\mu\mu + \text{Np5}\,(\text{LM})$	ALPGEN	HERWIG/JIMMY	0.46	1.25
116270	$Z\tau\tau + \text{Np0}\,(\text{LM})$	ALPGEN	HERWIG/JIMMY	3055.10	1.25
116271	$Z\tau\tau + \text{Np1}\,(\text{LM})$	ALPGEN	HERWIG/JIMMY	84.93	1.25
116272	$Z\tau\tau + \text{Np2}\,(\text{LM})$	ALPGEN	HERWIG/JIMMY	41.47	1.25
116273	$Z\tau\tau + \text{Np3}\,(\text{LM})$	ALPGEN	HERWIG/JIMMY	8.36	1.25
116274	$Z\tau\tau + \text{Np4}\,(\text{LM})$	ALPGEN	HERWIG/JIMMY	1.85	1.25
116275	$Z\tau\tau + \text{Np5}\,(\text{LM})$	ALPGEN	HERWIG/JIMMY	0.46	1.25

These Z+heavy quarks+jets samples have been generated with dileptons in the invariant

mass range of $30\,\text{GeV} < \text{M}_{ll} < 10000\,\text{GeV}$ [200].

DSID	Description	Matrix Element	Parton Shower	XSec [pb]	k-factor
109300	$Zee + bb + \text{Np0}$	ALPGEN	HERWIG/JIMMY	6.57	1.25
109301	$Zee + bb + \text{Np1}$	ALPGEN	HERWIG/JIMMY	2.48	1.25
109302	$Zee + bb + \text{Np2}$	ALPGEN	HERWIG/JIMMY	0.89	1.25
109303	$Zee + bb + \text{Np3}$	ALPGEN	HERWIG/JIMMY	0.39	1.25
109305	$Z\mu\mu + bb + \text{Np0}$	ALPGEN	HERWIG/JIMMY	6.56	1.25
109306	$Z\mu\mu + bb + \text{Np1}$	ALPGEN	HERWIG/JIMMY	2.47	1.25
109307	$Z\mu\mu + bb + \text{Np2}$	ALPGEN	HERWIG/JIMMY	0.89	1.25
109308	$Z\mu\mu + bb + \text{Np3}$	ALPGEN	HERWIG/JIMMY	0.39	1.25
109310	$Z\tau\tau + bb + \text{Np0}$	ALPGEN	HERWIG/JIMMY	6.57	1.25
109311	$Z\tau\tau + bb + \text{Np1}$	ALPGEN	HERWIG/JIMMY	2.49	1.25
109312	$Z\tau\tau + bb + \text{Np2}$	ALPGEN	HERWIG/JIMMY	0.89	1.25
109313	$Z\tau\tau + bb + \text{Np3}$	ALPGEN	HERWIG/JIMMY	0.39	1.25

A.3 Diboson Samples

DSID	Description	Matrix Element	Parton Shower	XSec [pb]	k-factor
105985	WW	HERWIG	HERWIG	11.5003	1.48
105986	ZZ	HERWIG	HERWIG	0.9722	1.30
105987	WZ	HERWIG	HERWIG	3.4641	1.60

Appendix B

Event Yields

B.1 Signal Monte Carlo Event Yields

In Table B.1 the event yields of the signal MC after each cut of the event selection are shown.

Cut	ee-Channel Event Yield	$\mu\mu$-Channel Event Yield	$e\mu$-Channel Event Yield
0	11545700.00 ± 11337.32	11545700.00 ± 11337.32	11545700.00 ± 11337.32
1	327954.50 ± 651.80	342943.66 ± 665.55	669805.13 ± 930.26
2	266871.91 ± 587.15	275324.53 ± 596.40	545467.50 ± 838.76
3	266675.59 ± 586.94	275185.63 ± 596.26	545094.81 ± 838.50
4	266675.59 ± 586.94	275185.63 ± 596.26	545094.81 ± 838.50
5	43773.16 ± 236.83	123776.27 ± 399.47	149817.61 ± 437.71
6	43773.16 ± 236.83	123480.91 ± 398.98	149798.45 ± 437.67
7	43773.16 ± 236.83	123480.91 ± 398.98	149798.45 ± 437.67
8	43293.38 ± 235.54	122019.82 ± 396.61	148015.45 ± 435.05
9	22622.67 ± 169.64	67970.31 ± 295.11	140497.84 ± 423.39
10	17734.44 ± 150.94	53482.55 ± 262.46	115154.86 ± 384.76
11	17728.23 ± 150.92	53475.57 ± 262.44	115137.32 ± 384.73
12	17599.84 ± 150.34	53473.13 ± 262.42	114637.30 ± 383.88
13	17504.56 ± 149.83	53013.76 ± 261.15	114637.30 ± 383.88
14	14713.56 ± 137.72	44978.57 ± 240.83	114637.30 ± 383.88
15	14575.07 ± 137.09	44978.57 ± 240.83	114186.45 ± 383.10
16	14575.07 ± 137.09	44978.57 ± 240.83	114186.45 ± 383.10
17	12359.53 ± 125.89	37967.86 ± 220.94	96622.87 ± 352.09

Table B.1.: This table shows the event yields (with statistical errors) for the $t\bar{t}$ non full hadronic signal MC as described in Section 6.3, the event yields take into account the scaling factors described in Section 6.4.4.

Cut	ee-Channel Event Yield	Eff.	$\mu\mu$-Channel Event Yield	Eff.	$e\mu$-Channel Event Yield	Eff.
0	453635.1 ± 445.5		453635.1 ± 445.5		453635.1 ± 445.5	
1	12885.5 ± 25.6	100.0%	13474.7 ± 26.2	100.0%	26317.2 ± 36.6	100.0%
2	10485.5 ± 23.1	81.4%	10817.6 ± 23.4	80.3%	21431.8 ± 32.9	81.4%
3	10477.8 ± 23.1	81.3%	10812.1 ± 23.4	80.2%	21417.2 ± 32.9	81.4%
4	10477.8 ± 23.1	81.3%	10812.1 ± 23.4	80.2%	21417.2 ± 32.9	81.4%
5	1719.9 ± 9.3	13.4%	4863.2 ± 15.7	36.1%	5886.5 ± 17.2	22.4%
6	1719.9 ± 9.3	13.4%	4851.6 ± 15.7	36.0%	5885.7 ± 17.2	22.4%
7	1719.9 ± 9.3	13.4%	4851.6 ± 15.7	36.0%	5885.7 ± 17.2	22.4%
8	1701.0 ± 9.3	13.2%	4794.2 ± 15.6	35.6%	5815.7 ± 17.1	22.1%
9	888.9 ± 6.7	6.9%	2670.6 ± 11.6	19.8%	5520.3 ± 16.7	21.0%
10	696.8 ± 5.9	5.4%	2101.3 ± 10.3	15.6%	4524.5 ± 15.1	17.2%
11	696.5 ± 5.9	5.4%	2101.1 ± 10.3	15.6%	4523.8 ± 15.2	17.2%
12	691.5 ± 5.9	5.4%	2100.9 ± 10.3	15.6%	4504.2 ± 15.1	17.1%
13	687.8 ± 5.9	5.3%	2082.9 ± 10.3	15.5%	4504.2 ± 15.1	17.1%
14	578.1 ± 5.4	4.5%	1767.2 ± 9.5	13.1%	4504.2 ± 15.1	17.1%
15	572.7 ± 5.9	4.4%	1767.2 ± 9.5	13.1%	4486.5 ± 15.1	17.1%
16	572.7 ± 5.4	4.4%	1767.2 ± 9.5	13.1%	4486.5 ± 15.1	17.1%
17	485.6 ± 4.9	3.4%	1491.8 ± 8.7	11.1%	3796.4 ± 13.1	4.4%

Table B.2.: Event yields with statistical errors and selection efficiencies for the $t\bar{t}$ non full hadronic signal MC as described in Section 6.3. The event yields take into account the scaling factors described in Section 6.4.4. The event yields are scaled to an integrated luminosity of $\mathcal{L}_{\text{int}} = 4.71\,\text{fb}^{-1}$.

B.2 Comparison of Data with Monte Carlo and Fake Lepton Background, Pretag

The data and Monte Carlo (MC) event yields and shapes of various reconstructed event properties, are compared to ensure that the MC mimics the data correctly (for details on MC scaling see Section 6.4.4). Table B.3 shows a comparison of the MC event yields with applied scaling factors (luminosity and MC scaling) and the data event yields. A good agreement between data and MC including fake lepton background is observed in the event yields and also in the shapes of the distributions shown in the control plots.

Channel	ee-Channel	$\mu\mu$-Channel	$e\mu$-Channel
Monte Carlo sig.:			
$t\bar{t}$	572.66 ± 5.39	1767.23 ± 9.46	4486.43 ± 15.05
Monte Carlo bkg.:			
$Z \to ee, (\mu\mu)$	19.04 ± 1.71	74.00 ± 3.70	2.62 ± 0.55
$Z \to \tau\tau$	15.25 ± 1.67	62.64 ± 3.48	161.36 ± 5.56
Single Top	28.31 ± 1.81	82.07 ± 2.98	215.01 ± 4.78
Diboson	8.70 ± 0.66	23.01 ± 1.05	67.50 ± 1.77
Data driven bkg.:			
Fake Lepton (FL)	80.01 ± 8.94	30.73 ± 5.54	256.35 ± 16.01
Total (MC + FL)	723.98 ± 10.88	2039.60 ± 12.49	5189.28 ± 23.24
Data	726	2005	5273

Table B.3.: This table shows the event yields for MC, fake lepton background and data in all three dilepton decay channels for the pretag event selection. MC scaling factors are applied and MC event yields are scaled to an integrated luminosity of $\mathcal{L}_{\text{int}} = 4.71\,\text{fb}^{-1}$. For the data event yields the following data streams are used: EGamma Stream for the ee- and $e\mu$-Channel, Muon Stream for the $\mu\mu$-Channel. The errors shown are statistical only and are added in quadrature for the total.

The following distributions of lepton (pseudorapidity, transverse momentum, pair mass, azimuth), jet (pseudorapidity, transverse momentum, multiplicity, azimuth) and event (H_T, $\not{E}$) properties are shown separately for the three dilepton decay channels for the pretag event selection (according to Section 7.1).

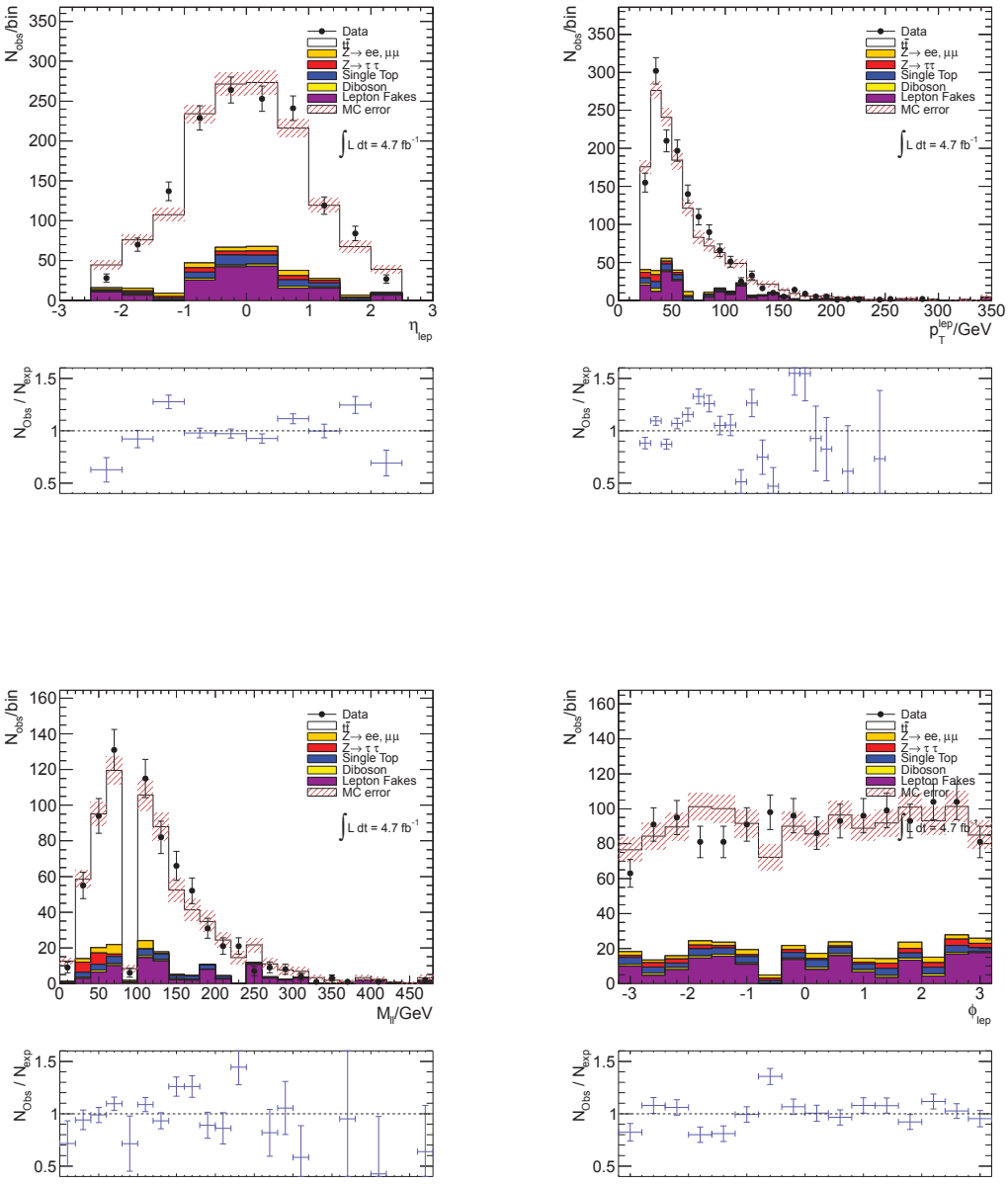

Figure B.1.: Lepton η (top left) and p_T (top right) distributions (lepton and antilepton combined). Invariant dilepton mass (bottom left) and lepton ϕ (bottom right) distributions. Data, MC- and fake lepton background selected according to the the pretag event selection in the *ee*-channel. The lower pads of the plots show the ratio between observed events in data (N_{obs}) and events expected from signal MC, background MC and fake lepton background (N_{exp}). All MC scale factors are applied and MC samples are scaled to an integrated luminosity of $\int L\,dt = 4.71\,\text{fb}^{-1}$.

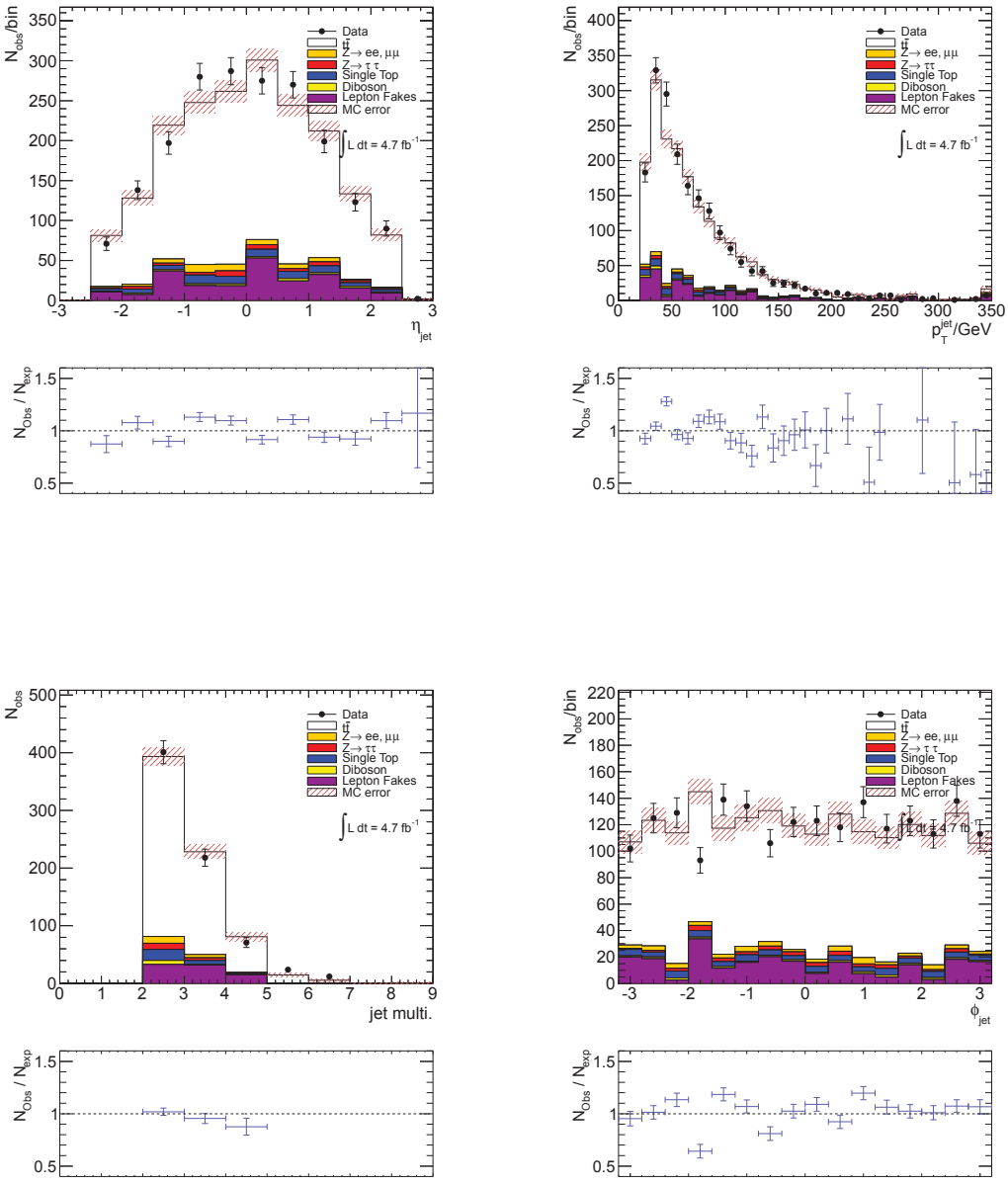

Figure B.2.: Jet η (top left) and p_T (top right) distributions. Jet multiplicity (bottom left) and ϕ (bottom right) distributions. Data, MC- and fake lepton background selected according to the the pretag event selection in the *ee*-channel. The lower pads of the plots show the ratio between observed events in data (N_{obs}) and events expected from signal MC, background MC and fake lepton background (N_{exp}).All MC scale factors are applied and MC samples are scaled to an integrated luminosity of $\int L\,dt = 4.71\,\mathrm{fb}^{-1}$.

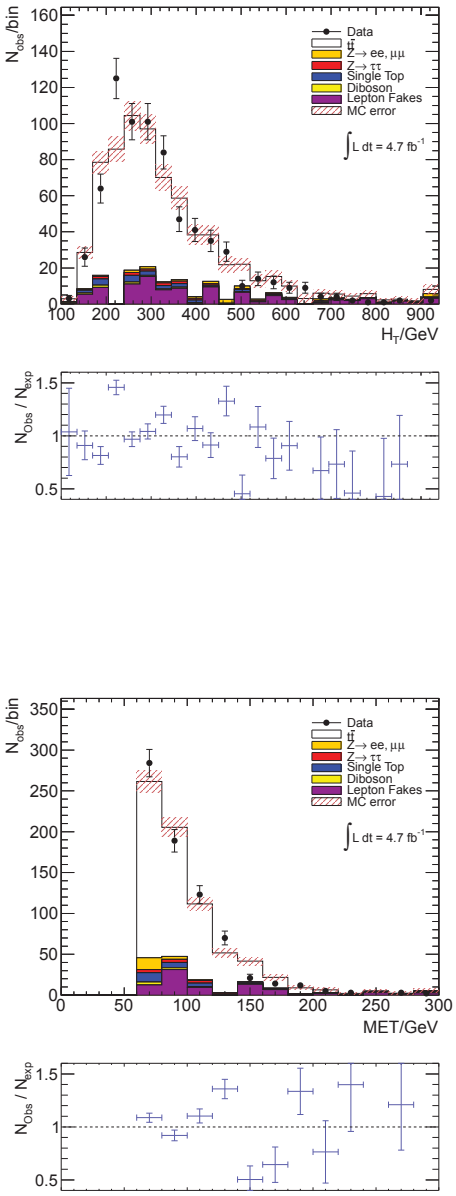

Figure B.3.: H_T (top) and $\not\!\!E$ (bottom) distributions. Data, MC- and fake lepton background selected according to the the pretag event selection in the *ee*-channel. The lower pads of the plots show the ratio between observed events in data (N_{obs}) and events expected from signal MC, background MC and fake lepton background (N_{exp}). All MC scale factors are applied and MC samples are scaled to an integrated luminosity of $\int L\,dt = 4.71\,\mathrm{fb}^{-1}$.

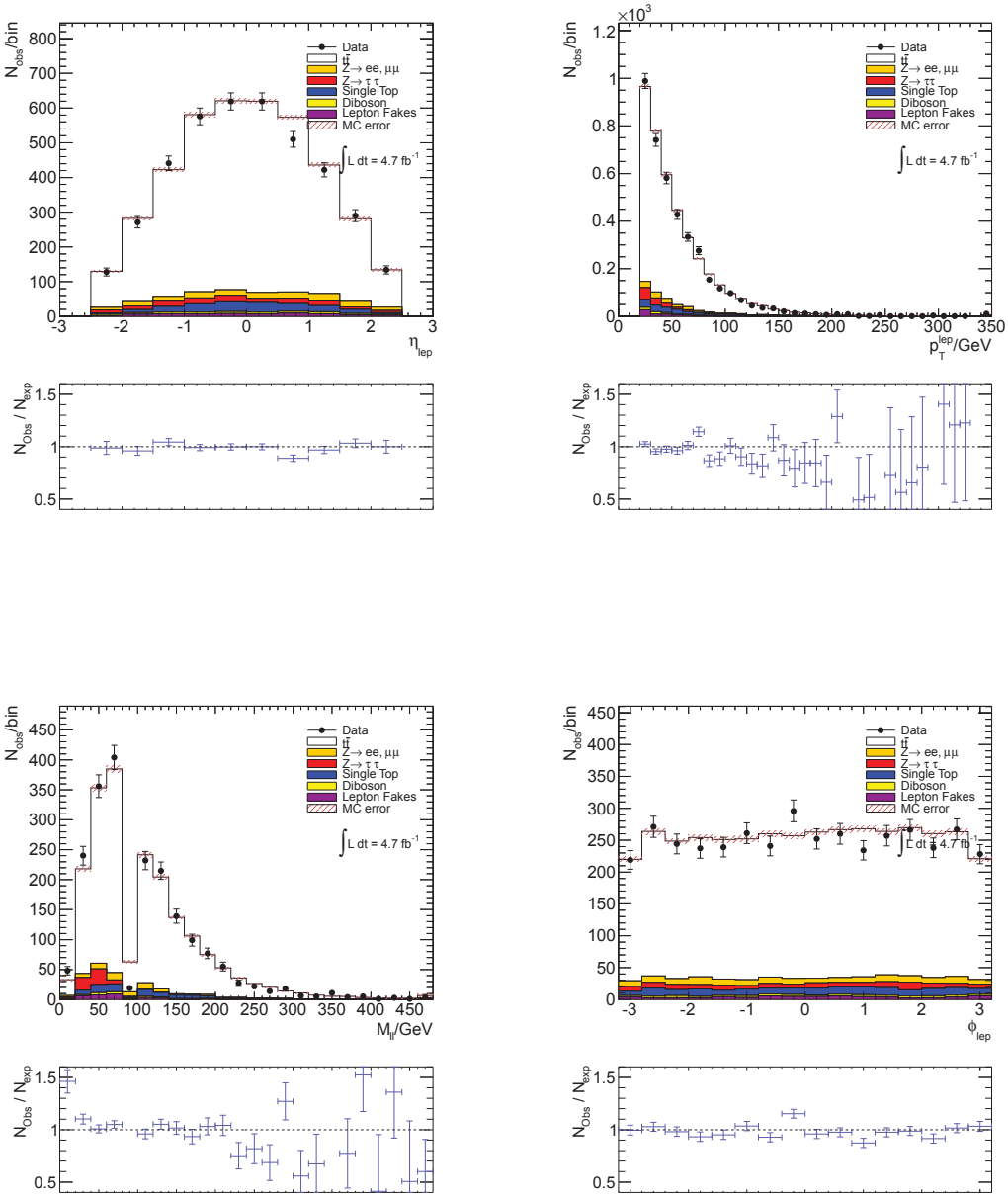

Figure B.4.: Lepton η (top left) and p_T (top right) distributions (lepton and antilepton combined). Invariant dilepton mass (bottom left) and lepton ϕ (bottom right) distributions. Data, MC- and fake lepton background selected according to the the pretag event selection in the $\mu\mu$-channel. The lower pads of the plots show the ratio between observed events in data (N_{obs}) and events expected from signal MC, background MC and fake lepton background (N_{exp}). All MC scale factors are applied and MC samples are scaled to an integrated luminosity of $\int L\,dt = 4.71\,\text{fb}^{-1}$.

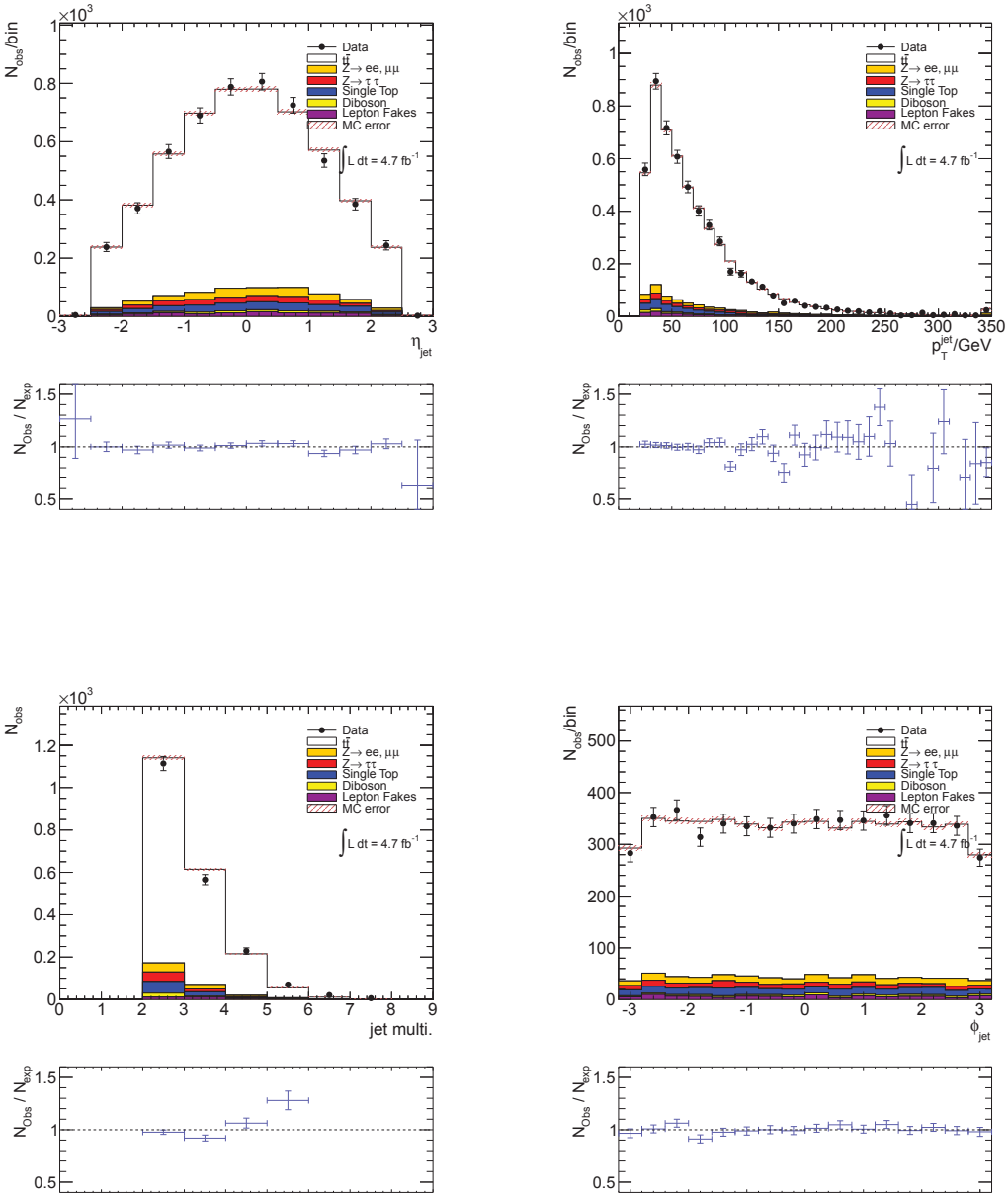

Figure B.5.: Jet η (top left) and p_T (top right) distributions. Jet multiplicity (bottom left) and ϕ (bottom right) distributions. Data, MC- and fake lepton background selected according to the the pretag event selection in the $\mu\mu$-channel. The lower pads of the plots show the ratio between observed events in data (N_{obs}) and events expected from signal MC, background MC and fake lepton background (N_{exp}). All MC scale factors are applied and MC samples are scaled to an integrated luminosity of $\int L\,dt = 4.71\,\text{fb}^{-1}$.

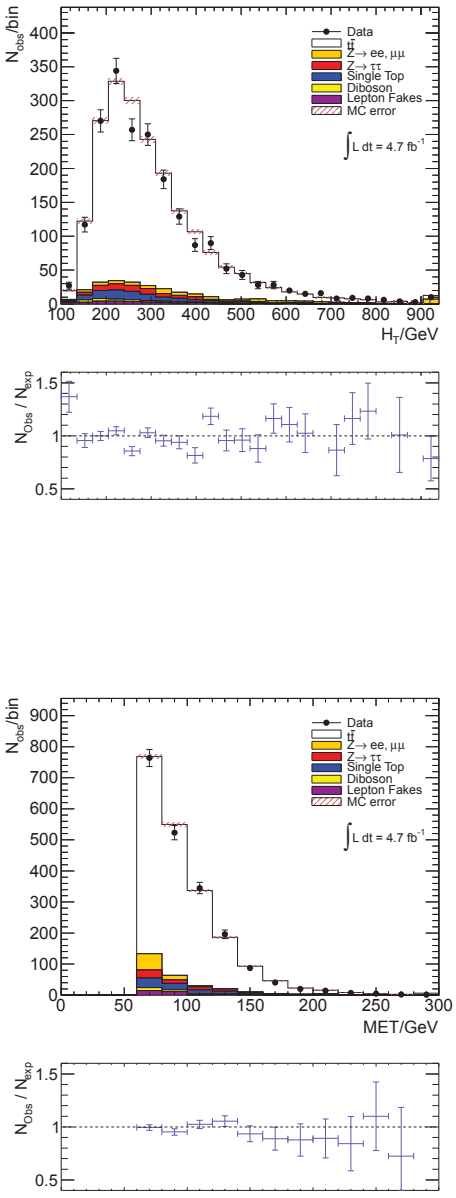

Figure B.6.: H_T (top) and $\not\!\!E$ (bottom) distributions. Data, MC- and fake lepton background selected according to the the pretag event selection in the $\mu\mu$-channel. The lower pads of the plots show the ratio between observed events in data (N_{obs}) and events expected from signal MC, background MC and fake lepton background (N_{exp}). All MC scale factors are applied and MC samples are scaled to an integrated luminosity of $\int L\,dt = 4.71\,\mathrm{fb}^{-1}$.

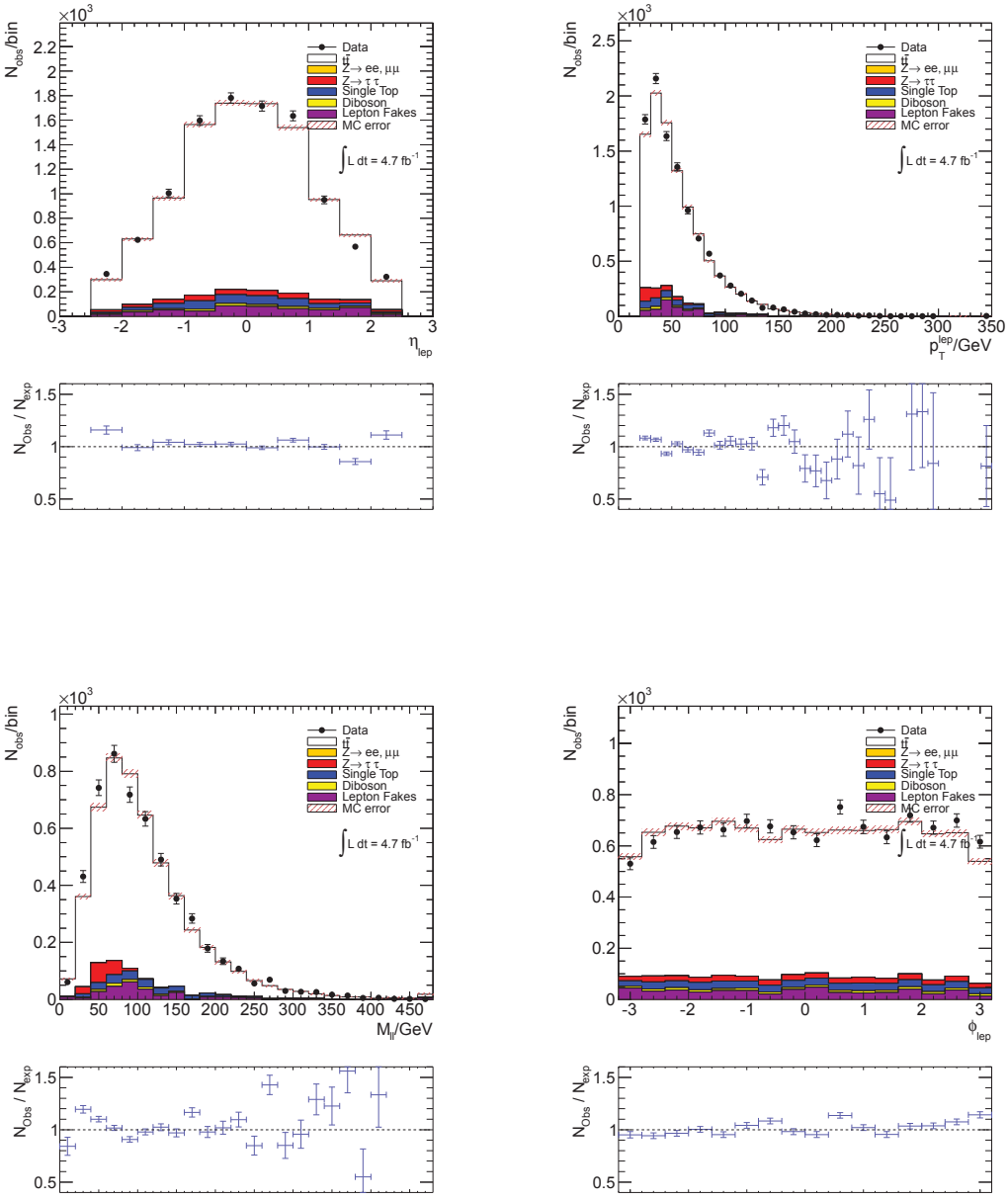

Figure B.7.: Lepton η (top left) and p_T (top right) distributions (lepton and antilepton combined). Invariant dilepton mass (bottom left) and lepton ϕ (bottom right) distributions. Data, MC- and fake lepton background selected according to the the pretag event selection in the $e\mu$-channel. The lower pads of the plots show the ratio between observed events in data (N_{obs}) and events expected from signal MC, background MC and fake lepton background (N_{exp}). All MC scale factors are applied and MC samples are scaled to an integrated luminosity of $\int L\,dt = 4.71\,\text{fb}^{-1}$.

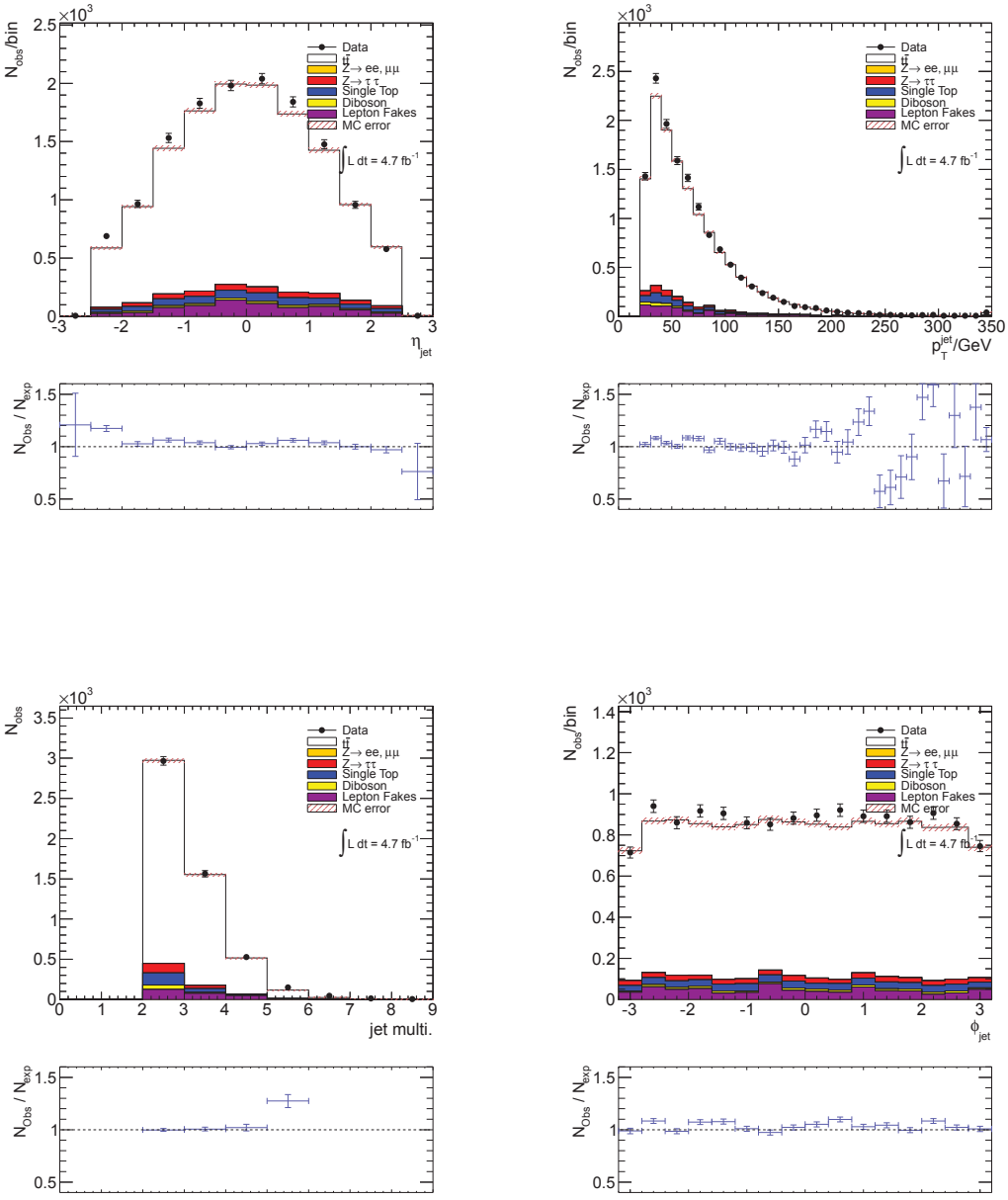

Figure B.8.: Jet η (top left) and p_T (top right) distributions. Jet multiplicity (bottom left) and ϕ (bottom right) distributions. Data, MC- and fake lepton background selected according to the the pretag event selection in the $e\mu$-channel. The lower pads of the plots show the ratio between observed events in data (N_{obs}) and events expected from signal MC, background MC and fake lepton background (N_{exp}). All MC scale factors are applied and MC samples are scaled to an integrated luminosity of $\int L\,dt = 4.71\,\text{fb}^{-1}$.

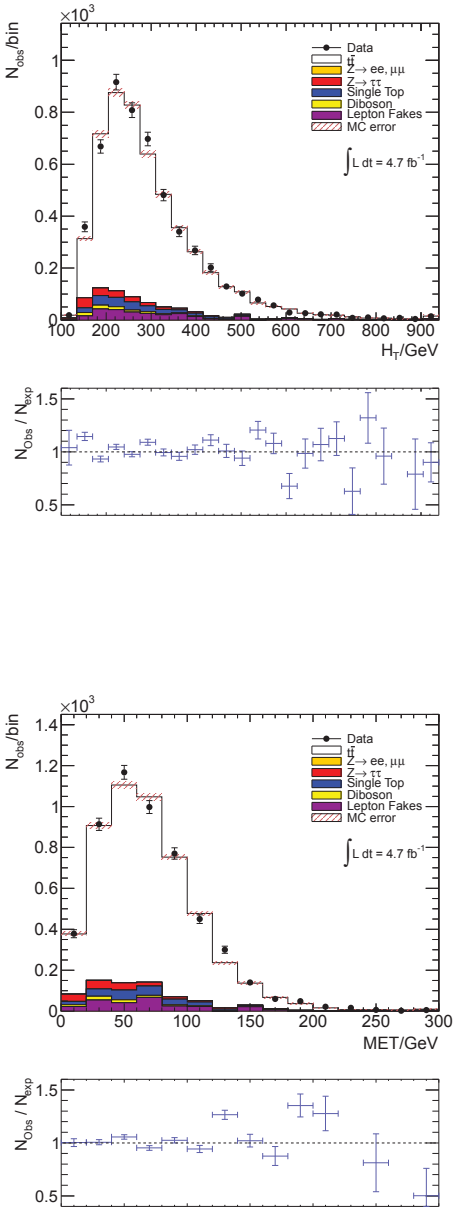

Figure B.9.: H_T (top) and $\not\!\!E$ (bottom) distributions. Data, MC- and fake lepton background selected according to the the pretag event selection in the $e\mu$-channel. The lower pads of the plots show the ratio between observed events in data (N_{obs}) and events expected from signal MC, background MC and fake lepton background (N_{exp}). All MC scale factors are applied and MC samples are scaled to an integrated luminosity of $\int L\,dt = 4.71\,\text{fb}^{-1}$.

B.3 Comparison of Data with Monte Carlo and Fake Lepton Background, Tagged

The data and Monte Carlo (MC) event yields and shapes of various reconstructed event properties, are compared to ensure that the MC mimics the data correctly (for details on MC scaling see Section 6.4.4). Table B.4 shows a comparison of the MC event yields with applied scaling factors (luminosity and MC scaling) and the data event yields. A good agreement between data and MC including fake lepton background is observed in the event yields and also in the shapes of the distributions shown in the control plots.

Channel	ee-Channel	$\mu\mu$-Channel	$e\mu$-Channel
Monte Carlo sig.:			
$t\bar{t}$	485.61 ± 4.95	1491.77 ± 8.68	3796.35 ± 13.83
Monte Carlo bkg.:			
$Z \to ee, (\mu\mu)$	2.91 ± 0.65	11.51 ± 1.40	0.37 ± 0.20
$Z \to \tau\tau$	1.38 ± 0.45	5.50 ± 0.95	15.19 ± 1.66
Single Top	21.03 ± 1.56	61.22 ± 2.57	162.12 ± 4.14
Diboson	0.56 ± 0.15	2.23 ± 0.38	4.23 ± 0.44
Data driven bkg.:			
Fake Lepton (FL)	67.24 ± 8.20	21.87 ± 4.68	204.68 ± 14.31
Total (MC + FL)	578.73 ± 9.74	1594.10 ± 10.34	4182.95 ± 20.40
Data	571	1556	4303

Table B.4.: This table shows the event yields for MC, fake lepton background and data in all three dilepton decay channels for the tagged event selection. MC scaling factors are applied and MC event yields are scaled to an integrated luminosity of $\int L\,dt = 4.71\,\mathrm{fb}^{-1}$. For the data event yields the following data streams are used: EGamma Stream for the ee- and $e\mu$-Channel, Muon Stream for the $\mu\mu$-Channel. The errors shown are statistical only and are added in quadrature for the total.

The following distributions of lepton (pseudorapidity, transverse momentum, pair mass, azimuth), jet (pseudorapidity, transverse momentum, multiplicity, azimuth) and event (H_T, $\not{E}$) properties are shown separately for the three dilepton decay channels for the pretag event selection (according to Section 7.1).

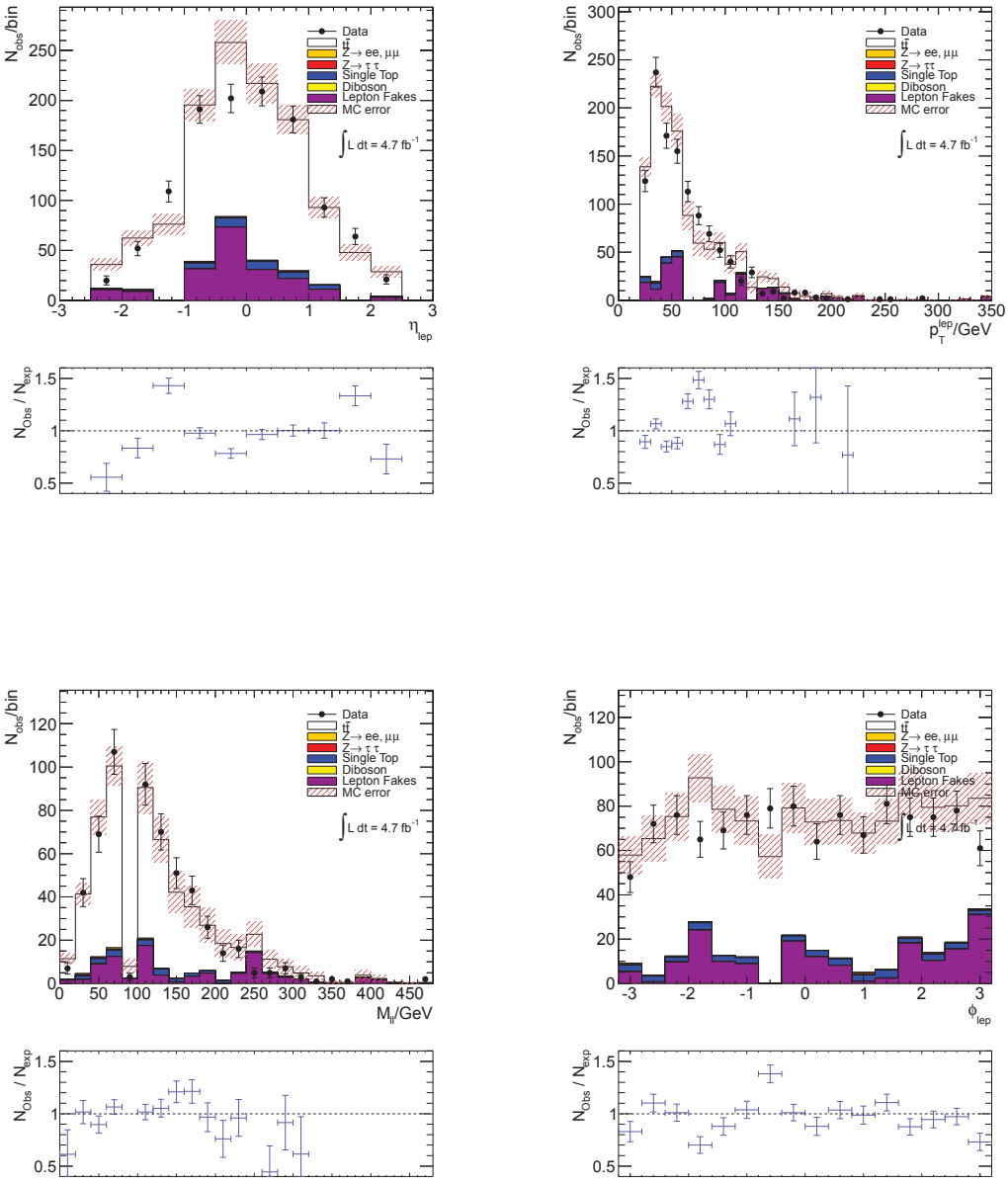

Figure B.10.: Lepton η (top left) and p_T (top right) distributions (lepton and antilepton combined). Invariant dilepton pair mass (bottom left) and lepton ϕ (bottom right) distributions. Data, MC- and fake lepton background selected according to the the tagged event selection in the *ee*-channel. The lower pads of the plots show the ratio between observed events in data (N_{obs}) and events expected from signal MC, background MC and fake lepton background (N_{exp}). All MC scale factors are applied and MC samples are scaled to an integrated luminosity of $\int L\,dt = 4.71\,\text{fb}^{-1}$.

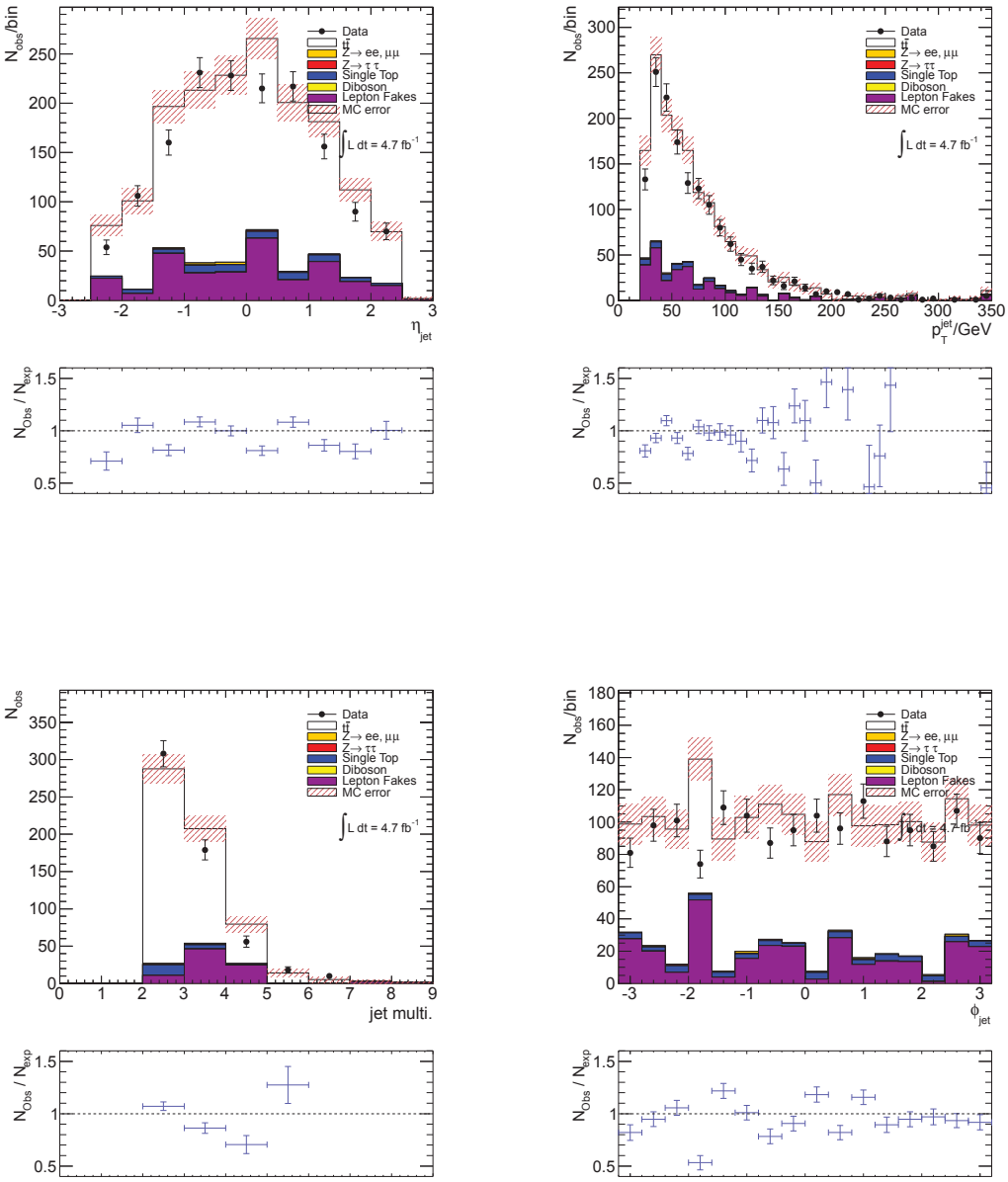

Figure B.11.: Jet η (top left) and p_T (top right) distributions. Jet multiplicity (bottom left) and jet ϕ (bottom right) distributions. Data, MC- and fake lepton background selected according to the the tagged event selection in the *ee*-channel. The lower pads of the plots show the ratio between observed events in data (N_{obs}) and events expected from signal MC, background MC and fake lepton background (N_{exp}). All MC scale factors are applied and MC samples are scaled to an integrated luminosity of $\int L\,dt = 4.71\,\text{fb}^{-1}$.

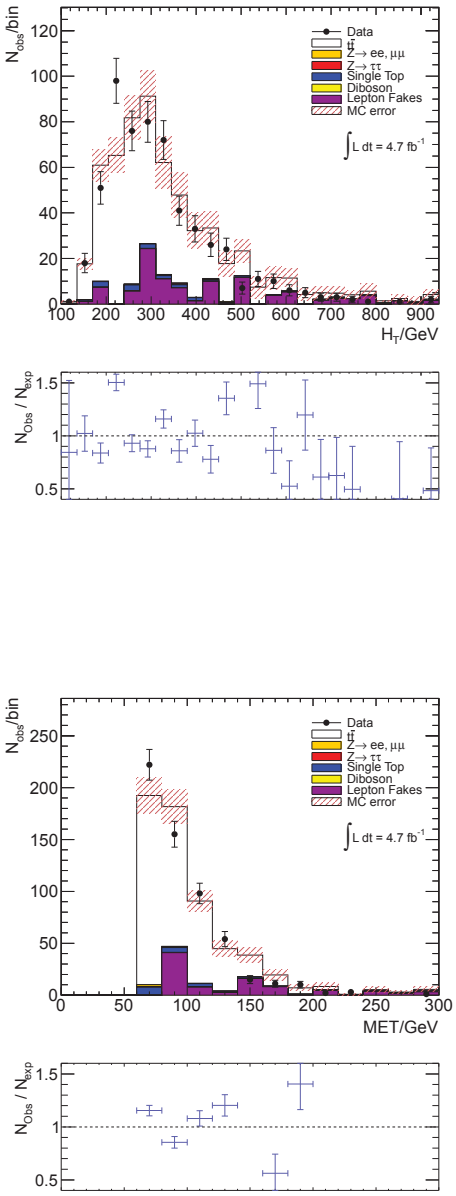

Figure B.12.: H_T (top) and $\not\!\!E$ (bottom) distributions. Data, MC- and fake lepton background selected according to the the tagged event selection in the *ee*-channel. The lower pads of the plots show the ratio between observed events in data (N_{obs}) and events expected from signal MC, background MC and fake lepton background (N_{exp}). All MC scale factors are applied and MC samples are scaled to an integrated luminosity of $\int L\,dt = 4.71\,\mathrm{fb}^{-1}$.

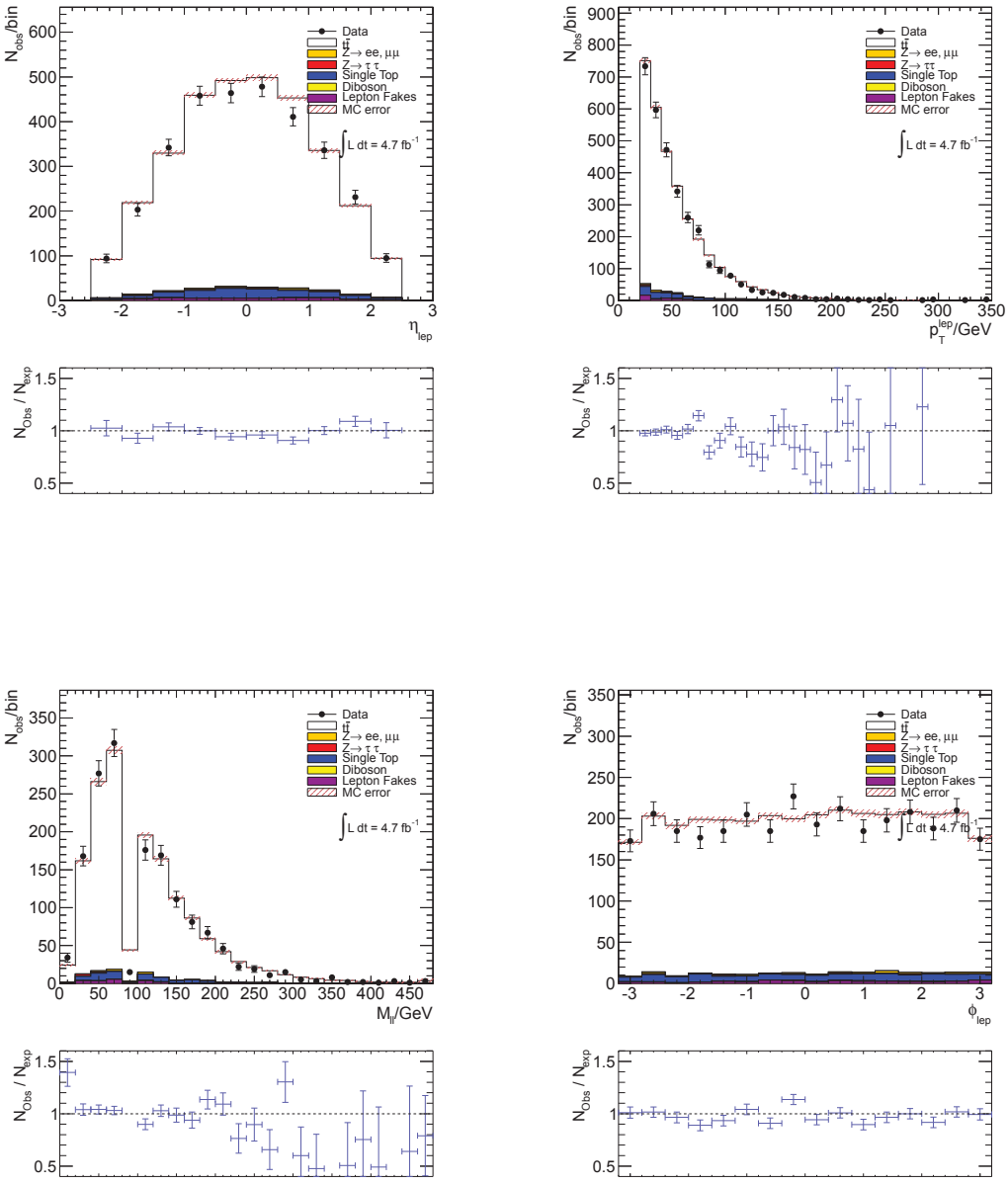

Figure B.13.: Lepton η (top left) and p_T (top right) distributions (lepton and antilepton combined). Invariant dilepton mass (bottom left) and lepton ϕ (bottom right) distributions. Data, MC- and fake lepton background selected according to the the tagged event selection in the $\mu\mu$-channel. The lower pads of the plots show the ratio between observed events in data (N_{obs}) and events expected from signal MC, background MC and fake lepton background (N_{exp}). All MC scale factors are applied and MC samples are scaled to an integrated luminosity of $\int L\,dt = 4.71\,\text{fb}^{-1}$.

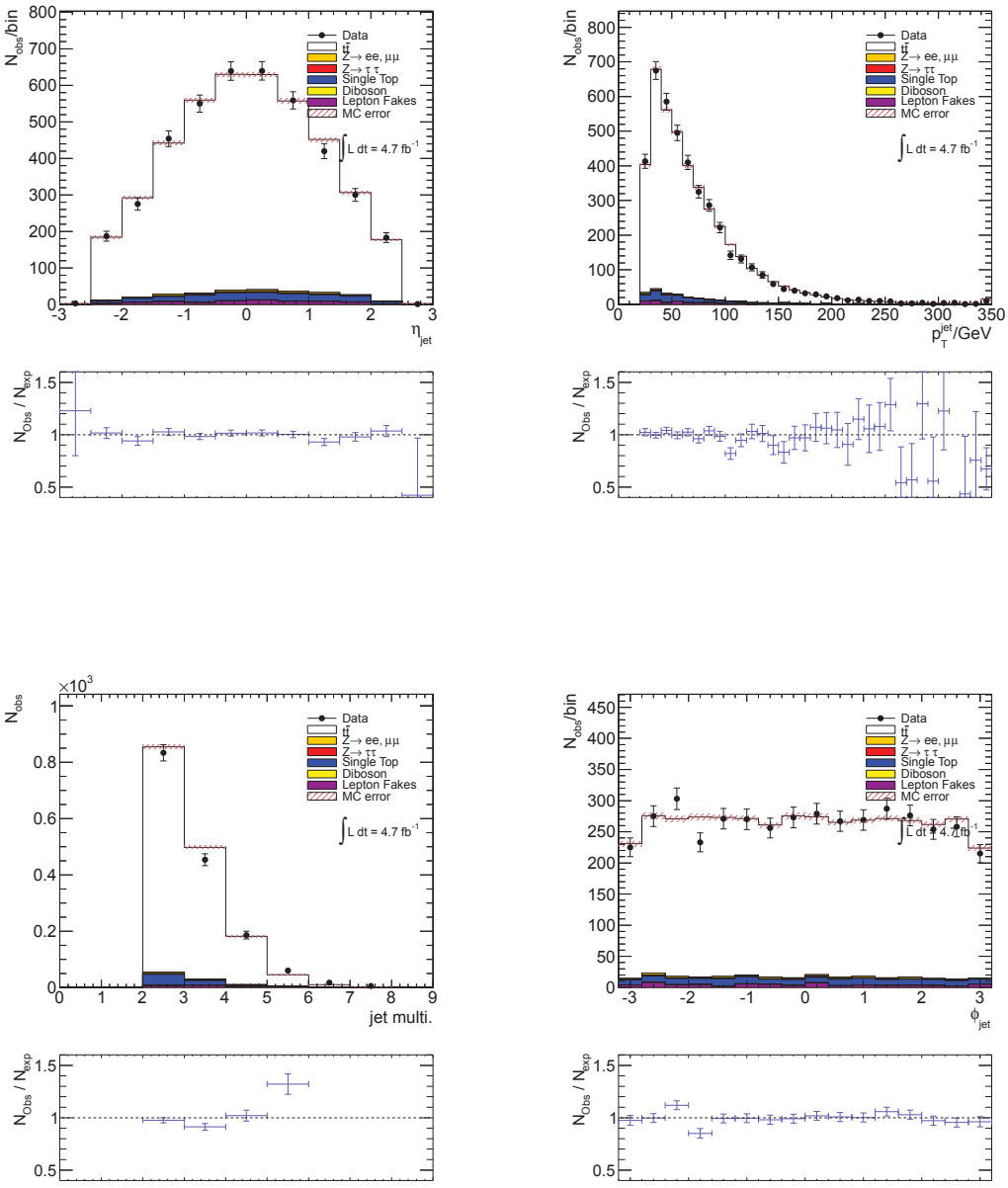

Figure B.14.: Jet η (top left) and p_T (top right) distributions. Jet multiplicity (bottom left) and ϕ (bottom right) distributions. Data, MC- and fake lepton background selected according to the the tagged event selection in the $\mu\mu$-channel. The lower pads of the plots show the ratio between observed events in data (N_{obs}) and events expected from signal MC, background MC and fake lepton background (N_{exp}). All MC scale factors are applied and MC samples are scaled to an integrated luminosity of $\int L\,dt = 4.71\,\text{fb}^{-1}$.

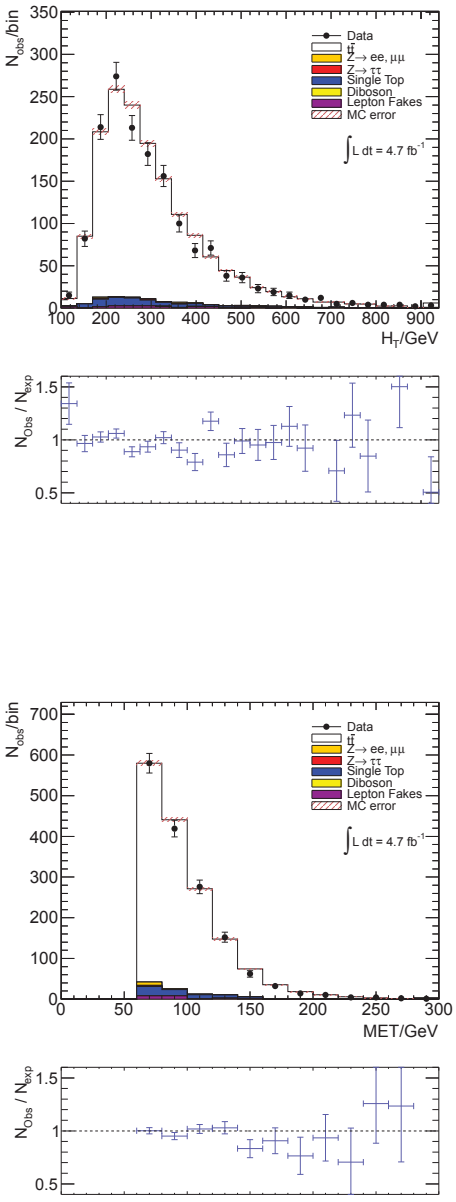

Figure B.15.: H_T (top) and $\not\!\!E$ (bottom) distributions. Data, MC- and fake lepton background selected according to the the tagged event selection in the $\mu\mu$-channel. The lower pads of the plots show the ratio between observed events in data (N_{obs}) and events expected from signal MC, background MC and fake lepton background (N_{exp}). All MC scale factors are applied and MC samples are scaled to an integrated luminosity of $\int L\,dt = 4.71\,\text{fb}^{-1}$.

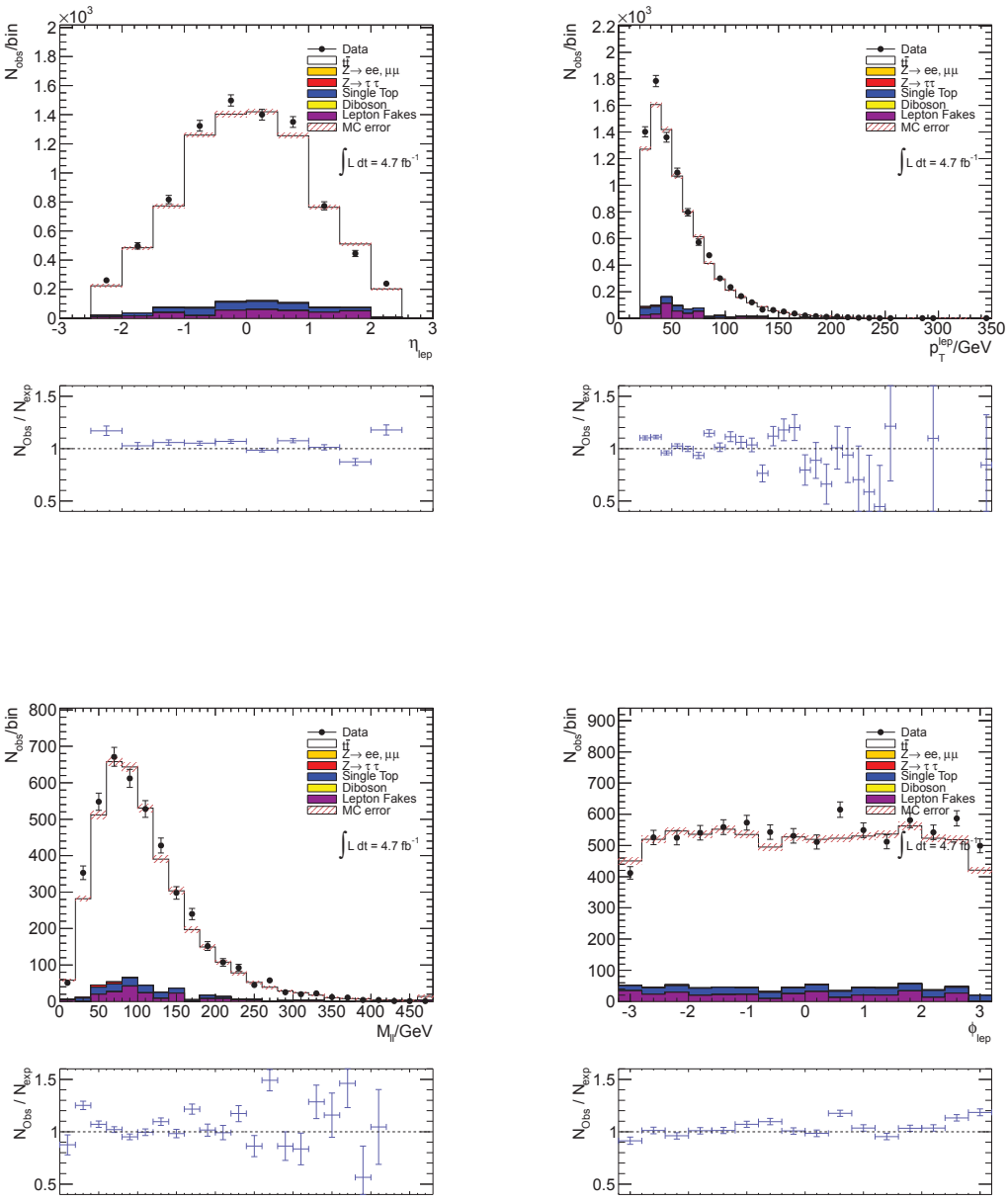

Figure B.16.: Lepton η (top left) and p_T (top right) distributions (lepton and antilepton combined). Invariant dilepton mass (bottom left) and lepton ϕ (bottom right) distributions. Data, MC- and fake lepton background selected according to the the tagged event selection in the $e\mu$-channel. The lower pads of the plots show the ratio between observed events in data (N_{obs}) and events expected from signal MC, background MC and fake lepton background (N_{exp}). All MC scale factors are applied and MC samples are scaled to an integrated luminosity of $\int L\,dt = 4.71\,\text{fb}^{-1}$.

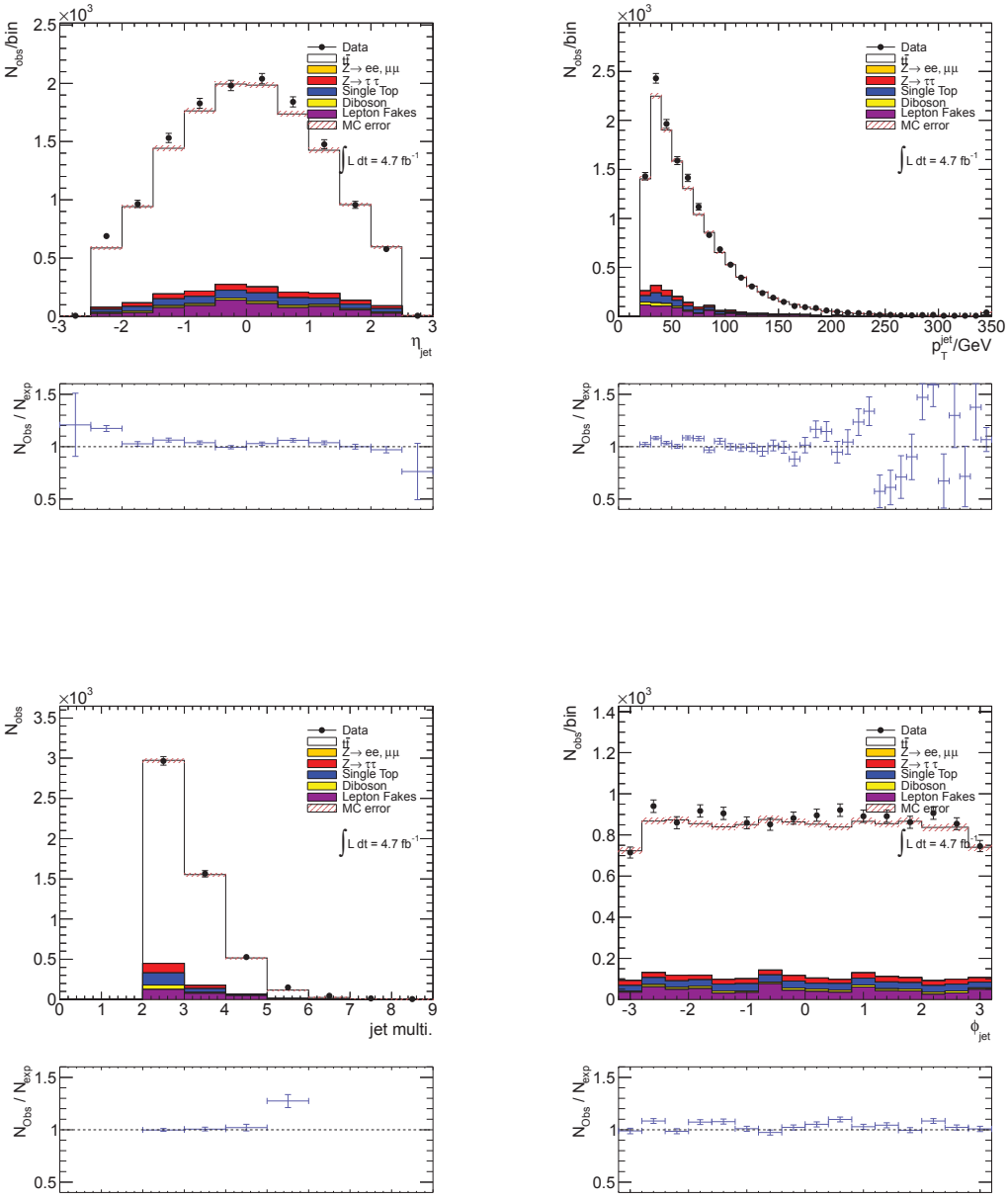

Figure B.17.: Jet η (top left) and p_T (top right) distributions. Jet multiplicity (bottom left) and ϕ (bottom right) distributions. Data, MC- and fake lepton background selected according to the the tagged event selection in the $e\mu$-channel. The lower pads of the plots show the ratio between observed events in data (N_{obs}) and events expected from signal MC, background MC and fake lepton background (N_{exp}). All MC scale factors are applied and MC samples are scaled to an integrated luminosity of $\int L\,dt = 4.71\,\text{fb}^{-1}$.

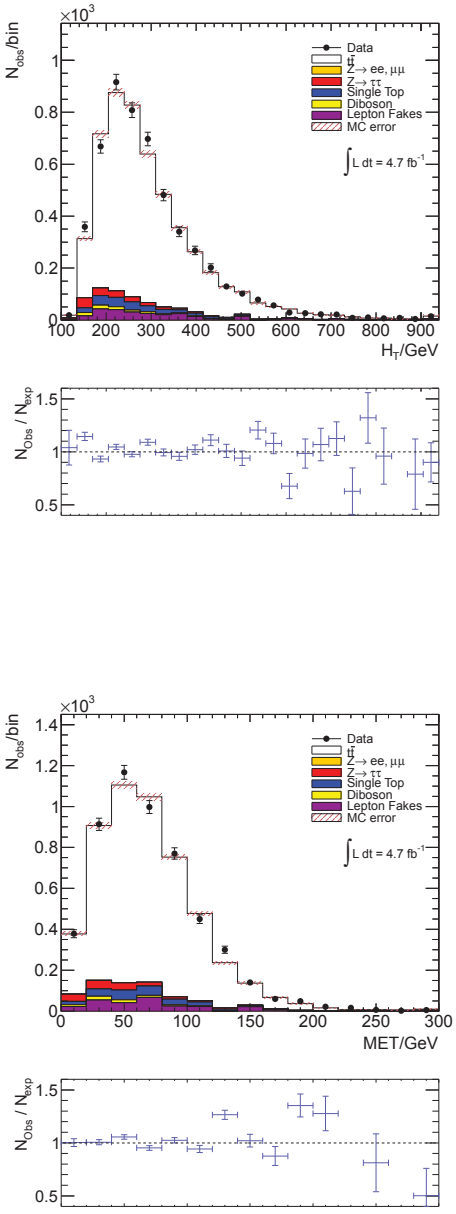

Figure B.18.: H_T (top) and $\not\!\!E$ (bottom) distributions. Data, MC- and fake lepton background selected according to the the tagged event selection in the $e\mu$-channel. The lower pads of the plots show the ratio between observed events in data (N_{obs}) and events expected from signal MC, background MC and fake lepton background (N_{exp}). All MC scale factors are applied and MC samples are scaled to an integrated luminosity of $\int L\,dt = 4.71\,\text{fb}^{-1}$.

Appendix C

Additional Information on the Kinematic Likelihood Fitter

In the dilepton likelihood function of the KLFitter a product of Gaussian functions is used (see Equation 8.6). This product calculates the Standard Model probability for the value of (anti-) neutrino pseudorapidity, which was estimated using the kinematic equations provided in [161, pp. 85-87]. The width of the Gaussian distributions ($\sigma_{\eta^{\bar{\nu},\nu}}$) weakly depends on the top-quark mass. This dependency is assumed to be linear

$$\sigma_{\eta^{\bar{\nu},\nu}} = a + b\, m_{\text{top}}. \tag{C.1}$$

The values for a and b are listed in Table C.1.

Channel	a	b
ee	1.207	-2.40×10^{-4}
$\mu\mu$	1.438	-8.55×10^{-4}
$e\mu$	1.295	-4.00×10^{-4}

Table C.1.: Parameters a and b for the individual $t\bar{t}$ decay channels. These quantities are taken directly from the KLFitter source code [160].

The parameters m_i are used in the double Gaussian parametrisation of the transfer functions, which are described in Section 8.1. The parameters m_i themselves are calculated using the Equations C.2 and C.3. Equations listed in C.2 are valid for light-jets and bottom-quark induced jets, while the equation listed in C.3 are valid for muons. The values for the constants a_i and b_i with $i = 1 \ldots 5$ can be found in [163].

$$\begin{aligned} m_1 &= a_1 + b_1\, E_{\text{truth}}\,, \\ m_2 &= a_2/\sqrt{E_{\text{truth}}} + b_2\,, \\ m_3 &= a_3 + b_3\, E_{\text{truth}}\,, \\ m_4 &= a_4 + b_4\, E_{\text{truth}}\,, \\ m_5 &= a_5 + b_5\, E_{\text{truth}}\,. \end{aligned} \quad \text{(C.2)}$$

$$\begin{aligned} m_1 &= a_1 + b_1\, p_T^{\text{truth}}\,, \\ m_2 &= a_2 + b_2\, p_T^{\text{truth}}\,, \\ m_3 &= a_3 + b_3\, p_T^{\text{truth}}\,, \\ m_4 &= a_4 + b_4\, p_T^{\text{truth}}\,, \\ m_5 &= a_5 + b_5\, p_T^{\text{truth}}\,, \end{aligned} \quad \text{(C.3)}$$

The Gaussian resolution of the missing energy is given by the following parametrisation

$$\sigma^{\text{miss}} = k_0 + \frac{k_1}{1 + \exp\left[-k_2 \cdot (\not{E}_T^{\text{sum}} - k_3)\right]}\,. \quad \text{(C.4)}$$

Where the parameters k_i are

$$\begin{aligned} k_0 &= 13.615\,\text{MeV}\,, \\ k_1 &= 20.881\,\text{MeV}\,, \\ k_2 &= 0.00323\,\text{MeV}^{-1}\,, \\ k_3 &= 739.223\,\text{MeV}\,. \end{aligned} \quad \text{(C.5)}$$

The parametrisation of σ^{miss} and the parameters k_i are taken directly from the KLFitter source code [160]. Table C.2 contains the percentage of truth matched events.

- *Lepton match* is the percentage of events for which the charged leptons are matched to MC truth leptons.
- *Bottom-quark match* is the percentage of events for which two of the selected jets are matched to MC truth bottom-quarks.
- *Full match* is the percentage of events which fulfil both the lepton and the bottom-quark matching.

Type	ee-Channel [%]	$\mu\mu$-Channel [%]	$e\mu$-Channel [%]
Lepton match	97.6 ± 1.2	100.0 ± 0.7	98.2 ± 0.4
Bottom-quark match	74.7 ± 1.4	73.7 ± 0.8	74.2 ± 0.5
Full Match	72.8 ± 1.4	73.7 ± 0.8	74.2 ± 0.5

Table C.2.: Listed are the percentages of truth matched events. Values are derived from the MC@NLO $t\bar{t}$-signal MC. The errors shown are statistical errors only.

C.1 Kinematic Reconstruction of the $t\bar{t}$ System in Dileptonic Decays

In the dileptonic decay channel the following particles are present in the final state:

$$t\bar{t} \rightarrow W^+ b\, W^- \bar{b} \rightarrow l_i^+ \nu_{l,i} b\, l_j^- \bar{\nu}_{l,j} \bar{b}\,. \tag{C.6}$$

The corresponding four-vectors of the final state particles are P_b, $P_{\bar{b}}$, P_{l^-}, P_{l^+}, P_ν and $P_{\bar{\nu}}$. The kinematic constraints described in Chapter 8 result in:

$$m_W^2 = (P_l + P_\nu)^2\,, \tag{C.7}$$
$$m_t^2 = (P_l + P_\nu + P_b)^2\,. \tag{C.8}$$

In the following the masses of the top- and bottom-quarks, as well as the mass of the W-boson are assumed to be known, lepton masses are neglected in the high energy approximation and neutrino masses are set to zero. The four vectors of the bottom-quarks P_b and the leptons P_l are measured by the ATLAS detector. The calculation of the missing neutrino and antineutrino momenta is described in [161, p. 85] and is summarised using the following equations. Expanding Equation C.7 leads to:

$$m_W^2 = (E_l + E_\nu)^2 - (\vec{p}_l + \vec{p}_\nu)^2 = 2\,(E_l E_\nu - \vec{p}_l \cdot \vec{p}_\nu)\,. \tag{C.9}$$

By solving this equation for E_ν follows:

$$E_\nu = \frac{1}{E_l}\left(\frac{m_W^2}{2} + \vec{p}_l \cdot \vec{p}_\nu\right). \tag{C.10}$$

From Equation C.8 follows (using Equation C.9):

$$\begin{aligned} m_t^2 &= (E_l + E_\nu + E_b)^2 - (\vec{p}_l + \vec{p}_\nu + \vec{p}_b)^2\,, \\ &= m_W^2 + m_b^2 + 2\,(E_l E_b + E_\nu E_b - \vec{p}_l \cdot \vec{p}_b - \vec{p}_\nu \cdot \vec{p}_b)\,. \end{aligned} \tag{C.11}$$

By solving this equation for E_ν follows:

$$E_\nu = \frac{m_t^2 - m_W^2 - m_b^2 - 2p_l p_b}{2E_b} - \frac{\vec{p}_\nu \cdot \vec{p}_b}{E_b}\,. \tag{C.12}$$

The system is transformed into a system with $p_z = 0\,\text{GeV}$ by using the Lorentz transformation Λ:

$$\Lambda P = \begin{pmatrix} \cosh\eta_\nu & 0 & 0 & -\sinh\eta_\nu \\ 0 & 1 & 0 & 0 \\ 0 & 0 & 1 & 0 \\ -\sinh\eta_\nu & 0 & 0 & \cosh\eta_\nu \end{pmatrix} \begin{pmatrix} E \\ p_x \\ p_y \\ p_z \end{pmatrix} = \begin{pmatrix} E\cosh\eta_\nu - p_z \sinh\eta_\nu \\ p_x \\ p_y \\ -E\sinh\eta_\nu + p_z\cosh\eta_\nu \end{pmatrix}. \tag{C.13}$$

From application of the Lorentz transformation Λ to Equation C.10 with $p_z = 0\,\text{GeV}$ follows:

$$E_{T,\nu} = p_{T,\nu} = \frac{1}{E_l \cosh\eta_\nu - p_{z,l}\sinh\eta_\nu}\left(\frac{1}{2}m_W^2 + p_{x,l}p_{x,\nu} + p_{y,l}p_{y,\nu}\right). \tag{C.14}$$

From application of the Lorentz transformation Λ to Equation C.12 with $p_z = 0\,\text{GeV}$

follows:

$$E_{T,\nu} = p_{T,\nu} = \frac{1}{E_b \cosh\eta_\nu - p_{z,b}\sinh\eta_\nu}\left[\frac{1}{2}\left(m_t^2 - m_W^2 - m_b^2 - 2p_l p_b\right) + p_{x,\nu}p_{x,b} + p_{y,\nu}p_{y,b}\right]. \tag{C.15}$$

Equation C.14 is equal to Equation C.15, solving this for $p_{x,\nu}$ yields:

$$p_{x,\nu} = Ap_{y,\nu} + B\,, \tag{C.16}$$

where A and B are defined as

$$A = \frac{p_{y,l}E'_b - p_{y,b}E'_l}{p_{x,b}E'_l - p_{x,l}E'_b}\,, \tag{C.17}$$

$$B = \frac{E'_l\left(m_t^2 - m_W^2 - m_b^2 - 2p_l p_b\right) - E'_b m_W^2}{2\left(p_{x,l}E'_b - p_{x,b}E'_l\right)}\,, \tag{C.18}$$

where E'_l and E'_b are defined as:

$$E'_l = E_l\cosh\eta_\nu - p_{z,l}\sinh\eta_\nu\,, \tag{C.19}$$

$$E'_b = E_b\cosh\eta_\nu - p_{z,b}\sinh\eta_\nu\,. \tag{C.20}$$

The terms containing p_T and $p_{x,\nu}$ are eliminated from Equation C.14 using $p_T = \sqrt{p_{x,\nu}^2 + p_{y,\nu}^2}$ and Equation C.16. this results in:

$$\sqrt{(A^2+1)p_{y,\nu} + 2ABp_{y,\nu} + B^2} = \frac{1}{E'_l}\left[\frac{1}{2}m_W^2 + p_{x,l}(Ap_{y,\nu} + B) + p_{y,l}p_{y,\nu}\right]. \tag{C.21}$$

After squaring of equation C.21 an equation quadratic in $p_{y,\nu}$ is obtained

$$Cp_{y,\nu}^2 + Dp_{y,\nu} + F = 0\,, \tag{C.22}$$

where C, D and F are defined as:

$$C = A^2 + 1 - \left(\frac{p_{x,l}}{E'_l}A + \frac{p_{y,l}}{E'_l}\right)^2, \tag{C.23}$$

$$D = 2AB - 2\frac{1}{E'_l}\left(\frac{m_W^2}{2} + p_{x,l}B\right)\left(p_{x,l}A + p_{y,l}\right), \tag{C.24}$$

$$F = B^2 - \left(\frac{m_W^2}{2E'_l} + \frac{p_{x,l}}{E'_l}B\right)^2. \tag{C.25}$$

The quadratic equation has up to two real solutions given by:

$$p_{y,\nu}^{a,b} = -\frac{D}{2C} \pm \frac{1}{2C}\sqrt{D^2 - 4CF}\,. \tag{C.26}$$

Using Equation C.16 the result for $p_{x,\nu}$ can then be calculated and $p_{\nu,z}$ can be determined using

$$p_{\nu,z} = p_{T,\nu}\sinh\eta_\nu\,. \tag{C.27}$$

C.2 KLFitter Reconstruction Quality, Pretag

C.2.1 *ee*-Channel

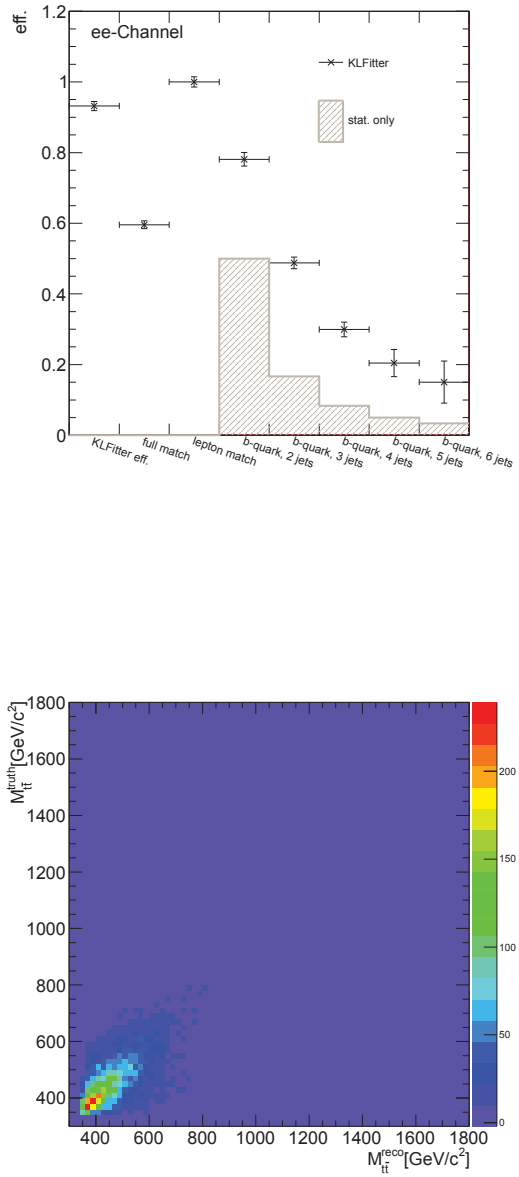

Figure C.1.: Top: Efficiency estimated for the $t\bar{t}$ signal sample. The plot shows the efficiency of the KLFitter reconstruction (*KLFitter*). Depicted in grey is the statistical probability (*stat. only*) to select the correct jet pair from the given multiplicity. Bottom: Top-quark-pair invariant mass distribution of the $t\bar{t}$ signal sample. The plot shows the KLFitter reconstructed value versus the true value from MC. All scale factors are applied except the luminosity scaling. Events are selected according to the pretag event selection.

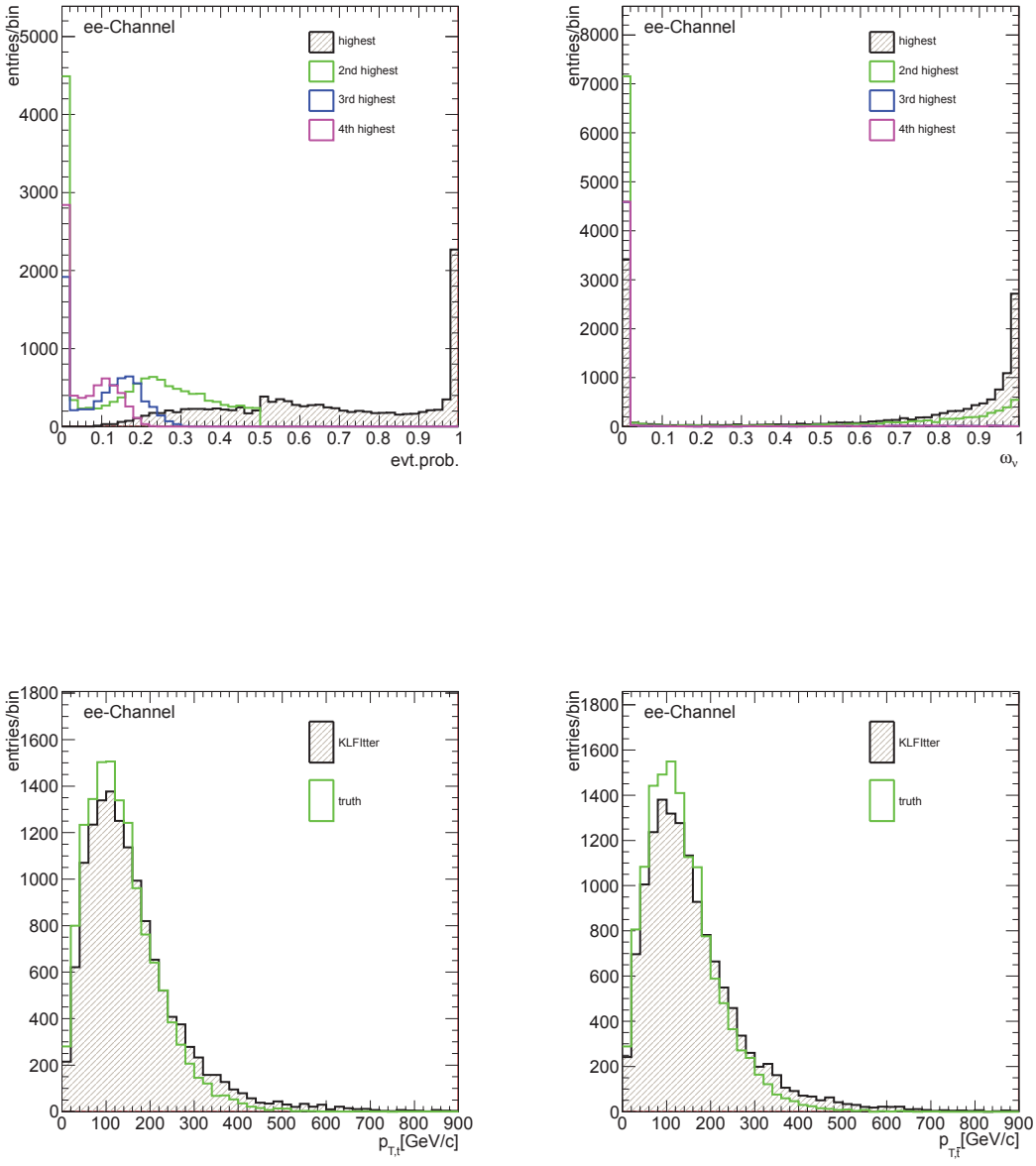

Figure C.2.: Distributions of highest event probabilities (top left) and four highest neutrino weights (top right) for the jet permutation with maximum event probability. Distributions of top-quark (bottom left) and antitop-quark (bottom right) transverse momentum from the $t\bar{t}$ signal sample. All scale factors are applied except the luminosity scaling. Events are selected according to the pretag event selection.

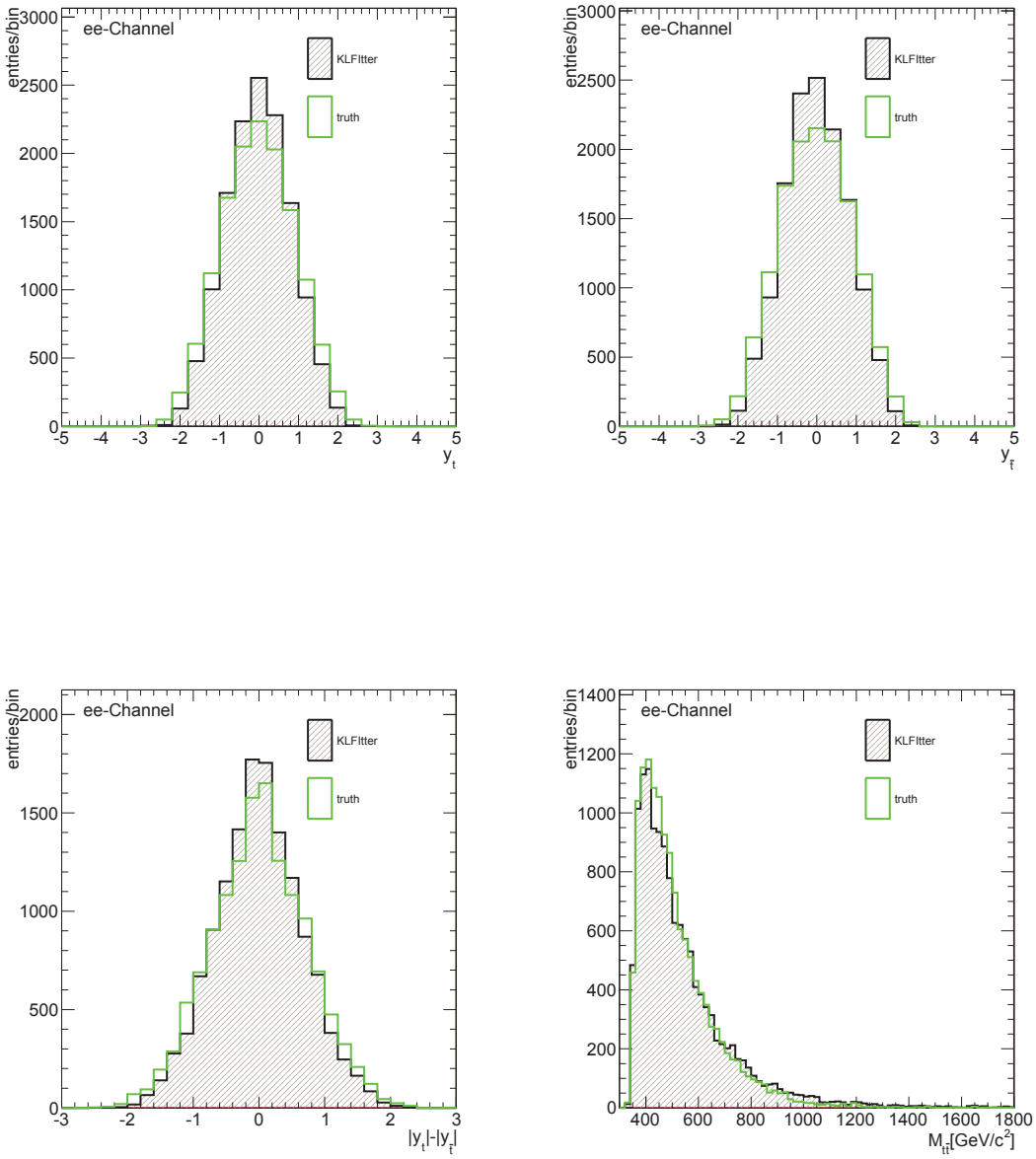

Figure C.3.: Distributions of top-quark (top left) and antitop-quark (top right) rapidity from the $t\bar{t}$ signal sample. Distributions of the difference of the absolute top- and antitop-quark rapidity $\Delta\,|y_{t\bar{t}}|$ (bottom left) and top-quark-pair invariant mass distribution (bottom right). All scale factors are applied except the luminosity scaling. Events are selected according to the pretag event selection.

C.2.2 $\mu\mu$-Channel

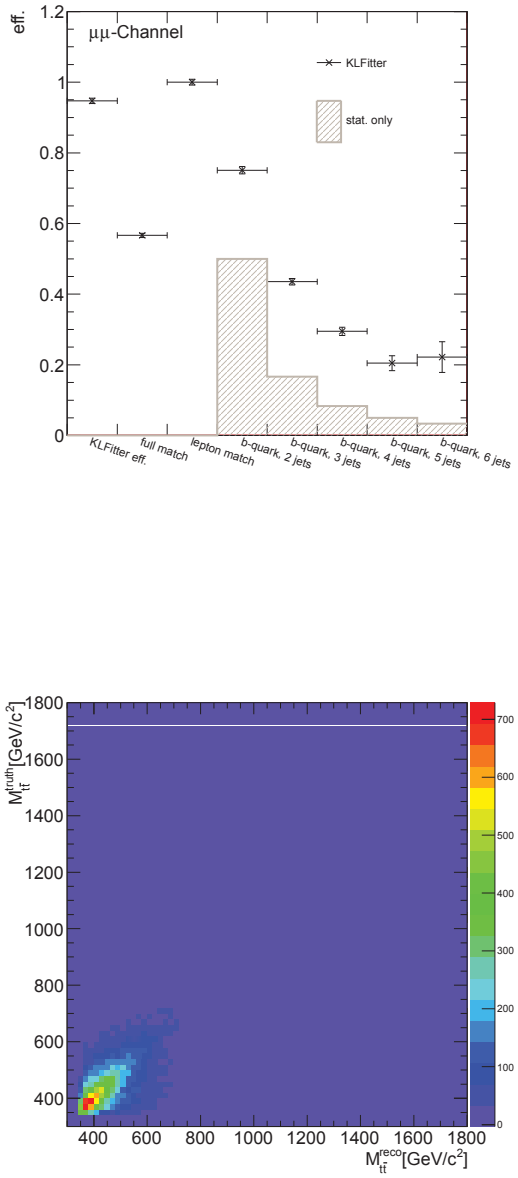

Figure C.4.: Distribution of the efficiency estimated for the $t\bar{t}$ signal sample (top). The plot shows the efficiency of the KLFitter reconstruction (*KLFitter*). Depicted in grey is the statistical probability (*stat. only*) to select the correct jet pair from the given multiplicity. Distribution of the top-quark-pair invariant mass distribution of the $t\bar{t}$ signal sample (bottom). The plot shows the KLFitter reconstructed value versus the true value vom MC. All scale factors are applied except the luminosity scaling. Events are selected according to the pretag event selection.

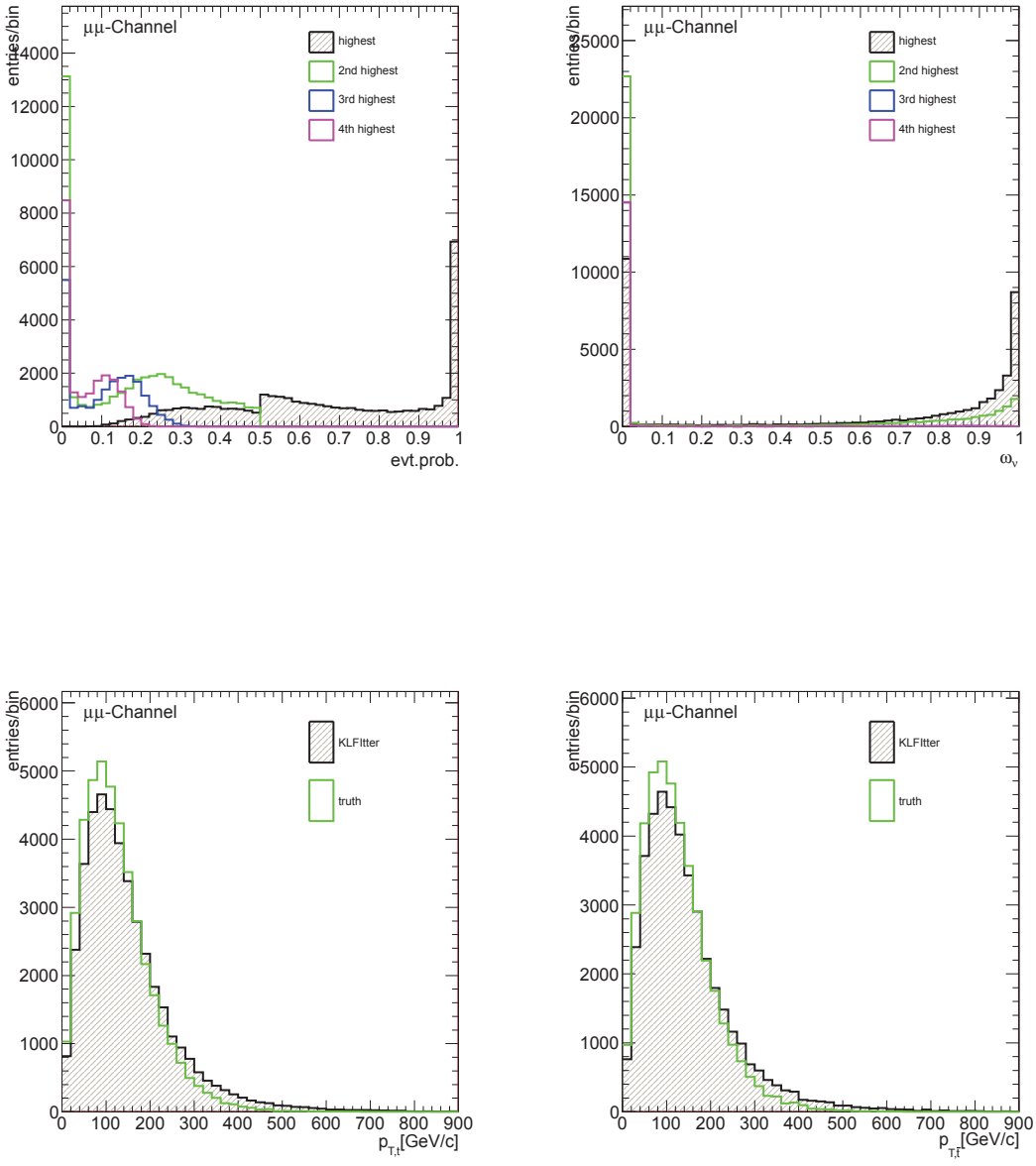

Figure C.5.: Distribution of four highest event probabilities (top left) and four highest neutrino weights for the jet permutation with maximum event probability (top right). Distributions of top-quark (left) and antitop-quark (right) transverse momentum from the $t\bar{t}$ signal sample. All scale factors are applied except the luminosity scaling. Events are selected according to the pretag event selection.

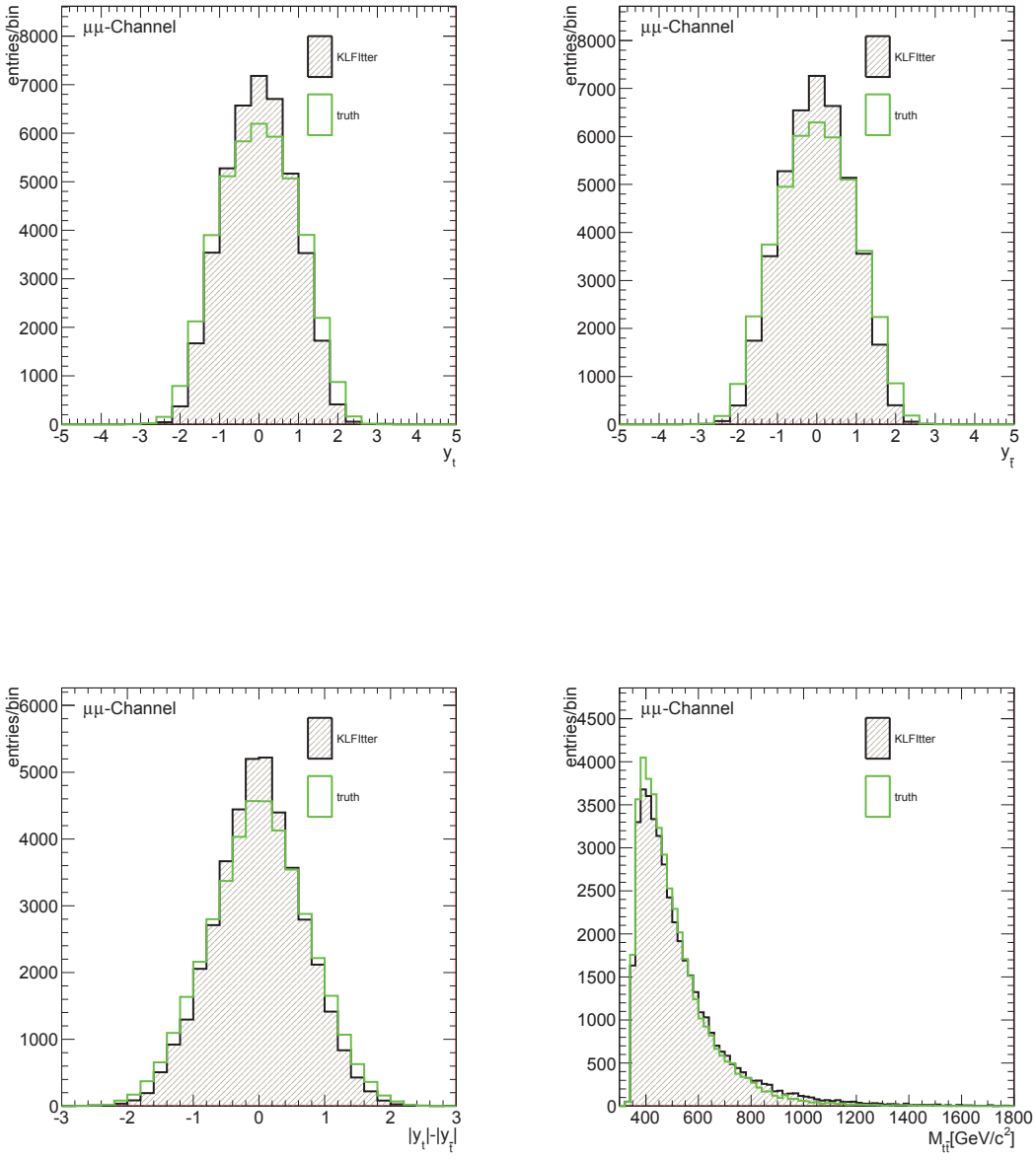

Figure C.6.: Distributions of top-quark (top left) and antitop-quark (top right) rapidity from the $t\bar{t}$ signal sample. Distributions of the difference of the absolute top- and antitop-quark rapidity $\Delta\,|y_{t\bar{t}}|$ (bottom left) and top-quark-pair invariant mass distribution (bottom right). All scale factors are applied except the luminosity scaling. Events are selected according to the pretag event selection.

C.2.3 $e\mu$-Channel

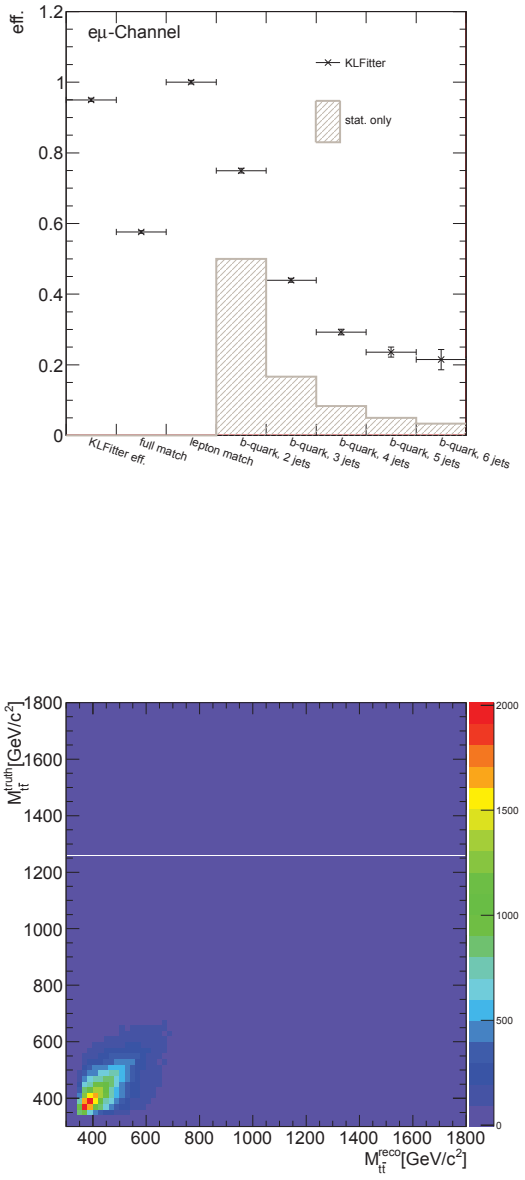

Figure C.7.: Distribution of the efficiency estimated for the $t\bar{t}$ signal sample (top). The plot shows the efficiency of the KLFitter reconstruction (*KLFitter*). Depicted in grey is the statistical probability (*stat. only*) to select the correct jet pair from the given multiplicity. Distribution of th top-quark-pair invariant mass distribution of the $t\bar{t}$ signal sample (bottom). The plot shows the KLFitter reconstructed value versus the true value from MC. All scale factors are applied except the luminosity scaling. Events are selected according to the pretag event selection.

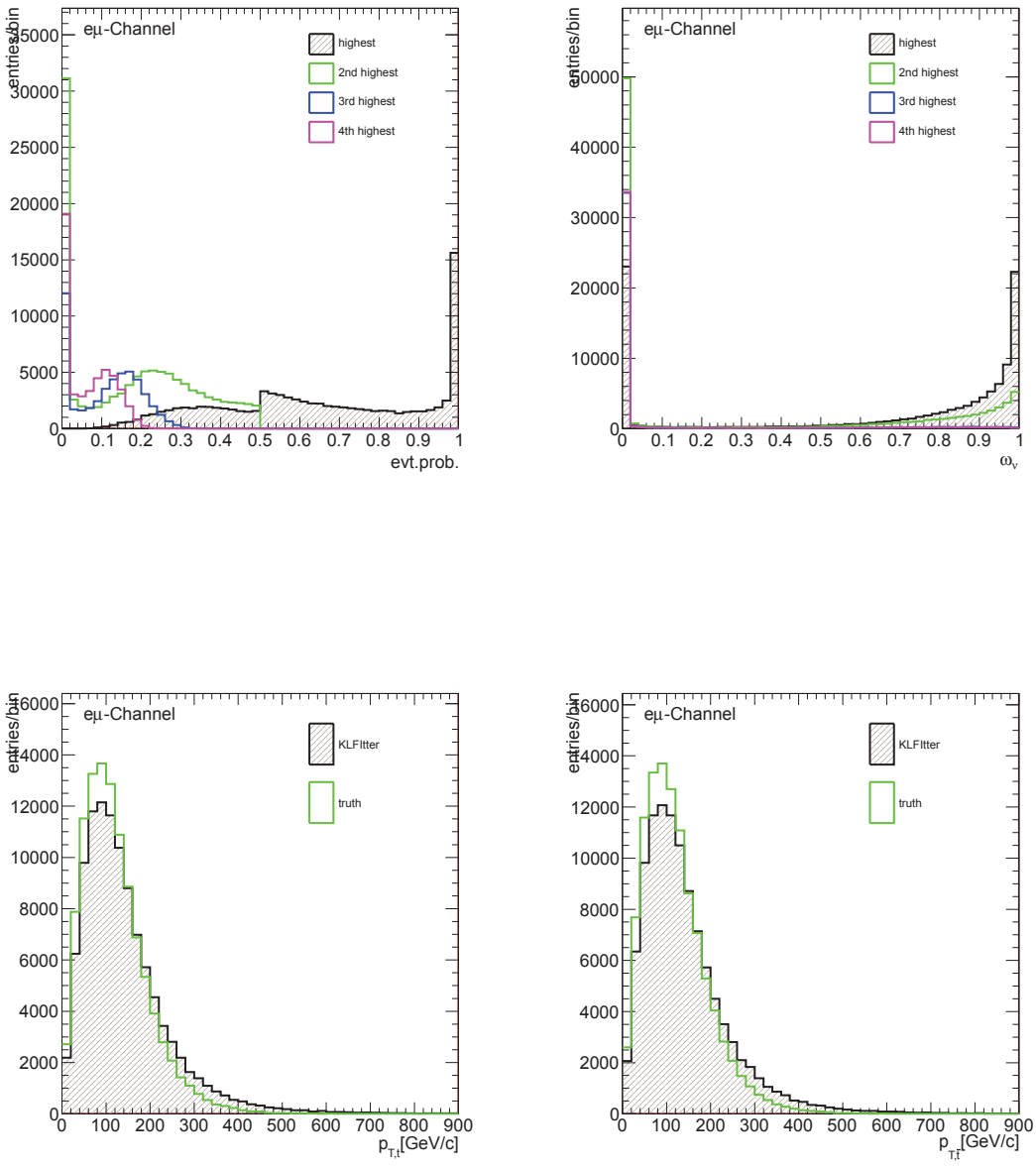

Figure C.8.: Distribution of four highest event probabilities (top left) and four highest neutrino weights for the jet permutation with maximum event probability (top right). Distributions of top-quark (left) and antitop-quark (right) transverse momentum from the $t\bar{t}$ signal sample. All scale factors are applied except the luminosity scaling. Events are selected according to the pretag event selection.

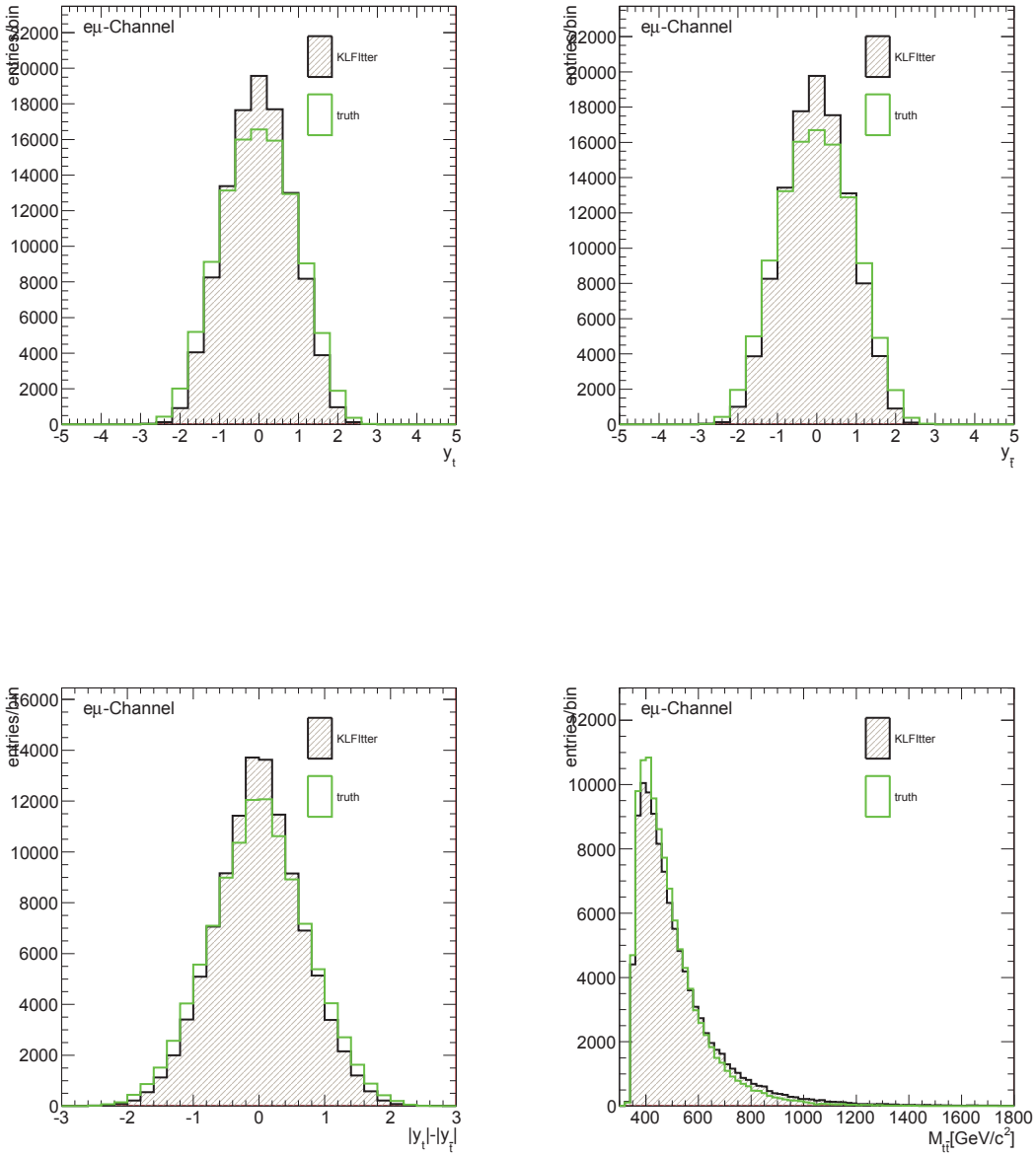

Figure C.9.: Distributions of top-quark (top left) and antitop-quark (top right) rapidity from the $t\bar{t}$ signal sample. Distributions of the difference of the absolute top- and antitop-quark rapidity $\Delta\,|y_{t\bar{t}}|$ (bottom left) and top-quark-pair invariant mass distribution (bottom right). All scale factors are applied except the luminosity scaling. Events are selected according to the pretag event selection.

C.3 KLFitter Reconstruction Quality, Tagged Selection

C.3.1 *ee*-Channel

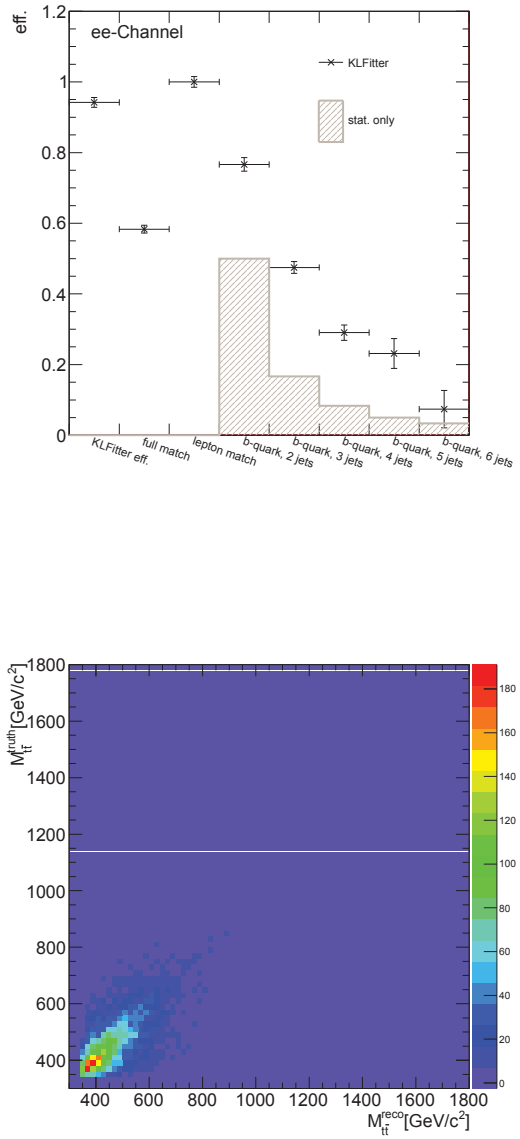

Figure C.10.: Distribution of the efficiency estimated for the $t\bar{t}$ signal sample (top). The plot shows the efficiency of the KLFitter reconstruction (*KLFitter*). Depicted in grey is the statistical probability (*stat. only*) to select the correct jet pair from the given multiplicity. Distribution of the top-quark-pair invariant mass distribution of the $t\bar{t}$ signal sample (bottom). The plot shows the KLFitter reconstructed value versus the true value from MC. All scale factors are applied except the luminosity scaling. Events are selected according to the tagged event selection. The KLFitter reconstruction was performed using the *kVeto* option.

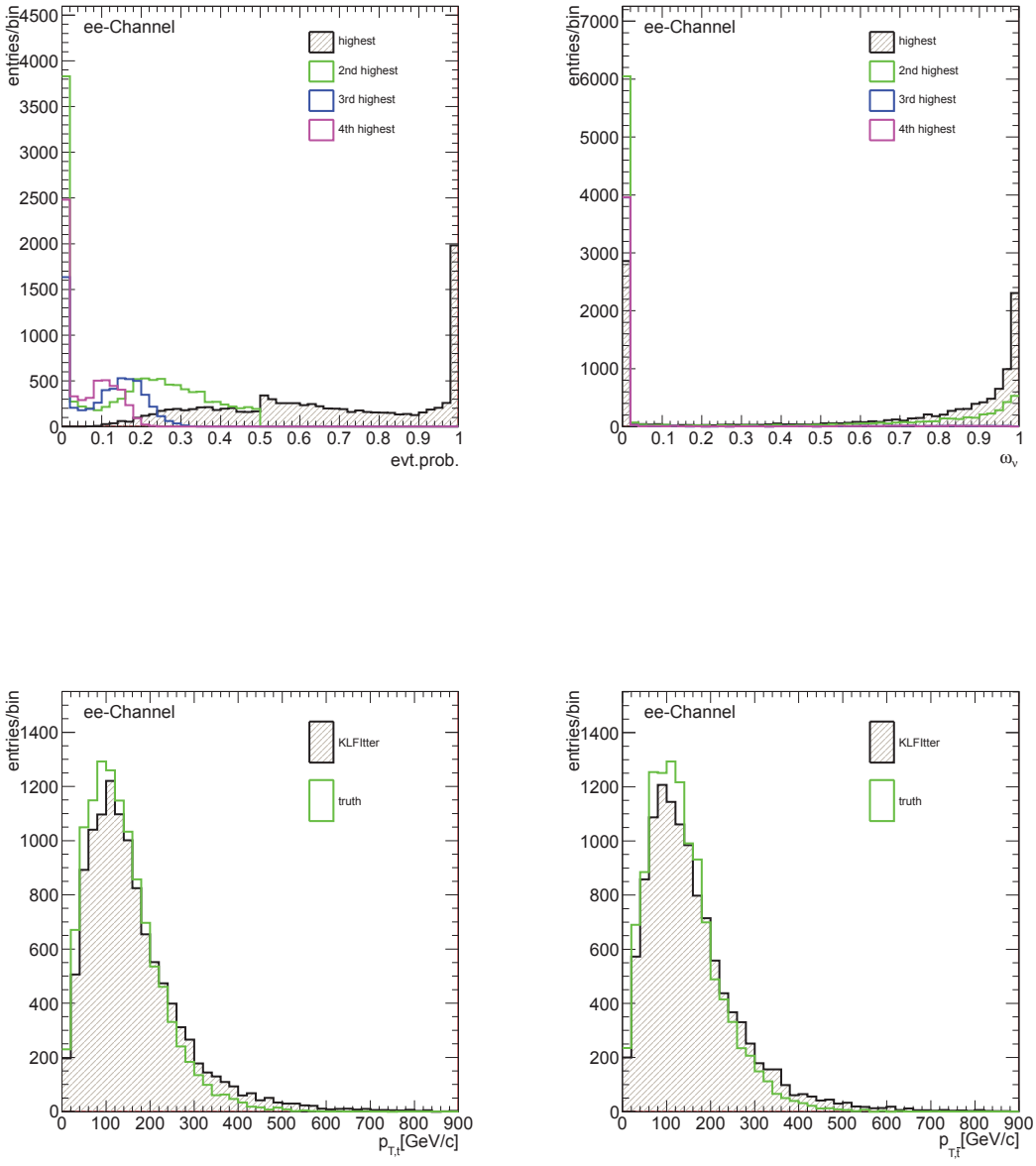

Figure C.11.: Distribution of four highest event probabilities (top left) and four highest neutrino weights for the jet permutation with maximum event probability (top right). Distributions of top-quark (left) and antitop-quark (right) transverse momentum from the $t\bar{t}$ signal sample. All scale factors are applied except the luminosity scaling. Events are selected according to the tagged event selection. The KLFitter reconstruction was performed using the *kVeto* option.

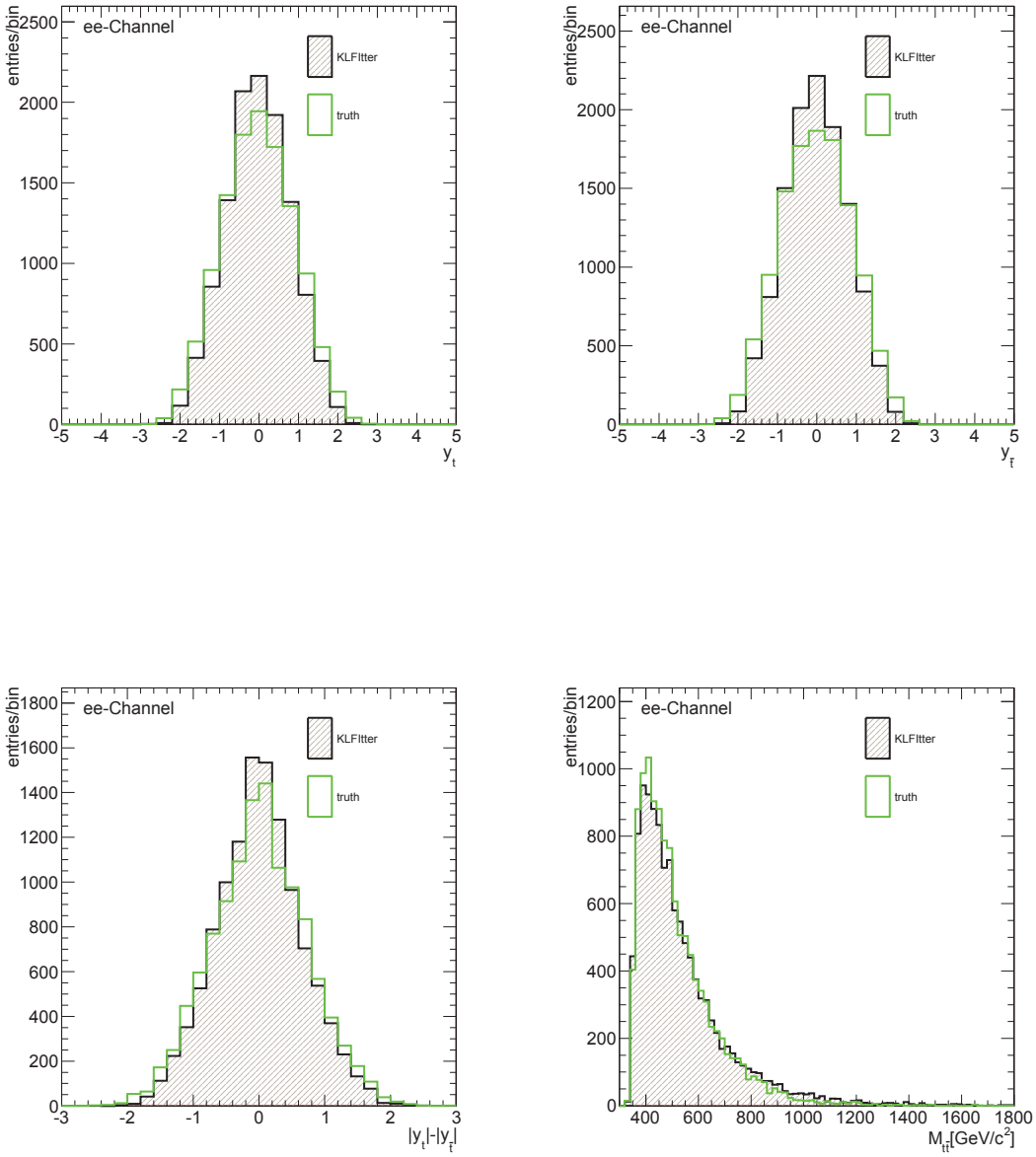

Figure C.12.: Distributions of top-quark (top left) and antitop-quark (top right) rapidity from the $t\bar{t}$ signal sample. Distributions of the difference of the absolute top- and antitop-quark rapidity $\Delta\,|y_{t\bar{t}}|$ (bottom left) and top-quark-pair invariant mass distribution (bottom right). All scale factors are applied except the luminosity scaling. Events are selected according to the tagged event selection. The KLFitter reconstruction was performed using the *kVeto* option.

C.3.2 $\mu\mu$-Channel

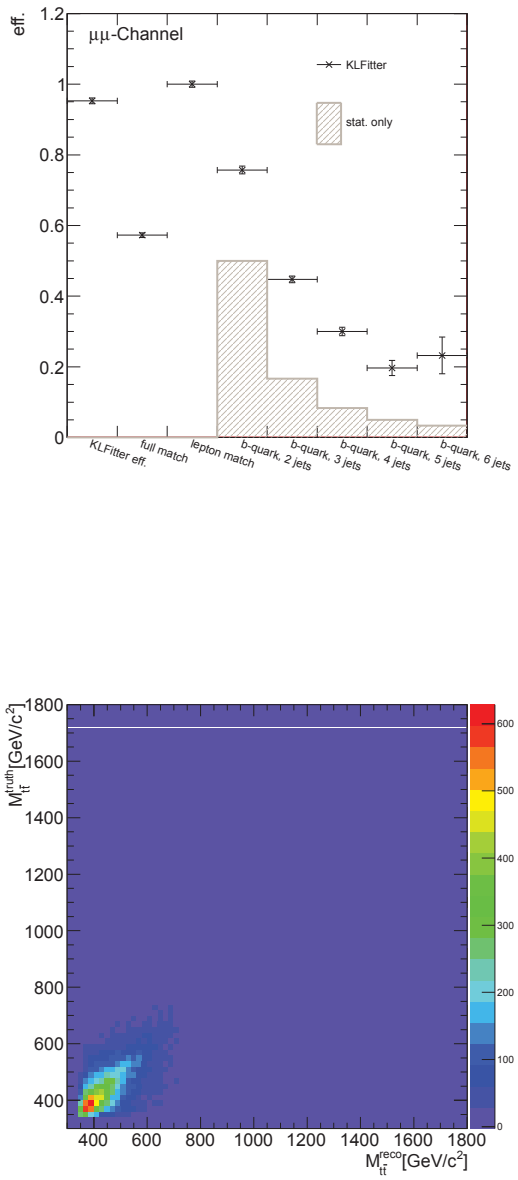

Figure C.13.: Distribution of the efficiency estimated for the $t\bar{t}$ signal sample (top). The plot shows the efficiency of the KLFitter reconstruction (*KLFitter*). Depicted in grey is the statistical probability (*stat. only*) to select the correct jet pair from the given multiplicity. Distribution of the top-quark-pair invariant mass distribution of the $t\bar{t}$ signal sample (bottom). The plot shows the KLFitter reconstructed value versus the true value from MC. All scale factors are applied except the luminosity scaling. Events are selected according to the tagged event selection. The KLFitter reconstruction was performed using the *kVeto* option.

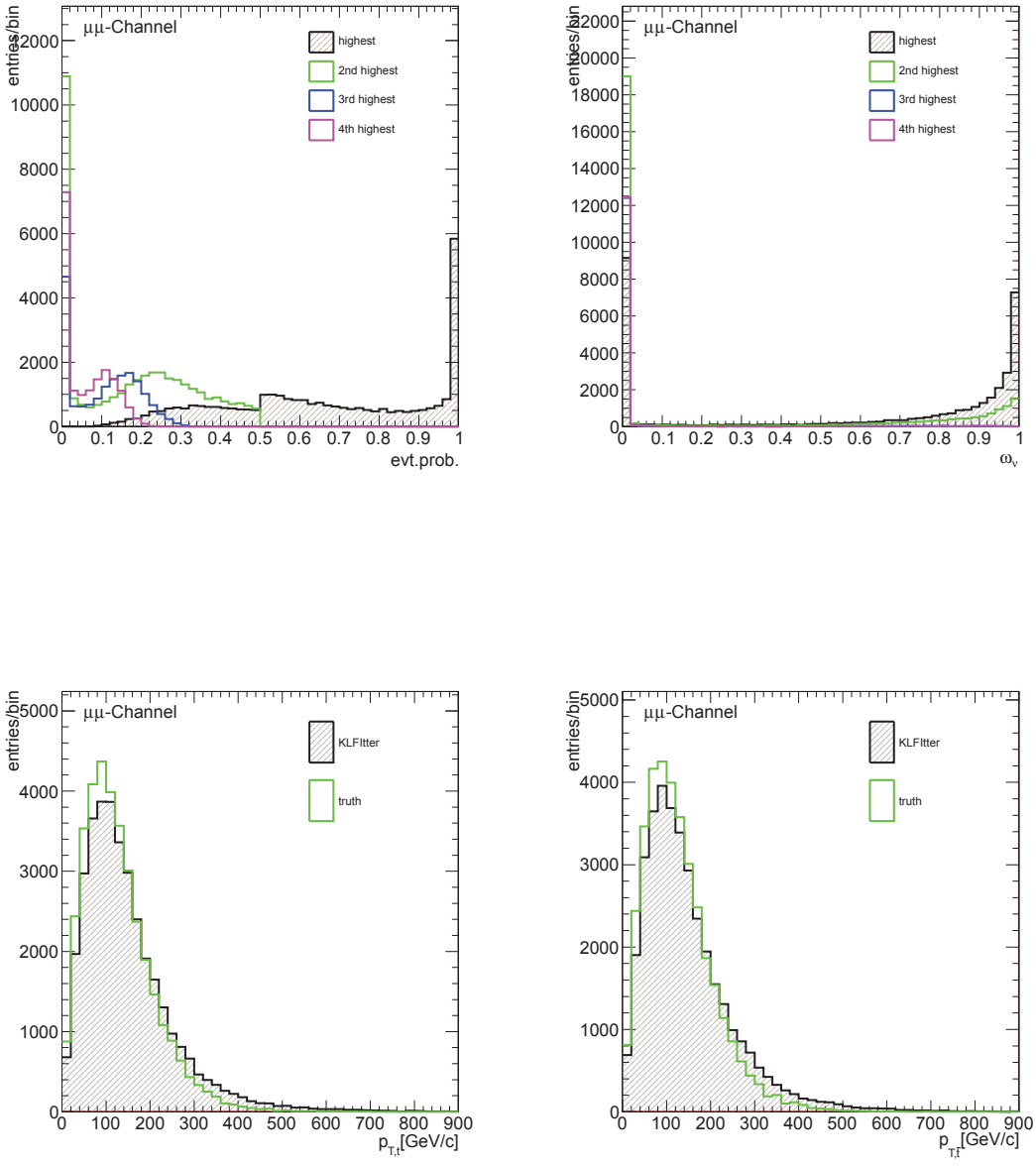

Figure C.14.: Distribution of four highest event probabilities (top left) and four highest neutrino weights for the jet permutation with maximum event probability (top right). Distributions of top-quark (left) and antitop-quark (right) transverse momentum from the $t\bar{t}$ signal sample. All scale factors are applied except the luminosity scaling. Events are selected according to the tagged event selection. The KLFitter reconstruction was performed using the *kVeto* option.

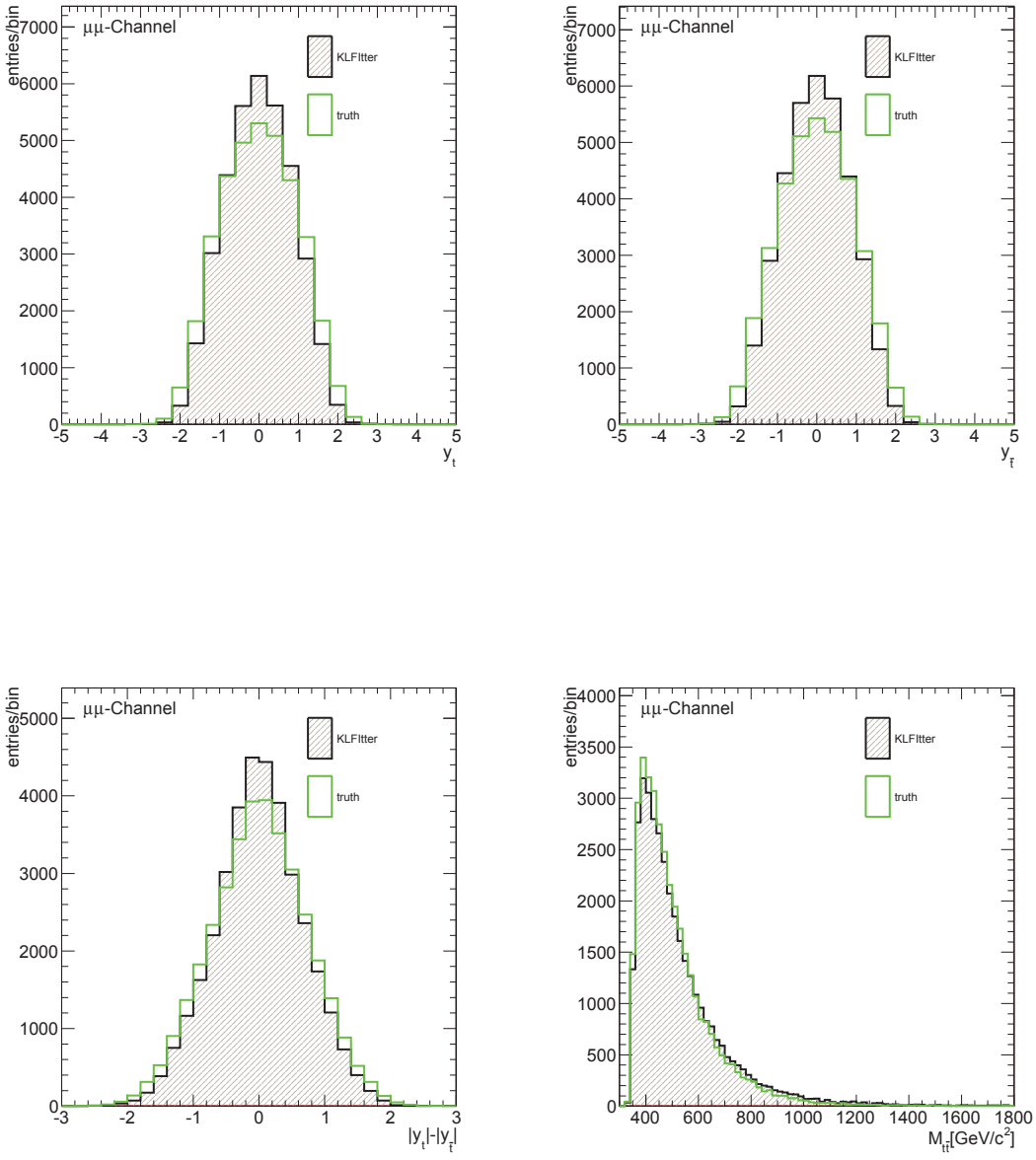

Figure C.15.: Distributions of top-quark (top left) and antitop-quark (top right) rapidity from the $t\bar{t}$ signal sample. Distributions of the difference of the absolute top- and antitop-quark rapidity $\Delta\,|y_{t\bar{t}}|$ (bottom left) and top-quark-pair invariant mass distribution (bottom right). All scale factors are applied except the luminosity scaling. Events are selected according to the tagged event selection. The KLFitter reconstruction was performed using the *kVeto* option.

C.3.3 $e\mu$-Channel

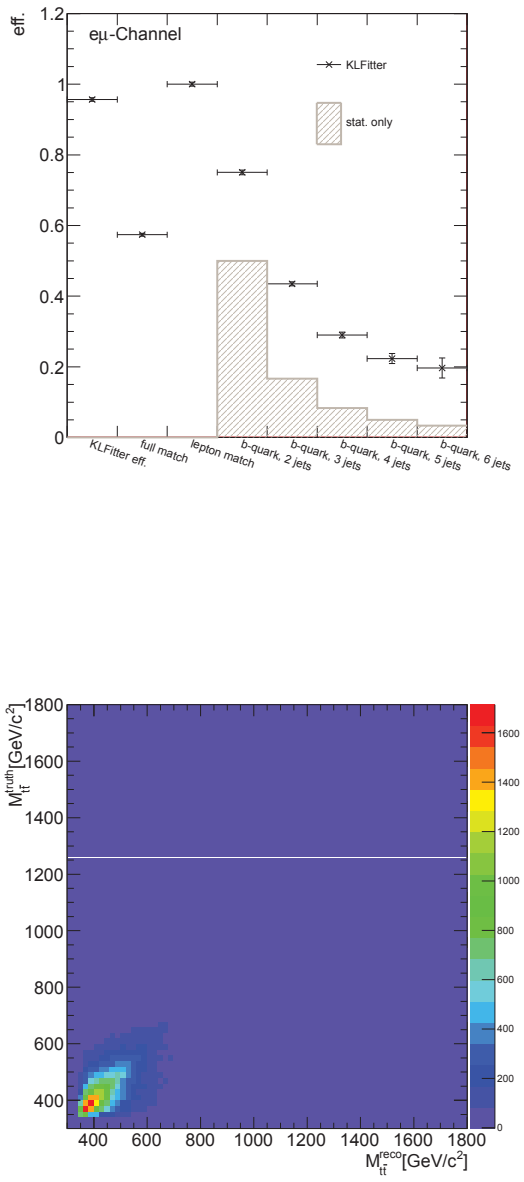

Figure C.16.: Distribution of the efficiency estimated for the $t\bar{t}$ signal sample (top). The plot shows the efficiency of the KLFitter reconstruction (*KLFitter*). Depicted in grey is the statistical probability (*stat. only*) to select the correct jet pair from the given multiplicity. Distribution of the top-quark-pair invariant mass distribution of the $t\bar{t}$ signal sample (bottom). The plot shows the KLFitter reconstructed value versus the true value from MC. All scale factors are applied except the luminosity scaling. Events are selected according to the tagged event selection. The KLFitter reconstruction was performed using the *kVeto* option.

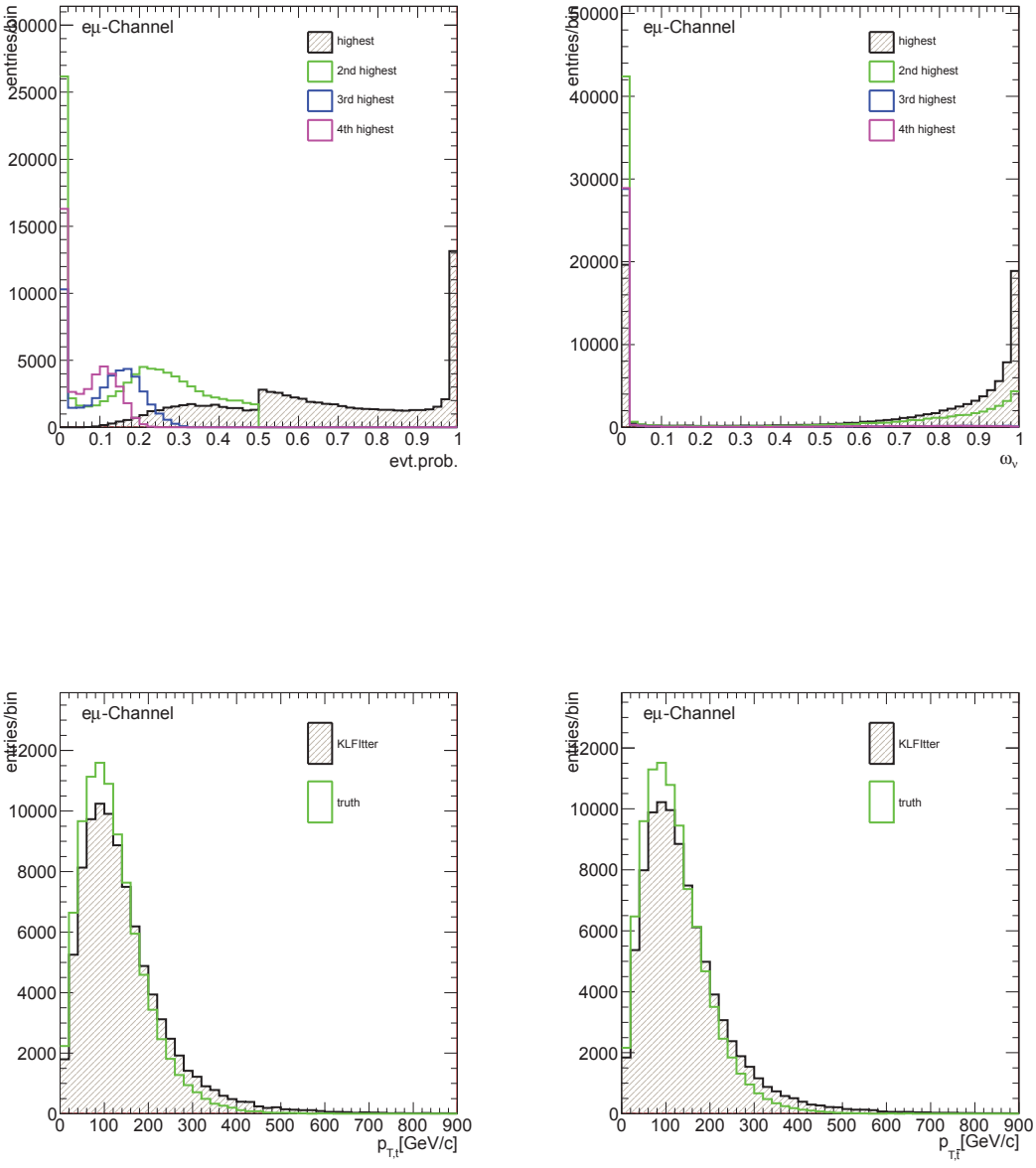

Figure C.17.: Distribution of four highest event probabilities (top left) and four highest neutrino weights for the jet permutation with maximum event probability (top right). Distributions of top-quark (left) and antitop-quark (right) transverse momentum from the $t\bar{t}$ signal sample. All scale factors are applied except the luminosity scaling. Events are selected according to the tagged event selection. The KLFitter reconstruction was performed using the *kVeto* option.

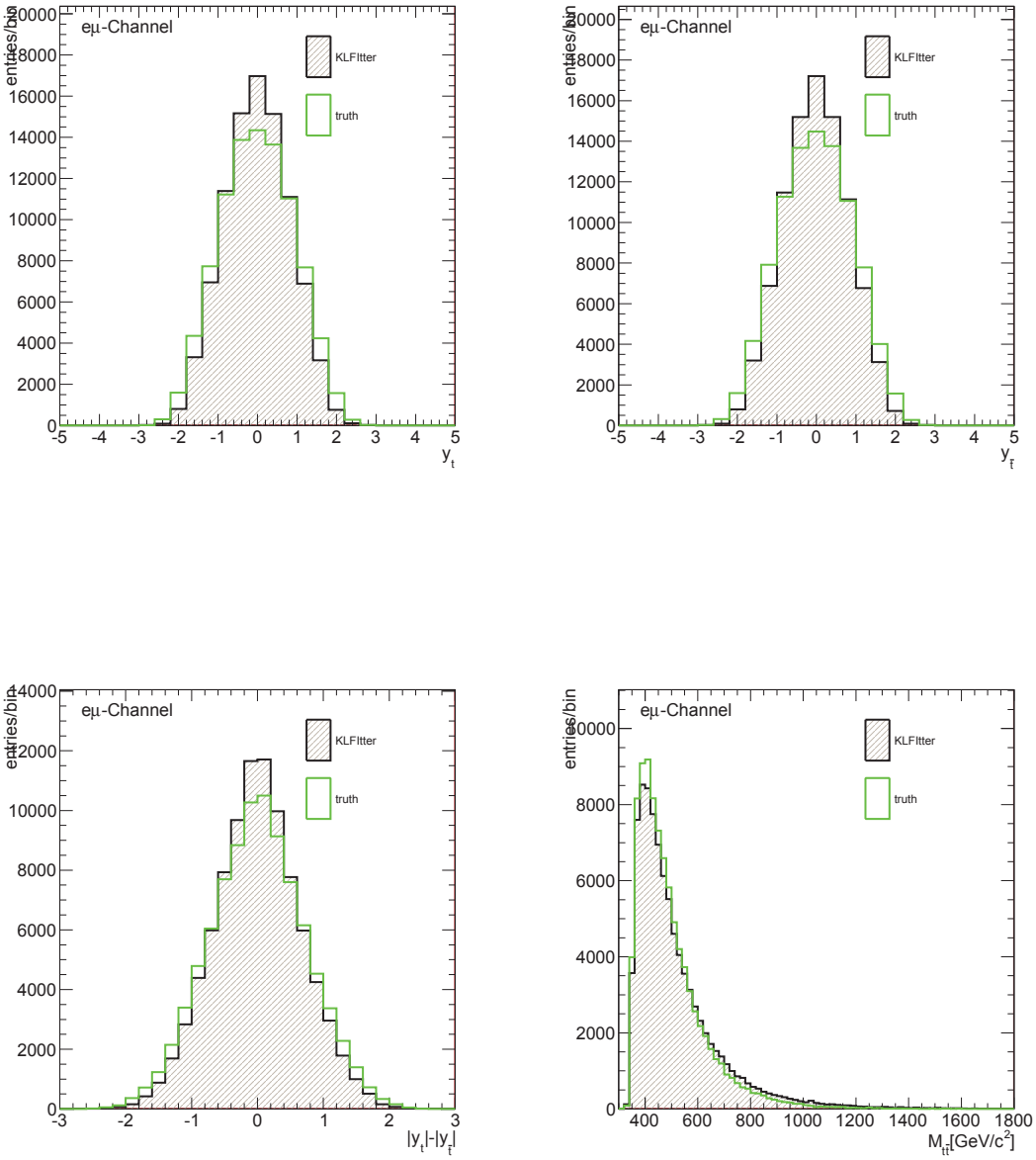

Figure C.18.: Distributions of top-quark (top left) and antitop-quark (top right) rapidity from the $t\bar{t}$ signal sample. Distributions of the difference of the absolute top- and antitop-quark rapidity $\Delta\,|y_{t\bar{t}}|$ (bottom left) and top-quark-pair invariant mass distribution (bottom right). All scale factors are applied except the luminosity scaling. Events are selected according to the tagged event selection. The KLFitter reconstruction was performed using the *kVeto* option.

C.4 KLFitter Reconstruction Control-Plots, Pretag Selection

C.4.1 *ee*-Channel

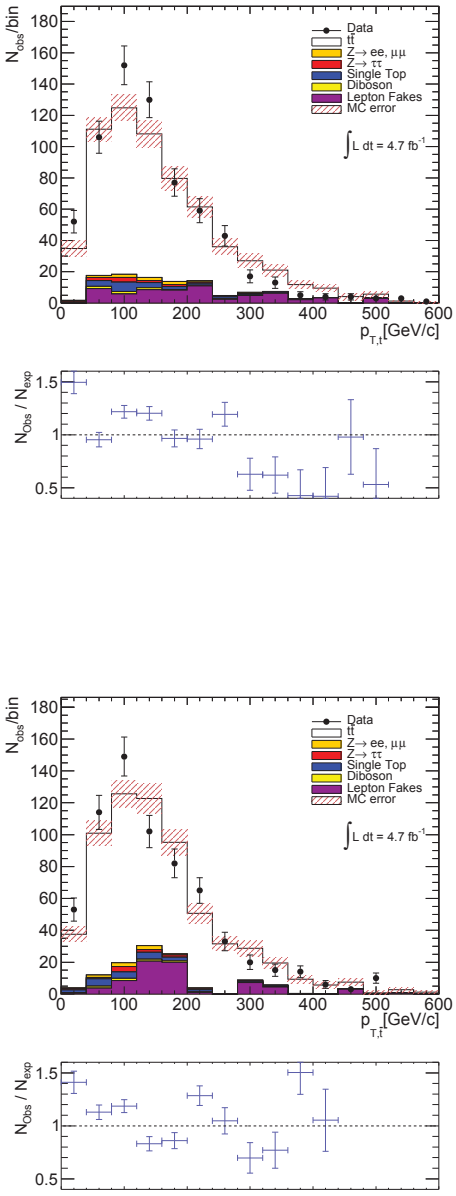

Figure C.19.: Distributions of KLFitter reconstructed top- (top) and antitop-quark (bottom) transverse momentum. The lower pads of the plots show the ratio between observed events in data (N_{obs}) and events expected from signal MC, background MC and fake lepton background (N_{exp}). All scale factors for MC are applied and samples are scaled to $\int L\,dt = 4.71\,\text{fb}^{-1}$. Events are selected according to the pretag event selection.

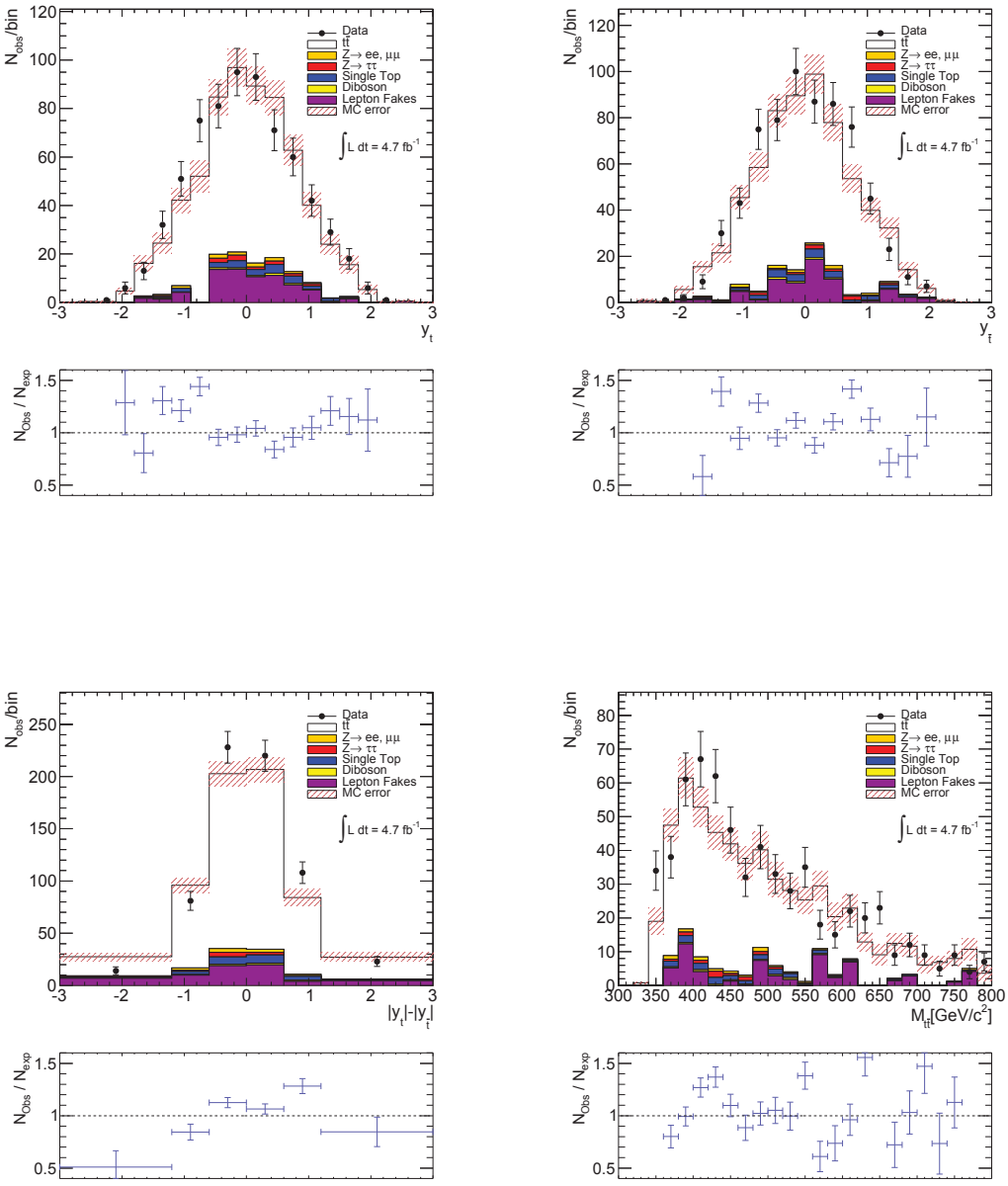

Figure C.20.: Distributions of KLFitter reconstructed top- (top left) and antitop-quark (top right) rapidity and the distribution of KLFitter reconstructed difference of the absolute top- and antitop- quark rapidity $\Delta\,|y_{t\bar{t}}|$ (bottom left) and the distribution of top-quark pair invariant mass (bottom right). The lower pads of the plots show the ratio between observed events in data (N_{obs}) and events expected from signal MC, background MC and fake lepton background (N_{exp}). All scale factors for MC are applied and samples are scaled to $\int L\,dt = 4.71\,\mathrm{fb}^{-1}$. Events are selected according to the pretag event selection.

C.4.2 $\mu\mu$-Channel

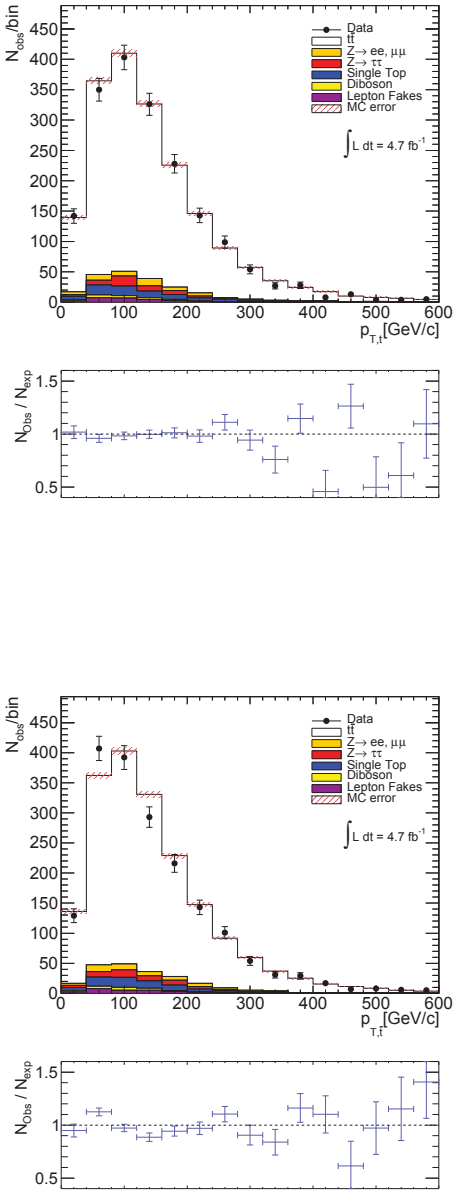

Figure C.21.: Distributions of KLFitter reconstructed top- (top) and antitop-quark (bottom) transverse momentum. The lower pads of the plots show the ratio between observed events in data (N_{obs}) and events expected from signal MC, background MC and fake lepton background (N_{exp}). All scale factors for MC are applied and samples are scaled to $\int L\,dt = 4.71\,\text{fb}^{-1}$. Events are selected according to the pretag event selection.

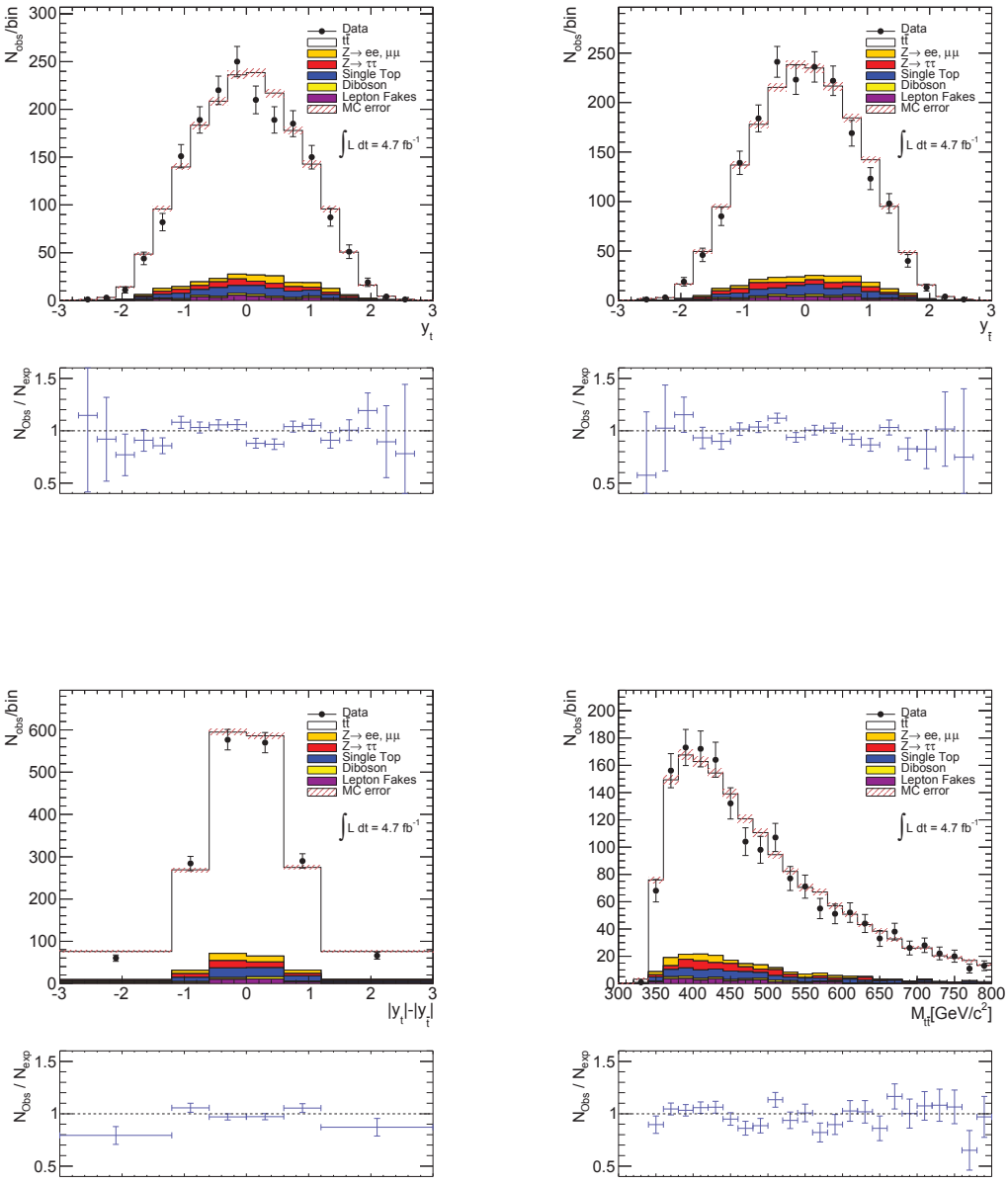

Figure C.22.: Distributions of KLFitter reconstructed top- (top left) and antitop-quark (top right) rapidity and the distribution of KLFitter reconstructed difference of the absolute top- and antitop- quark rapidity $\Delta\,|y_{t\bar{t}}|$ (bottom left) and the distribution of top-quark pair invariant mass (bottom right). The lower pads of the plots show the ratio between observed events in data (N_{obs}) and events expected from signal MC, background MC and fake lepton background (N_{exp}). All scale factors for MC are applied and samples are scaled to $\int L\,dt = 4.71\,\mathrm{fb}^{-1}$. Events are selected according to the pretag event selection.

C.4.3 $e\mu$-Channel

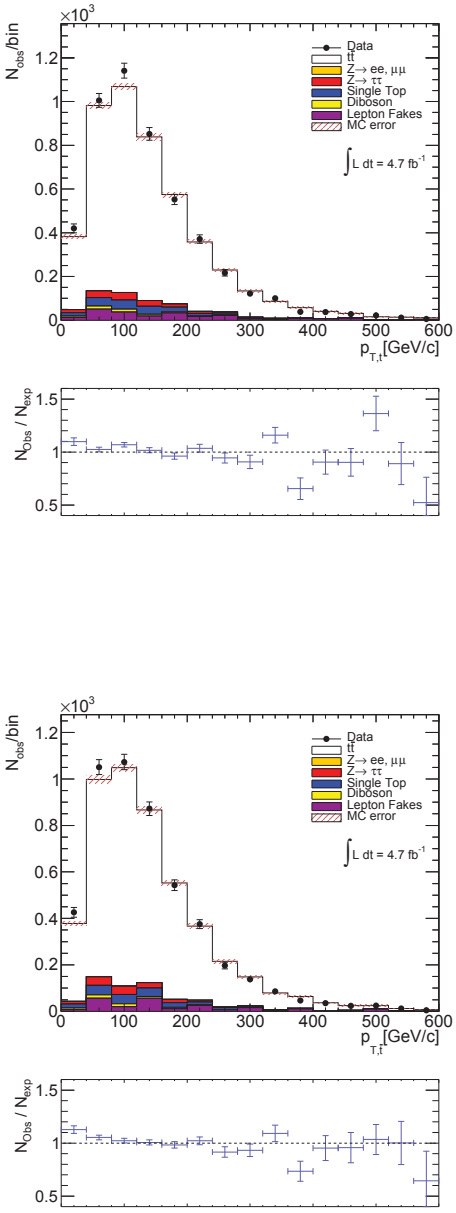

Figure C.23.: Distributions of KLFitter reconstructed top- (top) and antitop-quark (bottom) transverse momentum. The lower pads of the plots show the ratio between observed events in data (N_{obs}) and events expected from signal MC, background MC and fake lepton background (N_{exp}). All scale factors for MC are applied and samples are scaled to $\int L\,dt = 4.71\,\text{fb}^{-1}$. Events are selected according to the pretag event selection.

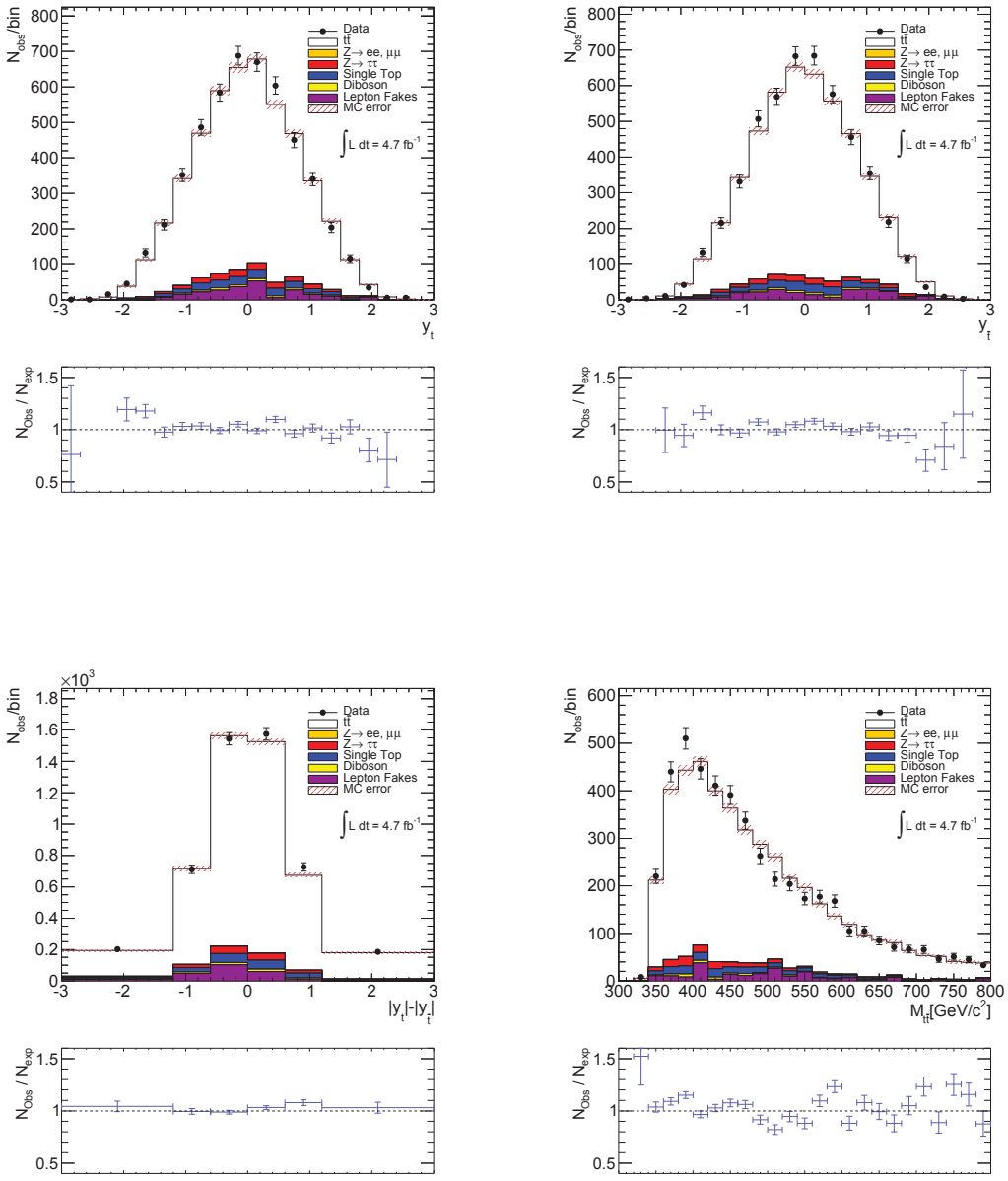

Figure C.24.: Distributions of KLFitter reconstructed top- (top left) and antitop-quark (top right) rapidity and the distribution of KLFitter reconstructed difference of the absolute top- and antitop- quark rapidity $\Delta\,|y_{t\bar{t}}|$ (bottom left) and the distribution of top-quark pair invariant mass (bottom right). The lower pads of the plots show the ratio between observed events in data (N_{obs}) and events expected from signal MC, background MC and fake lepton background (N_{exp}). All scale factors for MC are applied and samples are scaled to $\int L\,dt = 4.71\,\mathrm{fb}^{-1}$. Events are selected according to the pretag event selection.

C.5 KLFitter Reconstruction Control-Plots, Tagged Selection

C.5.1 *ee*-Channel

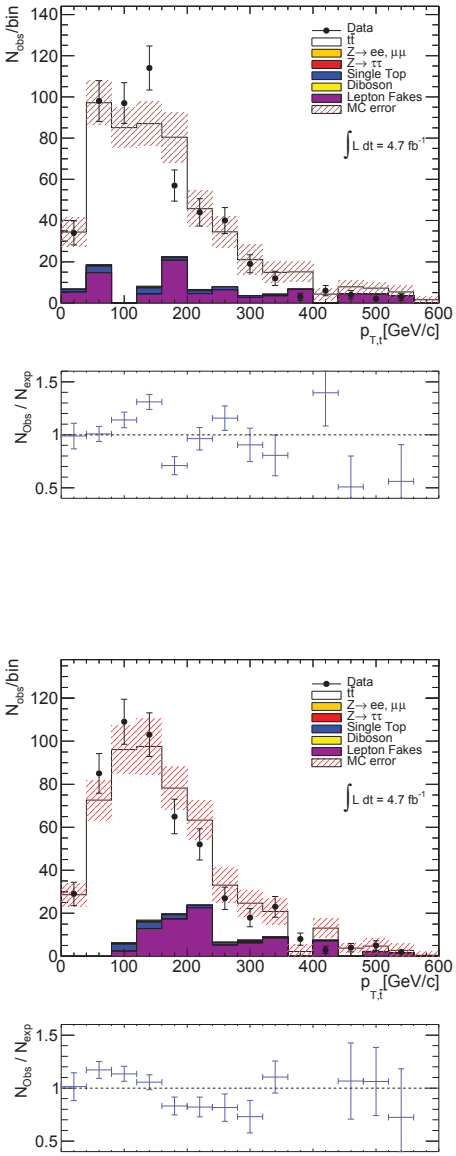

Figure C.25.: Distributions of KLFitter reconstructed top- (top left) and antitop-quark (top right) rapidity and the distribution of KLFitter reconstructed difference of the absolute top- and antitop- quark rapidity $\Delta|y_{t\bar{t}}|$ (bottom left) and the distribution of top-quark pair invariant mass (bottom right). The lower pads of the plots show the ratio between observed events in data (N_{obs}) and events expected from signal MC, background MC and fake lepton background (N_{exp}). All scale factors for MC are applied and samples are scaled to $\int L\,dt = 4.71\,\mathrm{fb}^{-1}$. Events are selected according to the tagged event selection. The KLFitter reconstruction was performed using the *kVeto* option.

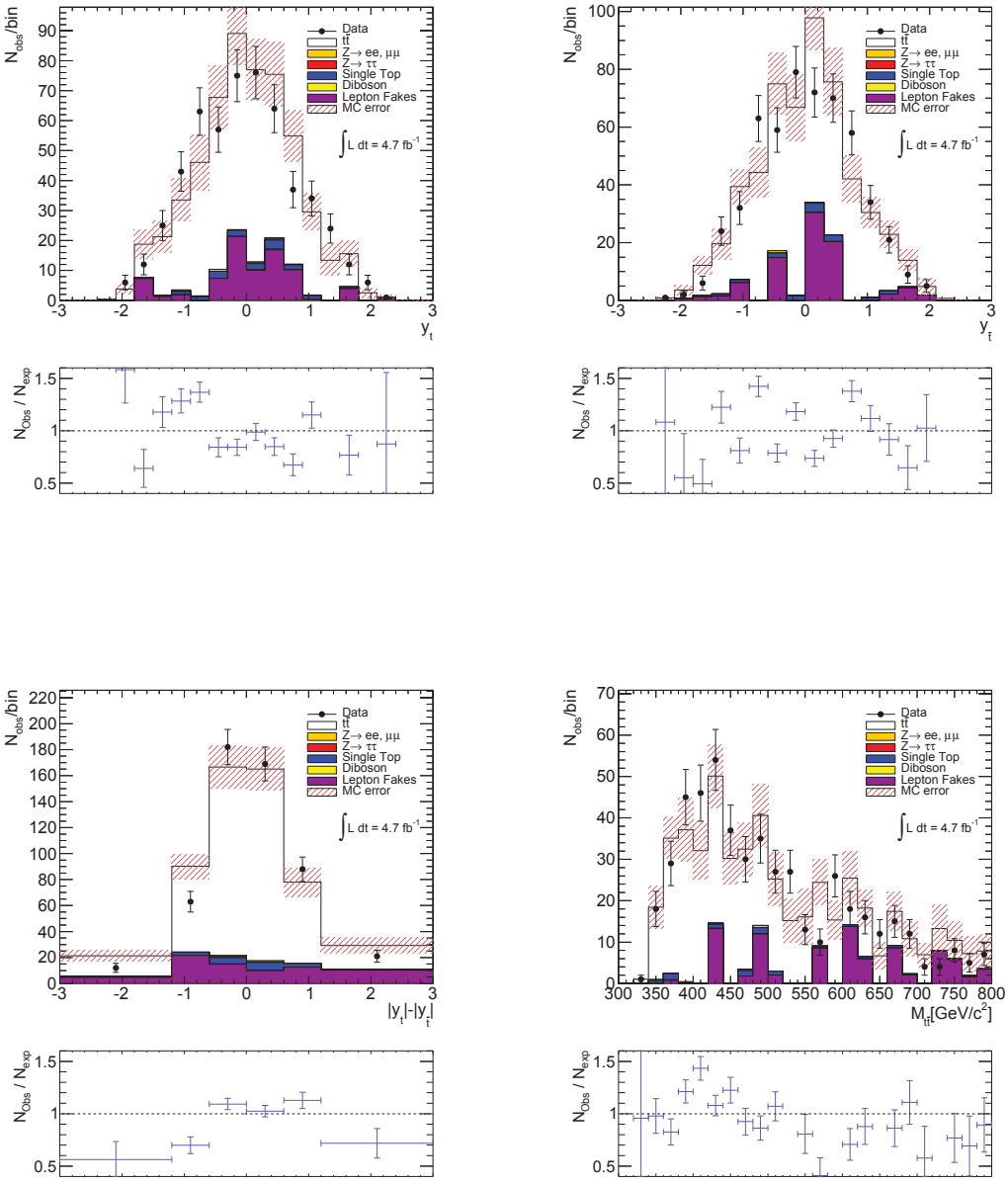

Figure C.26.: Distributions of KLFitter reconstructed top- (top left) and antitop-quark (top right) rapidity and the distribution of KLFitter reconstructed difference of the absolute top- and antitop- quark rapidity $\Delta\,|y_{t\bar{t}}|$ (bottom left) and the distribution of top-quark pair invariant mass (bottom right). The lower pads of the plots show the ratio between observed events in data (N_{obs}) and events expected from signal MC, background MC and fake lepton background (N_{exp}). All scale factors for MC are applied and samples are scaled to $\int L\,dt = 4.71\,\mathrm{fb}^{-1}$. Events are selected according to the tagged event selection. The KLFitter reconstruction was performed using the *kVeto* option.

C.5.2 $\mu\mu$-Channel

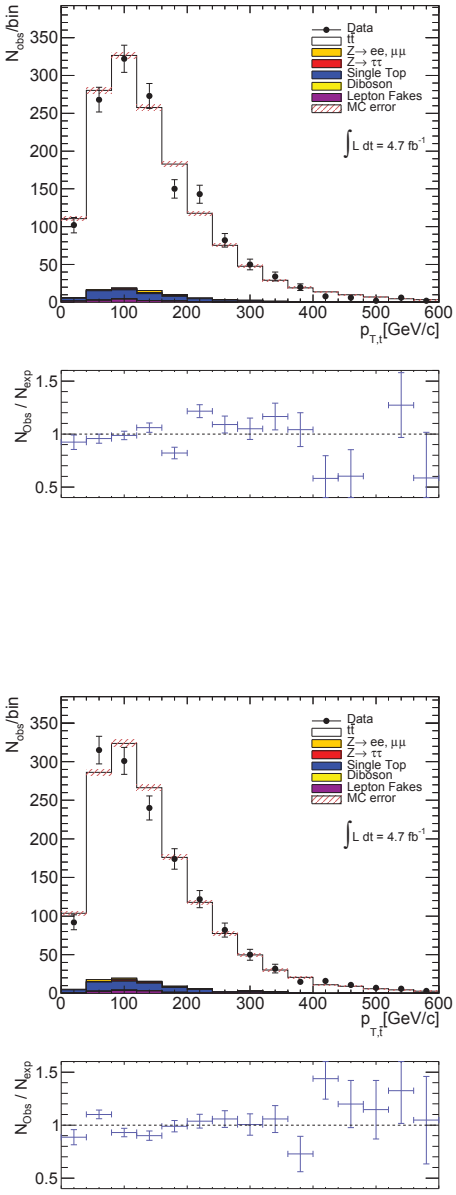

Figure C.27.: Distributions of KLFitter reconstructed top- (top left) and antitop-quark (top right) rapidity and the distribution of KLFitter reconstructed difference of the absolute top- and antitop- quark rapidity $\Delta\,|y_{t\bar{t}}|$ (bottom left) and the distribution of top-quark pair invariant mass (bottom right). The lower pads of the plots show the ratio between observed events in data (N_{obs}) and events expected from signal MC, background MC and fake lepton background (N_{exp}). All scale factors for MC are applied and samples are scaled to $\int L\,dt = 4.71\,\mathrm{fb}^{-1}$. Events are selected according to the tagged event selection. The KLFitter reconstruction was performed using the *kVeto* option.

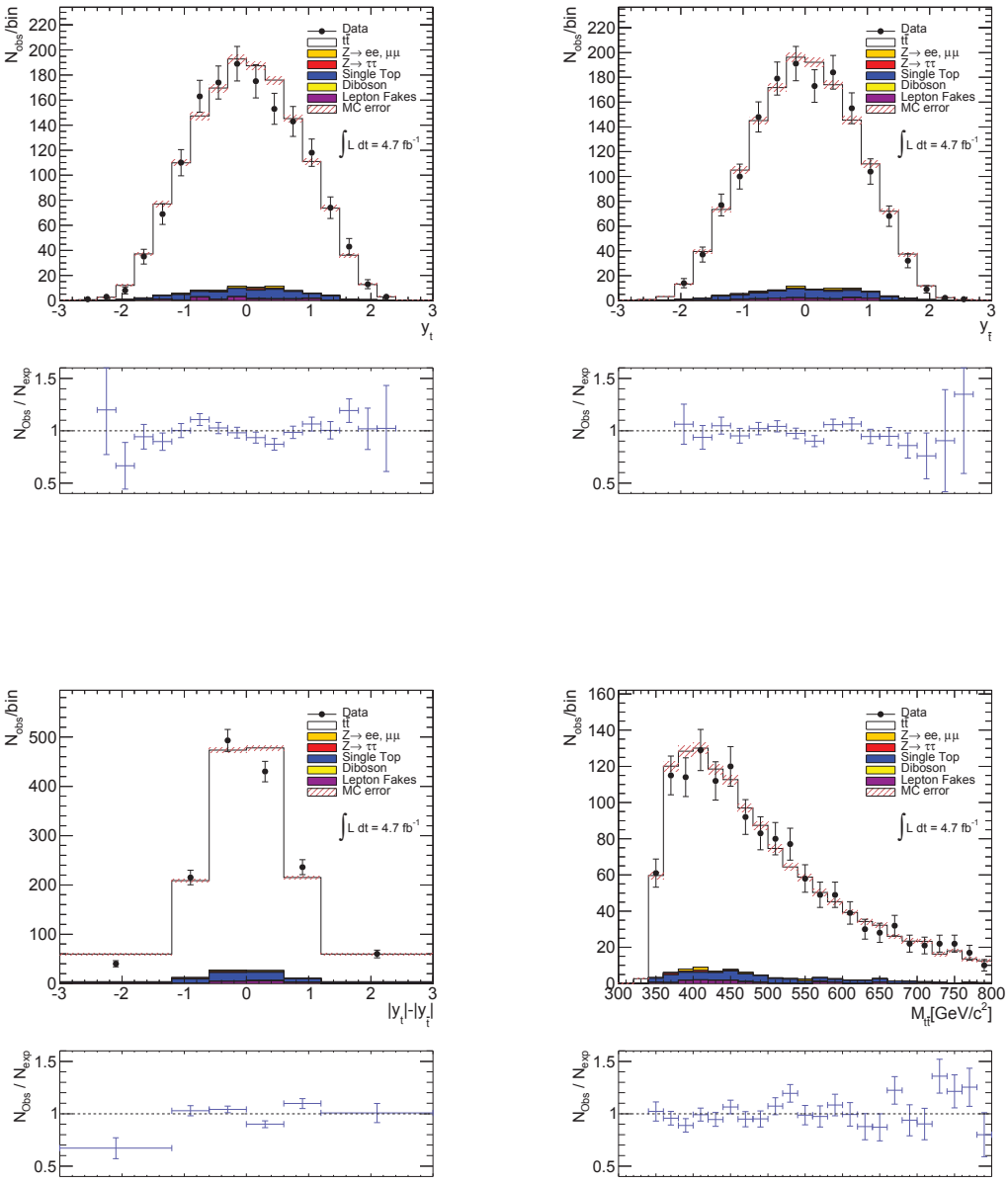

Figure C.28.: Distributions of KLFitter reconstructed top- (top left) and antitop-quark (top right) rapidity and the distribution of KLFitter reconstructed difference of the absolute top- and antitop- quark rapidity $\Delta\,|y_{t\bar{t}}|$ (bottom left) and the distribution of top-quark pair invariant mass (bottom right). The lower pads of the plots show the ratio between observed events in data (N_{obs}) and events expected from signal MC, background MC and fake lepton background (N_{exp}). All scale factors for MC are applied and samples are scaled to $\int L\,dt = 4.71\,\mathrm{fb}^{-1}$. Events are selected according to the tagged event selection. The KLFitter reconstruction was performed using the *kVeto* option.

C.5.3 $e\mu$-Channel

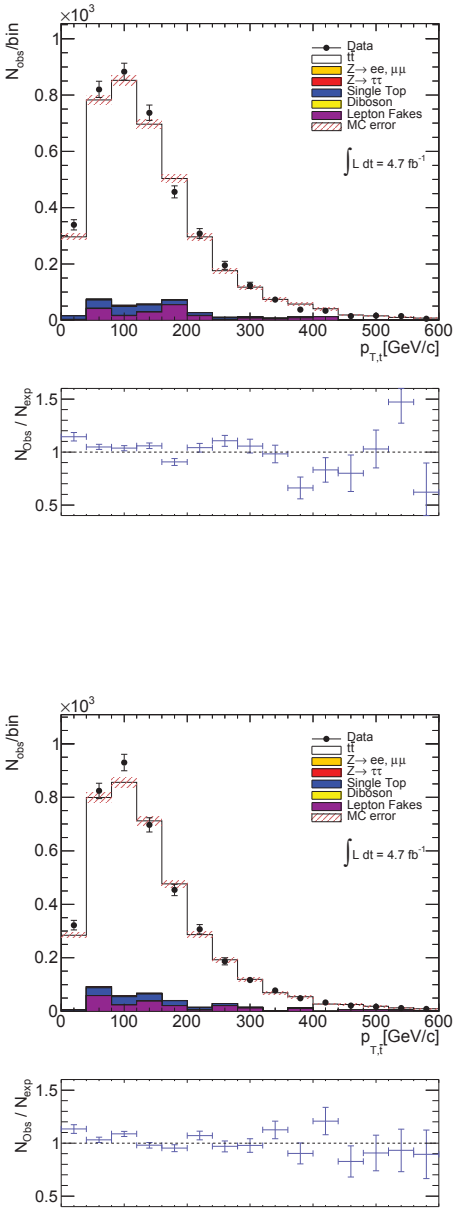

Figure C.29.: Distributions of KLFitter reconstructed top- (top left) and antitop-quark (top right) rapidity and the distribution of KLFitter reconstructed difference of the absolute top- and antitop- quark rapidity $\Delta\,|y_{t\bar{t}}|$ (bottom left) and the distribution of top-quark pair invariant mass (bottom right). The lower pads of the plots show the ratio between observed events in data (N_{obs}) and events expected from signal MC, background MC and fake lepton background (N_{exp}). All scale factors for MC are applied and samples are scaled to $\int L\,dt = 4.71\,\mathrm{fb}^{-1}$. Events are selected according to the tagged event selection. The KLFitter reconstruction was performed using the *kVeto* option.

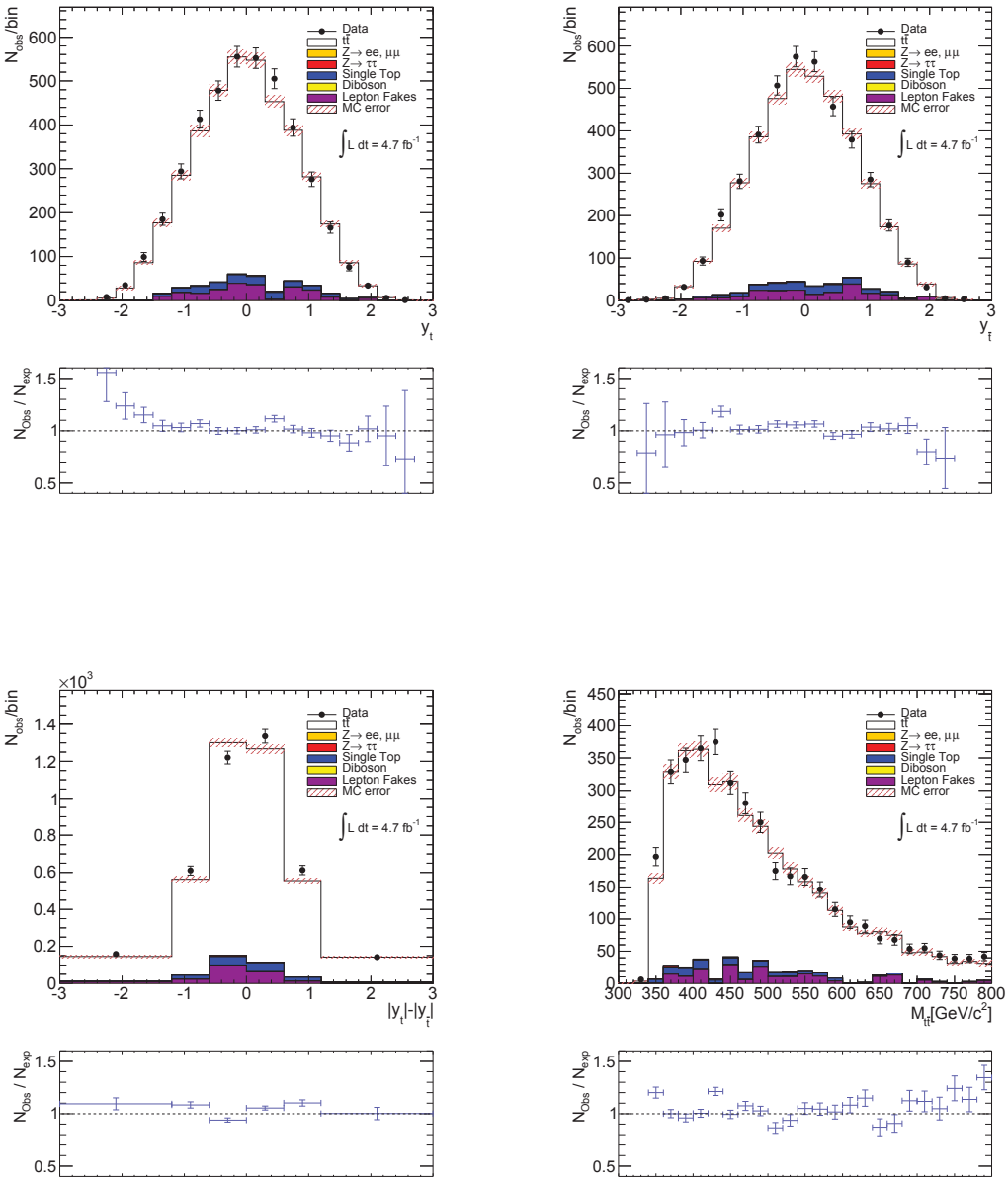

Figure C.30.: Distributions of KLFitter reconstructed top- (top left) and antitop-quark (top right) rapidity and the distribution of KLFitter reconstructed difference of the absolute top- and antitop- quark rapidity $\Delta\,|y_{t\bar{t}}|$ (bottom left) and the distribution of top-quark pair invariant mass (bottom right). The lower pads of the plots show the ratio between observed events in data (N_{obs}) and events expected from signal MC, background MC and fake lepton background (N_{exp}). All scale factors for MC are applied and samples are scaled to $\int L\,dt = 4.71\,\mathrm{fb}^{-1}$. Events are selected according to the tagged event selection. The KLFitter reconstruction was performed using the *kVeto* option.

Appendix D

Monte Carlo Unfolding Studies

In order to find the optimal settings and to verify the validity of the results of the unfolding procedure studies on MC are performed. The details on these studies are described in this section.

D.1 Charge Asymmetry Reweighting Procedure

The asymmetry reweighting procedure mentioned in Section 9.3 requires an additional event weight $\omega_{\pm}$. This weight has to be calculated for each channel separately and has two values ($\pm$) which are applied to every event according to the following conditions:

- if $\Delta\left|y_{t\bar{t}}^{\text{truth}}\right| < 0$, apply ω_{-},
- if $\Delta\left|y_{t\bar{t}}^{\text{truth}}\right| > 0$, apply ω_{+}.

The two additional event weights are determined from the events of the MC signal sample after selection cut 1 (selecting true dilepton events). The top-quark charge asymmetry is calculated as described in Section 2.4 using the number of events N_{-} with $\Delta\left|y_{t\bar{t}}\right| = |y_t| - |y_{\bar{t}}| < 0$, and the number of events N_{+} with $\Delta\left|y_{t\bar{t}}\right| > 0$:

$$A_{C,t\bar{t}} = \frac{N_{+} - N_{-}}{N_{+} + N_{-}}\,. \tag{D.1}$$

The weights $\omega_{\pm}$ are used as an additional factor so that the charge asymmetry of the MC signal sample can be changed to different values, $A_{C,\text{rew}}^{t\bar{t}}$, while the overall number of events remains the same

$$A_{C,t\bar{t}}^{\text{rew}} = \frac{\omega_{+}N_{+} - \omega_{-}N_{-}}{\omega_{+}N_{+} + \omega_{-}N_{-}}\,. \tag{D.2}$$

The weights are calculated using

$$\omega_{+} = \frac{N_{+}^{\text{rew}}}{N_{+}^{\text{truth}}} \;\text{ and }\; \omega_{-} = \frac{N_{-}^{\text{rew}}}{N_{-}^{\text{truth}}}\,, \tag{D.3}$$

where $N_{\pm}^{\text{truth}}$ are the scaled event numbers for $\Delta\left|y_{t\bar{t}}^{\text{truth}}\right| \gtrless 0$ and

$$N_{+}^{\text{rew}} = \frac{1}{2} N_{C1} \left(1 + A_C^{\text{rew}}\right) , \tag{D.4}$$

$$N_{-}^{\text{rew}} = N_{C1} - N_{+}^{\text{rew}} . \tag{D.5}$$

The number N_{C1} is the number of events after selection cut 1.

D.2 Estimation of the Settings for the BIU, Tagged Event Selection

This Section features plots of the evolution of the estimated error of the unfolded charge asymmetry (Figure D.1), the evolution of the convergence (Figure D.2) and the evolution of the pull (Figure D.3). Furthermore examples of the linear fit performed on a distribution of an average unfolded asymmetry are shown in the Figures D.4 and D.5. For a comprehensive description of the different properties and the derivation of the data points refer to Section 9.4.

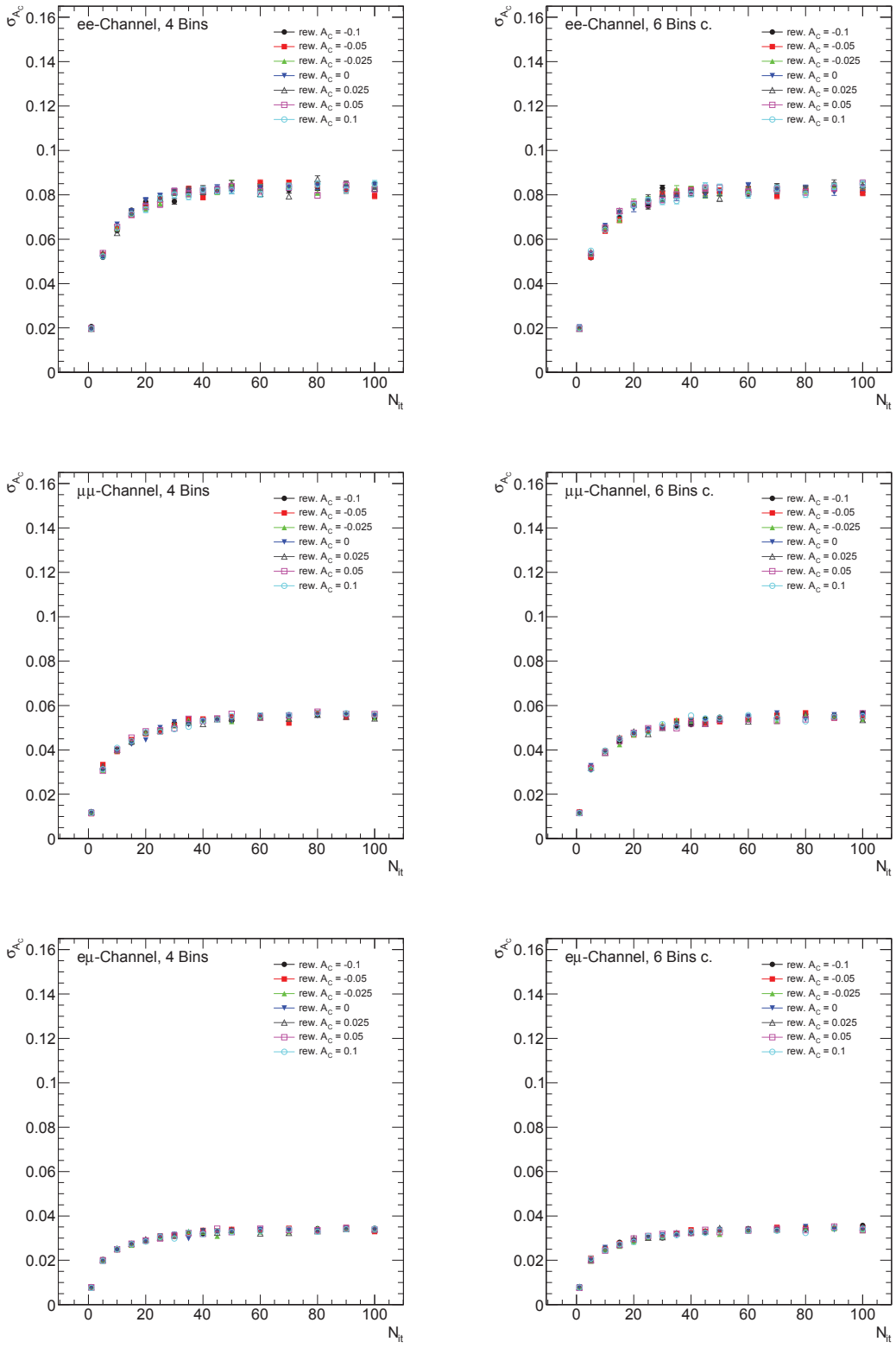

Figure D.1.: The expected statistical error σ_{A_C} of the charge asymmetry versus the regularisation strength N_{it} for different reweighted charge asymmetries *rew* A_C of the unfolding sample. The data points are derived for $N_P = 5000$ ensembles of pseudo-data. Top, middle and bottom row show the three dileptonic decay channels, using the *4 bins* (left) and the *6 bins c* (right) discretisations. The errors are statistical errors and the tagged selection is used.

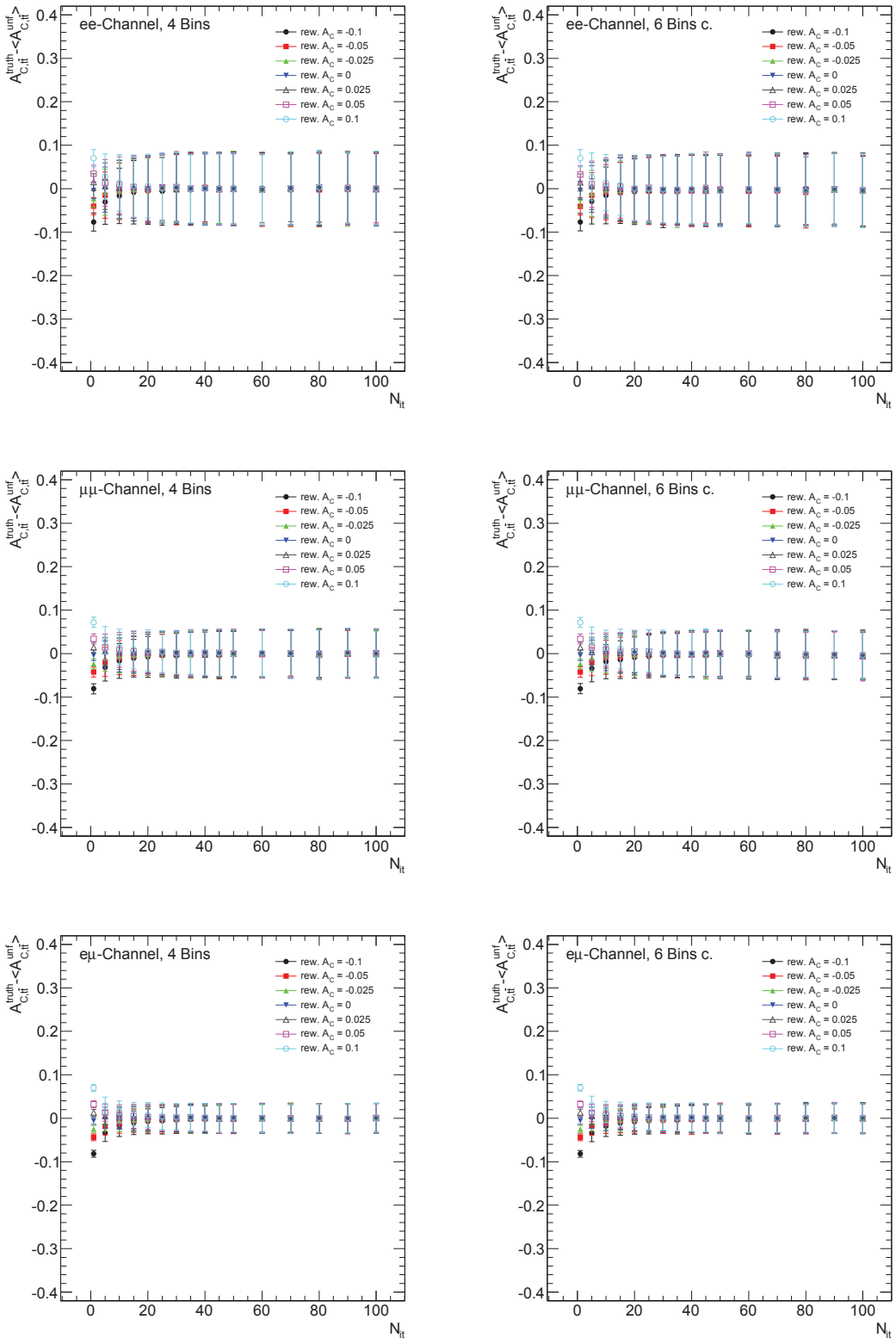

Figure D.2.: The convergence $A_{C,t\bar{t}}^{\text{truth}} - \langle A_{C,t\bar{t}}^{\text{unf}} \rangle$ of the charge asymmetry versus the regularisation strength N_{it} for different reweighted charge asymmetries *rew* A_C of the unfolding sample. The data points are derived for $N_P = 5000$ ensembles of pseudo-data. Top, middle and bottom row show the three dileptonic decay channels, using the *4 bins* (left) and the *6 bins c* (right) discretisations. The errors are statistical errors and the pretag selection is used.

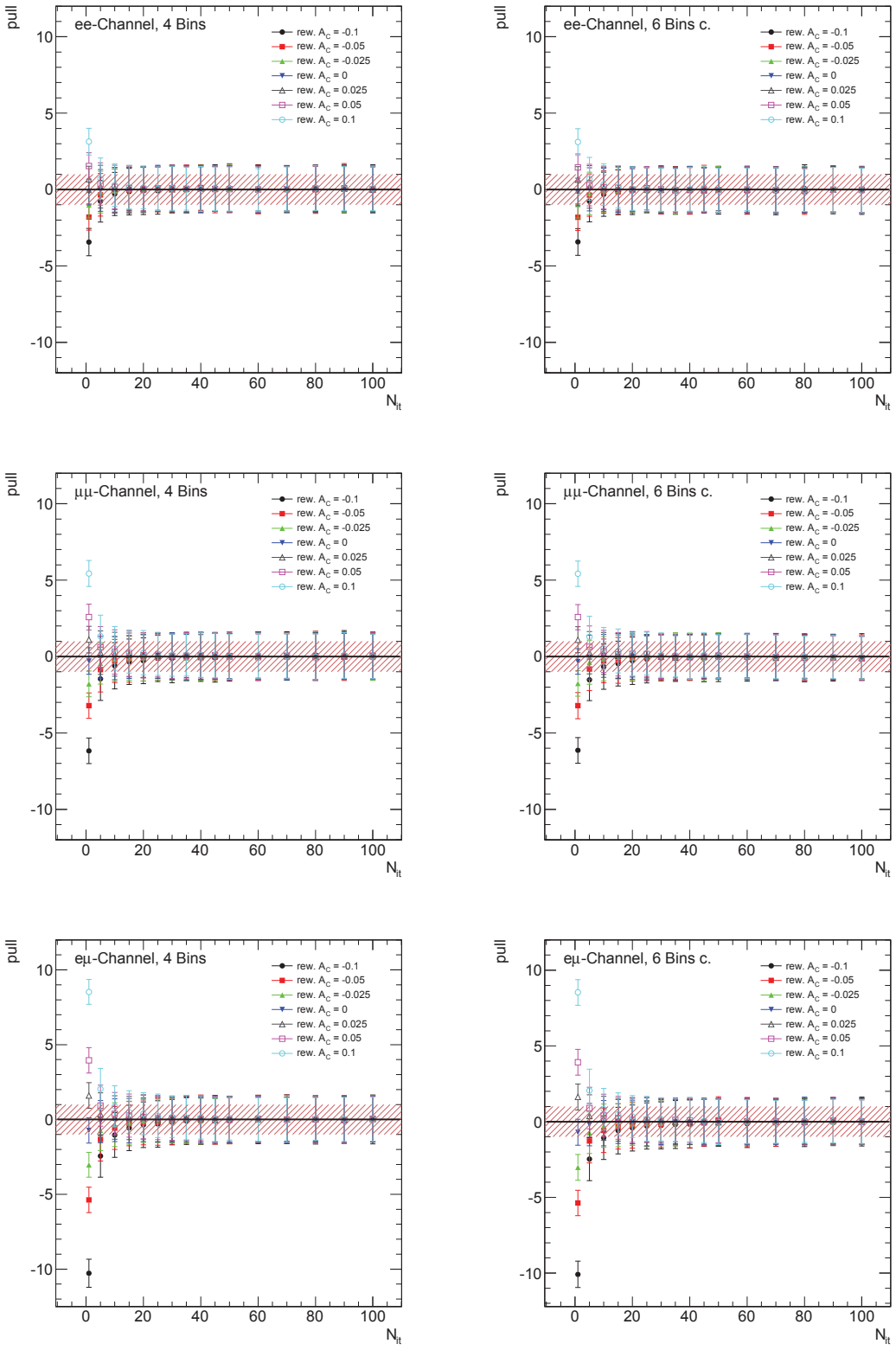

Figure D.3.: The averaged pull versus the regularisation strength N_{it} for different reweighted charge asymmetries *rew* A_C of the unfolding sample. The data points are derived for $N_P = 5000$ ensembles of pseudo-data. Top, middle and bottom row show the three dileptonic decay channels, using the *4 bins* (left) and the *6 bins c* (right) discretisations. The errors are statistical errors and the tagged selection is used.

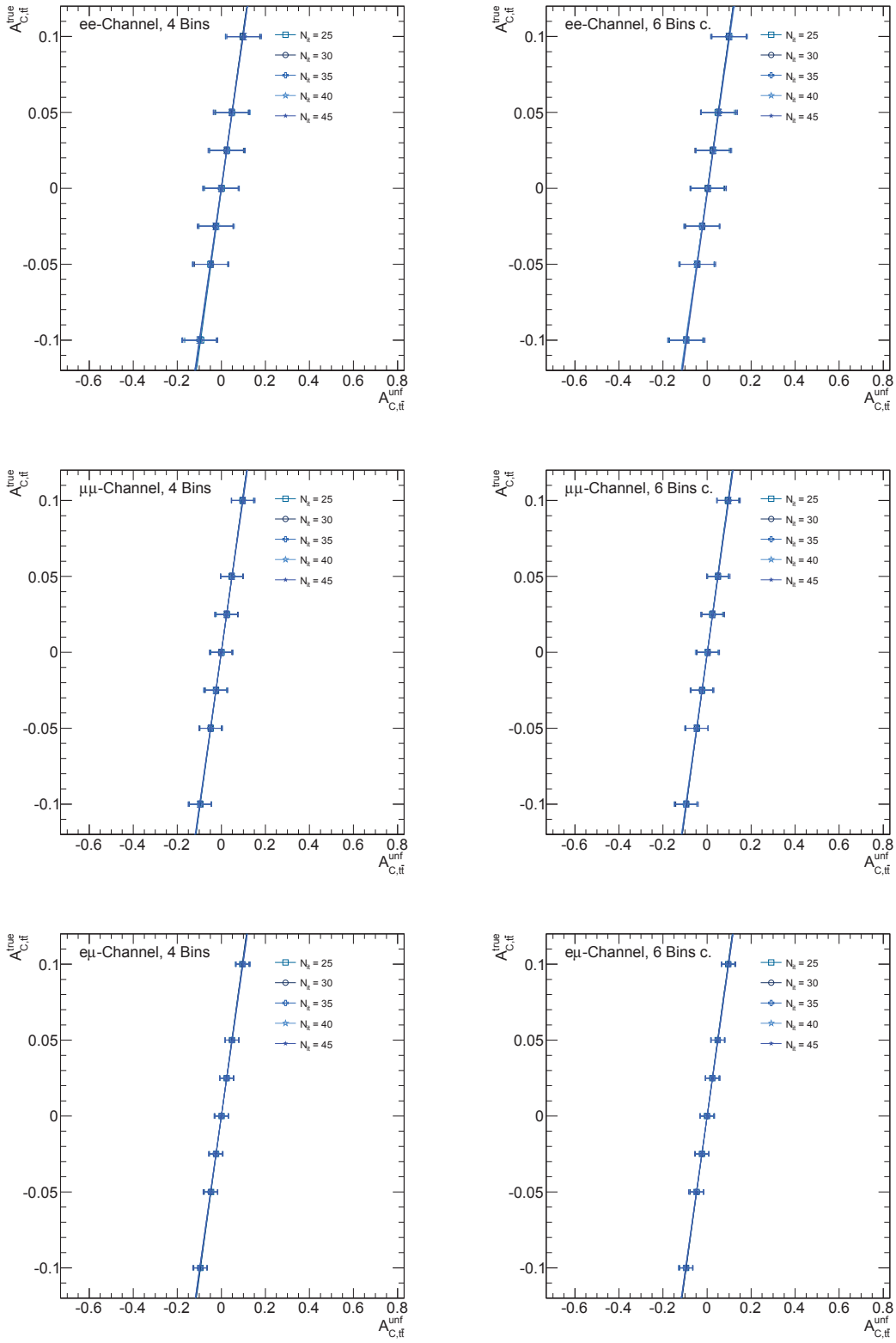

Figure D.4.: A compilation of linear fits of the $A^{\mathrm{unf}}_{c,t\bar{t}}$ versus $A^{\mathrm{true}}_{c,t\bar{t}}$ distribution for different regularisation strengths N_{it}. The fit is described in Section 9.3. Top, middle and bottom row show the three dileptonic decay channels, using the *4 bins* (left) and the *6 bins c* (right) discretisations. Shown are errors are statistical errors and the tagged selection is used.

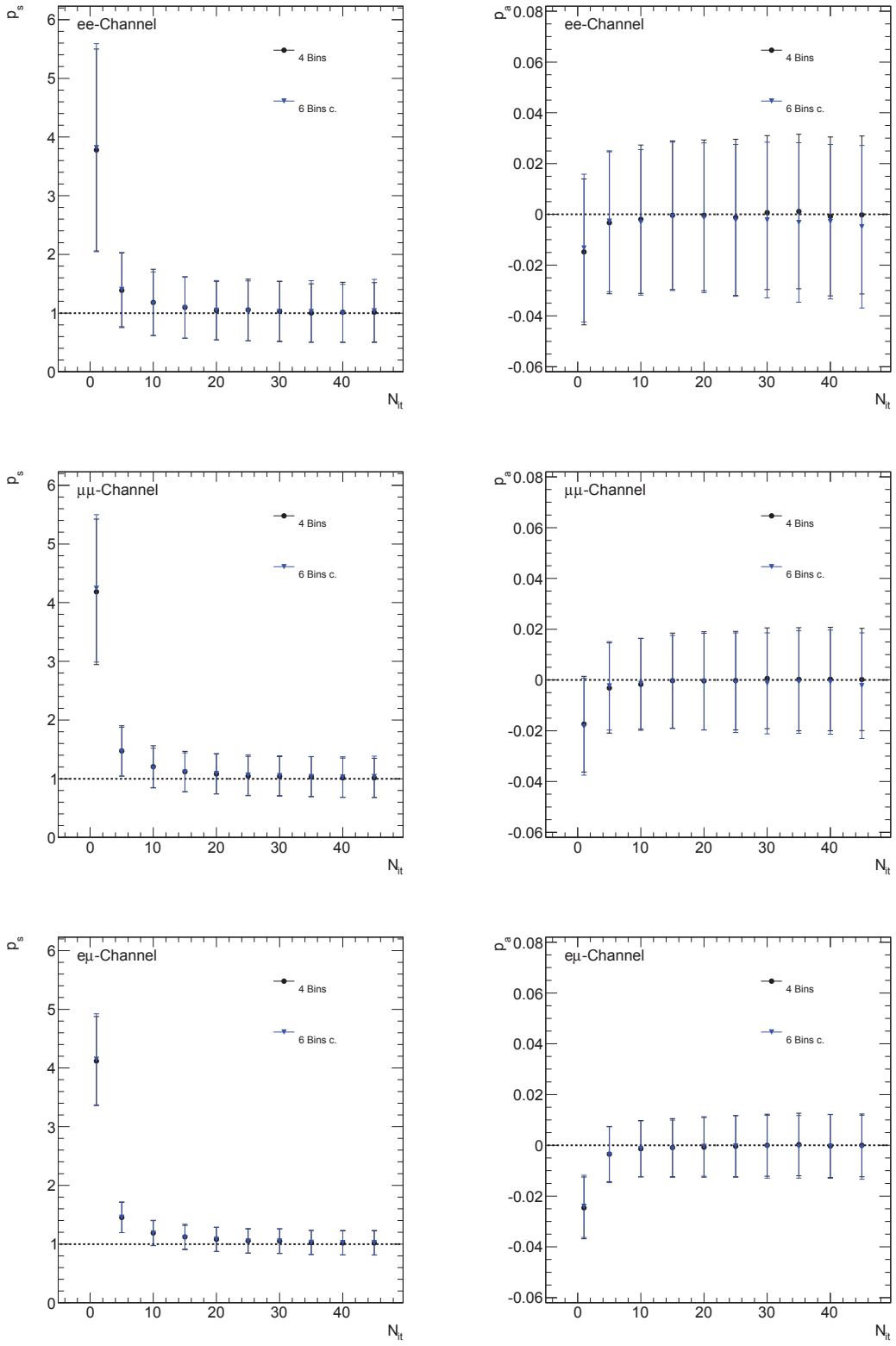

Figure D.5.: The slopes (left) and the axis intercept (right) of a linear fit versus the regularisation strength N_{it}. The fit is described in Section 9.3. Each plot features the results for different discretisations. Top, middle and bottom row show the results for the three top-quark pair decay channels, the errors are statistical errors and the tagged selection is used.

D.3 Calculation of the Linear Scaling Uncertainty

The statistical error of the unfolding procedure is estimated from the width of the posterior distribution of the unfolded charge asymmetries. Additionally the linear scaling (LS) of the chosen unfolding method has to be taken into account. LS means in this case that the result of the unfolding remains unbiased by the training sample and stable for different values of charge asymmetries. The chosen unfolding method proved to fulfil these requirements as is shown in Appendix D.2, but the uncertainty on the parameters of the linear fit (see Table 9.1) has to be taken into account. The linear scaling uncertainty (LSU) σ_{lin} is added in quadrature to the statistical error σ_{A_C} estimated from the posterior distribution of the unfolded charge asymmetry. The LSU is calculated from the Gaussian error propagation of Equation 9.22:

$$\sigma_{\text{lin}}^2 = \left(A_{C,t\bar{t}}^{\text{unf}} \;\sigma_{p_s}\right)^2 + \sigma_{p_a}^2 + \left(p_s \;\sigma_{A_C}^{\text{unf}}\right)^2 , \tag{D.6}$$

where $\sigma_{A_C}^{\text{unf}}$ is calculated using:

$$\sigma_{A_C}^{\text{unf}} = \frac{2}{\left(N_+ + N_-\right)^2} \sqrt{\left(N_- \;\sigma_{N_+}\right)^2 + \left(N_+ \;\sigma_{N_-}\right)^2}, \tag{D.7}$$

where $N_\pm$ are the numbers of events with

$$N_+ \;=\; N(|y_t| - |y_{\bar{t}}| > 0)\,, \tag{D.8}$$
$$N_- \;=\; N(|y_t| - |y_{\bar{t}}| < 0)\,. \tag{D.9}$$

Where y_t ($y_{\bar{t}}$) is the rapidity of the reconstructed top- (antitop-) quark. The uncertainty of $N_\pm$ is defined as

$$\sigma_{N_\pm}^2 = \sum_{i,j=1}^{n_{\text{bins}}} p_i^\pm \; c_{ij} \; p_j^\pm \,, \tag{D.10}$$

where c_{ij} are the entries of the covariance matrix provided by the unfolding procedure and p^+ and p^- are given by

$$p^+ = \begin{pmatrix} p_1 & = & 0 \\ & \vdots & \\ p_k & = & 0 \\ p_{k+1} & = & 1 \\ & \vdots & \\ p_{n_{\text{bins}}} & = & 1 \end{pmatrix} \quad \text{and} \quad p^- = \begin{pmatrix} p_1 & = & 1 \\ & \vdots & \\ p_k & = & 1 \\ p_{k+1} & = & 0 \\ & \vdots & \\ p_{n_{\text{bins}}} & = & 0 \end{pmatrix} . \tag{D.11}$$

Here n_{bins} is the number of bins in the chosen discretisation and $k = n_{\text{bins}}/2$. The covariance matrices of the results of the data unfolding are listed in Appendix E.2.1.

Appendix E

Additional Information on Data Unfolding

The central value of the top-quark charge asymmetry is derived from the $\Delta|y_{t\bar{t}}|$ distribution after a single application of Bayesian iterative unfolding (BIU). The $\Delta|y_{t\bar{t}}|$ distribution is derived (separately for each top-quark pair decay channel) from the ATLAS 2011 7 TeV dataset. The regularisation strength $N_{it} = 40$ and the *4 bins* discretisation is used. In order to study the influence of background contributions the unfolding is performed on the $\Delta|y_{t\bar{t}}|$ distribution directly after the KLFitter reconstruction and separately on the same distribution after bin-wise subtraction of the KLFitter reconstructed MC and fake leptonic backgrounds.

E.1 Unfolded $\Delta|y_{t\bar{t}}|$ Distributions in Data

Figure E.1 (tagged event selection) shows the $\Delta|y_{t\bar{t}}|$ distributions for the ATLAS 2011 7 TeV dataset, the MC@NLO signal MC and the background contributions before the unfolding is applied. Figure E.2 (tagged event selection) shows the unfolded $\Delta|y_{t\bar{t}}|$ distribution with and without bin-wise background subtraction. From this distribution the unfolded central value of charge asymmetry $A_{C,t\bar{t}}^{\text{meas}}$ is calculated. Figure E.3 (tagged event selection) shows the posterior distribution of $A_{C,t\bar{t}}^{\text{meas}}$ for $N_P = 100000$ ensembles of pseudo-data. From these distributions the statistical error σ_{A_C} is derived. A Gaussian model is fitted to these distributions and the width of the Gaussian results in σ_{A_C}.

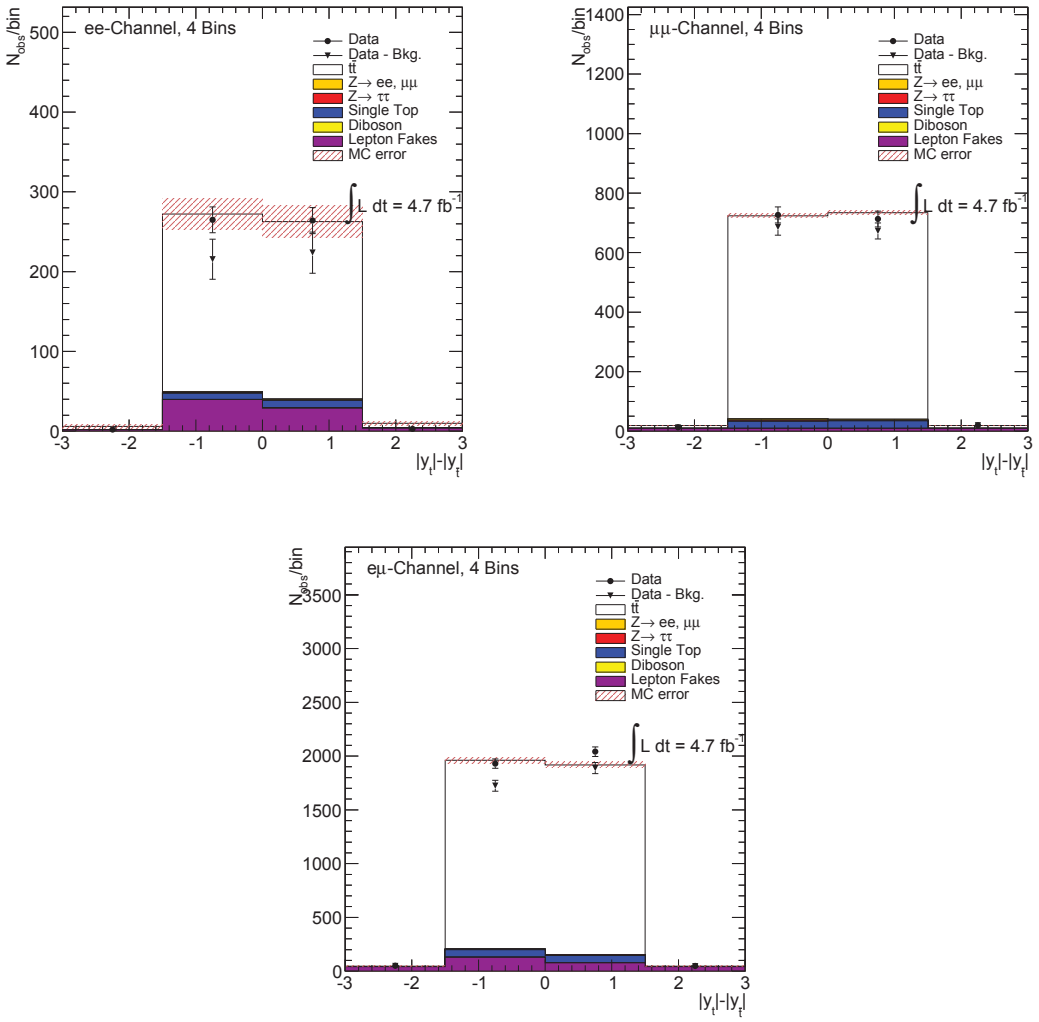

Figure E.1.: The $\Delta\,|y_{t\bar{t}}| = |y_t| - |y_{\bar{t}}|$ distributions for the ATLAS 2011 7 TeV dataset (with and without bin-wise background subtraction), the MC@NLO signal MC and the background contributions ($Z \to (ee, \mu\mu, \tau\tau)$, single top, diboson and lepton fakes). The MC contributions are scaled to an integrated luminosity of $\int L\,dt = 4.71\,\mathrm{fb}^{-1}$. The events are selected according to the tagged event selection. The errors shown are statistical errors.

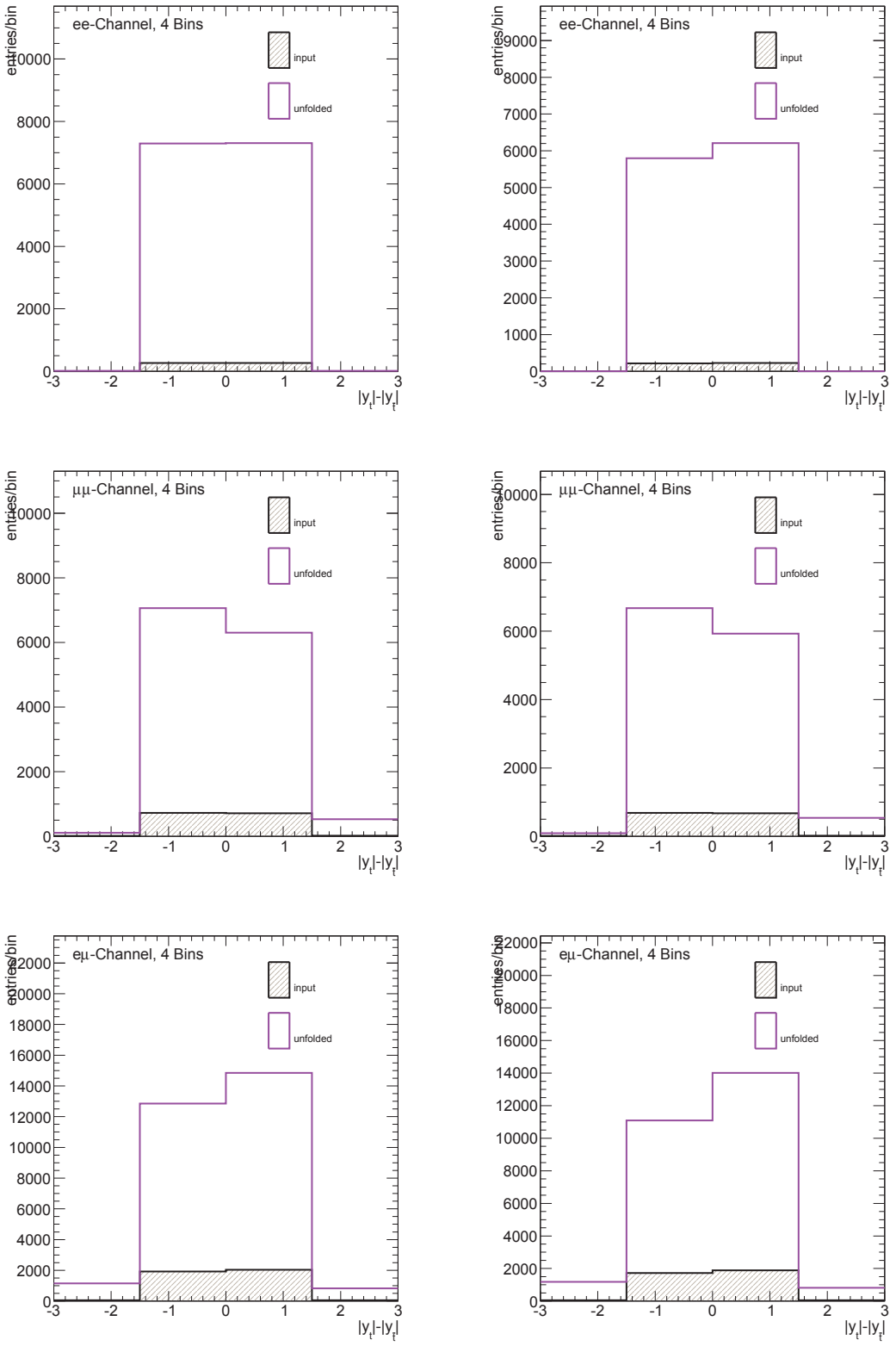

Figure E.2.: The unfolded $\Delta|y_{t\bar{t}}| = |y_t| - |y_{\bar{t}}|$ distributions for the ATLAS 2011 7 TeV dataset with (left) and without (right) bin-wise background subtraction. The top, middle and bottom rows show the distributions for the dielectron, dimuon and electron-muon top-quark pair decay channels. The events are selected according to the tagged event selection.

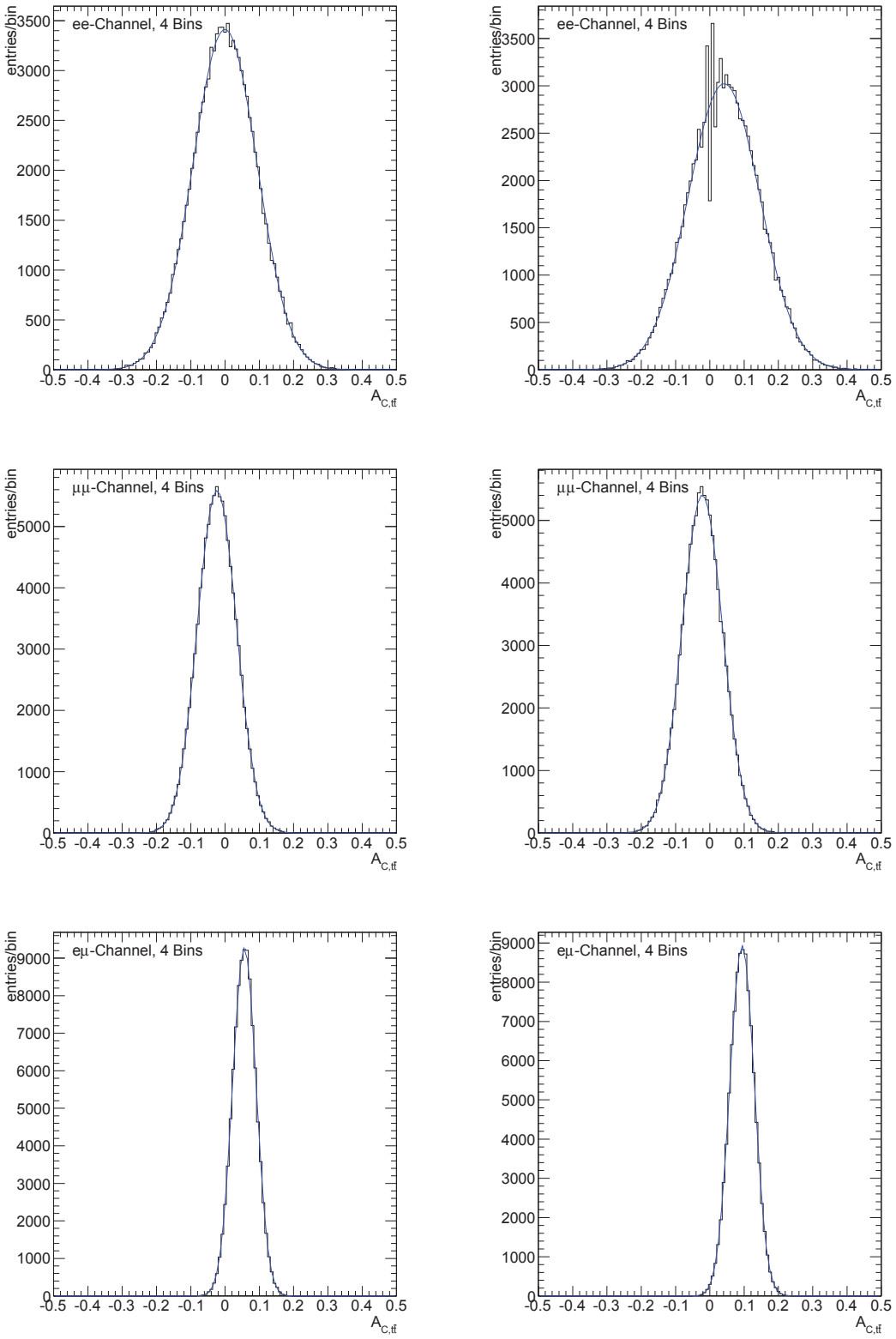

Figure E.3.: The posterior distributions of $A_{C,t\bar{t}}^{\text{meas}}$ for $N_P = 100000$ ensembles of pseudo-data for the ATLAS 2011 7 TeV dataset with (left) and without (right) bin-wise background subtraction. The top, middle and bottom rows show the distributions for the dielectron, dimuon and electron-muon top-quark pair decay channels. The events are selected according to the tagged event selection.

E.2 Statistical and Linear Scaling Uncertainty

As discussed in Section 9.5 the statistical uncertainty and the LSU are added in quadrature for a final error estimate. A detailed list containing the statistical and the LSU is given in the Tables E.1 and E.2.

Error	ee-Channel [%]	$\mu\mu$-Channel [%]	$e\mu$-Channel [%]	Bkg. subtraction
σ_{A_C}	8.1	5.2	3.1	×
$\sigma_{A_C}^{\text{lin}}$	6.0	4.0	2.6	×
σ_{A_C}	9.0	5.6	3.3	✓
$\sigma_{A_C}^{\text{lin}}$	9.0	4.6	3.6	✓

Table E.1.: The statistical error σ_{A_C} derived from $N_{it} = 100000$ ensembles of pseudo-data and the linear scaling uncertainty (LSU) $\sigma_{A_C}^{\text{lin}}$. The events are selected according to the pretag event selection.

Error	ee-Channel [%]	$\mu\mu$-Channel [%]	$e\mu$-Channel [%]	Bkg. subtraction
σ_{A_C}	9.3	5.7	3.4	×
$\sigma_{A_C}^{\text{lin}}$	6.0	4.3	2.8	×
σ_{A_C}	10.4	5.9	3.6	✓
$\sigma_{A_C}^{\text{lin}}$	10.8	4.5	3.6	✓

Table E.2.: The statistical error σ_{A_C} derived from $N_{it} = 100000$ ensembles of pseudo-data and the linear scaling uncertainty (LSU) $\sigma_{A_C}^{\text{lin}}$. The events are selected according to the tagged event selection.

In order to calculate the LSU of the unfolding procedure (Equation D.6) a full covariance matrix is needed. The covariance matrices for the unfolded asymmetries derived from the ATLAS 2011 7 TeV dataset are listed separately for each dileptonic top-quark pair decay channel, with/without background subtraction.

E.2.1 Covariance Matrices for Pretag Event Selection

- Without background subtraction:

  ee-Channel:

$$\mathbf{C}^{ee}_{\text{pretag}} = \begin{pmatrix} 87724.2 & -71125.0 & 22190.3 & 259.4 \\ -71125.0 & 578349.0 & -371989.0 & 32802.9 \\ 22190.3 & -371989.0 & 597498.0 & -95673.4 \\ 259.4 & 32802.9 & -95673.4 & 112134.0 \end{pmatrix} \quad \text{(E.1)}$$

  $\mu\mu$-Channel:

$$\mathbf{C}^{\mu\mu}_{\text{pretag}} = \begin{pmatrix} 45589.4 & -42431.2 & 14292.5 & -183.1 \\ -42431.2 & 224414.0 & -149627.0 & 16156.6 \\ 14292.5 & -149627.0 & 231310.0 & -56506.2 \\ -183.1 & 16156.6 & -56506.2 & 69660.2 \end{pmatrix} \quad \text{(E.2)}$$

  $e\mu$-Channel:

$$\mathbf{C}^{e\mu}_{\text{pretag}} = \begin{pmatrix} 105665.0 & -86328.7 & 27603.3 & -646.3 \\ -86328.7 & 346332.0 & -232781.0 & 32098.2 \\ 27603.3 & -232781.0 & 368991.0 & -96524.8 \\ -646.3 & 32098.2 & -96524.8 & 115149.0 \end{pmatrix} \quad \text{(E.3)}$$

- With background subtraction:

  ee-Channel:

$$\mathbf{C}^{ee}_{\text{pretag}} = \begin{pmatrix} 3358.9 & 4318.4 & -3912.9 & 495.7 \\ 4318.4 & 820505.0 & -565816.0 & 49327.1 \\ -3912.9 & 565816.0 & 949059.0 & -145834.0 \\ 495.7 & 49327.1 & -145834.0 & 177274.0 \end{pmatrix} \quad \text{(E.4)}$$

  $\mu\mu$-Channel

$$\mathbf{C}^{\mu\mu}_{\text{pretag}} = \begin{pmatrix} 44543.0 & -40832.1 & 13431.1 & -60.6 \\ -40832.1 & 226663.0 & -151473.0 & 15996.8 \\ 13431.1 & -151473.0 & 235024.0 & -56605.3 \\ -60.6 & 15996.8 & -56605.3 & 70094.2 \end{pmatrix} \quad \text{(E.5)}$$

  $e\mu$-Channel:

$$\mathbf{C}^{e\mu}_{\text{pretag}} = \begin{pmatrix} 131043.0 & -104340.0 & 32086.4 & -524.3 \\ -104340.0 & 416057.0 & -277085.0 & 38048.1 \\ 32086.4 & -277085.0 & 436811.0 & 113591.0 \\ -524.3 & 38048.1 & -113591.0 & 134214.0 \end{pmatrix} \quad \text{(E.6)}$$

E.2.2 Covariance Matrices for Tagged Event Selection

- Without background subtraction:

  ee-Channel:

$$\mathbf{C}^{ee}_{\text{pretag}} = \begin{pmatrix} 2175.1 & -696.9 & -163.5 & 38.5 \\ -696.9 & 572703.0 & -366838.0 & 347.5 \\ -163.8 & -366838.0 & 562455.0 & -2027.5 \\ 38.4 & 347.5 & -2027.5 & 3380.6 \end{pmatrix} \quad \text{(E.7)}$$

  $\mu\mu$-Channel:

$$\mathbf{C}^{\mu\mu}_{\text{pretag}} = \begin{pmatrix} 18885.4 & -15859.6 & 4652.2 & -36.6 \\ -15859.6 & 214762.0 & -146209.0 & 17296.7 \\ 4652.2 & -146209.0 & 234511.0 & -57853.1 \\ -36.7 & 17296.7 & -57853.1 & 74601.5 \end{pmatrix} \quad \text{(E.8)}$$

  $e\mu$-Channel:

$$\mathbf{C}^{e\mu}_{\text{pretag}} = \begin{pmatrix} 130463.0 & -104614.0 & 34575.8 & -390.7 \\ -104614.0 & 393842.0 & -257069.0 & 28158.6 \\ 34575.8 & -257069.0 & 393181 & -85805.7 \\ -390.7 & 28158.6 & -85805.7 & 107283.0 \end{pmatrix} \quad \text{(E.9)}$$

- With background subtraction:

  ee-Channel:

$$\mathbf{C}^{ee}_{\text{pretag}} = \begin{pmatrix} 0.0 & 21.6 & -13.4 & 0.0 \\ 21.6 & 1436620.0 & -964480.0 & -0.1 \\ -13.4 & -964480.0 & 1471940.0 & 0.2 \\ 0.0, & -0.1 & 0.2 & 0.0 \end{pmatrix} \quad \text{(E.10)}$$

  $\mu\mu$-Channel:

$$\mathbf{C}^{\mu\mu}_{\text{pretag}} = \begin{pmatrix} 16224.7 & -13194.2 & 3704.5 & 19.9 \\ -13194.2 & 214273.0 & -146927.0 & 17612.3 \\ 3704.5 & -146927.0 & 236817.0 & -58662.1 \\ 19.9 & 17612.3 & -58662.1 & 75326.7 \end{pmatrix} \quad \text{(E.11)}$$

  $e\mu$-Channel:

$$\mathbf{C}^{e\mu}_{\text{pretag}} = \begin{pmatrix} 184253.0 & -148012.0 & 49103.4 & -758.2 \\ -148012.0 & 543498.0 & -350241.0 & 37432.4 \\ 49103.4 & -350241.0 & 527411.0 & -111156.0 \\ -758.2 & 37432.4 & -111156.0 & 135793.0 \end{pmatrix} \quad \text{(E.12)}$$

Appendix F

Unfolding using Singular Value Decomposition

Unfolding using singular value decomposition (SVD) is performed as a cross check to verify the findings of the Bayesian iterative unfolding. The SVD unfolding was subject to the same studies regarding, binning and regularisation as the BIU. The same convergence and linear scaling checks are performed. These checks showed that the SVD unfolding provides less linear results for different regularisations. The results improve if the number of bins of the unfolded distribution is increased, but this sacrifices statistical power. The result of the LS of the *4 bins* discretisation is shown in Tables F.1 (pretag event selection) and F.2 (tagged event selection).
The unfolding using SVD is described in detail in Section 9.2. The regularisation parameter τ (given in Equation 9.20) directly corresponds to the number of bins of the chosen discretisation. The regularisation parameter comprises integer values of $\tau \in \{2, 3, \ldots, n_{\text{bins}}\}$. For $\tau = 1$ the training truth input (used for the response matrix) is returned. For the application on data the *4 bins* discretisation and the regularisation $\tau = 4$ is used. Since the LS of the unfolding using SVD is limited the result given in Table F.3 is the result including the LS correction as described in Equation 9.22. The results for the ATLAS 7 TeV dataset are in good agreement for BIU and unfolding using SVD.

	ee-Channel		$\mu\mu$-Channel		$e\mu$-Channel	
τ	p_s	p_a	p_s	p_a	p_s	p_a
2	2.4 ± 1.1	0.00 ± 0.03	2.4 ± 0.7	0.01 ± 0.02	2.4 ± 0.4	-0.01 ± 0.01
3	1.2 ± 0.5	0.00 ± 0.03	1.2 ± 0.4	0.00 ± 0.02	1.2 ± 0.2	0.00 ± 0.01
4	1.1 ± 0.5	0.00 ± 0.03	1.1 ± 0.3	0.00 ± 0.02	1.1 ± 0.2	0.00 ± 0.01

Table F.1.: The slope p_s and the axis intercept p_a of the LS test performed using $N_P = 5000$ ensembles of pseudo-data per datapoint fitted and singular value decomposition. The results are derived for the *4 bins* discretisation and different regularisation parameters τ. The results for the pretag event selection are shown. The errors are statistical errors only.

	ee-Channel		$\mu\mu$-Channel		$e\mu$-Channel	
τ	p_s	p_a	p_s	p_a	p_s	p_a
2	2.5 ± 1.5	-0.01 ± 0.03	2.5 ± 0.7	-0.01 ± 0.02	2.5 ± 0.5	-0.01 ± 0.01
3	1.2 ± 0.6	0.00 ± 0.03	1.2 ± 0.4	-0.00 ± 0.02	1.2 ± 0.2	0.00 ± 0.01
4	1.1 ± 0.5	0.00 ± 0.03	1.1 ± 0.3	-0.00 ± 0.02	1.1 ± 0.2	0.00 ± 0.01

Table F.2.: The slope p_s and the axis intercept p_a of the LS check performed using $N_P = 5000$ ensembles of pseudo-data per datapoint fitted and singular value decomposition. The results are derived for the *4 bins* discretisation and different regularisation parameters τ. The results for the tagged event selection are shown. The errors are statistical errors only.

ee-Channel [%]	$\mu\mu$-Channel [%]	$e\mu$-Channel [%]	Bkg. subtraction
	Pretag:		
2.1 ± 9.9	2.5 ± 6.5	6.0 ± 4.0	✗
6.9 ± 12.6	3.5 ± 7.1	11.2 ± 4.9	✓
	≥ 1 b-tagged jet:		
0.16 ± 10.6	-1.3 ± 6.9	5.6 ± 4.3	✗
6.67 ± 15.5	-0.3 ± 7.6	12.4 ± 5.5	✓

Table F.3.: The unfolded top-quark charge asymmetries $A_{C,t\bar{t}}^{\text{meas}}$, derived from the ATLAS 2011 7 TeV dataset. Unfolding using singular value decomposition is applied $\tau = 4$ and the *4 bins c.* discretisation. The error is the quadratic sum of the statistical error derived from the posterior distribution for $N_P = 10000$ ensembles of pseudo-data and the linear scaling uncertainty.

Appendix G

Additional Information on Systematic Uncertainties

G.1 Monte Carlo Files used for MC Modelling Systematics

In the following the Monte Carlo files used for the evaluation of the MC modelling systematics are listed. For the determination of the corresponding uncertainty refer to Section 10.1. For detailed information about the MC samples (cross section, k-factor) see [201].

ISR/FSR:

DSID	Description	Matrix Element	Parton Shower
117525	$t\bar{t} \to ll\nu\nu$ + Np0 P2011radHi	ALPGEN	PYTHIA
117526	$t\bar{t} \to ll\nu\nu$ + Np1 P2011radHi	ALPGEN	PYTHIA
117527	$t\bar{t} \to ll\nu\nu$ + Np2 P2011radHi	ALPGEN	PYTHIA
117528	$t\bar{t} \to ll\nu\nu$ + Np3 P2011radHi	ALPGEN	PYTHIA
117529	$t\bar{t} \to ll\nu\nu$ + Np4incl P2011radHi	ALPGEN	PYTHIA
117520	$t\bar{t} \to l\nu qq$ + Np0 P2011radHi	ALPGEN	PYTHIA
117521	$t\bar{t} \to l\nu qq$ + Np1 P2011radHi	ALPGEN	PYTHIA
117522	$t\bar{t} \to l\nu qq$ + Np2 P2011radHi	ALPGEN	PYTHIA
117523	$t\bar{t} \to l\nu qq$ + Np3 P2011radHi	ALPGEN	PYTHIA
117524	$t\bar{t} \to l\nu qq$ + Np4incl P2011radHi	ALPGEN	PYTHIA
117535	$t\bar{t} \to ll\nu\nu$ + Np0 P2011radLo	ALPGEN	PYTHIA
117536	$t\bar{t} \to ll\nu\nu$ + Np1 P2011radLo	ALPGEN	PYTHIA
117537	$t\bar{t} \to ll\nu\nu$ + Np2 P2011radLo	ALPGEN	PYTHIA
117538	$t\bar{t} \to ll\nu\nu$ + Np3 P2011radLo	ALPGEN	PYTHIA
117539	$t\bar{t} \to ll\nu\nu$ + Np4incl P2011radLo	ALPGEN	PYTHIA
117530	$t\bar{t} \to l\nu qq$ + Np0 P2011radLo	ALPGEN	PYTHIA
117531	$t\bar{t} \to l\nu qq$ + Np1 P2011radLo	ALPGEN	PYTHIA

DSID	Description	Matrix Element	Parton Shower
117532	$t\bar{t} \to l\nu qq$ + Np2 P2011radLo	ALPGEN	PYTHIA
117533	$t\bar{t} \to l\nu qq$ + Np3 P2011radLo	ALPGEN	PYTHIA
117534	$t\bar{t} \to l\nu qq$ + Np4incl P2011radLo	ALPGEN	PYTHIA

MC Generator:

DSID	Description	Matrix Element	Parton Shower
117050	$t\bar{t}$ incl.	POWHEG	PYTHIA
105890	$t\bar{t} \to ll\nu\nu$ + NP0	ALPGEN	JIMMY/HERWIG
105891	$t\bar{t} \to ll\nu\nu$ + NP1	ALPGEN	JIMMY/HERWIG
105892	$t\bar{t} \to ll\nu\nu$ + NP2	ALPGEN	JIMMY/HERWIG
117897	$t\bar{t} \to ll\nu\nu$ + NP3	ALPGEN	JIMMY/HERWIG
117898	$t\bar{t} \to ll\nu\nu$ + NP4	ALPGEN	JIMMY/HERWIG
117899	$t\bar{t} \to ll\nu\nu$ + NP5	ALPGEN	JIMMY/HERWIG
105894	$t\bar{t} \to l\nu qq$ + NP0	ALPGEN	JIMMY/HERWIG
105895	$t\bar{t} \to l\nu qq$ + NP1	ALPGEN	JIMMY/HERWIG
105896	$t\bar{t} \to l\nu qq$ + NP2	ALPGEN	JIMMY/HERWIG
117887	$t\bar{t} \to l\nu qq$ + NP3	ALPGEN	JIMMY/HERWIG
117888	$t\bar{t} \to l\nu qq$ + NP4	ALPGEN	JIMMY/HERWIG
117889	$t\bar{t} \to l\nu qq$ + NP5	ALPGEN	JIMMY/HERWIG
117050	$t\bar{t}$ incl.(*ATLFAST2*)	POWHEG	PYTHIA
105860	$t\bar{t}$ incl.(*ATLFAST2*)	POWHEG	JIMMY/HERWIG

Colour Reconnection:

DSID	Description	Matrix Element	Parton Shower
117428	$t\bar{t}$, no colour rec.	POWHEG	PYTHIA
117430	$t\bar{t}$, no colour rec.	POWHEG	PYTHIA

Underlying Event:

DSID	Description	Matrix Element	Parton Shower
117428	$t\bar{t}$, mpiHi	POWHEG	PYTHIA
117429	$t\bar{t}$, nominal	POWHEG	PYTHIA

Ren/Fac Scale:

DSID	Description	Matrix Element	Parton Shower
110006	$t\bar{t}$, mudown, lepton filter	MC@NLO	HERWIG/JIMMY
110007	$t\bar{t}$, muup, lepton filter	MC@NLO	HERWIG/JIMMY

$t\bar{t}$-Mass Variation:

DSID	Description	Matrix Element	Parton Shower
117838	$t\bar{t}$, $m_t = 167.5\,\text{GeV}$	POWHEG	PYTHIA
117840	$t\bar{t}$, $m_t = 170.0\,\text{GeV}$	POWHEG	PYTHIA
117842	$t\bar{t}$, $m_t = 175.0\,\text{GeV}$	POWHEG	PYTHIA
117844	$t\bar{t}$, $m_t = 177.5\,\text{GeV}$	POWHEG	PYTHIA
117050	$t\bar{t}$, $m_t = 172.5\,\text{GeV}$	POWHEG	PYTHIA

G.2 Linear Scaling Correction for MC Modelling Systematics

The plots provided in this section show the linear scaling corrections divided by channel and event selection for all MC modelling systematic samples. The parameters shown are the slope p_s and the axis intercept p_a. The line each plott shows the nominal value derived using the MCNLO $t\bar{t}$-signal sample. The shaded region depicts the corresponding uncertainty. The plots show that all parameters are in agreement with the nominal values.

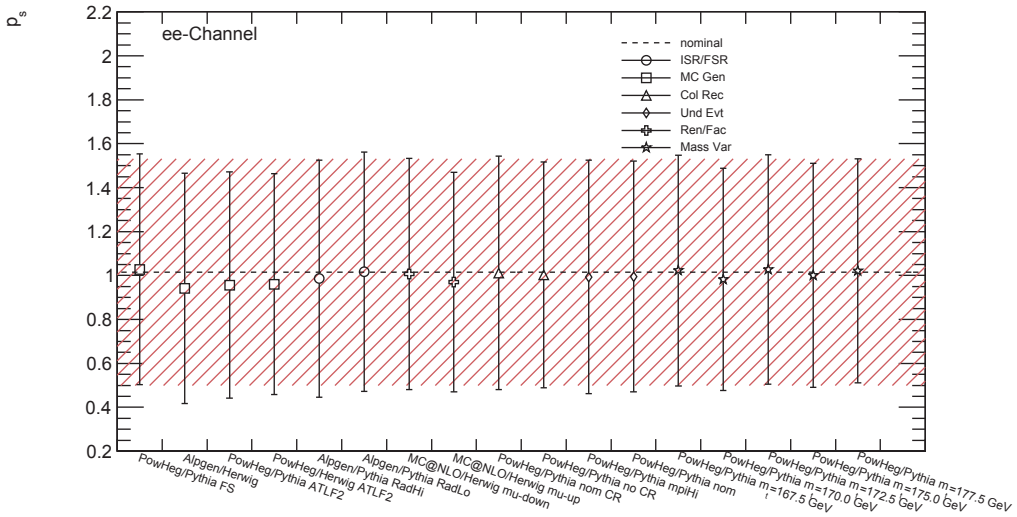

Figure G.1.: The slope parameter p_s of the linear scaling correction. This parameter is determined for the MC samples used in the evaluation of the MC generator modelling systematics. The plot is derived in the dielectron channel using the pretag event selection.

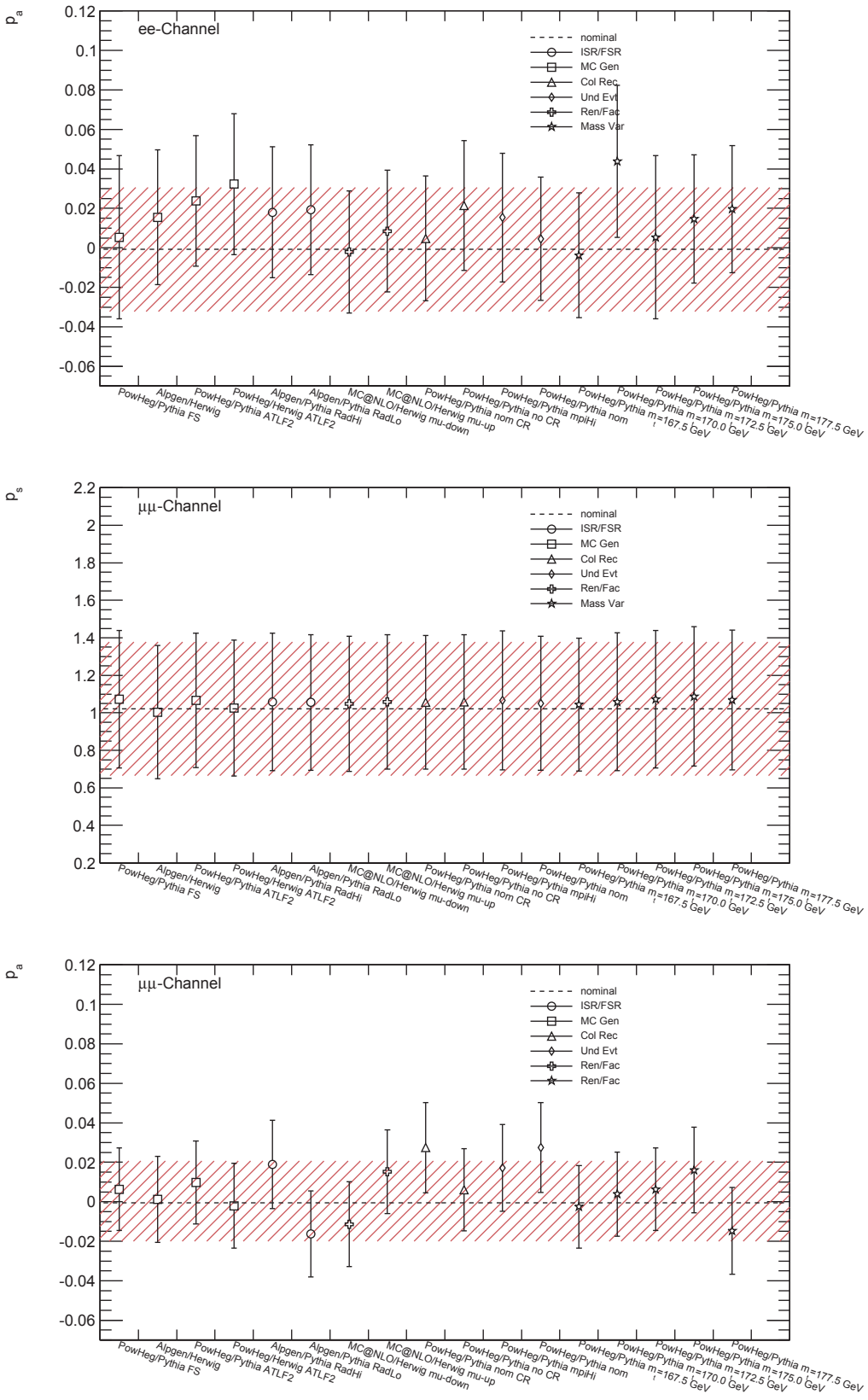

Figure G.2.: The two parameters (slope p_s, axis intercept p_a) of the linear scaling correction. These parameters are determined for the MC samples used in the evaluation of the MC generator modelling systematics. The plots are derived in the dielectron channel (top) and the dimuon channel (centre and bottom) using the pretag event selection.

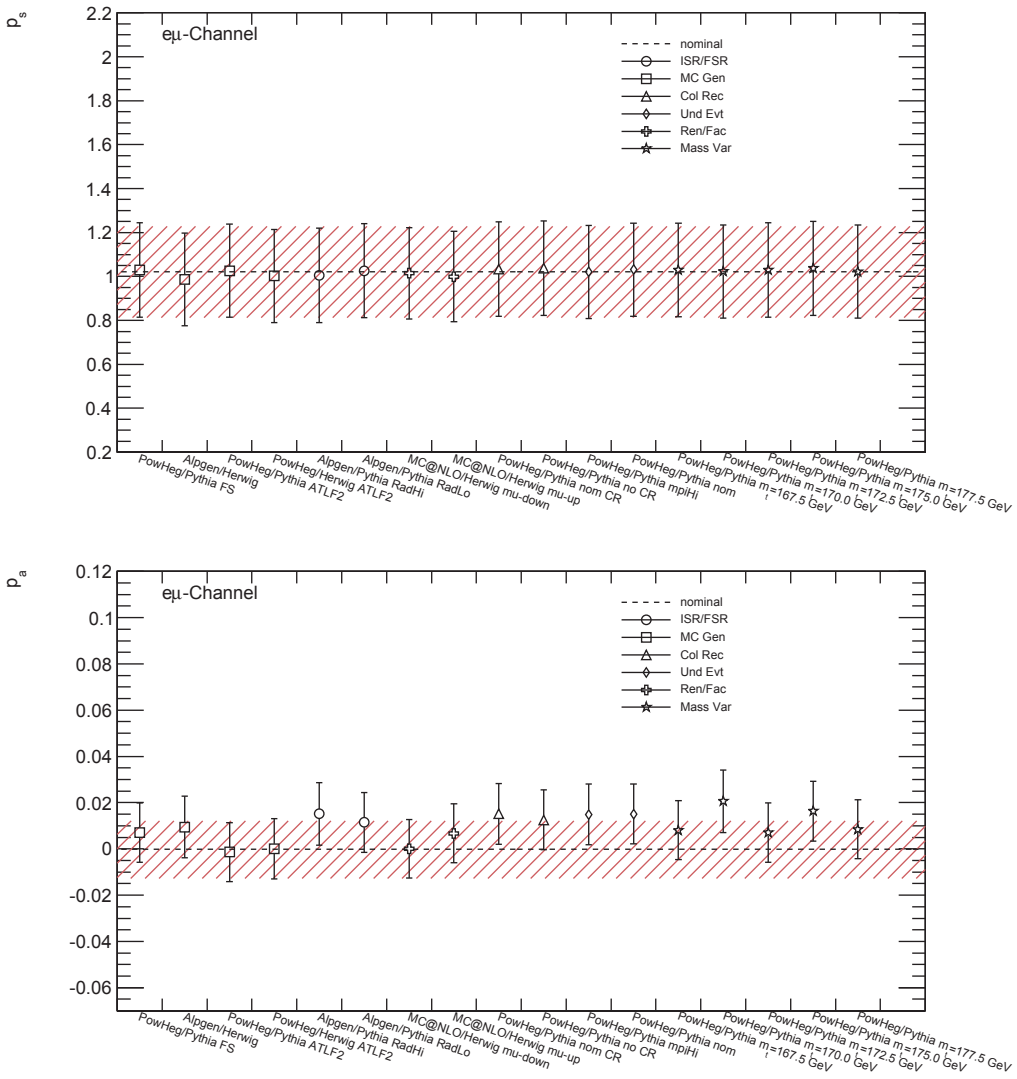

Figure G.3.: The two parameters (slope p_s, axis intercept p_a) of the linear scaling correction. These parameters are determined for the MC samples used in the evaluation of the MC generator modelling systematics. The plots are derived in the electron-muon channel using the pretag event selection.

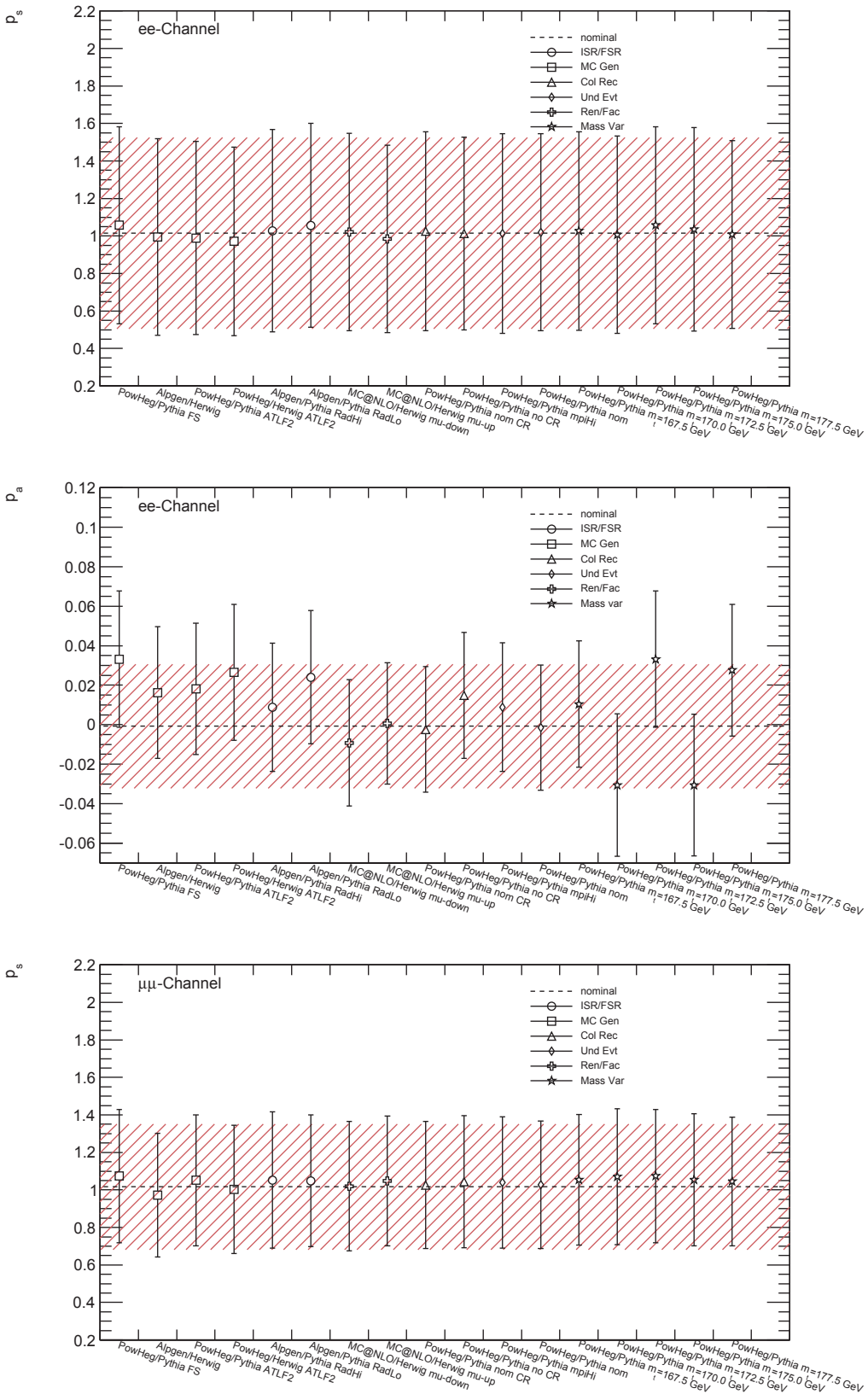

Figure G.4.: The two parameters (slope p_s, axis intercept p_a) of the linear scaling correction. These parameters are determined for the MC samples used in the evaluation of the MC generator modelling systematics. The plots are derived in the dielectron channel (top and centre) and the dimuon channel (bottom) using the tagged event selection.

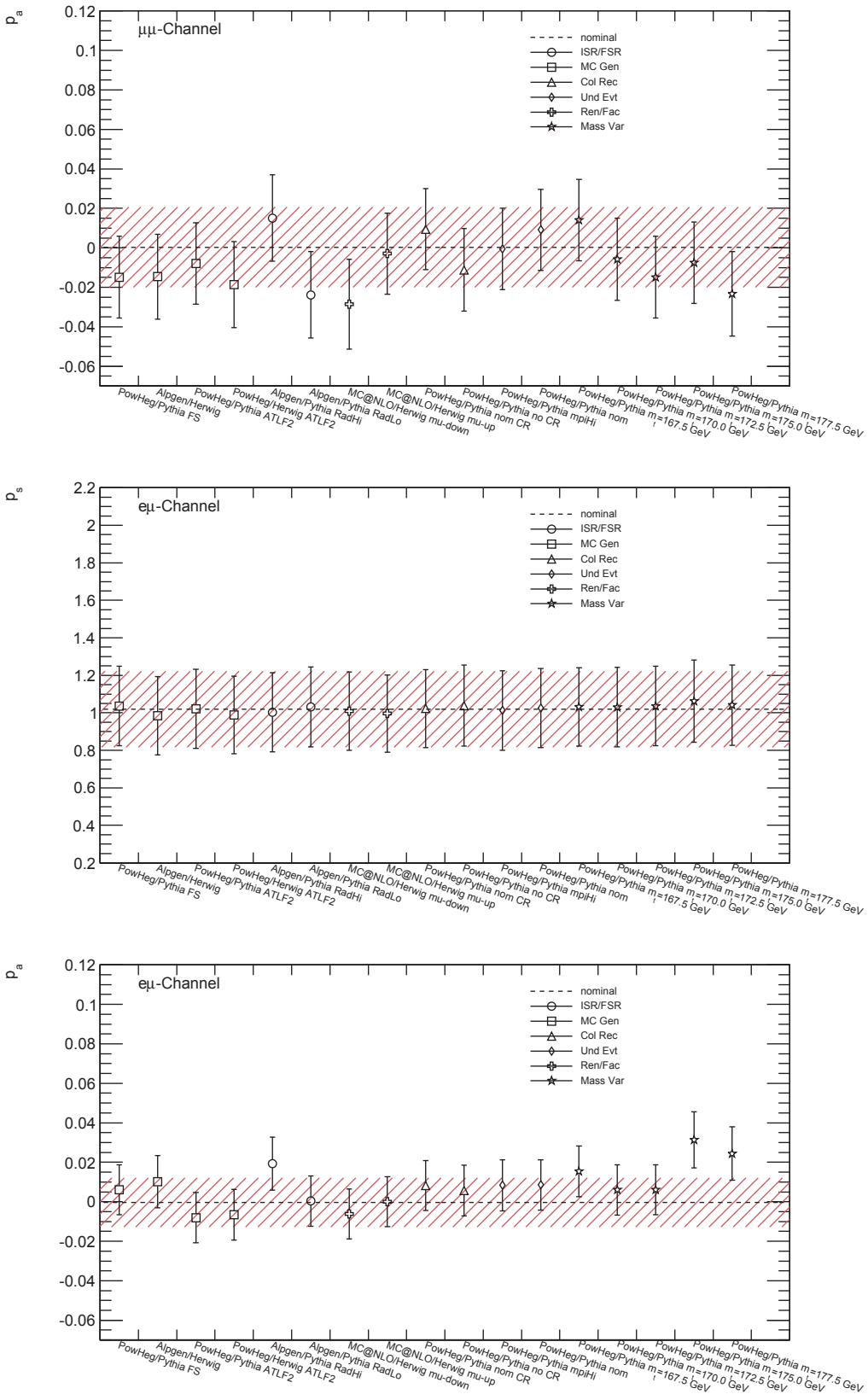

Figure G.5.: The two parameters (slope p_s, axis intercept p_a) of the linear scaling correction. These parameters are determined for the MC samples used in the evaluation of the MC generator modelling systematics. The plots are derived in the dimuon channel (top) and the electron-muon channel (centre and bottom) using the tagged event selection.

G.3 Additional Information on Monte Carlo modelling Systematics

MC Generator:

Difference	ee-Channel	$\mu\mu$-Channel	$e\mu$-Channel
	Pretag:		
1.	**0.044**	0.006	0.002
2.	0.007	0.003	**0.006**
3.	0.003	**0.016**	0.005
	≥ 1 b-tagged jet:		
1.	0.015	<0.001	0.005
2.	**0.023**	0.006	0.003
3.	0.002	**0.016**	**0.005**

Table G.7.: The absolute values of the differences of the unfolded top-quark charge asymmetry $A_{C,t\bar{t}}$ (including individual linear scaling) for the three sample pairings described in Section 10.1.1. The largest value is highlighted.

Initial/Final State Radiation:

Difference	ee-Channel	$\mu\mu$-Channel	$e\mu$-Channel
	Pretag:		
(nom-radHi)/2	-0.002	**-0.002**	**-0.002**
(nom-radLo)/2	**0.003**	<0.001	<0.001
	≥ 1 b-tagged jet:		
(nom-radHi)/2	**-0.007**	**-0.002**	**-0.003**
(nom-radLo)/2	-0.004	<0.001	<0.001

Table G.8.: The absolute values of the differences of the unfolded top-quark charge asymmetry $A_{C,t\bar{t}}$ (including individual linear scaling) for the two sample pairings described in Section 10.1.3. The largest value is highlighted.

Renormalisation and Factorisation:

Difference	ee-Channel	$\mu\mu$-Channel	$e\mu$-Channel
	Pretag:		
muup-mudown	0.015	0.003	0.001
	≥ 1 b-tagged jet:		
muup-mudown	0.013	0.005	0.002

Table G.9.: The absolute values of the differences of the unfolded top-quark charge asymmetry $A_{C,t\bar{t}}$ (including individual linear scaling) for the MC@NLO sample with modified RFSs.

Top-Quark Mass Variation:

$A^{\text{nom}}_{C,t\bar{t}} - A^{x}_{C,t\bar{t}}$	ee-Channel	$\mu\mu$-Channel	$e\mu$-Channel
	Pretag:		
$x = 167.5\,\text{GeV}$	<0.001	0.003	0.007
$x = 170.0\,\text{GeV}$	0.003	0.006	0.006
$x = 172.5\,\text{GeV}$	0.043	0.006	0.002
$x = 175.0\,\text{GeV}$	0.015	0.004	0.001
$x = 177.5\,\text{GeV}$	0.002	0.004	0.002
$\sigma_m = 0.08\,\text{GeV}$	**0.001**	**<0.001**	**0.001**
	≥ 1 b-tagged jet:		
$x = 167.5\,\text{GeV}$	0.035	0.013	0.041
$x = 170.0\,\text{GeV}$	0.015	0.009	0.044
$x = 172.5\,\text{GeV}$	0.015	<0.001	0.041
$x = 175.0\,\text{GeV}$	0.032	0.002	0.041
$x = 177.5\,\text{GeV}$	0.018	0.005	0.046
$\sigma_m = 0.08\,\text{GeV}$	**0.001**	**0.001**	**0.001**

Table G.10.: The absolute values of the differences of the nominal unfolded top-quark charge asymmetry $A^{\text{nom}}_{C,t\bar{t}}$ for the MC@NLO signal sample and the m_t-varied POWHEG samples. The lines $\sigma_m = 0.08\,\text{GeV}$ state the systematic uncertainty originating from the mass variation.

G.4 Linear Scaling Correction for Detector Modelling Systematics

The plots provided in this section show the linear scaling (LC) corrections divided by channel and event selection for all modelling systematic samples. The parameters shown are the slope p_s and the axis intercept p_a. The line in the plots shows the nominal value and the shaded region depicts the corresponding uncertainty. The plots show that all parameters are in agreement with the nominal values.

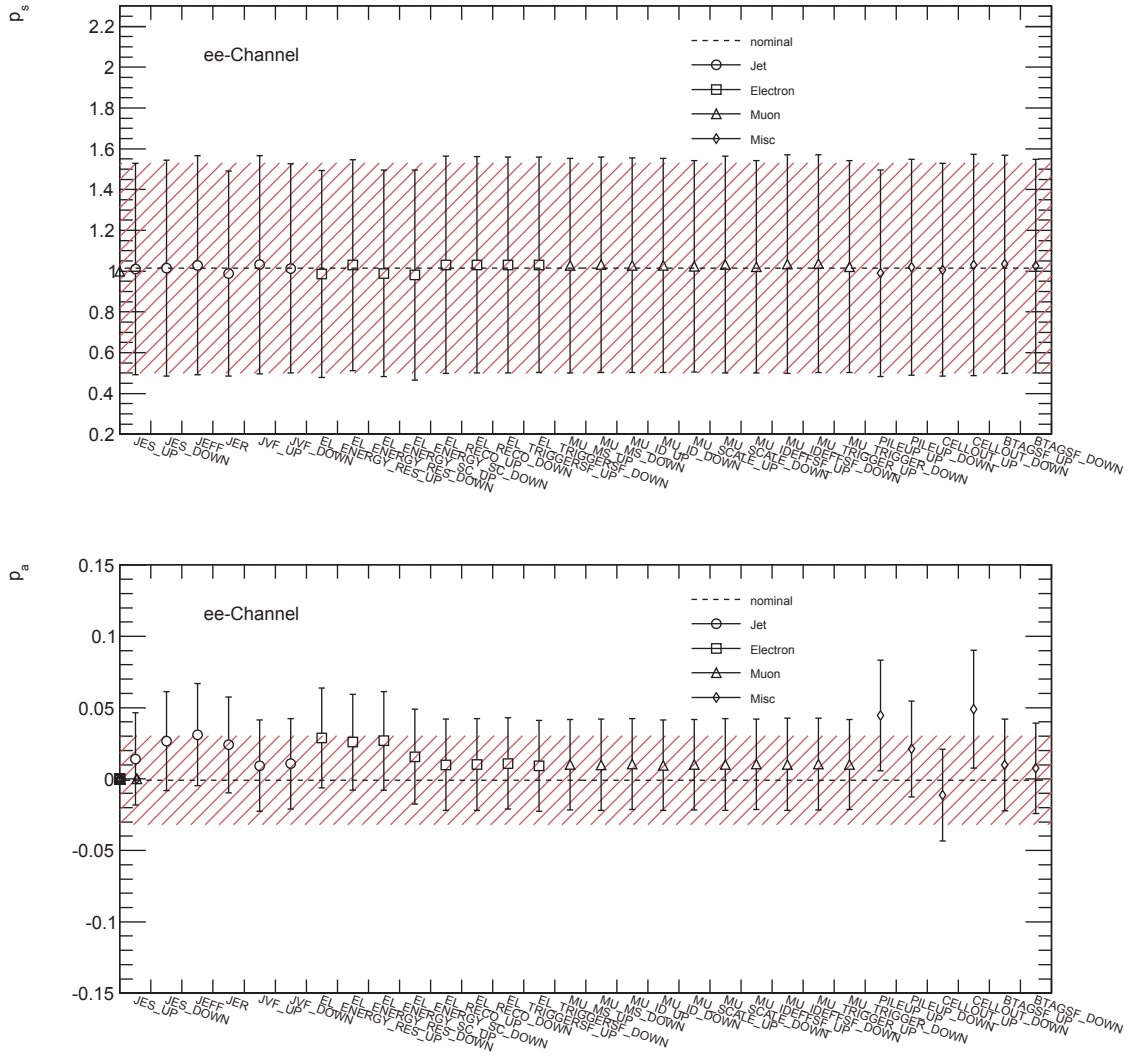

Figure G.6.: The two parameters (slope p_s, axis intercept p_a) of the linear scaling correction. These parameters are determined for shifted scale and smearing parameters as discussed in Section 10.2. The plots are derived in the dielectron channel using the pretag event selection.

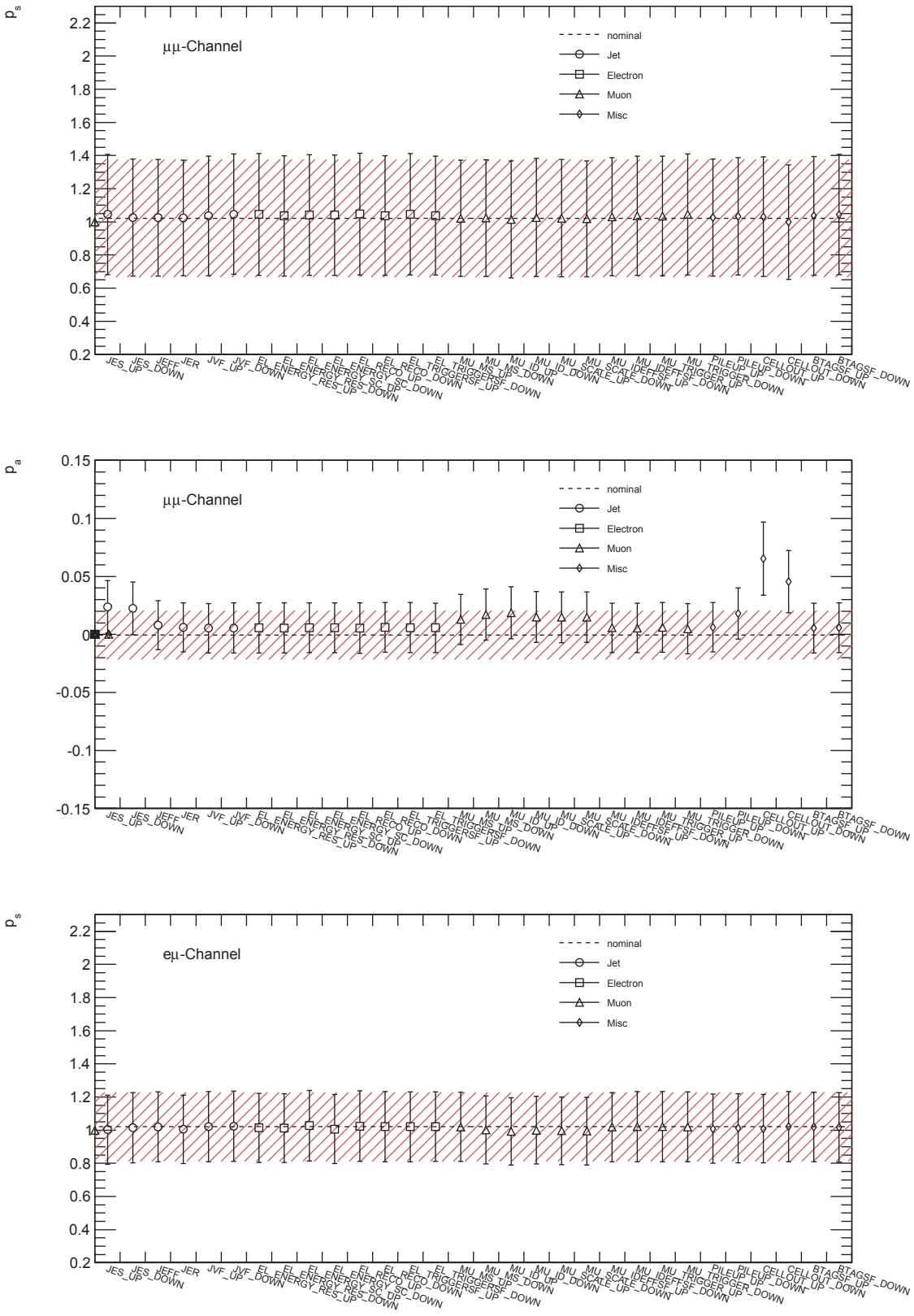

Figure G.7.: The two parameters (slope p_s, axis intercept p_a) of the linear scaling correction. These parameters are determined for shifted scale and smearing parameters as discussed in Section 10.2. The plots are derived in the dimuon channel (top, centre) and the electron-muon channel (bottom) using the pretag event selection.

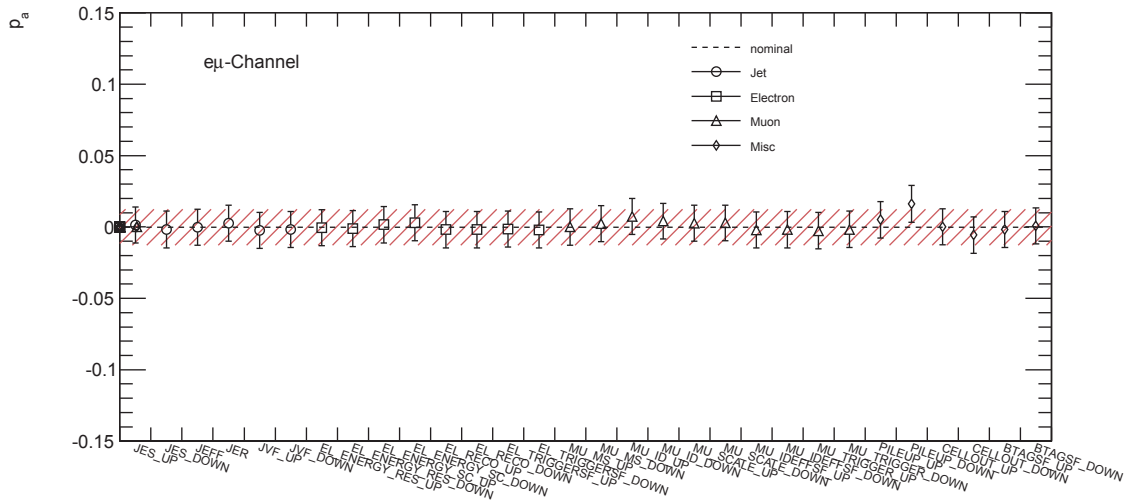

Figure G.8.: The axis intercept p_a of the linear scaling correction. These parameter is determined for shifted scale and smearing parameters as discussed in Section 10.2. The plot is derived in the electron-muon channel using the pretag event selection.

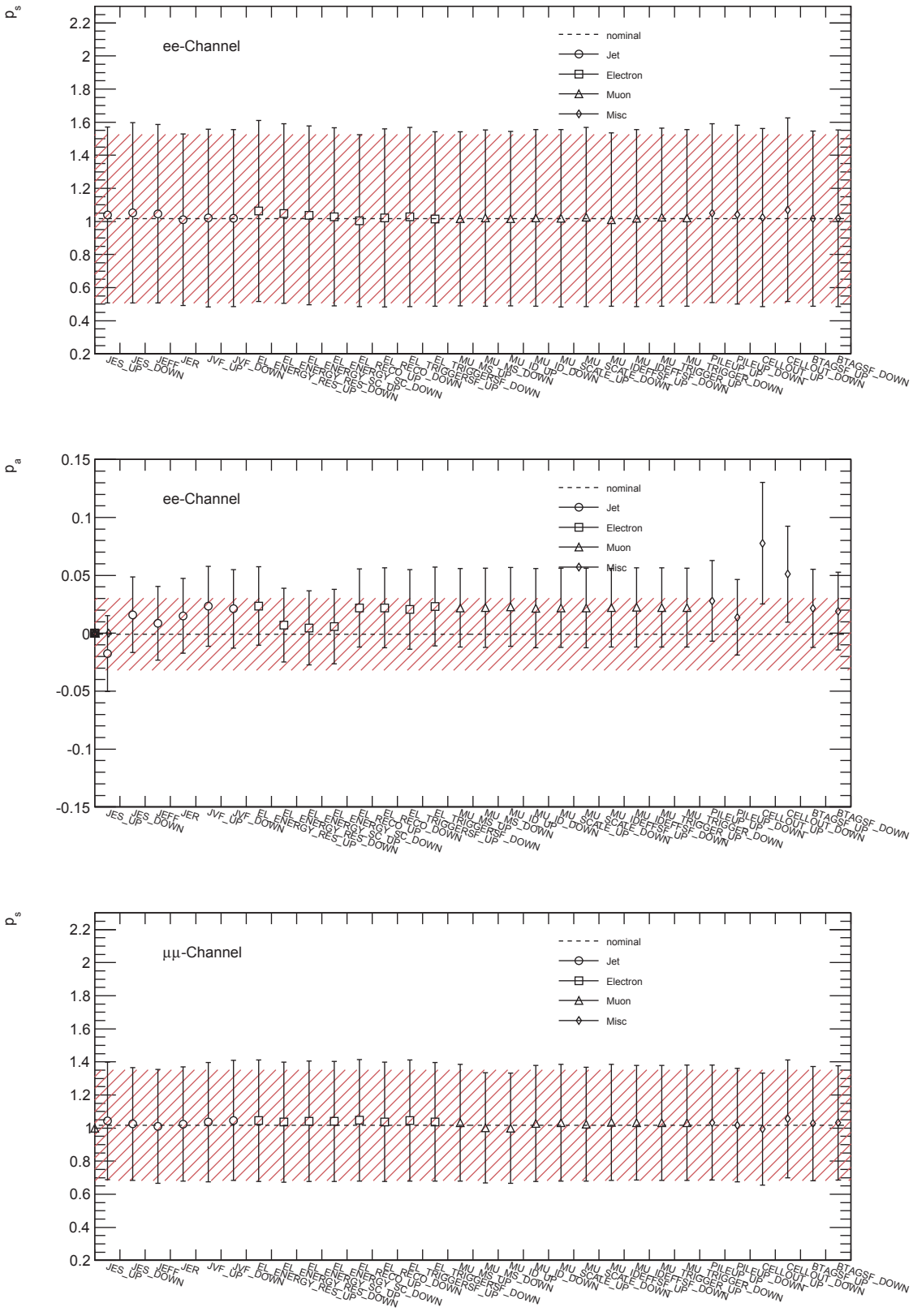

Figure G.9.: The two parameters (slope p_s, axis intercept p_a) of the linear scaling correction. These parameters are determined for shifted scale and smearing parameters as discussed in Section 10.2. The plots are derived in the dielectron channel (top, centre) and the dimuon channel (bottom) using the tagged event selection.

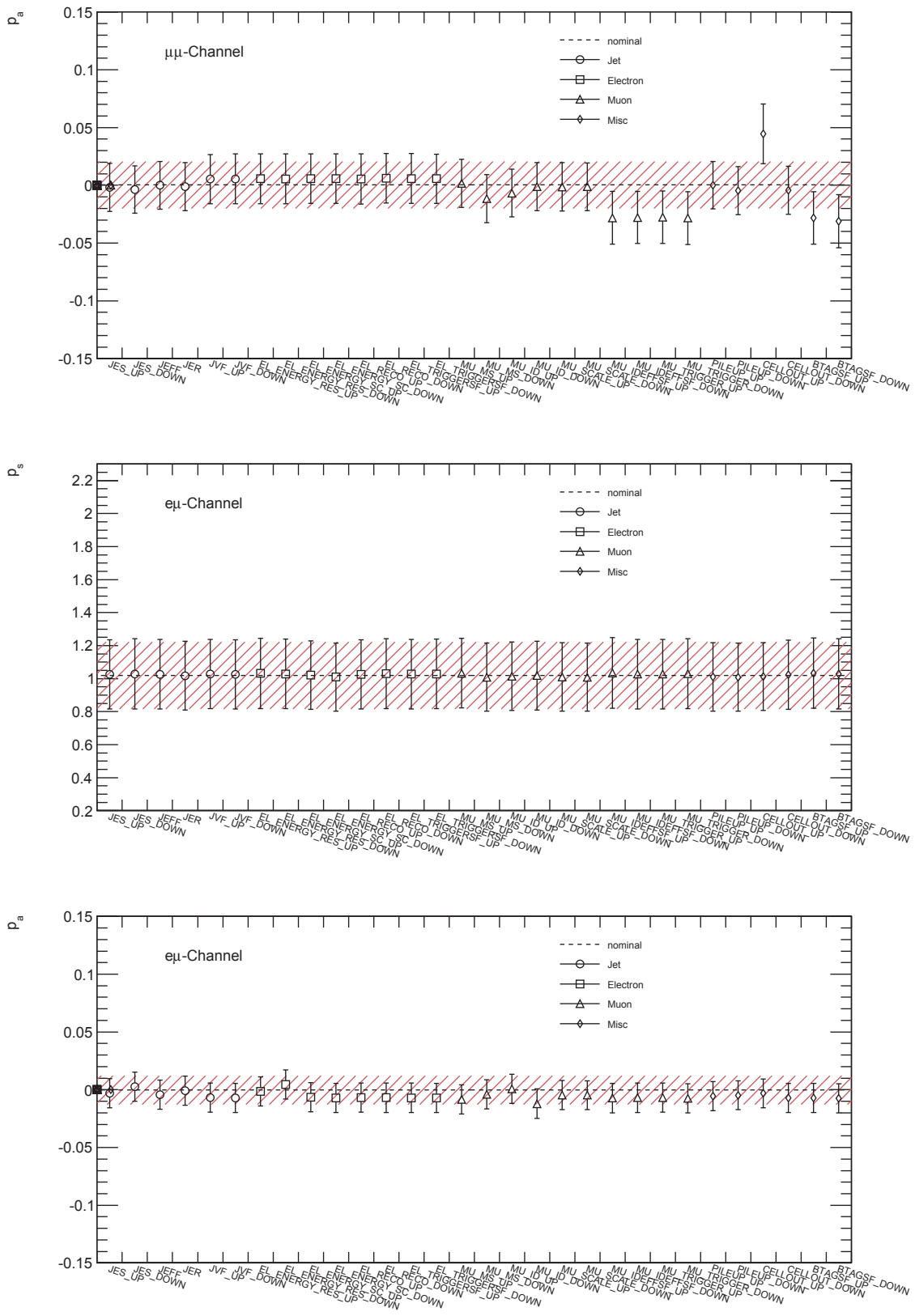

Figure G.10.: The two parameters (slope p_s, axis intercept p_a) of the linear scaling correction. These parameters are determined for shifted scale and smearing parameters as discussed in Section 10.2. The plots are derived in the dimuon channel (top) and the electron-muon channel (centre and bottom) using the tagged event selection.

G.5 Additional Information on Detector modelling Systematics

Jet Systematics:

Systematic	ee-Channel	$\mu\mu$-Channel	$e\mu$-Channel
		Pretag:	
JES_UP	0.002	0.001	**0.001**
JES_DOWN	**0.002**	**0.002**	<0.001
JER	**0.001**	**-0.002**	**0.003**
JEFF	**0.005**	**-0.001**	<0.001
JVF_UP	**0.003**	**0.001**	**0.001**
JVF_DOWN	0.002	0.001	0.001

Table G.11.: The differences between the individual means of the posterior distributions (derived for the corresponding systematic) and the nominal measured top-quark charge asymmetry. The largest absolute values are highlighted. For details refer to Section 10.2.

Jet Systematics:

Systematic	ee-Channel	$\mu\mu$-Channel	$e\mu$-Channel
		≥ 1 b-tagged jet:	
JES_UP	0.008	<0.001	0.003
JES_DOWN	**0.014**	**0.001**	**0.004**
JER	**0.011**	**-0.001**	**0.003**
JEFF	**0.016**	**-0.002**	**0.003**
JVF_UP	**0.014**	**-0.007**	**0.003**
JVF_DOWN	0.014	-0.007	0.003

Table G.12.: The differences between the individual means of the posterior distributions (derived for the corresponding systematic) and the nominal measured top-quark charge asymmetry. The largest absolute values are highlighted. For details refer to Section 10.2.

Lepton Reconstruction:

Systematic	ee-Channel	$\mu\mu$-Channel	$e\mu$-Channel
	Pretag:		
EL_ENERGY_RES_UP	**0.007**	**0.002**	<0.001
EL_ENERGY_RES_DOWN	0.003	0.001	**0.001**
EL_ENERGY_SC_UP	0.003	0.001	<0.001
EL_ENERGY_SC_DOWN	**0.005**	**0.001**	**-0.001**
EL_RECO_UP	**0.003**	**0.002**	**0.001**
EL_RECO_DOWN	0.003	0.002	0.001
EL_TRIGGER_SF_UP	**0.003**	0.001	0.001
EL_TRIGGER_SF_DOWN	0.003	**0.002**	**0.001**
MU_MS_UP	0.065	0.026	0.113
MU_MS_DOWN	0.065	0.029	0.116
MU_ID_UP	0.065	0.029	0.113
MU_ID_DOWN	0.065	0.027	0.115
(max-min)/2	<**0.001**	**0.002**	**0.001**
MU_SCALE_UP	**0.003**	**-0.003**	**0.002**
MU_SCALE_DOWN	0.003	-0.003	0.001
MU_RECO_UP	0.003	0.001	<0.001
MU_RECO_DOWN	**0.004**	**0.001**	**0.001**
MU_TRIGGER_SF_UP	**0.004**	**0.001**	<0.001
MU_TRIGGER_SF_DOWN	0.003	0.001	<0.001

Table G.13.: The differences between the individual means of the posterior distributions (derived for the corresponding systematic) and the nominal measured top-quark charge asymmetry. The highlighted values are used for the estimation of the systematic uncertainty. For details refer to Section 10.2.

Lepton Reconstruction:

Systematic	ee-Channel	$\mu\mu$-Channel	$e\mu$-Channel
	≥ 1 b-tagged jet:		
EL_ENERGY_RES_UP	**0.015**	**-0.007**	0.003
EL_ENERGY_RES_DOWN	0.010	-0.006	**0.004**
EL_ENERGY_SC_UP	0.011	**-0.007**	**0.003**
EL_ENERGY_SC_DOWN	**0.013**	-0.007	0.003
EL_RECO_UP	0.013	**-0.007**	**0.003**
EL_RECO_DOWN	**0.014**	-0.007	0.003
EL_TRIGGER_SF_UP	**0.014**	**-0.007**	**0.003**
EL_TRIGGER_SF_DOWN	0.013	-0.007	0.003
MU_MS_UP	0.048	-0.025	0.096
MU_MS_DOWN	0.049	-0.024	0.097
MU_ID_UP	0.049	-0.023	0.100
MU_ID_DOWN	0.048	-0.021	0.096
(max-min)/2	**0.001**	**-0.002**	**0.002**
MU_SCALE_UP	**0.014**	**0.001**	**0.003**
MU_SCALE_DOWN	0.014	0.001	0.003
MU_RECO_UP	**0.014**	**-0.007**	**0.003**
MU_RECO_DOWN	0.014	-0.007	0.003
MU_TRIGGER_SF_UP	0.014	-0.007	0.003
MU_TRIGGER_SF_DOWN	**0.015**	**-0.007**	**0.003**

Table G.14.: The differences between the individual means of the posterior distributions (derived for the corresponding systematic) and the nominal measured top-quark charge asymmetry. The highlighted values are used for the estimation of the systematic uncertainty. For details refer to Section 10.2.

Miscellaneous Detector Modelling Systematics:

Systematic	ee-Channel	$\mu\mu$-Channel	$e\mu$-Channel
	Pretag:		
PILEUP_UP	**0.009**	0.001	0.001
PILEUP_DOWN	<0.001	**0.002**	**0.004**
CELL_OUT/SOFTJET_UP	0.011	0.001	**0.003**
CELL_OUT/SOFTJET_DOWN	**0.035**	**0.019**	0.002
BTAG_SF_UP	**0.003**	0.001	**0.001**
BTAG_SF_DOWN	0.002	**0.002**	<0.001
	≥ 1 b-tagged jet:		
PILEUP_UP	**0.018**	**0.003**	0.003
PILEUP_DOWN	0.013	0.002	**0.004**
CELL_OUT/SOFTJET_UP	0.045	**0.019**	**0.003**
CELL_OUT/SOFTJET_DOWN	**0.050**	-0.001	0.003
BTAG_SF_UP	0.013	**-0.007**	**0.004**
BTAG_SF_DOWN	**0.015**	-0.007	0.003

Table G.15.: The differences between the individual means of the posterior distributions (derived for the corresponding systematic) and the nominal measured top-quark charge asymmetry. The highlighted values are used for the estimation of the systematic uncertainty. For details refer to Section 10.2.

G.6 Additional Information on Background and Luminosity Systematics

Monte Carlo Background Normalisation:

Systematic	ee-Channel	$\mu\mu$-Channel	$e\mu$-Channel
	Pretag:		
ST_NORM_UP	**-0.001**	**0.001**	**0.002**
ST_NORM_DOWN	< 0.001	< 0.001	0.002
DB_NORM_UP	**-0.001**	< 0.001	**0.003**
DB_NORM_DOWN	< 0.001	< 0.001	0.001
ZJETS_NORM_UP	0.006	**0.005**	**0.004**
ZJETS_NORM_DOWN	**-0.007**	-0.004	< 0.001

Table G.16.: The differences between the individual means of the posterior distributions (derived for the corresponding systematic) and the nominal measured top-quark charge asymmetry. The highlighted values are used for the estimation of the systematic uncertainty. For details refer to Section 10.3.1.

Monte Carlo Background Normalisation:

Systematic	ee-Channel	$\mu\mu$-Channel	$e\mu$-Channel
	≥ 1 b-tagged jet:		
ST_NORM_UP	**0.007**	**0.001**	**0.002**
ST_NORM_DOWN	0.007	0.001	0.001
DB_NORM_UP	**0.007**	< 0.001	**0.001**
DB_NORM_DOWN	0.007	< 0.001	0.001
ZJETS_NORM_UP	**0.008**	**0.002**	**0.002**
ZJETS_NORM_DOWN	0.006	< 0.001	0.001

Table G.17.: The differences between the individual means of the posterior distributions (derived for the corresponding systematic) and the nominal measured top-quark charge asymmetry. The highlighted values are used for the estimation of the systematic uncertainty. For details refer to Section 10.3.1.

Fake Lepton Background Uncertainty:

Systematic	ee-Channel	$\mu\mu$-Channel	$e\mu$-Channel
	Pretag:		
MU_REAL_EFF_UP	-0.002	<0.001	-0.004
MU_REAL_EFF_DOWN	**-0.009**	**-0.005**	**-0.004**
MU_FAKE_EFF_UP	-0.002	**-0.005**	**-0.020**
MU_FAKE_EFF_DOWN	**0.0151**	-0.002	-0.004
EL_REAL_EFF_UP	**0.011**	-0.001	**-0.011**
EL_REAL_EFF_DOWN	-0.004	**-0.002**	-0.003
EL_FAKE_EFF_UP	**-0.007**	**-0.002**	-0.001
EL_FAKE_EFF_DOWN	-0.006	<0.001	**-0.003**

Table G.18.: The differences between the individual means of the posterior distributions (derived for the corresponding systematic) and the nominal measured top-quark charge asymmetry. The highlighted values are used for the estimation of the systematic uncertainty. For details refer to Section 10.3.2.

Fake Lepton Background Uncertainty:

Systematic	ee-Channel	$\mu\mu$-Channel	$e\mu$-Channel
	≥ 1 b-tagged jet:		
MU_REAL_EFF_UP	-0.003	-0.001	0.002
MU_REAL_EFF_DOWN	**-0.003**	**0.002**	**0.016**
MU_FAKE_EFF_UP	**0.008**	<0.001	0.003
MU_FAKE_EFF_DOWN	-0.007	<0.001	**-0.010**
EL_REAL_EFF_UP	0.004	**0.003**	**-0.009**
EL_REAL_EFF_DOWN	**0.026**	<0.001	0.005
EL_FAKE_EFF_UP	0.001	**0.004**	**0.019**
EL_FAKE_EFF_DOWN	**0.005**	<0.001	0.001

Table G.19.: The differences between the individual means of the posterior distributions (derived for the corresponding systematic) and the nominal measured top-quark charge asymmetry. The highlighted values are used for the estimation of the systematic uncertainty. For details refer to Section 10.3.2.

Appendix H

Best Linear Unbiased Estimate

In order to compare the measured top-quark charge asymmetry to the theoretical value the results for the three decay channels are combined using the best linear unbiased estimate (BLUE) method [202], [203]. Using the BLUE method the measured top-quark charge asymmetries can be combined in one step while taking into account the correlations between the systematic uncertainties. The BLUE method can combine N quantities under the hypothesis that all sources of uncertainties are multivariate Gaussian distributed. It is necessary that the total covariance matrix for the input data is known and that it does not depend on the results of the measurements [203, p. 2]. The detailed results on the combination of the central values and uncertainties for the top-quark charge asymmetry are given in Tables H.2 and H.3. The weights used in the combination of the three channels and the resulting pulls are listed in Table H.1. The pull is defined as the difference between the combined and the input value of the charge asymmetry divided by the square root of the difference of the variances. The results are calculated using the BLUE package version 1.9.2 [204]. The statistical errors, the electron (muon) related systematics and the fake lepton background uncertainty are uncorrelated for the three decay channels. The rest of the systematic uncertainties are assumed to be 100% correlated.

Estimates	ee-Channel	$\mu\mu$-Channel	$e\mu$-Channel
	Pretag:		
Weights ($A_{C,t\bar{t}}$)	0.065	0.292	0.643
Pull	-0.170	-0.859	0.870
	≥ 1 b-tagged jet:		
Weights ($A_{C,t\bar{t}}$)	0.048	0.310	0.642
Pull	-0.124	-1.157	1.145

Table H.1.: The linear combination weights and pulls of the BLUE combination for the three top-quark pair decay channels.

Uncertainty	ee-Channel	$\mu\mu$-Channel	$e\mu$-Channel	Combination
$A_{C,t\bar{t}}$	0.062	0.030	0.113	**0.085**
Stat	0.128	0.072	0.049	**0.039**
MC Generator	0.044	0.016	0.006	0.011
Parton Shower	0.003	0.016	0.005	0.008
ISR/FSR	0.003	0.002	0.002	0.002
RFS	0.015	0.003	0.001	0.002
CR	0.002	0.007	0.003	0.004
UE	0.002	0.004	<0.001	0.001
Mass variation	0.001	<0.001	0.001	0.001
PDF	0.013	0.004	0.003	0.004
JES	0.002	0.002	0.001	0.001
JER	0.001	0.002	0.003	0.002
JEFF	0.005	0.001	0.001	<0.001
JVF	0.003	0.001	0.001	0.001
EL_ENERGY_RES	0.008	0.002	0.001	0.001
EL_ENERGY_SC	0.005	0.001	0.001	0.001
EL_RECO	0.003	0.002	0.001	0.001
EL_TRIGGER_SF	0.003	0.002	0.001	0.001
MU_MS/MU_ID	<0.001	0.002	0.001	0.001
MU_SCALE	0.003	0.003	0.002	0.001
MU_RECO_SF	0.004	0.001	0.001	0.001
MU_TRIGGER_SF	0.004	0.001	<0.001	<0.001
PILEUP	0.009	0.002	0.004	0.004
CELL_OUT/SOFTJET	0.035	0.019	0.003	0.010
BTAG_SF	0.003	0.002	0.001	0.001
ST_NORM	0.001	0.001	0.002	0.002
DB_NORM	0.001	<0.001	0.003	0.002
ZJETS_NORM	0.007	0.005	0.004	0.005
MU_REAL_EFF	0.009	0.004	0.004	0.003
MU_FAKE_EFF	0.016	0.004	0.020	0.013
EL_REAL_EFF	0.011	0.002	0.011	0.007
EL_FAKE_EFF	0.007	0.005	0.003	0.003
Total Syst	0.067	0.034	0.027	**0.025**
Full	0.144	0.080	0.056	0.046

Table H.2.: The detailed results of the combination of the measurements of the three top-quark pair decay channels. The highlighted values are the central charge asymmetry values $A_{C,t\bar{t}}$, the statistical error (*Stat* and the full systematic error (*Total Syst*). The data is selected according to the pretag event selection.

Uncertainty	ee-Channel	$\mu\mu$-Channel	$e\mu$-Channel	Combination
$A_{C,t\bar{t}}$	0.034	-0.023	0.094	**0.055**
Stat	0.151	0.074	0.051	**0.041**
MC Generator	0.023	0.016	0.005	0.009
Parton Shower	0.002	0.016	0.005	0.008
ISR/FSR	0.007	0.002	0.003	0.003
RFS	0.013	0.005	0.002	0.003
CR	0.004	0.005	0.001	0.002
UE	0.008	0.004	0.001	0.002
Mass variation	0.001	0.001	<0.001	0.001
PDF	0.005	0.007	0.003	0.004
JES	0.014	0.001	0.004	0.003
JER	0.011	0.001	0.003	0.003
JEFF	0.016	0.002	0.003	0.004
JVF	0.014	0.007	0.003	0.005
EL_ENERGY_RES	0.015	0.007	0.004	0.003
EL_ENERGY_SC	0.013	0.007	0.003	0.003
EL_RECO	0.014	0.007	0.003	0.003
EL_TRIGGER_SF	0.014	0.007	0.003	0.003
MU_MS/MU_ID	0.001	0.002	0.002	0.002
MU_SCALE	0.014	0.001	0.003	0.002
MU_RECO_SF	0.014	0.007	0.003	0.003
MU_TRIGGER_SF	0.015	0.007	0.003	0.003
PILEUP	0.018	0.003	0.004	0.004
CELL_OUT/SOFTJET	0.050	0.019	0.003	0.010
BTAG_SF	0.015	0.007	0.004	0.005
ST_NORM	0.007	0.001	0.002	0.002
DB_NORM	0.008	<0.001	0.001	0.001
ZJETS_NORM	0.009	0.002	0.002	0.002
MU_REAL_EFF	0.003	0.002	0.016	0.010
MU_FAKE_EFF	0.008	0.001	0.010	0.007
EL_REAL_EFF	0.026	0.003	0.009	0.006
EL_FAKE_EFF	0.005	0.004	0.019	0.012
Total Syst	0.084	0.038	0.032	**0.029**
Full	0.172	0.083	0.060	0.050

Table H.3.: The detailed results of the combination of the measurements of the three top-quark pair decay channels. The highlighted values are the central charge asymmetry values $A_{C,t\bar{t}}$, the statistical error (*Stat* and the full systematic error (*Total Syst*). The data is selected according to the tagged event selection.

Bibliography

[1] Werner Bernreuther and Zong-Guo Si. "Top quark and leptonic charge asymmetries for the Tevatron and LHC". In: arXiv:1205.6580 [hep-ph] (Sept. 2012).

[2] CDF Collaboration. "Observation of Top Quark Production in $\bar{p}p$ Collisions with the Collider Detector at Fermilab". In: *Phys. Rev. Lett.* 74 (14 1995), pp. 2626–2631. DOI: 10.1103/PhysRevLett.74.2626. URL: http://link.aps.org/doi/10.1103/PhysRevLett.74.2626.

[3] D0 Collaboration. "Observation of the Top Quark". In: *Phys. Rev. Lett.* 74 (14 1995), pp. 2632–2637. DOI: 10.1103/PhysRevLett.74.2632. URL: http://link.aps.org/doi/10.1103/PhysRevLett.74.2632.

[4] V. M. Abazov et al. "Forward-backward asymmetry in top quark-antiquark production". In: *Phys. Rev. D* 84 (11 2011), p. 112005. DOI: 10.1103/PhysRevD.84.112005. URL: http://link.aps.org/doi/10.1103/PhysRevD.84.112005.

[5] ATLAS Collaboration. *Measurement of the charge asymmetry in top quark pair production in pp collisions at $\sqrt{s} = 7$ TeV using the ATLAS detector*. Tech. rep. ATLAS-CONF-2011-106. Geneva: CERN, 2011.

[6] ATLAS Collaboration and CMS Collaboration. *Combination of ATLAS and CMS $t\bar{t}$ charge asymmetry measurements using LHC proton-proton collisions at 7 TeV*. Tech. rep. CMS-PAS-TOP-14-006. Geneva: CERN, 2014.

[7] ATLAS Collaboration. "Observation of a new particle in the search for the Standard Model Higgs boson with the ATLAS detector at the LHC". In: arXiv:1207.7214v2 [hep-ex] (Aug. 2012).

[8] The CMS Collaboration. "Observation of a new boson at a mass of 125 GeV with the CMS experiment at the LHC". In: arXiv:1207.7235 [hep-ex] (July 2012).

[9] Mary K. Gaillard and Paul D. Grannis and Frank J. Sciulli. "The Standard Model of Particle Physics". In: arXiv:hep-ph/9812285v1 (Dec. 1998).

[10] Michael E. Peskin and Daniel V. Schroeder. *An Introduction to Quantum Field Theory*. Westview Press, 1995.

[11] David Griffiths. *Introduction to Elementary Particles*. 2nd revised edition. Wiley-VCH Verlag GmbH and CO. KGaA, 2008.

[12] ATLAS Collaboration. "A search for flavour changing neutral currents in top-quark decays in pp collision data collected with the ATLAS detector at $\sqrt{s} = 7$ TeV ". English. In: *Journal of High Energy Physics* 2012.9, 139 (2012). DOI: 10.1007/JHEP09(2012)139. URL: http://dx.doi.org/10.1007/JHEP09\%282012\%29139.

[13] J. Beringer et al. (Particle Data Group). *The Standard Model of Particle Physics*. Tech. rep. Phys. Rev. D86, 010001. 2012. URL: http://pdg.lbl.gov/.

[14] H. Fritzsch, Murray Gell-Mann, and H. Leutwyler. "Advantages of the Color Octet Gluon Picture". In: *Phys.Lett.* B47 (1973), pp. 365–368. DOI: 10.1016/0370-2693(73)90625-4.

[15] E. Noether. "Invariante Variationsprobleme". In: *Nachrichten von der Gesellschaft der Wissenschaften zu Göttingen, Mathematisch-Physikalische Klasse* 1918 (1918), pp. 235–257. URL: http://eudml.org/doc/59024.

[16] Peter Schmüser. *Feynman-Graphen und Eichtheorien fuer Experimentalphysiker*. Berlin Heidelberg New York London Paris Tokyo: Springer, 1995.

[17] Sheldon L. Glashow. "Partial-symmetries of weak interactions". In: *Nuclear Physics* 22.4 (1961), pp. 579–588. ISSN: 0029-5582. DOI: http://dx.doi.org/10.1016/0029-5582(61)90469-2. URL: http://www.sciencedirect.com/science/article/pii/0029558261904692.

[18] Abdus Salam. "Weak and Electromagnetic Interactions". In: *Conf.Proc.* C680519 (1968), pp. 367–377.

[19] Steven Weinberg. "A Model of Leptons". In: *Phys. Rev. Lett.* 19 (21 1967), pp. 1264–1266. DOI: 10.1103/PhysRevLett.19.1264. URL: http://link.aps.org/doi/10.1103/PhysRevLett.19.1264.

[20] Nicola Cabibbo. "Unitary Symmetry and Leptonic Decays". In: *Phys. Rev. Lett.* 10 (12 1963), pp. 531–533. DOI: 10.1103/PhysRevLett.10.531. URL: http://link.aps.org/doi/10.1103/PhysRevLett.10.531.

[21] S.L. Glashow, J. Iliopoulos, and L. Maiani. "Weak Interactions with Lepton-Hadron Symmetry". In: *Phys.Rev.* D2 (1970), pp. 1285–1292. DOI: 10.1103/PhysRevD.2.1285.

[22] M. Kobayashi and T. Maskawa. "CP-Violation in the Renormalization Theory of Weak interaction". In: *Progress of Theoretical Physics* 49 (1973), pp. 652–657.

[23] Nicola Cabibbo. "Unitary Symmetry and Leptonic Decays". In: *Phys. Rev. Lett.* 10 (12 1963), pp. 531–533. DOI: 10.1103/PhysRevLett.10.531. URL: http://link.aps.org/doi/10.1103/PhysRevLett.10.531.

[24] ATLAS Collaboration et al. "First combination of Tevatron and LHC measurements of the top-quark mass". In: arXiv:1403.4427. ATLAS-CONF-2014-008. CDF-NOTE-11071. CMS-PAS-TOP-13-014. D0-NOTE-6416 (Mar. 2014). Comments: 34 pages, 7 figures.

[25] CMS Collaboration. *Public Results of measurements of the properties of the new boson with a mass near 125 GeV*. July 2014. URL: https://twiki.cern.ch/twiki/bin/view/CMSPublic/Hig13005TWiki.

[26] ATLAS Collaboration. "Measurement of the Higgs boson mass from the $H \to \gamma\gamma$ and $H \to ZZ^* \to 4\ell$ channels with the ATLAS detector using 25 fb^{-1} of pp collision data". In: (2014). eprint: 1406.3827.

[27] ATLAS Collaboration. *Search for the Standard Model Higgs boson produced in association with top quarks and decaying to $b\bar{b}$ in pp collisions at $\sqrt{s} = 8$ TeV with the ATLAS detector at the LHC*. Tech. rep. ATLAS-CONF-2014-011. Geneva: CERN, 2014.

[28] ATLAS Collaboration. *Search for $H \to \gamma\gamma$ produced in association with top quarks and constraints on the top quark-Higgs boson Yukawa coupling using data taken at 7 TeV and 8 TeV with the ATLAS detector*. Tech. rep. ATLAS-CONF-2014-043. Geneva: CERN, 2014.

[29] LHC Higgs Cross Section Working Group. *LHC Higgs Cross Section Working Group*. July 2014. URL: https://twiki.cern.ch/twiki/bin/view/LHCPhysics/CrossSections.

[30] Bogdan Malaescu and Pavel Starovoitov. "Evaluation of the Strong Coupling Constant α_s Using the ATLAS Inclusive Jet Cross-Section Data". In: *Eur. Phys. J. C* 72.arXiv:1203.5416. CERN-PH-EP-2012-064. DESY-12-039 (Feb. 2012). Comments: 14 pages, 6 figures, p. 2041. 14.

[31] Antonio Pich. "Review of α_s determinations". In: arXiv:1303.2262 [hep-ph] (Mar. 2013).

[32] M. L. Perl et al. "Evidence for Anomalous Lepton Production in $e^+ e^-$ Annihilation". In: *Phys. Rev. Lett.* 35 (22 1975), pp. 1489–1492. DOI: 10.1103/PhysRevLett.35.1489. URL: http://link.aps.org/doi/10.1103/PhysRevLett.35.1489.

[33] S. W. Herb et al. "Observation of a Dimuon Resonance at 9.5 GeV in 400-GeV Proton-Nucleus Collisions". In: *Phys. Rev. Lett.* 39 (5 1977), pp. 252–255. DOI: 10.1103/PhysRevLett.39.252. URL: http://link.aps.org/doi/10.1103/PhysRevLett.39.252.

[34] A. Quadt. "Top quark physics at hadron colliders". In: *The European Physical Journal C - Particles and Fields* 48.3 (1434-6044 2006), pp. 835–1000. DOI: 10.1140/epjc/s2006-02631-6. URL: http://dx.doi.org/10.1140/epjc/s2006-02631-6.

[35] Nadolsky et al. "Implications of CTEQ global analysis for collider observables". In: *Phys.Rev.* D78 (2008), p. 013004. DOI: 10.1103/PhysRevD.78.013004. eprint: 0802.0007.

[36] S Catani. *Aspects of QCD, from the Tevatron to the LHC*. Tech. rep. hep-ph/0005233. CERN-TH-2000-073. Geneva: CERN, 2000.

[37] Matteo Cacciari et al. *Top-pair production at hadron colliders with next-to-next-to-leading logarithmic soft-gluon resummation*. Tech. rep. CERN-PH-TH/2011-277, TTK-11-54. 2011.

[38] Peter Bärnreuther, Michal Czakon, and Alexander Mitov. "Percent Level Precision Physics at the Tevatron: First Genuine NNLO QCD Corrections to $q\bar{q} \to t\bar{t}$". In: *Phys. Rev. Lett.* 109 (13 2012), p. 132001. DOI: 10.1103/PhysRevLett.109.132001. URL: http://link.aps.org/doi/10.1103/PhysRevLett.109.132001.

[39] ATLAS Collaboration. *Combination of ATLAS and CMS top-quark pair cross section measurements using up to 1.1 fb-1 of data at 7 TeV*. Tech. rep. ATLAS-CONF-2012-134. Geneva: CERN, 2012.

[40] ATLAS Collaboration. "Public Summary Plots of from the ATLAS physics group". In: (July 2014). URL: https://atlas.web.cern.ch/Atlas/GROUPS/PHYSICS/CombinedSummaryPlots/TOP/.

[41] C. P. Yuan. "New method to detect a heavy top quark at the Fermilab Tevatron". In: *Phys. Rev. D* 41 (1 1990), pp. 42–51. DOI: 10.1103/PhysRevD.41.42. URL: http://link.aps.org/doi/10.1103/PhysRevD.41.42.

[42] Martin C. Smith and Scott S. Willenbrock. "QCD and Yukawa corrections to single-top-quark production via $q\bar{q} \to t\bar{b}$". In: *Phys. Rev. D* 54 (11 1996), pp. 6696–6702. DOI: 10.1103/PhysRevD.54.6696. URL: http://link.aps.org/doi/10.1103/PhysRevD.54.6696.

[43] S. Cortese and R. Petronzio. "The single top production channel at Tevatron energies". In: *Physics Letters B* 253.3–4 (1991), pp. 494–498. ISSN: 0370-2693. DOI: http://dx.doi.org/10.1016/0370-2693(91)91758-N. URL: http://www.sciencedirect.com/science/article/pii/037026939191758N.

[44] T. Stelzer and S. Willenbrock. "Single-top-quark production via $qq \to tb$". In: *Physics Letters B* 357.1–2 (1995), pp. 125–130. ISSN: 0370-2693. DOI: http://dx.doi.org/10.1016/0370-2693(95)00861-E. URL: http://www.sciencedirect.com/science/article/pii/037026939500861E.

[45] Nikolaos Kidonakis. "Next-to-next-to-leading-order collinear and soft gluon corrections for t-channel single top quark production". In: arXiv:1103.2792 [hep-ph] (Mar. 2011).

[46] Nikolaos Kidonakis. "NNLL resummation for s-channel single top quark production". In: arXiv:1001.5034 [hep-ph] (Jan. 2010).

[47] Nikolaos Kidonakis. *Two-loop soft anomalous dimensions for single top quark associated production with a W^- or H^-*. Tech. rep. arXiv:1005.4451 [hep-ph]. 2010.

[48] ATLAS Collaboration. *Measurement of the t-channel single top-quark and top-antiquark production cross-sections and their ratio in pp collisions at $\sqrt{s}$ = 7 TeV*. Tech. rep. ATLAS-CONF-2012-056. Geneva: CERN, 2012.

[49] DB Ta. *Single top-quarks at the LHC*. Tech. rep. ATL-PHYS-PROC-2013-051. Geneva: CERN, 2013.

[50] ATLAS Collaboration. "Evidence for the associated production of a W boson and a top quark in ATLAS at $\sqrt{s} = 7\,\text{TeV}$". In: *Physics Letters B* 716.1 (2012), pp. 142–159. ISSN: 0370-2693. DOI: http://dx.doi.org/10.1016/j.physletb.2012.08.011. URL: http://www.sciencedirect.com/science/article/pii/S0370269312008489.

[51] ATLAS Collaboration. *Measurement of t-Channel Single Top-Quark Production in pp Collisions at $\sqrt{s} = 8$ TeV with the ATLAS detector*. Tech. rep. ATLAS-CONF-2012-132. Geneva: CERN, 2012.

[52] Daniel Wicke. "Properties of the Top Quark". In: *Eur.Phys.J.* C71 (2011), p. 1627. DOI: 10.1140/epjc/s10052-011-1627-0. eprint: 1005.2460.

[53] ATLAS Collaboration. *Measurement of the $t\bar{t}$ production cross section in the all-hadronic channel in ATLAS with $\sqrt{s}$ = 7 TeV data*. Tech. rep. ATLAS-CONF-2012-031. Geneva: CERN, 2012.

[54] Martin C. Smith and Scott S. Willenbrock. "Top-quark Pole Mass". In: *Phys. Rev. Lett.* 79 (20 1997), pp. 3825–3828. DOI: 10.1103/PhysRevLett.79.3825. URL: http://link.aps.org/doi/10.1103/PhysRevLett.79.3825.

[55] ATLAS Collaboration. *Measurement of the top quark charge in pp collisions at $\sqrt{s}$ = 7 TeV in the ATLAS experiment*. Tech. rep. ATLAS-CONF-2011-141. Geneva: CERN, 2011.

[56] Andrzej Czarnecki, Jürgen G. Körner, and Jan H. Piclum. "Helicity fractions of W bosons from top quark decays at next-to-next-to-leading order in QCD". In: *Phys. Rev. D* 81 (11 2010), p. 111503. DOI: 10.1103/PhysRevD.81.111503. URL: http://link.aps.org/doi/10.1103/PhysRevD.81.111503.

[57] ATLAS Collaboration. "Measurement of the W boson polarization in top quark decays with the ATLAS detector". English. In: *Journal of High Energy Physics* 2012.6, 88 (2012). DOI: 10.1007/JHEP06(2012)088. URL: http://dx.doi.org/10.1007/JHEP06\%282012\%29088.

[58] ATLAS Collaboration. *Combination of the ATLAS and CMS measurements of the W-boson polarization in top-quark decays*. Tech. rep. ATLAS-CONF-2013-033. Geneva: CERN, 2013.

[59] ATLAS Collaboration. "Observation of Spin Correlation in $t\bar{t}$ Events from pp Collisions at $\sqrt{s} = 7$ TeV Using the ATLAS Detector". In: *Phys. Rev. Lett.* 108 (21 2012), p. 212001. DOI: 10.1103/PhysRevLett.108.212001. URL: http://link.aps.org/doi/10.1103/PhysRevLett.108.212001.

[60] ATLAS Collaboration. *Measurements of spin correlation in top-antitop quark events from proton-proton collisions at s = 7 TeV using the ATLAS detector*. Tech. rep. ATLAS-CONF-2013-101. Geneva: CERN, 2013.

[61] U. Baur et al. "Probing electroweak top quark couplings at hadron colliders". In: *Phys. Rev. D* 71 (5 2005), p. 054013. DOI: 10.1103/PhysRevD.71.054013. URL: http://link.aps.org/doi/10.1103/PhysRevD.71.054013.

[62] S. Chatrchyan et al. "Measurement of associated production of vector bosons and top quark-antiquark pairs in pp collisions at $\sqrt{s}$=7 TeV". In: *Phys. Rev. Lett.* 110 (17 2013), p. 172002. DOI: 10.1103/PhysRevLett.110.172002. URL: http://link.aps.org/doi/10.1103/PhysRevLett.110.172002.

[63] M.V. Garzelli et al. "$t\bar{t}W^{\pm} + t\bar{t}$ Z hadroproduction at NLO accuracy in QCD with Parton Shower and Hadronization effects". English. In: *Journal of High Energy Physics* 2012.11, 56 (2012). DOI: 10.1007/JHEP11(2012)056. URL: http://dx.doi.org/10.1007/JHEP11\%282012\%29056.

[64] ATLAS Collaboration. *Measurement of the inclusive $t\bar{t}\gamma$ cross section with the ATLAS detector*. Tech. rep. ATLAS-CONF-2011-153. Geneva: CERN, 2011.

[65] Kirill Melnikov, Markus Schulze, and Andreas Scharf. "QCD corrections to top quark pair production in association with a photon at hadron colliders". In: *Phys. Rev. D* 83 (7 2011), p. 074013. DOI: 10.1103/PhysRevD.83.074013. URL: http://link.aps.org/doi/10.1103/PhysRevD.83.074013.

[66] J. H. Kühn and G. Rodrigo. "Charge asymmetry of heavy quarks at hadron colliders". In: *Phys. Rev. D* 59 (5 1999), p. 054017. DOI: 10.1103/PhysRevD.59.054017. URL: http://link.aps.org/doi/10.1103/PhysRevD.59.054017.

[67] Oscar Antuñano, Johann H. Kühn, and Germán Rodrigo. "Top quarks, axigluons, and charge asymmetries at hadron colliders". In: *Phys. Rev. D* 77 (1 2008), p. 014003. DOI: 10.1103/PhysRevD.77.014003. URL: http://link.aps.org/doi/10.1103/PhysRevD.77.014003.

[68] Valentin Ahrens et al. "Renormalization-Group Improved Predictions for Top-Quark Pair Production at Hadron Colliders". In: arXiv:1003.5827 [hep-ph] (Mar. 2010).

[69] Johann H. Kuhn and German Rodrigo. "Charge asymmetries of top quarks at hadron colliders revisited". In: arXiv:1109.6830v2 [hep-ph] (Dec. 2011).

[70] D0 Collaboration. *Asymmetries in t tbar production: LHC versus Tevatron*. Tech. rep. D0 Note 6425-CONF. 2014. URL: http://www-d0.fnal.gov/Run2Physics/WWW/results/prelim/TOP/T100/T100.pdf.

[71] T. Aaltonen et al. "Measurement of the top quark forward-backward production asymmetry and its dependence on event kinematic properties". In: *Phys. Rev. D* 87 (9 2013), p. 092002. DOI: 10.1103/PhysRevD.87.092002. URL: http://link.aps.org/doi/10.1103/PhysRevD.87.092002.

[72] Paola Ferrario and Germáno Rodrigo. "Massive color-octet bosons and the charge asymmetries of top quarks at hadron colliders". In: *Phys. Rev. D* 78 (9 2008), p. 094018. DOI: 10.1103/PhysRevD.78.094018. URL: http://link.aps.org/doi/10.1103/PhysRevD.78.094018.

[73] Jonathan L. Rosner. "Prominent decay modes of a leptophobic Z". In: *Physics Letters B* 387.1 (1996), pp. 113–117. ISSN: 0370-2693. DOI: http://dx.doi.org/10.1016/0370-2693(96)01022-2. URL: http://www.sciencedirect.com/science/article/pii/0370269396010222.

[74] Debajyoti Choudhury et al. "Top production at the Tevatron/LHC and nonstandard, strongly interacting spin one particles". In: *Physics Letters B* 657.1–3 (2007), pp. 69–76. ISSN: 0370-2693. DOI: http://dx.doi.org/10.1016/j.physletb.2007.09.057. URL: http://www.sciencedirect.com/science/article/pii/S0370269307012117.

[75] German Rodrigo and Paola Ferrario. "Charge asymmetry: a theory appraisal". In: arXiv:1007.4328v1 [hep-ph] (July 2010).

[76] German Rodrigo. "Axigluon signatures at hadron colliders". In: arXiv:0803.2992v1 [hep.ph] (Mar. 2008).

[77] Bastian Diaz and Alfonso R. Zerwekh. "Axigluon Phenomenology using ATLAS dijet data". In: arXiv:1308.0166v1 [hep-ph] (Aug. 2013).

[78] Pavel Fileviez Pérez, Hoernisa Iminniyaz, and Germán Rodrigo. "Proton stability, dark matter, and light color octet scalars in adjoint $SU(5)$ unification". In: *Phys. Rev. D* 78 (1 2008), p. 015013. DOI: 10.1103/PhysRevD.78.015013. URL: http://link.aps.org/doi/10.1103/PhysRevD.78.015013.

[79] Ilja Dor šner et al. "Light colored scalars from grand unification and the forward-backward asymmetry in $t\bar{t}$ production". In: *Phys. Rev. D* 81 (5 2010), p. 055009. DOI: 10.1103/PhysRevD.81.055009. URL: http://link.aps.org/doi/10.1103/PhysRevD.81.055009.

[80] Jing Shu, Tim M. P. Tait, and Kai Wang. "Explorations of the top quark forward-backward asymmetry at the Tevatron". In: *Phys. Rev. D* 81 (3 2010), p. 034012. DOI: 10.1103/PhysRevD.81.034012. URL: http://link.aps.org/doi/10.1103/PhysRevD.81.034012.

[81] Dong-Won Jung and P. Ko and Jae Sik Lee and Soo-hyeon Nam. "Model independent analysis of the forward-backward asymmetry of top quark production at the Tevatron". In: arXiv:0912.1105v2 [hep-ph] (June 2010).

[82] Marcela Carena et al. "Z' Gauge Bosons at the Fermilab Tevatron". In: *Phys. Rev. D* 70 (9 2004), p. 093009. DOI: 10.1103/PhysRevD.70.093009. URL: http://link.aps.org/doi/10.1103/PhysRevD.70.093009.

[83] ATLAS Collaboration. *Measurement of the top quark pair production charge asymmetry in proton-proton collisions at $\sqrt{s} = 7$ TeV using the ATLAS detector*. Tech. rep. ATLAS-CONF-2013-078. Geneva: CERN, 2013.

[84] J.A. Aguilar-Saavedra and M. Pérez-Victoria. "No like-sign tops at Tevatron: Constraints on extended models and implications for the asymmetry". In: *Physics Letters B* 701.1 (2011), pp. 93–100. ISSN: 0370-2693. DOI: http://dx.doi.org/10.1016/j.physletb.2011.05.037. URL: http://www.sciencedirect.com/science/article/pii/S0370269311005545.

[85] ATLAS Collaboration. "Search for same-sign top-quark production and fourth-generation down-type quarks in pp collisions at $\sqrt{s} = 7$ TeV with the ATLAS detector". English. In: *Journal of High Energy Physics* 2012.4, 69 (2012). DOI: 10.1007/JHEP04(2012)069. URL: http://dx.doi.org/10.1007/JHEP04\%282012\%29069.

[86] J. A. Aguilar-Saavedra and M. Perez-Victoria. "Asymmetries in t tbar production: LHC versus Tevatron". In: arXiv:1105.4606v4 [hep-ph] (Dec. 2011).

[87] Oliver Sim Brüning et al. *LHC Design Report Vol.2*. Geneva: CERN, 2004.

[88] Maximilien Brice. "Cross section of an LHC dipole in the tunnel." 2011.

[89] *CERN Archive CERN-ARCH-LEP-01-001 to 06-017*. Geneva: CERN, 1978–2000.

[90] Oliver Sim Brüning et al. *LHC Design Report Vol.1*. Geneva: CERN, 2004.

[91] Christiane Lefvre. "The CERN accelerator complex." Dec. 2008.

[92] ATLAS Collaboration. "Improved luminosity determination in pp collisions at $\sqrt{s} = 7$ TeV using the ATLAS detector at the LHC". In: arXiv:1302.4393v2 [hep-ex] (July 2013).

[93] ATLAS Collaboration. *ATLAS Twiki Page: ATLAS Experiment Public Results (Luminosity)*. Jan. 2014. URL: https://twiki.cern.ch/twiki/bin/view/AtlasPublic/LuminosityPublicResults.

[94] *ATLAS detector and physics performance: Technical Design Report, 1. oai:cds.cern.ch:391176*. Technical Design Report ATLAS. http://atlasinfo.cern.ch/Atlas/GROUPS/PHYSICS/TDR/access.html. Geneva: CERN, 1999.

[95] Doug Schouten and Michel Vetterli. *In Situ Jet Calibration and the Effects of Pileup in ATLAS*. Tech. rep. ATL-PHYS-INT-2007-011. ATL-COM-PHYS-2007-057. Geneva: CERN, 2007.

[96] JC Chollet. *Elementary Pile up. oai:cds.cern.ch:685694*. Tech. rep. ATL-CAL-95-075. ATL-AC-PN-75. Geneva: CERN, 1995.

[97] P Cortese et al. *ALICE Electromagnetic Calorimeter Technical Design Report*. Tech. rep. CERN-LHCC-2008-014. ALICE-TDR-014. Geneva: CERN, 2008.

[98] G L Bayatian et al. *CMS Physics Technical Design Report Volume I: Detector Performance and Software*. Technical Design Report CMS. Geneva: CERN, 2006.

[99] R Antunes-Nobrega et al. *LHCb reoptimized detector design and performance: Technical Design Report. oai:cds.cern.ch:630827*. Technical Design Report LHCb. Geneva: CERN, 2003.

[100] O Adriani et al. *LHCf experiment: Technical Design Report*. Technical Design Report LHCf. Geneva: CERN, 2006.

[101] V Berardi et al. *Total cross-section, elastic scattering and diffraction dissociation at the Large Hadron Collider at CERN: TOTEM Technical Design Report. oai:cds.cern.ch:704349*. Technical Design Report TOTEM. Geneva: CERN, 2004.

[102] ATLAS Collaboration. "The ATLAS Experiment at the CERN Large Hadron Collider". In: *J. Instrum.* 3 (2008). Also published by CERN Geneva in 2010, S08003. 437 p.

[103] *The ATLAS Experiment at the CERN Large Hadron Collider*. 2008 JINST 3 S08003 `http://jinst.sissa.it/LHC/ATLAS/2008_JINST_3_S08003.pdf`. 2008.

[104] Norbert Wermes and G Hallewel. *ATLAS pixel detector: Technical Design Report*. Technical Design Report ATLAS. Geneva: CERN, 1998.

[105] Joao Pequenao. "Computer generated image of the ATLAS inner detector". Mar. 2008.

[106] ATLAS Collaboration. *ATLAS pixel detector electronics and sensors*. 2008 JINST 3 P07007 `http://iopscience.iop.org/1748-0221/3/07/P07007`. 2008.

[107] *ATLAS inner detector: Technical Design Report, 1*. Technical Design Report ATLAS. Geneva: CERN, 1997.

[108] Joao Pequenao. "Computer Generated image of the ATLAS calorimeter". Mar. 2008.

[109] Joao Pequenao. "Computer generated image of the ATLAS Muon subsystem". Mar. 2008.

[110] ATLAS Collaboration. "ATLAS muon spectrometer: Technical design report". In: CERN-LHCC-97-22, ATLAS-TDR-10 (1997).

[111] (Ed.) Duckeck G. et al. "ATLAS computing: Technical design report". In: CERN-LHCC-2005-022, ATLAS-TRD-017 (2005).

[112] ATLAS Collaboration. "Electron performance measurements with the ATLAS detector using the 2010 LHC proton-proton collision data". In: arXiv:1110.3174v2 [hep-ex] (Mar. 2012).

[113] ATLAS Collaboration. *Performance of the ATLAS Electron and Photon Trigger in p-p Collisions at $\sqrt{s} = 7$ TeV in 2011*. Tech. rep. ATLAS-CONF-2012-048. Geneva: CERN, 2012.

[114] ATLAS Collaboration. *Expected electron performance in the ATLAS experiment*. Tech. rep. ATL-PHYS-PUB-2011-006. Geneva: CERN, 2011.

[115] ATLAS Collaboration. "Readiness of the ATLAS Liquid Argon Calorimeter for LHC Collisions". In: arXiv:0912.2642v4 [physics.ins-det] (May 2010).

[116] ATLAS Collaboration. *ATLAS Twiki Page: Calorimeter Isolation Corrections*. Jan. 2014. URL: `https://twiki.cern.ch/twiki/bin/viewauth/AtlasProtected/CaloIsolationCorrection`.

[117] ATLAS Collaboration. *ATLAS Twiki Page: Top Common Objects 2011, Top WG object definitions*. Jan. 2014. URL: `https://twiki.cern.ch/twiki/bin/viewauth/AtlasProtected/TopCommonObjects2011`.

[118] ATLAS Collaboration. "Electron performance measurements with the ATLAS detector using the 2010 LHC proton-proton collision data". In: *Eur. Phys. J. C* 72.arXiv:1110.3174. CERN-PH-EP-2011-117 (Oct. 2011). Comments: 33 pages plus author list (45 pages total), 24 figures, 12 tables, submitted to Eur. Phys. J. C, 1909. 45 p.

[119] B Acharya et al. *Object selection and calibration, background estimations and MC samples for the Autumn 2012 Top Quark analyses with 2011 data*. Tech. rep. ATL-COM-PHYS-2012-1197. Geneva: CERN, 2012.

[120] ATLAS Collaboration. *Performance of the ATLAS muon trigger in 2011*. Tech. rep. ATLAS-CONF-2012-099. Geneva: CERN, 2012.

[121] B Acharya et al. *Object selection and calibration, background estimations and MC samples for the Winter 2012 Top Quark analyses with 2011 data*. Tech. rep. ATL-COM-PHYS-2012-224. Geneva: CERN, 2012.

[122] Matteo Cacciari, Gavin P. Salam, and Gregory Soyez. "The anti-k_t jet clustering algorithm". In: arXiv:0802.1189v2 [hep-ph] (Apr. 2008).

[123] Gavin P. Salam and Gregory Soyez. "A practical Seedless Infrared-Safe Cone jet algorithm". In: arXiv:0704.0292v2 [hep-ph] (Apr. 2007).

[124] ATLAS Collaboration. "Jet energy measurement with the ATLAS detector in proton-proton collisions at $\sqrt{s} = 7\,\text{TeV}$". In: arXiv:1112.6426v1 [hep-ex] (Dec. 2011).

[125] N Makovec. *Selection of jets produced in proton-proton collisions with the ATLAS detector using 2011 data*. Tech. rep. ATL-COM-PHYS-2012-067. Geneva: CERN, 2012.

[126] ATLAS Collaboration. *Commissioning of the ATLAS high-performance b-tagging algorithms in the 7 TeV collision data*. Tech. rep. ATLAS-CONF-2011-102. Geneva: CERN, 2011.

[127] ATLAS Collaboration. *Expected performance of the ATLAS experiment: detector, trigger and physics*. Geneva: CERN, 2009.

[128] ATLAS Collaboration. *Measurement of the b-tag Efficiency in a Sample of Jets Containing Muons with* $5\,fb^{1}$ *of Data from the ATLAS Detector*. Tech. rep. ATLAS-CONF-2012-043. Geneva: CERN, 2012.

[129] ATLAS Collaboration. "Performance of missing transverse momentum reconstruction in proton-proton collisions at $\sqrt{s} = 7\,\text{TeV}$ with ATLAS". In: arXiv:1108.5602v2 [hep-ex] (Dec. 2011).

[130] Stefano Frixione and Bryan R. Webber. "Matching NLO QCD computations and parton shower simulations". In: *Journal of High Energy Physics* 2002.06 (2002), p. 029. URL: http://stacks.iop.org/1126-6708/2002/i=06/a=029.

[131] Michelangelo L. Mangano et al. "ALPGEN, a generator for hard multiparton processes in hadronic collisions". In: *JHEP* 0307 (2003), p. 001. eprint: hep-ph/0206293.

[132] Borut Paul Kersevan and Elzbieta Richter-Wąs. "The Monte Carlo event generator AcerMC versions 2.0 to 3.8 with interfaces to PYTHIA 6.4, HERWIG 6.5 and ARIADNE 4.1". In: *Computer Physics Communications* 184.3 (2013), pp. 919–985. ISSN: 0010-4655. DOI: 10.1016/j.cpc.2012.10.032. URL: http://www.sciencedirect.com/science/article/pii/S001046551200375X.

[133] Gennaro Corcella et al. "HERWIG 6: an event generator for hadron emission reactions with interfering gluons (including supersymmetric processes)". In: *Journal of High Energy Physics* 2001.01 (2001), p. 010. URL: http://stacks.iop.org/1126-6708/2001/i=01/a=010.

[134] S. Mrenna T. Sjostrand and P. Skands. *PYTHIA 6.4 physics and manual*. JHEP 05 026, 2006.

[135] J. M. Butterworth, J. R. Forshaw, and M. H. Seymour. *Multiparton Interactions in Photoproduction at HERA. Z. Phys.* Tech. rep. Z. Phys., C72:637646. 1996.

[136] Piotr Golonka and Zbigniew Was. "PHOTOS Monte Carlo: a precision tool for QED corrections in Z and W decays". In: arXiv:hep-ph/0506026v2 (June 2005).

[137] Allison J. et al. *Geant4 developments and applications*. Tech. rep. Nuclear Science, IEEE Transactions Vol.53 issue 1. 2006.

[138] C Debenedetti. *Concepts for fast large scale Monte Carlo production for the ATLAS experiment*. Tech. rep. ATL-SOFT-PROC-2013-032. Geneva: CERN, 2013.

[139] Rená Brun F.Rademakers. "ROOT: An Object-Oriented Data Analysis Framework". In: Linux Journal (1998).

[140] RD Schaffer et al. *Optimization and performance measurements of ROOT-based data formats in the ATLAS experiment*. Tech. rep. ATL-SOFT-PROC-2011-027. Geneva: CERN, 2011.

[141] Hung-Liang Lai et al. *New parton distributions for collider physics*. Tech. rep. Phys.Rev.D82:074024. 2010.

[142] ATLAS Collaboration. *New ATLAS event generator tunes to 2010 data*. Tech. rep. ATL-PHYS-PUB-2011-008. Geneva: CERN, 2011.

[143] M.Aliev et al. "HATHOR Hadronic Top and Heavy quarks cross section calculator Comput. Phys. Commun.182 (2011) 1034-1046". In: arXiv:1007:1327 [hep-ph] (2010).

[144] A. Sherstnev and R.S. Thorne. "Different PDF approximations useful for LO Monte Carlo generators". In: arXiv:0807.2132 [hep-ph] (July 2008).

[145] ATLAS Collaboration. *ATLAS tunes of PYTHIA 6 and Pythia 8 for MC11*. Tech. rep. ATL-PHYS-PUB-2011-009. Geneva: CERN, 2011.

[146] ATLAS Collaboration. *ATLAS Twiki Page: TopMC2011, Single Top Baseline Samples*. Jan. 2014. URL: `https://twiki.cern.ch/twiki/bin/viewauth/AtlasProtected/TopMC11#Single_Top_Baseline_Samples`.

[147] Johan Alwall et al. "MadGraph 5 : Going Beyond". In: arXiv:1106.0522v1 (June 2011).

[148] Borut Paul Kersevan and Elzbieta Richter-Was. "Improved Phase Space Treatment of Massive Multi-Particle Final States". In: arXiv:hep-ph/0405248v2 (Nov. 2004).

[149] ATLAS Collaboration. *ATLAS Twiki Page: Heavy flavour overlap removal tool twiki*. Jan. 2014. URL: `https://twiki.cern.ch/twiki/bin/viewauth/AtlasProtected/HforTool`.

[150] J Butterworth et al. *Single Boson and Diboson Production Cross Sections in pp Collisions at* $\sqrt{s} = 7$ *TeV*. Tech. rep. ATL-COM-PHYS-2010-695. Geneva: CERN, 2010.

[151] ATLAS Collaboration. *ATLAS Twiki Page: TopMC2011, Diboson Herwig Baseline Samples*. Jan. 2014. URL: `https://twiki.cern.ch/twiki/bin/viewauth/AtlasProtected/TopMC11#Diboson_Production_in_MC11_Produ`.

[152] John M Campbell and R. K. Ellis. "MCFM for the Tevatron and the LHC". In: arXiv:1007.3492 (July 2010).

[153] ATLAS Collaboration. *ATLAS Twiki Page: Pile-Up Reweighting for MC11 Analysis and $\sqrt{s} = 7\,TeV$ MC simulation*. Jan. 2014. URL: https://twiki.cern.ch/twiki/bin/viewauth/AtlasProtected/PileupReweighting.

[154] ATLAS Collaboration. *Updated Luminosity Determination in pp Collisions at $\sqrt{s} = 7\,TeV$ using the ATLAS Detector*. Tech. rep. ATLAS-CONF-2011-011. Geneva: CERN, 2011.

[155] J Adelman et al. "ATLAS Offline Data Quality Monitoring". In: *J. Phys.: Conf. Ser.* 219.ATL-SOFT-PROC-2009-003 (July 2009), 042018. 6 p.

[156] ATLAS Collaboration. *ATLAS Run Queries, Detailed Information on Atlas Runs*. Jan. 2014. URL: http://atlas-runquery.cern.ch.

[157] ATLAS Collaboration. *ATLAS Twiki Page: GoodRunLists for Analysis*. Jan. 2014. URL: https://twiki.cern.ch/twiki/bin/viewauth/AtlasProtected/GoodRunListsForAnalysis.

[158] ATLAS Collaboration. *ATLAS Twiki Page: dAOD Skimming Criteria for 2011 Data*. Jan. 2014. URL: https://twiki.cern.ch/twiki/bin/viewauth/AtlasProtected/TopPhysD2PDEventFilters.

[159] ATLAS Collaboration. "Measurement of the top quark pair production cross section in pp collisions at $\sqrt{s} = 7\,\text{TeV}$ in dilepton final states with ATLAS". In: arXiv:1108.3699v2 [hep-ex], CERN-PH-EP-2011-103 (Dec. 2011).

[160] Johannes Erdmann et al. "A likelihood-based reconstruction algorithm for top-quark pairs and the KLFitter framework". In: arXiv:1312.5595 [hep-ex] (Dec. 2013).

[161] Jörg Meyer. *Measurement of the Top Quark Mass unsing Dilepton Events and a Neutrino Weighting Algorithm with the D0 Experiment at the Tevatron (RUM II)*. Tech. rep. PhD Thesis. Rheinische Friedrich-Willhelms-Universitaet Bonn, 2007.

[162] Johannes Erdmann et al. *ATLAS Twiki Page: KLFitter*. Jan. 2014. URL: https://twiki.cern.ch/twiki/bin/viewauth/AtlasProtected/KLFitter.

[163] Johannes Erdmann et al. *ATLAS Twiki Page: KLFitter Transfer Functions*. Jan. 2014. URL: https://twiki.cern.ch/twiki/bin/viewauth/AtlasProtected/KLFitterTF.

[164] Allen Caldwell, Daniel Kollar, and Kevin Kroeninger. "BAT - The Bayesian Analysis Toolkit". In: arXiv:0808.2552 [physics.data-an] (Aug. 2008).

[165] Nicholas Metropolis et al. *Equation of State Calculations by Fast Computing Machines*. Tech. rep. Journal of Chem. Phys. 21 1087. 1953.

[166] S. Kirkpatrick, C.D. Gelatt Jr., and M.P. Vecchi. *Optimization by Simulated Annealing*. Tech. rep. Science, Vol. 220, pp. 671680. 1983.

[167] V. Blobel and E. Lohrmann. *Statistische und numerische Methoden der Datenanalyse*. Teubner Stuttgart, Leipzig: Teubner Studienbücher, 1998.

[168] O. Behnke, K. Kröninger und G. Schott, and T. Schörner-Sadenius. *Data Analysis in High Energy Physics*. WILEY-VCH Verlag GmbH und Co. KGaA: Teubner Studienbücher, 2013.

[169] G. D'Agostini. "A Multidimensional unfolding method based on Bayes' theorem". In: *Nucl.Instrum.Meth.* A362 (1995), pp. 487–498. DOI: 10.1016/0168-9002(95)00274-X.

[170] Andreas Hoecker and Vakhtang Kartvelishvili. “SVD Approach to Data Unfolding”. In: arXiv:hep-ph/9509307v2 (Sept. 1995).

[171] G.E. Forsythe, M.A. Malcom, and C.B. Moler. *Computer Methods for Mathematical Computations*. Englewood Cliffs: Prentice-Hall Inc., 1977.

[172] C.E. Lawson and R.J. Hanson. *Solving Least Square Problems*. Englewood Cliffs: Prentice-Hall Inc., 1974.

[173] Tim Adye. “Unfolding algorithms and tests using RooUnfold”. In: arXiv:1105.1160v1 (May 2011).

[174] Mark Owen et al. *ATLAS Twiki Page: Top Systematic Uncertainties*. July 2014. URL: `https://twiki.cern.ch/twiki/bin/viewauth/AtlasProtected/TopSystematicUncertainties2011`.

[175] Peter Z. Skands. “Tuning Monte Carlo generators: The Perugia tunes”. In: *Phys. Rev. D* 82 (7 2010), p. 074018. DOI: `10.1103/PhysRevD.82.074018`. URL: `http://link.aps.org/doi/10.1103/PhysRevD.82.074018`.

[176] ATLAS Collaboration et al. “First combination of Tevatron and LHC measurements of the top-quark mass”. In: arXiv:1403.4427 (Mar. 2014).

[177] Michiel Botje et al. “The PDF4LHC Working Group Interim Recommendations”. In: arXiv:1101.0538 [hep-ph] (2011).

[178] ULC HEP Group. *PDF4LHC Recommendations for LHC cross section calculations*. July 2014. URL: `http://www.hep.ucl.ac.uk/pdf4lhc/`.

[179] A.D. Martin et al. “Parton distributions for the LHC”. In: arXiv:0901.0002v3 [hep-ph] (July 2009).

[180] The NNPDF Collaboration: Richard D. Ball et al. “Unbiased global determination of parton distributions and their uncertainties at NNLO and at LO”. In: arXiv:1107.2652v4 [hep-ph] (Nov. 2011).

[181] Duc Bao Ta. *ATLAS Twiki: Top PDF Uncertainty*. July 2014. URL: `https://twiki.cern.ch/twiki/bin/view/AtlasProtected/TopPdfUncertainty#PDF_weight_ntuples`.

[182] ATLAS Collaboration. *In-situ pseudorapidity intercalibration for evaluation of jet energy scale uncertainty using dijet events in proton-proton collisions at* $\sqrt{s} = 7$ *TeV*. Tech. rep. ATLAS-CONF-2011-014. Geneva: CERN, 2011.

[183] J A Aguilar-Saavedra et al. *Measurement of the ttbar charge asymmetry in the lepton+jets channel*. Tech. rep. ATL-COM-PHYS-2012-1399. Editorial board TOPQ-2012-17. Geneva: CERN, 2012.

[184] A Leyko. *Measurement of the b-jet tagging efficiency using top quark pair events with ATLAS data*. Tech. rep. ATL-PHYS-PROC-2012-281. Geneva: CERN, 2012.

[185] S van der Meer. *Calibration of the effective beam height in the ISR*. Tech. rep. CERN-ISR-PO-68-31. ISR-PO-68-31. Geneva: CERN, 1968.

[186] ATLAS Collaboration. “Luminosity Determination in pp Collisions at $\sqrt{s} = 7$ TeV Using the ATLAS Detector at the LHC”. In: arXiv:1101.2185 [hep-ex] (Jan. 2011).

[187] The Luminosity Group. *Improved Luminosity Determination in* **pp** *Collisions at* $\sqrt{s} = 7$ *TeV using the ATLAS Detector at the LHC*. Tech. rep. ATL-COM-PHYS-2012-821. Transferred from ATLAS-COM-CONF-2012-086 (https://cdsweb.cern.ch/record/1452595). Geneva: CERN, 2012.

[188] B Acharya et al. *Estimation of the W+Jets Background for Top Quark Re-Discovery in the Single Lepton+Jets Channel*. Tech. rep. ATL-COM-PHYS-2010-834. Supporting document for top paper. Geneva: CERN, 2010.

[189] Duc Bao Ta. *Private Communication (top fake estimation group)*. Tech. rep. 2014.

[190] Georgios Choudalakis. "Fully Bayesian Unfolding". In: arXiv:1201.4612v4 [physics.data-an] (May 2012).

[191] ATLAS Collaboration. "Measurement of the top quark pair production charge asymmetry in proton-proton collisions at 7 TeV using the ATLAS detector". In: arXiv:1311.6724 [hep-ex] (Mar. 2014).

[192] Michal Czakon and Alexander Mitov. "NNLO corrections to top-pair production at hadron colliders: the all-fermionic scattering channels". In: arXiv:1207.0236 [hep-ph] (2012).

[193] Michal Czakon and Alexander Mitov. "NNLO corrections to top pair production at hadron colliders: the quark-gluon reaction". In: arXiv:1210.6832 [hep-ph] (2012).

[194] Michal Czakon, Paul Fiedler, and Alexander Mitov. "The total top quark pair production cross-section at hadron colliders through $\mathcal{O}(\alpha_S^4)$". In: arXiv:1303.6254 [hep-ph] (2013).

[195] M.Czakon and A.Mitov. "Top++: a program for the calculation of the top-pair cross-section at hadron colliders". In: arXiv:1112.5675 [hep-ph] (2011).

[196] A.D. Martin et al. "Parton distributions for the LHC, Eur. Phys. J. C63 (2009) 189-285". In: arXiv: 0901.0002 [hep-ph] (2009).

[197] A.D. Martin et al. "Uncertainties on α_S in global PDF analyses, and implications for predicted hadronic cross sections, Eur. Phys. J. C64 (2009) 653-680". In: arXiv:0905.3531 [hep-ph] (2009).

[198] Jun Gao et al. "The CT10 NNLO Global Analysis of QCD". In: arXiv:1302.6246 [hep-ph] (2013).

[199] Richard D. Ball et al. "Parton distributions with LHC data". In: arXiv:1207.1303 [hep-ph] (2012).

[200] ATLAS Collaboration. *ATLAS Twiki Page: TopMC2011, Z+jets Baseline Samples*. Jan. 2014. URL: `https://twiki.cern.ch/twiki/bin/viewauth/AtlasProtected/TopMC11#Z_jets`.

[201] ATLAS Collaboration. *ATLAS Twiki Page: TopMC2011, Full list of MC11 samples*. July 2014. URL: `https://twiki.cern.ch/twiki/bin/viewauth/AtlasProtected/TopMC11`.

[202] Louis Lyons, Duncan Gibaut, and Peter Clifford. "How to Combine Correlated Estimates of a Single Physical Quantity". In: *Nucl.Instrum.Meth.* A270 (1988), p. 110. DOI: 10.1016/0168-9002(88)90018-6.

[203] Andrea Valassi. "Combining correlated measurements of several different physical quantities". In: *Nucl. Instrum. Methods Phys. Res., A* 500 (2003), pp. 391–405.

[204] Richard Nisius. "BLUE. A software package to combine correlated estimates withon ROOT. Program manual version 1.9.2". In: (May 2014). URL: `http://blue.hepforge.org/`.